University of Tennessee, Knoxville

TRACE: Tennessee Research and Creative Exchange

Doctoral Dissertations

Graduate School

5-2009

Passive and active components development for broadband applications

Song Lin
University of Tennessee

Follow this and additional works at: https://trace.tennessee.edu/utk_graddiss

Recommended Citation

Lin, Song, "Passive and active components development for broadband applications. " PhD diss., University of Tennessee, 2009.
https://trace.tennessee.edu/utk_graddiss/6005

This Dissertation is brought to you for free and open access by the Graduate School at TRACE: Tennessee Research and Creative Exchange. It has been accepted for inclusion in Doctoral Dissertations by an authorized administrator of TRACE: Tennessee Research and Creative Exchange. For more information, please contact trace@utk.edu.

To the Graduate Council:

I am submitting herewith a dissertation written by Song Lin entitled "Passive and active components development for broadband applications." I have examined the final electronic copy of this dissertation for form and content and recommend that it be accepted in partial fulfillment of the requirements for the degree of Doctor of Philosophy, with a major in Electrical Engineering.

Aly E. Fathy, Major Professor

We have read this dissertation and recommend its acceptance:

Accepted for the Council:

Carolyn R. Hodges

Vice Provost and Dean of the Graduate School

(Original signatures are on file with official student records.)

To the Graduate Council:

I am submitting herewith a dissertation written by Song Lin entitled "Passive and Active Components Development for Broadband Applications." I have examined the final electronic copy of this dissertation for form and content and recommend that it be accepted in partial fulfillment of the requirements for the degree of Doctor of Philosophy, with a major in Electrical Engineering.

Aly E. Fathy, Major Professor

We have read this dissertation

and recommend its acceptance:

Paul B. Crilly

Mohamed Mahfouz

Marshall O. Pace

Accepted for the Council:

Carolyn R. Hodges

Vice Provost and Dean of the Graduate School

(Original signatures are on file with official student records.)

Passive and Active Components Development for Broadband Applications

A Dissertation
Presented for the
Doctor of Philosophy Degree
The University of Tennessee, Knoxville

Song Lin
May 2009

Dedication

This dissertation is dedicated to my family. I would like to thank for my mother, Ronggui Deng and my lovely wife, Jing Song for their supports over last several years.

Acknowledgements

The writing of a dissertation can be a challenging experience, and was, obviously, not possible without the personal and practical support of numerous people. Thus, my sincerest gratitude is given to my wife, my parents, my friends, my companions, and my superiors in the Electrical Engineering and Computer Science (EECS) Department at the University of Tennessee for their support and patience over the last few years.

I wish to thank Profs. Marshall Pace and Paul Crilly of the EECS Department, and Prof. Mohamed Mahfouz of the Mechanical, Aerospace, and Biomedical Department at the University of Tennessee (UT) for inspiring and encouraging me to pursue a career in Electrical Engineering, and for their participation as members of my dissertation committee.

My research for this dissertation was made more efficient, and also more extensive, through the use of several research facilities. Thus, I gladly express my gratitude to Dr. Gamal Hegazi and the staff at Rockwell Collins in Cedar Rapids, IA, for providing partial financial support for the LINC project, supporting my training at their facilities and providing continued guidance over the last few years. I would also like to thank Dr. Murat Eron of Miteq Inc., Hauppauge, NY, for both his partial financial support and the opportunities provided by the two summer internships at the Miteq facilities. Included in my thanks is Mr. Ray Pengally of Cree Inc, North Carolina for providing unlimited support on GaN devices, modeling, and design, and Dr. Yoon Kang for assistance in conducting high frequency measurements at Oak Ridge National Lab. On the other hand, most of my work relied heavily on the publication of Journal and Symposium papers. For this, I am thankful for having received much assistance in editing these publications, and this dissertation, from Ms. Shara Galloway.

Many people on the faculty and staff at the UT Graduate School and in EECS assisted and encouraged me in various ways during the course of my studies. I am especially grateful to Profs. Samir El-Ghazaly, Syed Islam, Benjamin Blalock, and Donald Bouldin for all they have taught me. I was also greatly inspired pedagogically by Prof. Marshall Pace for whom I was a Graduate Teaching Assistant for more than three years. I would also like thank the students whom I was privileged to teach, and who also taught me.

My graduate studies would not have been the same without the social and academic challenges and diversions provided by all my student-colleagues in EECS. I am particularly thankful to my friends Dr. Songnan Yang and Mr. Adel Elsherbini. We not only studied, relaxed, and traveled together, but they were even willing to assist me with portions of this dissertation and thus, provided me with useful experiences and thoughtful insights. My enormous debt of gratitude cannot be repaid to Dr. Suren

Gigoyan, Fulbright visiting scholar to UT, who not only helped me with my work on dielectric image guides, but also provided many suggestions and substantive challenges to assist me in improving my experimental and theoretical arguments.

Finally, this dissertation would not have been possible without the expert guidance of my esteemed advisor, Prof. Aly E. Fathy. Not only was he readily available for me, as he is so generously for all his students, but he always read and responded to the drafts of each chapter of my work more quickly than I could have hoped. His oral and written comments were always extremely perceptive, helpful, and appropriate. Of course, despite all assistance provided by Prof. Fathy and the others, I alone remain responsible for the content of the following dissertation, including any errors or omissions which may unwittingly remain.

Abstract

Recently, GaN HEMTs have been proven to have numerous physical properties, resulting in transistors with greatly increased power densities when compared to the other well-established FET technologies. This advancement spurred research and product development towards power-band applications that require both high power and high efficiency over the wide band. Even though the use of multiple narrow band PAs covering the whole band has invariably led to better performance in terms of efficiency and noise, there is an associated increase in cost and in the insertion loss of the switches used to toggle between the different operating bands. The goal, now, of the new technology is to replace the multiple narrow band PAs with one broadband PA that has a comparable efficiency performance.

In our study here, we have investigated a variety of wide band power amplifiers, including class AB PAs and their implementation in distributed and feedback PAs. Additionally, our investigation has included switching-mode PAs as they are well-known for achieving a relatively high efficiency. Besides having a higher efficiency, they are also less susceptible to parameter variations and could impose a lower thermal stress on the transistors than the conventional-mode PAs. With GaN HEMTs, we have demonstrated: a higher than 37 dBm output power and a more than 30% drain efficiency over 0.02 to 3 GHz for the distributed power amplifier; a higher than 30 dBm output power with more than a 22% drain efficiency over 0.1 to 5 GHz for the feedback amplifier; and at least a 43 dBm output power with a higher than 63% drain efficiency over 0.05 to 0.55 GHz for the class D PA.

In many communication applications, however, achieving both high efficiency and linearity in the PA design is required. Therefore, in our research, we have evaluated several linearization and efficiency enhancement techniques. We selected the LInear amplification with Nonlinear Components (LINC) approach. Highly efficient combiner and novel efficiency enhancement techniques like the power recycling combiner and adaptive bias LINC schemes have been successfully developed and verified to achieve a combined high efficiency with a relatively high linearity.

Table of Contents

List of Figures

List of Tables

List of Symbols and Acronyms

ACPR	Adjacent channel power ratio
ADS	Advance Design System
CMCD	Current-Mode Class D power amplifier
DE	Drain Efficiency
DSP	Digital Signal Processing
EER	Envelope Elimination and Restoration
ET	Envelope Tracking
EVM	Error vector Magnitude
FM	Frequency Modulation
GaN	Gallium Nitride
HEMT	High Electron Mobility Transistor
IMD	Inter-Modulation Distortion
LINC	Linear Amplification with Nonlinear Components
MIC	Microwave Integrated Circuit
MMIC	Monolithic Microwave Integrated Circuit
NPR	Noise-Power Ratio
OFDM	Orthogonal Frequency Division Multiplexing
PA	Power Amplifier
PAE	Power Added Efficiency
PAR	Peak to Average Ratio
PD	Pre-Distortion
PDF	Probability Distribution Function
QAM	Quadrature Amplitude Modulation
RF	Radio Frequency
SCS	Signal Component Separator
SMPA	Switching-Mode Power Amplifier
VMCD	Voltage-Mode Class D power amplifier

Chapter 1 Introduction

1.1 Background and the State of the Art

The ever-increasing growth in the wireless communication market, such as digital microwave radio, cellular and wireless infrastructure, CATV, test instrumentation, defense and space, and satellite communications applications, plus many more, requires that future RF/Microwave/Millimeter wave front-ends operate over wider bandwidths and at higher frequencies. To function effectively for all these services with different frequencies and formats, transparent broadband transmitting and receiving architectures are required. Excellent examples of these architectures exist. One is software defined radios and another is the fourth generation "4G" converged wireless service RF front ends.

A vital component in any communication system is the power amplifier. In most cases, the PA is not just a small-signal amplifier driven into saturation, but there exists a variety of different PAs that can be designed for maximum efficiency or maximum output power while sustaining linear performance to minimize the signal distortion. These PAs are usually divided into two operational modes. One type is the conventional mode, such as A, AB, B, and C classes, while the other is the switching-mode classes such as D, E, and F, etc. Here, the classes A and AB are linear PAs. The other classes are nonlinear PAs.

Recently, gallium nitride high electron mobility transistor (GaN HEMT) devices have been added as an excellent candidate for designing highly efficient and extraordinary high power PAs. They are proven to have numerous physical properties, resulting in transistors with greatly increased power densities when compared to other, well-established FET technologies (e.g. GaAs or Si). The GaN devices have a relatively high power density and smaller die size due to the superior thermal and voltage breakdown properties of the material utilized, and the feasibility of growing it on high thermal conductivity SiC substrates. Furthermore, the GaN devices, when compared to silicon LDMOS FETs and GaAs MESFETs of similar output power, have smaller parasitic capacitances. The smaller parasitic capacitances and associated large input and load impedances assist the GaN HEMTs in exhibiting a broader bandwidth than the bandwidth demonstrated by other technologies. Additionally, their higher breakdown voltage/supply voltage, combined with a low supply current, make GaN HEMTs the optimal choice to handle high power output. This new technological advancement turned research and product development towards power-band applications that require both high power and wide band performance.

The new implementation of this technology is different from the previous implementation that relied on switched narrow-band PAs to cover the whole wide-band frequency range, but it rather address wide-band PAs. Narrow-band PAs invariably have better performance in terms of efficiency and noise. However, the use of multiple narrowband amplifiers increases the cost of production and the associated increase in the insertion loss of the switches used to toggle between the different bands for transmission and reception operation. The goal of the new activity is to replace narrow band PAs with a broadband PA that has comparable efficiency performance.

A need for linearity has become apparent, and is now one of the principal factors in the design of modern PAs. Linear amplification is required when the signal contains both amplitude and phase modulation. Nonlinearities distort the amplified signal, resulting in splatter into the adjacent channels, as well as errors in detection. Amplitude nonlinearity causes the instantaneous output amplitude, or envelope, to differ in shape from its corresponding input. Thus, linearity is of great concern for communication systems in order to ensure signal integrity and reliable performance. Linearity amplification is created by either a chain of linear PAs (classes A/AB), or a combination of nonlinear PAs with external technologies, such as LInear amplification with Nonlinear Components (LINC) or Envelope Elimination and Restoration (EER).

In our study, we have investigated a variety of wide-band PAs, including the class AB PA. Their implementation in distributed and feedback amplifiers has been explored for wideband applications, because of their broadband performance and low circuit sensitivities while sustaining an adequate linear performance. The amplifiers have been employed in both broadband communication systems and measurement equipment for many years. Their conventional designs, however, are based on utilizing low power devices, and are generally analyzed using small signal analysis. Significant impact on the progress of broadband PAs can be achieved by developing distributed power amplifiers and feedback PAs which utilize power devices like the recently developed GaN HEMTs instead of conventional small-signal devices.

Our investigation also included switching-mode power amplifiers (SMPA) which are well-known to achieve a relatively high efficiency. A comparison between various switching-mode PA operations (class D, E and F) that employ the transistors as switches and conventional mode PAs that employ the transistors as current-sources shows that the efficiencies of the SMPAs are substantially higher. Therefore, SMPAs can compete with the conventional mode PAs in LINC applications. Besides having a higher efficiency, SMPAs are also less susceptible to parameter variations and could impose a lower thermal stress on the transistors than the conventional mode PAs.

In many applications, however, simultaneously achieving both high efficiency and linearity in the PA design is required. Therefore, in our research, we have evaluated several efficiency enhancement techniques such as the Doherty amplifier, LINC, EER, and Envelope Tracking (ET). However, signals with a time-varying envelope, as used in base stations, require complex architectures such as Chireix (LINC) or EER/ET. Here, we have selected the LINC approach, believing it to be a good candidate to simultaneously achieve both relatively high efficiency and linearity. In an LINC approach, the two input amplifiers which create the nonlinear input waveforms are designed, from a DC power perspective, to be efficient. Their two nonlinear output signals are properly combined to produce a waveform that is relatively linear. Subsequently, it is essential to develop highly efficient, extremely wideband networks as part of our study to combine the outputs of the individual PAs to achieve the desired output power, high efficiency, and linearity.

In our study, we have explored the impact of the combiner's selection on overall system performance. The basic parameters of the studied power combiners are bandwidth, insertion, and return losses. Generally, power combiners are either non-isolated (without isolation between the input ports) or isolated (with adequate isolation between the input ports). In practical circuits, the non-isolated power combiner designed for high efficiency operation will produce a significant interaction between the two combined PAs, thus leading to an unacceptable distortion. Alternatively, to preserve the high linearity, the employment of power combiners with adequate isolation between the two input ports must occur. However, this might degrade overall efficiency, so a compromise is required.

To combine our approach with the current trend in developing wireless systems operating at various frequencies, including RF/ microwave and millimeter wave frequencies, it is imperative to identify and overcome the various challenges presented. First, based on Table 1-1, most of the wireless communication systems today tend to utilize higher frequencies, such as 60 GHz, or even 90 GHz. Second, we need to overcome other hurdles in our pursuit for improved operating systems, such as mm-wave utilization. This includes the availability of efficient active devices for power amplifications, low noise devices, and low-cost passive devices.

Here, we investigate two low-cost technologies for developing such high frequency systems—the dielectric image guide and the substrate integrated waveguides. Dielectric image guides (DIG) are excellent candidates for developing a low-cost alternative technology for mm-wave applications. They have an extremely low loss and wideband operation. The basic components for mm-wave systems include power dividers, modulators, and circulators. They can be integrated as part of the antennas for wideband millimeter wave communication systems. The other low-cost technology which can also be utilized at higher frequencies is the substrate integrated waveguides (SIW). Utilization of such technologies should

Table 1-1 Frequency Allocations

Frequency range	Application
VHF/UHF (30-512 MHz)	Software-Defined Radio
(900/1800 MHz)	GSM
1900 MHz	CDMA
2.3 & 3.5 GHz	WIMAX
3-10 GHz	UWB
Ku/K/Ka band	Satellite Communications
60 GHz	MIMO system

assist in lowering the cost of developing commercial wireless components at these frequencies. Otherwise, they are prohibitively expensive.

1.2 Our Contributions

In an effort to address the various challenges associated with developing efficient high power transmitting and receiving over wideband, we have preformed extensive research to address the above challenges.

1.2.1 In the area of high power amplifiers

Background:

Recently, GaN HEMTs have been extensively researched. The achieved higher thermal conductivity of the GaN on the SiC substrate makes it superior to its GaAs or Si counterparts, especially for high power and high temperature applications. GaN HEMTs have higher power density, higher break down voltage, and lower parasitic capacitance, making it suitable for high power and high efficiency SMPA implementations, even at higher frequencies. At the same time, GaN HEMTs have great potential for broadband applications.

- Broadband Power Amplifiers

For a low-cost and efficient operation, it is important to have power amplifiers suitable for multiband operations. The feedback amplifier employs the shunt feedback between the gate and drain of the active device used in the circuit to achieve wideband applications. However, the feedback amplifier usually has a low gain, output power, and drain efficiency due to the negative feedback. On the other hand, distributed power amplifiers are generally excellent candidates for ultra wideband applications due to their broadband performance and low circuit sensitivities. Their conventional designs have already been employed in both broadband communication systems and measurement equipment for many years. Conventional distributed amplifier designs, similar to conventional feedback amplifier design, however, are based on utilizing low power devices, and therefore, generally analyzed using small signal analysis. Our efforts here are to use high gain, high efficiency GaN HEMTs, and bias the device at class AB mode, then apply large signal analysis to optimize the output performance both for the feedback and distributed power amplifiers.

Contributions:

- *Developed a GaN HEMT feedback class AB power amplifier using hybrid microwave integrated circuit technology. The measured P_{3dB} output power is higher than 30 dBm and the drain efficiency is higher than 22% over 0.1 to 5 GHz.*

- *Developed a discrete ultra wideband GaN HEMT distributed power amplifier (DPA) with over a 5 W (37 dBm) output power and drain efficiency exceeding 30% in the 0.02 to 3 GHz frequency range*

The design details and experiment results are shown in Chapter 2.

➢ Class D Power Amplifiers

We have picked class D amplifiers to research for their potential use in our wide band investigation, sponsored by Rockwell Collins, Inc. Various narrow band class D PAs have been developed and published [1-6], but here, we are addressing their wideband implementation.

Contributions:

- *Developed a wideband class D power amplifier based on GaN HMETs which achieved a 63% drain efficiency and at least 20W over 50 to 550 MHz bandwidth.*

Wideband implementation is a challenging task. We parallel this effort to the effort of the Rockwell Collins' group, where we have investigated the use of a Cree GaN device operating at 28 V. The

Rockwell Collins' team investigated a Eudyna GaN device and pushed its operating point to 50V. The design details and flow will be shown in Chapter 4.

1.2.2 In the area of power combining

Background:

Recently, there has been an increased interest in developing highly linear and efficient high power transmitters for a wide variety of VHF/UHF wireless applications. Out-phasing amplifier architecture is sometimes utilized, where two out-phase constant-envelope signals are used to drive two nonlinear SMPAs. Their optimally designed nonlinear output signals are properly combined to sustain simultaneous high linearity and efficiency performance. Generally, these combiners are either non-isolated or isolated. In our efforts, we have focused on the VHF/UHF frequency range. Rather than using wire-wound transformer combiners that have an unacceptable insertion loss at their self-resonant frequency, limiting their usable frequency range, or using the lumped elements with limited power handling capabilities, or quarter-wave length transformers that are bulky at low frequencies, we chose to use ferrite loaded coaxial line segments for fabricating transmission line transformers to circumvent size, bandwidth, and power handling constraints.

Contributions:

- *Developed equivalent circuits and 3D EM models to simulate the combiner structures to reduce the design period.*
- *Developed a wideband low-loss non-isolated combiner.*
- *Applied a novel flux canceling scheme to improve the isolation between the two input ports and to prevent core saturation based on EM analysis for isolated combiner.*
- *Developed a power recycling combiner to improve the overall system efficiency.*

Extensive EM analysis has been performed to achieve an extremely wide band performance with very low insertion losses. The developed design operates over a 30 to 450 MHz bandwidth with less than a 0.5 dB insertion loss. The details of the power combiner design and modeling will be presented in Chapter 5.

1.2.3 In the area of LINC transmitter

Background:

In modern digital communication systems, various modulation schemes have been applied to achieve high spectrum efficiency. The schemes include a high order M-ary quadrature amplitude modulation (QAM) and orthogonal frequency division multiplexing (OFDM). However, these signals are characterized by high peak-to-average power ratios (PAPRs) which exploit deep envelope fluctuations. These unavoidable phenomena constitute a serious problem for the nonlinear behavior of power amplifiers. They also cause a major problem for modern communication systems as it is essential to achieve a high linear-efficient RF amplification. Therefore, linearity is crucial in minimizing signal distortion in order to maintain low levels of error vector magnitude (EVM) and an adjacent channel leakage ratio (ACLR). At the same time, efficiency enhancement techniques are needed to achieve the highest possible performance and cost savings for the next generation of base-station applications. The LINC approach is a good candidate in order to simultaneously achieve both a relatively high efficiency and a high linearity. After development by Cox [2], the LINC approach has been applied to a variety of wireless applications. Multiple variations/modifications on the LINC approach have been proposed to improve the linearity and efficiency of modern wireless communication systems. However, no perfect solution to achieve both a high efficiency and high linearity for high PAPRs signal yet exists. Here, our contributions are focused primarily on improving the LINC transmitter and developing new concepts.

Contributions:

- *Used advanced EDA tools to analyze the overall efficiency of the LINC transmitter with various types of combiners in terms of narrow band and wideband operation.*
- *Proposed and analyzed a novel adaptive bias LINC transmitter, and then used advance EDA tools to verify the concept.*

This novel adaptive bias LINC transmitter can simultaneously achieve high efficiency and relatively high linearity, even with high PAPRs signal. The details of the adaptive bias LINC will be presented in Chapter 6.

1.2.4 *In the area of low cost microwave/mm wave implementations*

- SIW Background

Conventionally, metallic waveguides are utilized to fabricate high performance antennas and associated feed networks for their extremely low loss performance. However, they are bulky, heavy, and expensive to fabricate. Hence, for consumer-type applications, we propose to use a low-cost alternative technology -- substrate integrated waveguides (SIWs) structures fabricated on printed circuit boards. Where SIW sidewalls are constructed from lined via holes, rather than solid fences, the SIW technology is simple, less expensive, and renders light structures.

Contributions:

- *Developed a UWB Vivaldi antenna array with a novel GCPW to SIW transition to demonstrate the use of SIW technology*.

In our implementation, the SIW structure was optimally designed and fabricated on a thick substrate to minimize conductor losses. The array employs a SIW binary divider to minimize the insertion loss of the feeding network. It has a common Grounded Coplanar Waveguide (GCPW) feed to sustain a satisfactory input match while preventing higher order modes excitation over a wide frequency range. The use of optimized T-junctions, and the integration of a GCPW feed, has also led to an even more improved performance with a significant loss reduction. The developed Vivaldi antenna array, which has a high gain, narrow beam width in the E-plane & H-plane, and relatively wide bandwidth, is extremely useful for ultra wideband antenna applications such as See-Through-Wall Imaging, Indoor Localization Systems, and Breast Tumor Detection. Here, the Vivaldi antenna array design can easily be scaled to an mm-wave.

- DIG Background

The Dielectric Image Guide (DIG) lines are excellent candidates for use in developing a low-cost alternative technology for millimeter wave applications. The use of a high dielectric constant image guide (with the dimension $a<b$) makes it easier to couple the guides to alumina, silicon, GaAs, and ferrite dielectric resonators, thus initiating a new set of applications.

Contributions:

- *Developed various dielectric image guide components for millimeter wave applications, such as low-cost feed networks and antennas.*
- *Demonstrated reconfigurability using optical techniques.*
- *Developed accurate models for various components based on EM-CAD tools.*

Here, we designed an alternative wideband metal waveguide-to-dielectric image guide transition first. Next, we developed low-loss optically controlled devices (such as variable attenuators). At the same time, we also applied the DIG as a feeding structure to design diverse types of antennas and arrays, including beam forming and end-fire antennas.

Examples of using low-cost technology, with design, simulation, and fabrication details, will be given in Chapter 7.

Chapter 2 Broadband Power Amplifier Development using GaN HEMTs

2.1 Introduction

PAs are conventionally separated into two broad categories according to their operation bandwidth: narrow band and broad band PAs. They are categorized according to the bandwidth over which they can provide a constant output power. Usually, the narrow band PA is defined by a relative bandwidth of less than 1% (bandwidth/center frequency). Meanwhile, the broadband PA is defined by over a 10% relative bandwidth. However, in this chapter, the broadband PA used refers to a PA that has a bandwidth of over an octave (f_H /f_L=10 and relative bandwidth=164%). To achieve both high power and a broad bandwidth, both the circuit architecture and device technology need to be considered. The most popular and well-established circuit techniques employed in the design of the broadband amplifiers using hybrid technology [1] are:

- Reactively matched circuit;
- Distributed circuit;
- Feedback circuit;
- Lossy matched circuit

At the same time, a gallium nitride high electron mobility transistor (GaN HEMT) has been recently introduced with a superior performance over other transistor technologies. In this chapter, both feedback PAs and distributed PAs based on GaN HEMTs will be discussed in detail.

2.2 Classes of PA Operation

A high efficiency power amplifier (PA) is the heart of the transmitter. To illustrate the single PA transistor performance, let us consider its several operating regions. When the input power is less than a certain threshold level, the PA is not conducting or in the cut-off region. Meanwhile, when the input power exceeds a certain threshold level, the PA starts to conduct and linearly amplifies the input signal or operating in the linear region. When the input power increases and reaches the clip region (soft/hard clip region, usually refers to P_{1dB}), the output power is not linearly proportional to the input power any longer, but the output power would still increase. Finally the input power reaches the saturation level where the output power flattens to a maximum level (saturation region, usually refers to P_{sat}), and if it does not flatten out, begins to decrease.

The threshold level is determined by the biasing circuitry and is basically defined by its class of operation (class A, AB, B, and C). Other classes of operation are switching mode power amplifiers (SMPA), named class D, E, F, G, H, and S. However, these classes refer to the circuit topology rather than to its biasing. Figure 2.1 shows the different operating regions of the above mentioned power amplifiers. Generally, the power amplifiers can be divided into linear and non-linear power amplifiers. Their related linearity and efficiency are shown in Figure 2.2.

The most popular class of PAs applicable for broadband applications is class A, AB, and B. The bias point, the optimized load line, the drain efficiency, and waveform of the three classes of PAs will be given in Table 2-1 and Figure 2.3. Choosing an optimal load can lead to the minimization of the total device periphery required for a given RF output power. A smaller device periphery means a lower parasitic input and output capacitance, and subsequently, a wider associated bandwidth. As we will see in the next section, a GaN device has a high power density, which allows it to have the same output power as other devices while having a smaller device's periphery. This allows a GaN application to reap the benefits associated with high power and high frequency.

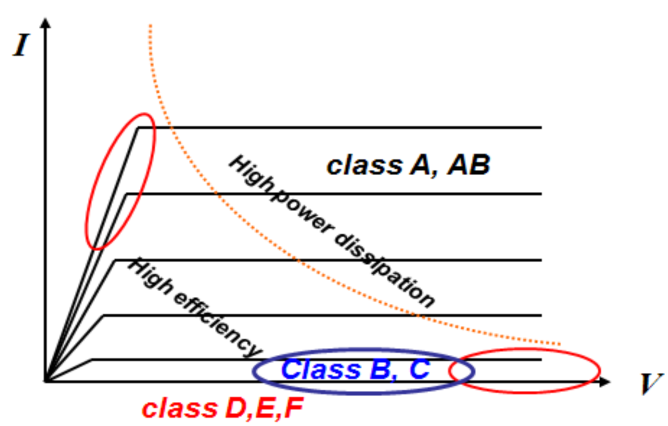

Figure 2.1 Operation regions for different power amplifiers' classes

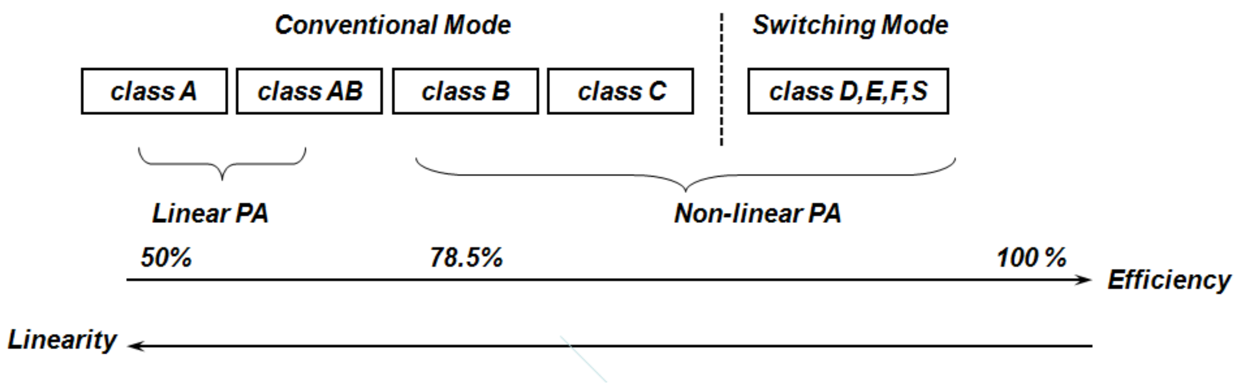

Figure 2.2 Power amplifiers' classes [3]

Table 2-1 Class A, AB, B PA basic parameters

class	Bias point	Optimum load	Maximum output power (P_{out})	Maximum Drain efficiency(η)	Conduction angle (θ)
A	$V_Q = \frac{V_{br} - V_k}{2}$ $I_Q = \frac{I_{dss}}{2}$	$R_{L,opt} = \frac{V_{br} - V_k}{I_{dss}}$	$P_{out} = \frac{(V_{br} - V_k) I_{dss}}{8}$	50%	2π
AB	$V_Q > \frac{V_{br} - V_k}{2}$ $I_Q < \frac{I_{dss}}{2}$	$R_{L,opt} = \frac{V_Q}{I_Q}$	$P_{out} < \frac{(V_{br} - V_k) I_{dss}}{8}$	50% <η< 78.5%	$\pi < \theta < 2\pi$
B	$V_Q = \frac{V_{br} - V_k}{2}$ $I_Q = 0$	$R_{L,opt} = \frac{V_{br} - V_k}{2 I_{dss}}$	$P_{out} = \frac{(V_{br} - V_k) I_{dss}}{8}$	78.5%	π

Note: V_{br} : the breakdown voltage; V_k : knee voltage; I_{dss} : saturation current;

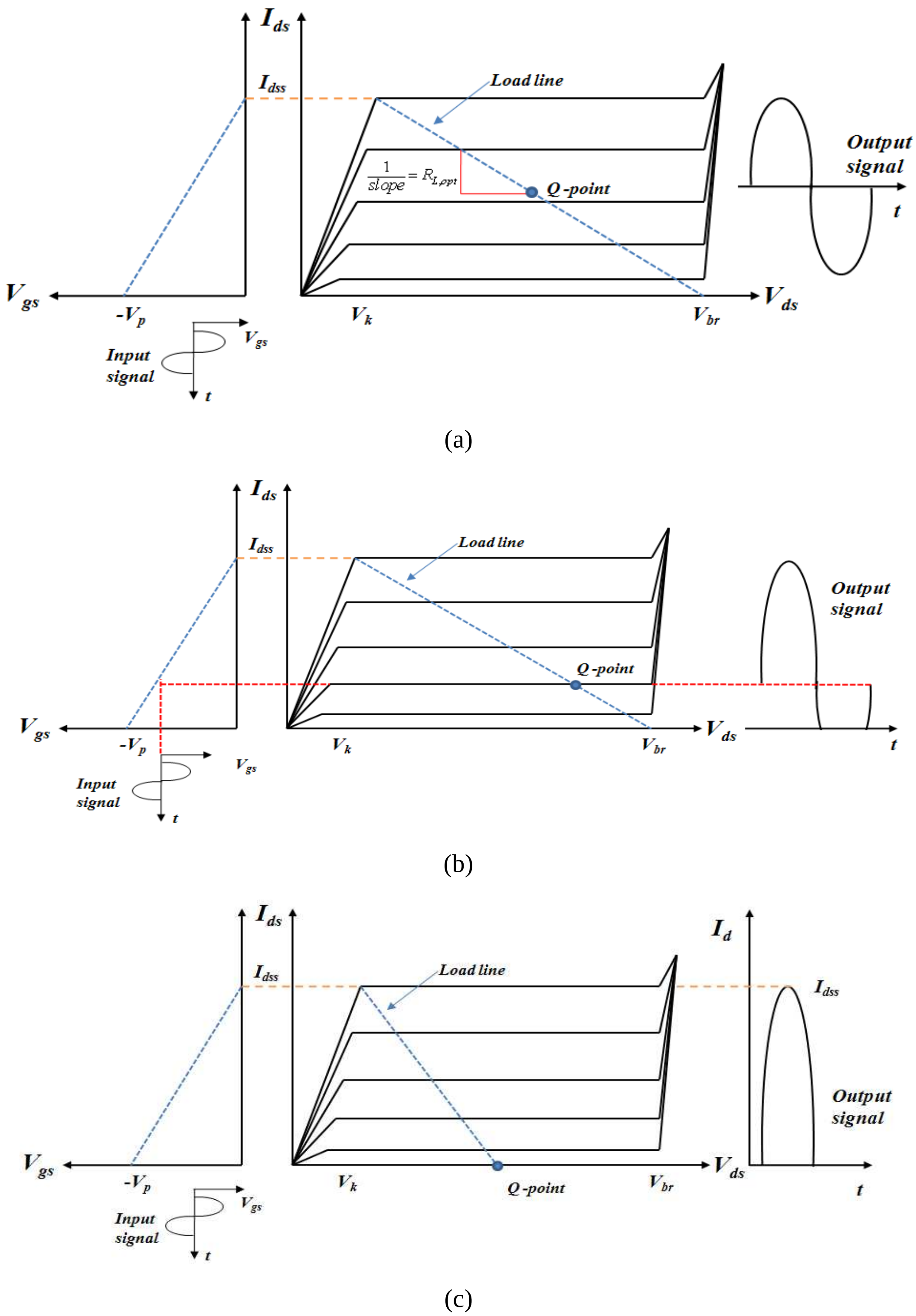

Figure 2.3 Waveform of PA's operations: (a) class A; (b) class AB; (c) class B

2.3 Characteristics of Power Amplifiers

2.3.1 Linearity

The relationship of input and output signals for a power amplifier is well known and can be presented by a power series, as shown in Figure 2.4. The output of the amplifier consists of not only the linear gain ($a_1V_i(t)$), but also of an infinite series of nonlinear products. The equation shown here only presents a weak nonlinear effect, but the Volterra series can be used to present a stronger nonlinear effect [4]. The nonlinearities usually create signal distortion, such as amplitude distortion and amplitude-to-phase conversion. Linearity is an important aspect of a PA. Even for the same PA, with varying power inputs (low power or over-drive), the linearity of the PA can be significantly changed. Thus, various techniques can be used to characterize and measure the linearity of the PA depending upon the utilized modulation and targeted application. Table 2-2 presents techniques to characterize the linearity, with further details of each technique found in [5].

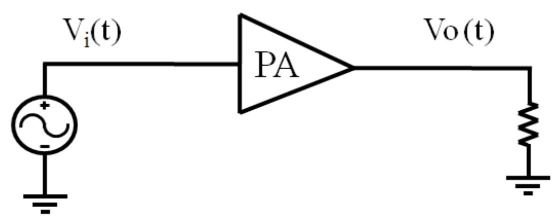

$$V_o(t) = a_1 V_i(t) + a_2 V_i^2(t) + a_3 V_i^3(t) + a_4 V_i^4(t) + \cdots\cdots$$

Figure 2.4 Simplified PA

Table 2-2 Techniques for power amplifier linearity characterization

Techniques	Signal modulation/application
Carrier-to-Intermodulation ratio (C/I)	Two-tone signal
Noise-Power Ratio (NPR)	Broadband and noise-like signal
Adjacent channel power ratio (ACPR)	Modern shaped pulse digital signal
Error vector Magnitude (EVM)	Vector signal

Table 2-3 Different efficient definitions

Name	Definition
Drain Efficiency (DE)/DC to RF Efficiency	$\eta = P_{out} / P_{dc}$
Power-Added Efficiency (PAE)	$\eta = (P_{out} - P_{in})P_{dc}$
Average efficiency (P_{ave})	$\eta_{AVG} = P_{outAVG} / P_{inAVG} = mean(\eta_{\text{instant}})$

2.3.2 *Efficiency*

Similar to linearity, efficiency is another important facet of PA design. Generally, there are three conventional definitions for the efficiency of a PA, shown in

Table 2-3.

2.4 GaN HEMTs Overview

GaN HEMT devices are a new addition to the PA arena. They are proven to have numerous physical properties that have resulted in transistors with greatly increased power densities when compared to other well-established FET technologies (e.g. GaAs or Si). The GaN devices have a relatively high power density and a smaller die size due to the superior thermal and voltage breakdown properties of the material used in construction and the feasibility of growing it on high thermal conductivity SiC substrates. Furthermore, the GaN devices, when compared to silicon LDMOS FETs and GaAs MESFETs of similar output power, have smaller parasitic capacitances. The smaller parasitic capacitances and its associated large input and load impedances make the GaN HEMTs exhibit broader bandwidth than those demonstrated by the other technologies. Additionally, their higher breakdown voltage/supply voltage, combined with a low supply current, has made GaN HEMTs the optimal device for high power handling.

2.4.1 *Material properties*

As shown in Table 2-4, the GaN device has the highest bandgap and breakdown field, which makes the GaN device the most feasible choice for high power applications. With a high thermal conductivity, a GaN device can have higher power density. Additionally, the high electron mobility and saturated electron velocity of the GaN devices lead to a higher transconductance (g_m).

Table 2-4 Material Properties of Common Semiconductors [6]

	Si	GaAs	InP	GaN	SiC
Bandgap (eV)	1.1	1.43	1.35	3.4	3.26
Breakdown Field (V/μm)	30	40	50	300	200<300
Electron Mobility (cm^2/Vs)	1500	8500	5400	1500 (2DEG)	700
Saturated Electron Velocity (10^7cm/s)	1	<1.0	1	1.3	2
Peak Electron Velocity (10^7cm/s)	1	2.1	2.3	2.5	2
Thermal Conductivity (W/cmK)	1.3	0.55	0.68	>1.5	<3.8
Lattice Constant (A)	5.43	5.65	5.87	3.19	3.07
Dielectric Constant (ε_r)	11.7	12.9	12.5	9	9.7

2.4.2 Device structure

Figure 2.5 shows the various constituent layers of a GaN HEMTs. The current passes from source to drain through a two- dimensional electron gas (2DEG) layer, which leads to large electron motilities and improves noise and gain characteristics. The AlGaN/GaN modulation-doped heterostructure is the only heterostructure system among the wide band-gap semiconductors and exploits the power-handling capabilities of wide band-gap semiconductors, as well as the high frequency potential of a modulation-doped structure.

2.4.3 Comparison of GaN HEMT and other device

The material's property and the device's structure combination make the GaN/ AlGaN HEMTs suitable for high-power, high-frequency applications. Figure 2.6 shows a plot of the output power versus frequency for different transistor technologies [7]. It is obvious that the GaN HEMTs have the highest possible output power over a wide frequency range. Until recently, the principle disadvantage of a GaN HEMT was its cost, since GaN HEMTs are usually fabricated on a SiC substrate. GaN HEMTs have a higher drain voltage than other devices. The high drain voltage increases the transistor's input/output impedance (close to 50 Ω), which makes the GaN HEMT devices much easier to match for broadband applications. Another property of the GaN is that the device exhibits a soft power compression characteristic. This characteristic makes the GaN HEMTs' gain start to have compressions even at 10 dB below their rated power output, so GaN HEMTs are usually evaluated by P_{3dB} instead of P_{1dB} (where the gain drops by a 1 dB when compared to its linear gain). This soft power compression characteristic also impacts the device's linearity [8]. Table 2-5 compares the GaN with other semiconductor materials in terms of its power handling, operation frequency, and fabrication costs.

With regard to the above mentioned advantages, the GaN HEMTs are used for broadband PA development. The simulation and design details about the feedback and distributed PA will be given in the following sections.

2.5 Negative Feedback Power Amplifier Development

2.5.1 Feedback amplifier overview

A well known fact regarding FETs is that they usually have a low input resistance and a high output resistance at low frequencies, which makes it difficult to use a single device to achieve a multi-octave bandwidth. Niclas, et al [9, 10] proposed a feedback amplifier topology to achieve a multi-octave bandwidth employing a single device. The FET feedback amplifier is useful for broadband applications. It can be used as a general purpose gain block, or as an IF amplifier. Here, we will use the feedback amplifier as a medium power amplifier. The feedback amplifier, as shown in Figure 2.7, employs an RLC shunt feedback network (an inductor: L_{FB}, a resistor: $R_{FB,}$ and a capacitor: C_{FB}) between the gate and drain of the FET. The negative feedback RLC network is useful to stabilize the device and make the input/output impedances approach the desired 50 Ω level. Table 2-6 presents the advantages and disadvantages of the feedback amplifier [7].

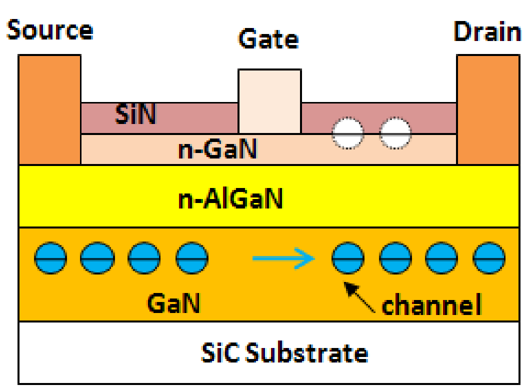

Figure 2.5 GaN HEMT structure [11]

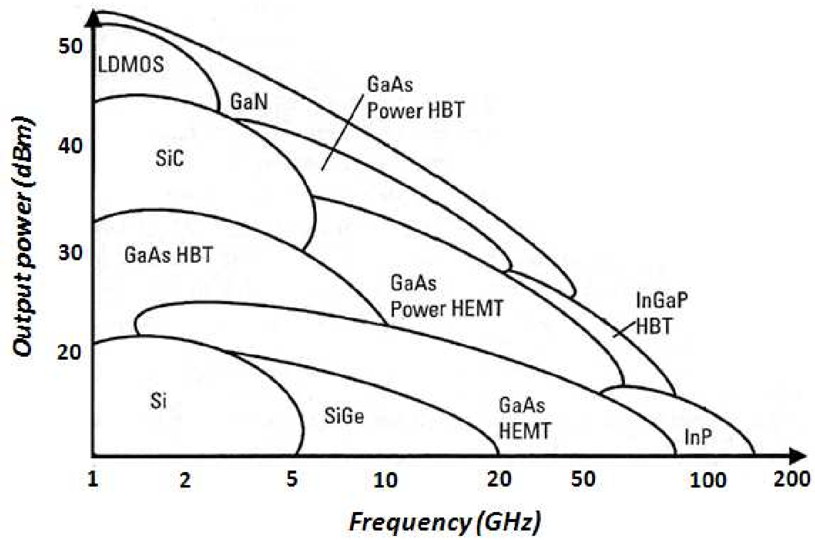

Figure 2.6 Plot of output power vs. frequency for different transistor technologies [7]

Table 2-5 GaN and other device comparison summary [12]

Property	Si	GaAs	SiC	GaN
Suitability for High Power	Medium	Low	High	High
Suitability for High Frequencies	Low	High	Medium	High
HEMT structures	No	Yes	No	Yes
Low Cost Substrate	Yes	No	No	Yes

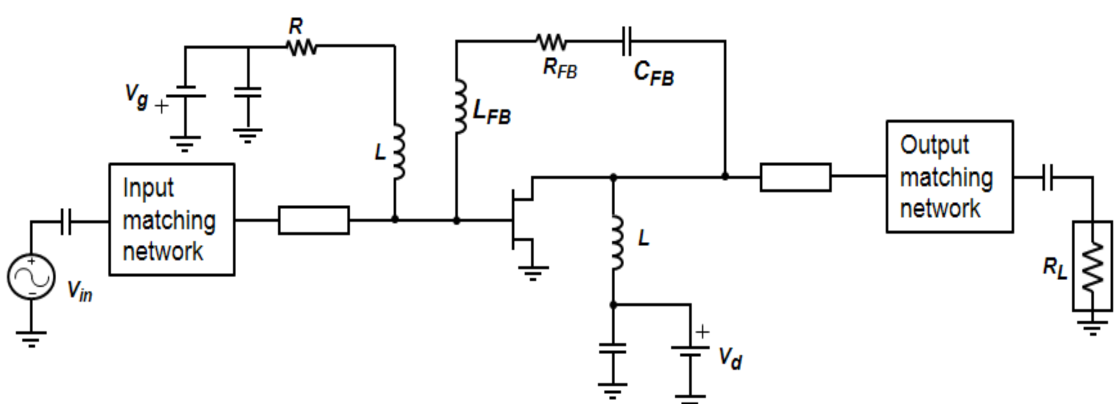

Figure 2.7 Simplified feedback amplifier

Table 2-6 Advantage and disadvantage of feedback amplifier

Advantages	Has a simple structure, low cost and easy for either hybrid MIC or MMIC fabrication
	Proved to have higher efficiency than conventional distributed amplifiers [6]
	Easy to achieve a flat gain, an unconditional stability and have a good input/output match
	Less parameters' sensitivity and distortion due to device variation
Disadvantages	Poor noise figure and high loss at the low frequency end due to its resistive feedback network, lower gain than conventional single-ended amplifier

As shown in Figure 2.7, in the RLC feedback network, each component has a specific role to perform in order to achieve maximum performance in terms of gain, bandwidth, and input/output matching [13]. The feedback resistance, $R_{FB,}$ is the key element. It can initially be determined simply from the following expression: $R_{FB} = g_m Z_0^2$ (where g_m is the trans-conductance of the device and Z_0 is 50 Ω). The gain of the feedback amplifier can be presented as $S_{21} = (Z_0 - R_{FB}) / Z_0$ [1]. This indicates that the S_{21} parameter depends only on the R_{FB}, not on other S-parameters. More design details can be found in Appendix A.

The mechanism of the negative feedback is well-known and is summarized here. The design goal is the achievement of a flattened gain, accomplished by using a parallel resistive feedback network over a broadband frequency range. However, since the gain-bandwidth product is a constant for a certain device, the R_{FB} has to be traded for an increased gain and bandwidth. The L_{FB} has no effect at the low frequency end. Meanwhile, the R_{FB} controls the gain level. Thus, a maximum negative feedback is provided to reduce the device gain at the low frequency end. Meanwhile, as the gain of the FET device decreases when frequency increases, the amount of negative feedback is reduced due to the increase of the reactance of L_{FB} with frequency. This could be used to flatten the gain. C_{FB} is used to block the DC between the gate bias and the drain bias. Even though the RLC feedback network already brings the input/output impedance close to 50 Ω, adding a simple input/output matching network should reduce the input/output return losses even further.

2.5.2 State of the art of feedback power amplifier and design goal

The feedback power amplifier can be developed using either monolithic (MMIC) or discrete devices (Hybrid MIC). Compared to a monolithic design, a hybrid MIC implementation has some well-known advantages, such as a higher power capability, lower cost, and faster turnaround. Additionally, it is easier to implement and develop a custom design. It is also simpler to integrate with the large inductors required for low frequency operation and high current applications. However, the hybrid implementation generally has worse frequency performance. Table 2-7 presents the state of the art of the feedback amplifiers. As shown here, our work here achieved a medium output power and bandwidth, but to maximize the gain (per stage) over a broadband for a low implementation cost. The design details, simulation results will be presented in the next section.

2.5.3 Feedback power amplifier development

As pointed out by Marsh [7], small-signal S-parameters are useful when designing the input/output matching and biasing network. They provide a fast and simple way to achieve the basic bandwidth, gain, and input match. The small-signal S-parameters are generally not sufficient to fully design a PA, such as the switching-mode PA, for optimum power and efficiency. It is acceptable, though, in our case to initially design the feedback power amplifier using a small signal analysis since the transistor is primarily a linear device over the majority of the load line. In this work, small-signal S-parameters are first used to achieve broadband operation with a good input match and flat gain. Then, the matching network is re-optimized for the best performance under the device's large-signal operating conditions to take the "weak" nonlinearities encountered at the extreme ends of the load line into account [7].

Here, we summarize our design steps for a feedback power amplifier as follows:

- Device selection
- Bias point selection
- Small signal simulation
- Large signal optimization/tuning

Table 2-7 State of the art of feedback amplifier

	This work (Achieved)	Y.Chung [14]	Ahmed Sayed [15]	Kevin W. Kobayashi [16]	H. J. Siweris [17]	Karthikeyan [18]
Power Level	>30 dBm (1W) 3 dB Compression	<29.5 dBm (0.89W) Mid-band Saturated	>37 dBm (5W) 1 dB Compression	33 dBm (2W) 1 dB Compression	8 dBm (6mW) 1 dB Compression	31.5 dBm (1.4 W) Mid-band Saturated
Gain	>12 dB	>9 dB	>8 dB	>11dB	>22 dB	~11 dB
Drain Efficiency	>22%	>20%	>38%	>28%	N/A	<15%
Operating Band	0.05 to 5 GHz	DC to 5GHz	0.01 to 2.4 GHz	1 to 4 GHz	DC to 20 GHz	0.2 to 7.5 GHz
Device Technology	commercial GaN HEMT Die	customized GaN HEMT Die	commercial SiC MESFET Package	customized GaN HEMT Die	customized GaAs HEMT Die	customized GaN HEMT Die
Assembly	HMIC	HMIC	PCB	MMIC	MMIC	MMIC
# stages	Single	Single	Single	Single	Three	Two devices

➢ Device Selection

As discussed at the beginning of this chapter, the GaN HEMT is one of the best candidates for a broadband high-power, high-efficiency PA design. However the high g_m (transconductance) and the small drain-source resistance R_{ds} of the large size GaN HEMTs are not conducive for feedback amplifier design at low frequency. Specifically, the input, $S_{11,}$ of a small size device feedback amplifier can be adequate, but as the HEMT device size increases, the input reflection S_{11} climbs rapidly at low frequencies [19].

Here, the CREE CGH60002DE was selected for this study and was investigated for low frequency operation and output power levels. The CREE device is a 2W, RF Power GaN HEMT die, the electrical parameters of CGH60002DE is shown as following:

Gate Length: L=0.35 μm;

Gate Periphery: W=2x360 μm;

Power Density: 4W/mm (28V bias);

Cut-off Frequency: f_T= 20 GHz;

Maximum Frequency of Oscillation: f_{max}=36 GHz;

Saturated Drain-Source Current: I_{dss}=400 mA with 28V (drain bias)

➢ Bias Point Selection

Both class A and class AB can be selected for a broadband single-ended feedback PA design. A class A operation can achieve a higher gain while a class AB operation can realize higher efficiency. In this study, a slight ($I_{ds}=0.375I_{dss}$) class AB bias point is selected as a compromise between gain and efficiency. Also, drain-source voltage V_{DS} (18V) was selected. The DC bias point is V_{DS}=18V, I_{DS}=150mA, as shown in Figure 2.8.

➢ Small Signal Simulation

There are two ways to achieve small signal S-parameters. One way is to acquire the S2p file from the vendor for a certain bias point. The second method is to directly use the large signal nonlinear model supported by the vendor to extract the linear S2p file. Here, we use the latter method. We bias the device for a class AB operation point (18V, 150mA), and drive the amplifier with a very low power signal to guarantee the amplifier working within the linear region to extract the small signal S-parameters, as shown in Figure 2.9 Schematic to extract S-parameter from large signal model. A number of small signal RF equivalent circuits exist for FETs. We have adapted a seven-element small signal FET model for this simulation, proposed by Curtice [20]. The details of the seven-element model and how to extract the seven elements from S-parameters are shown in Appendix A.

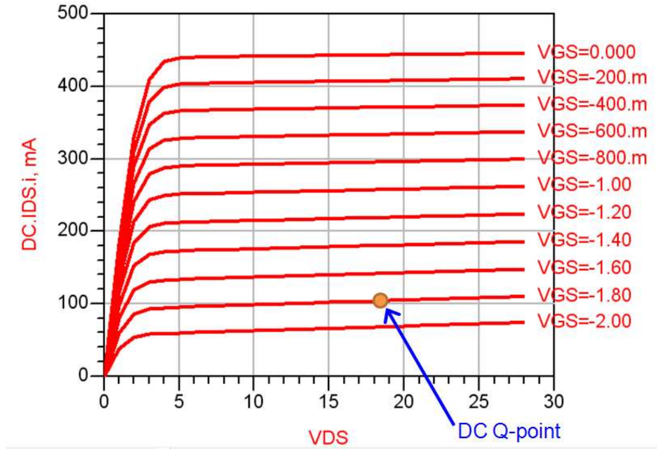

Figure 2.8 DC IV curve

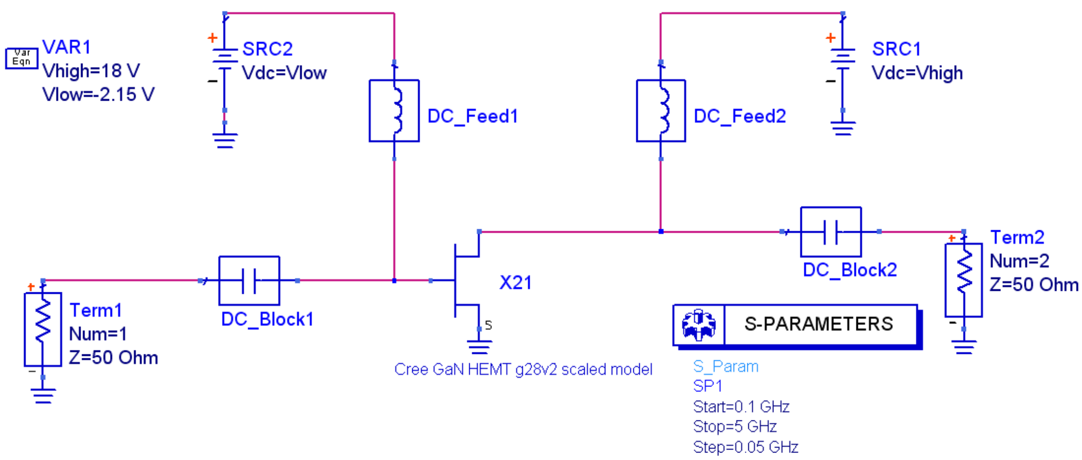

Figure 2.9 Schematic to extract S-parameter from large signal model

Figure 2.10 shows the extracted seven elements, in terms of frequency, based on the equations described in Appendix A. The seven elements are frequency dependent, so an optimization is applied to find the optimal element values to fit the extracted S-parameters with the seven-element model over a wideband operation. This is shown in Figure 2.11.

Figure 2.12 shows that the S-parameters of the seven-element model are in agreement with the extracted S-parameters. With the extracted g_m, we have

$$R_{FB} = g_m Z_0^2 = 0.148 \times 2500 = 370\,; \qquad \text{(Eq 2.1)}$$

$$Gain = S_{21}(dB) = 20\log(\left|1 - g_m Z_0\right|) = 16.1dB \qquad \text{(Eq 2.2)}$$

However, the above equations only work for low frequency and assist in the initial design. Figure 2.13 shows the simulation schematic of a simplified resistive negative feedback amplifier.

Figure 2.14 shows the simulated gain and input/output reflection coefficients as a function of the feedback resistor value. As shown here, a medium value (300 Ω) feedback resistor helps both the input/output return loss and the gain flatness. However, the parasitic effects make the feedback ineffective at the high frequency end. Thus, the input/output matching networks are still needed to improve the VSWR of the amplifier and the gain flatness at high operating frequencies.

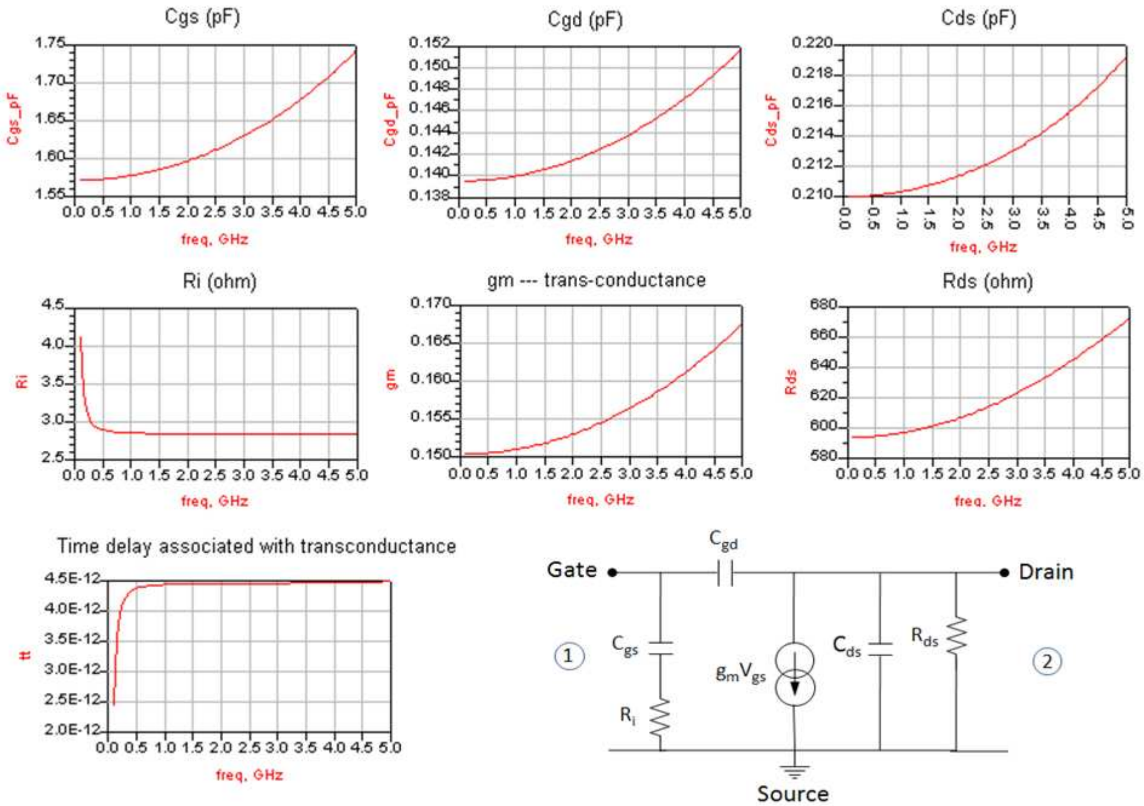

Figure 2.10 Extracted component values

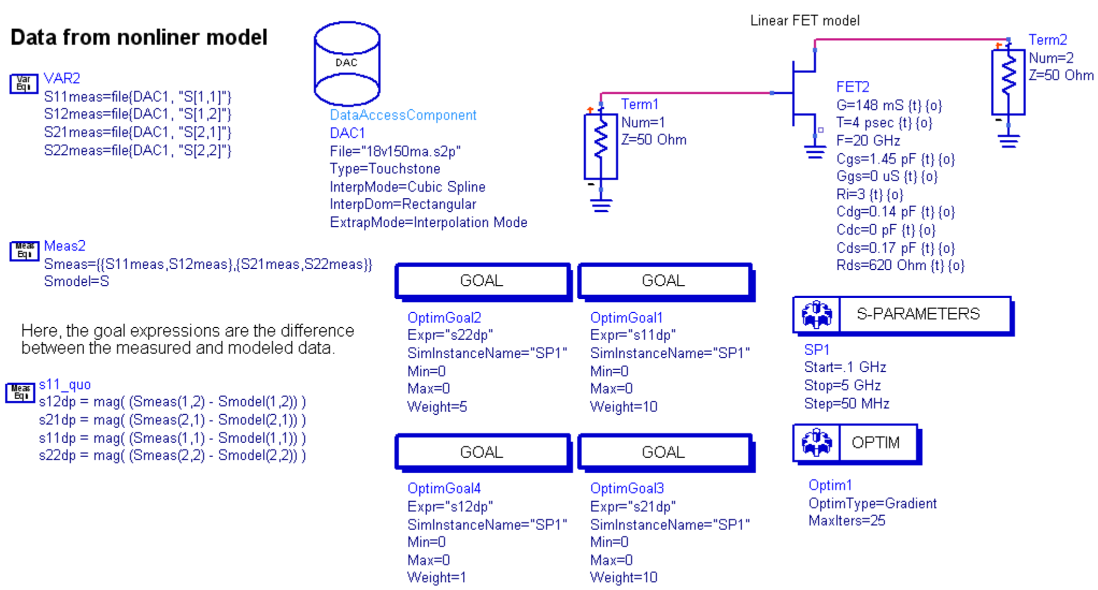

Figure 2.11 Schematic to optimize the component values for wideband operation

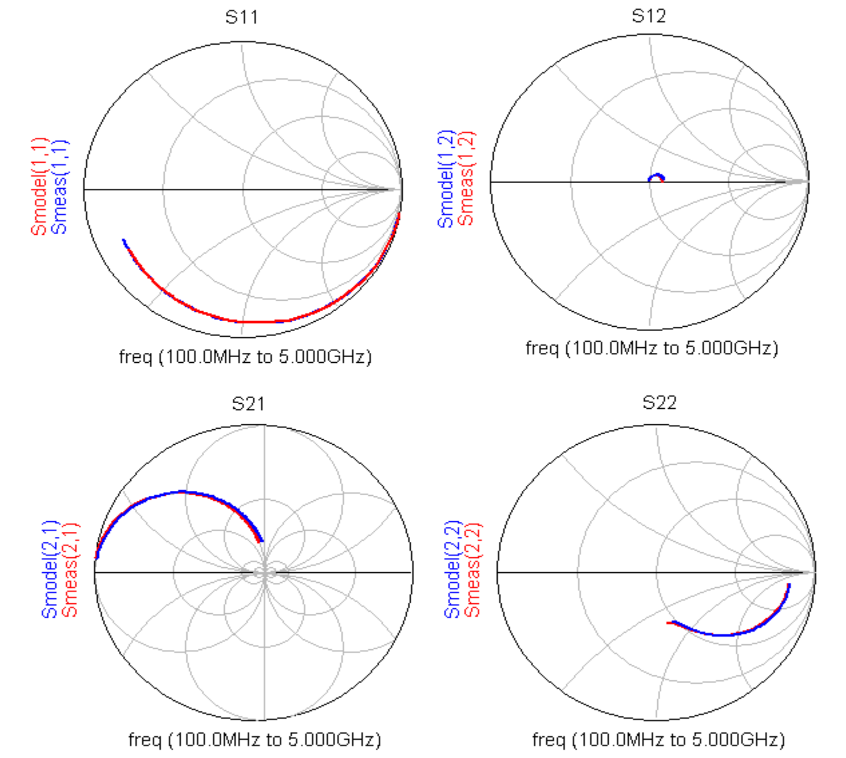

Figure 2.12 Comparison of the S-parameters of optimized linear equivalent model with extracted S-parameters

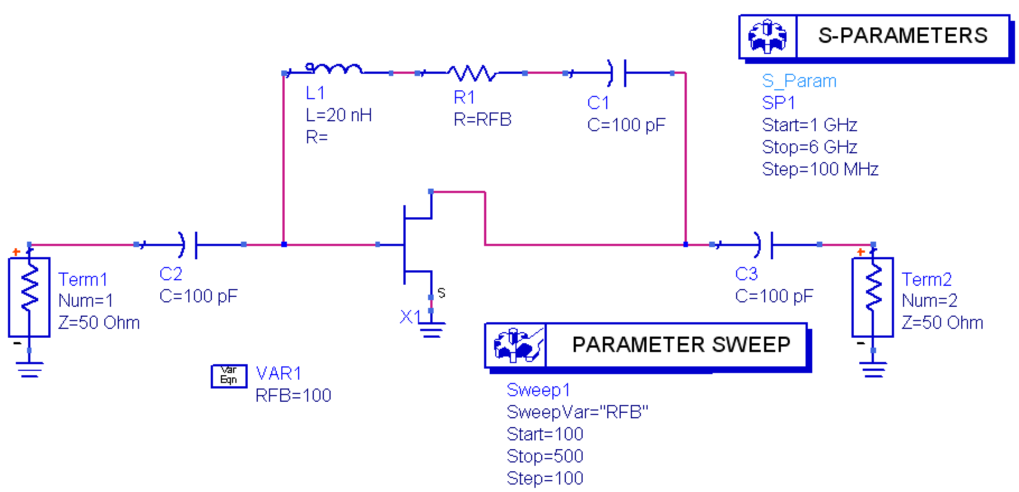

Figure 2.13 Schematic of simplified feedback amplifier

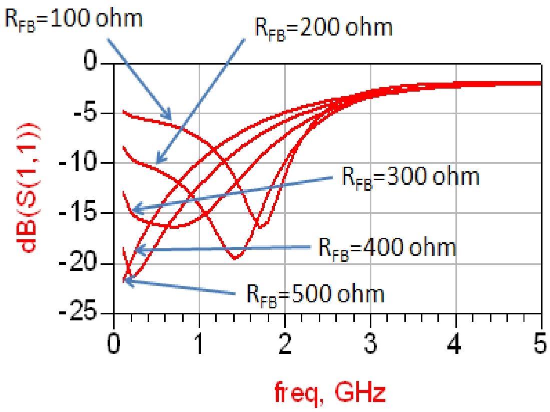

(a)

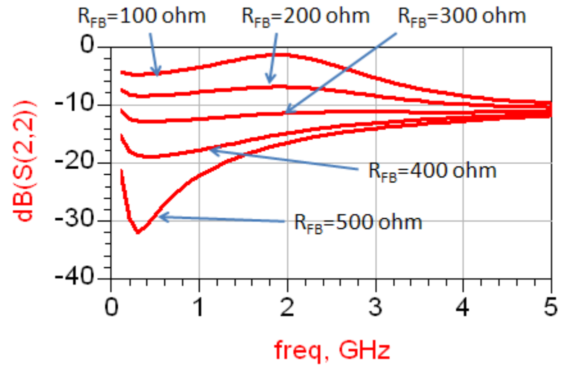

(b)

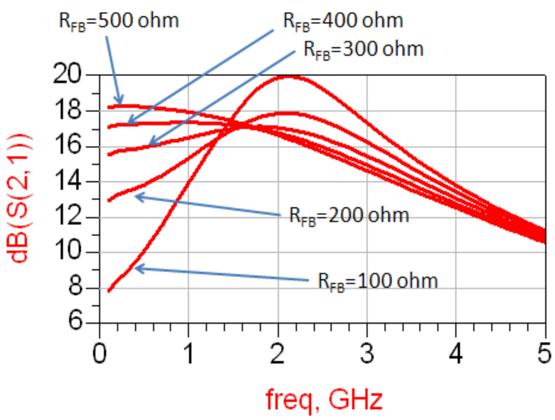

(c)

Figure 2.14 Simulation S-parameters with different feedback resistor: (a) S_{11}; (b) S_{22}; (c) S_{21}

As shown in Figure 2.15 for the input part, the length of the bonding wire (wire 4) can be selected to compensate for the C_{gs} of the GaN HEMT. For the output part, the length of the bonding wire (wire 3) is selected to let L_D compensate for the C_{ds} of the GaN HEMT. These compensations can provide gain peaking at the upper edge of the frequency in response to the extension of the bandwidth. Although the RLC feedback network already has the input/output impedance close to 50 Ω, the transmission lines TL8, TL9, and the capacitor C7 are still needed to improve the input match. This is also necessary for the TL10, TL11 and C8 transmission lines for the output matching network. TL13 and TL14 are used to model the open-end effects of the transmission line. Figure 2.16 shows the small signal simulation results, which indicates that the input/output return loss is less than 10 dB and the gain is 13±0.5 dB over a 0.1 to 4.5 GHz frequency range. Although the initial calculation of R_{FB} is 370 Ω and the low frequency gain is 16.1 dB, after optimization, the gain flatness and input/output return loss are clearly improved with setting R_{FB}=230 Ω. As a stability check, we use the geometrically derived stability factors [20] of the input and output parts. All were greater than one. This indicates that the amplifier is unconditionally stable, as shown in Figure 2.16b. However, the amplifier needs to be optimized using a large signal simulation to achieve the desired power performance, which will be shown in the next section.

- Large Signal Optimization/Tuning

In an S-parameter simulation, the active device is considered a linear device. In order to evaluate and optimize the power performance of the amplifier, it is necessary to use a large signal simulation, like the Harmonic Balance simulation. The optimal goal is to have a flat output power over a wideband, given that the optimal load varies with frequency. Figure 2.17 shows the large signal performance, either with a constant 21 dBm input power or an input power that leads to a 3-dB compression in the output power. Based on our simulation, the flatness of the output power is within ± 0.5 dB over a 0.1 to 4.5 GHz frequency range. Meanwhile, the drain efficiency of both cases is higher than 32% over the entire operating bandwidth. It is known that the inter-modulation distortion (IMD) level of a power amplifier relates to the power level of the two-tone signal. Here, we use a two-tone signal (10MHz away from each other) with 0 dBm power for each tone as the input signal to check the IMD level over the wideband. Figure 2.18 shows the simulated IMD as a function of frequency. It is clear this amplifier has a low IMD level.

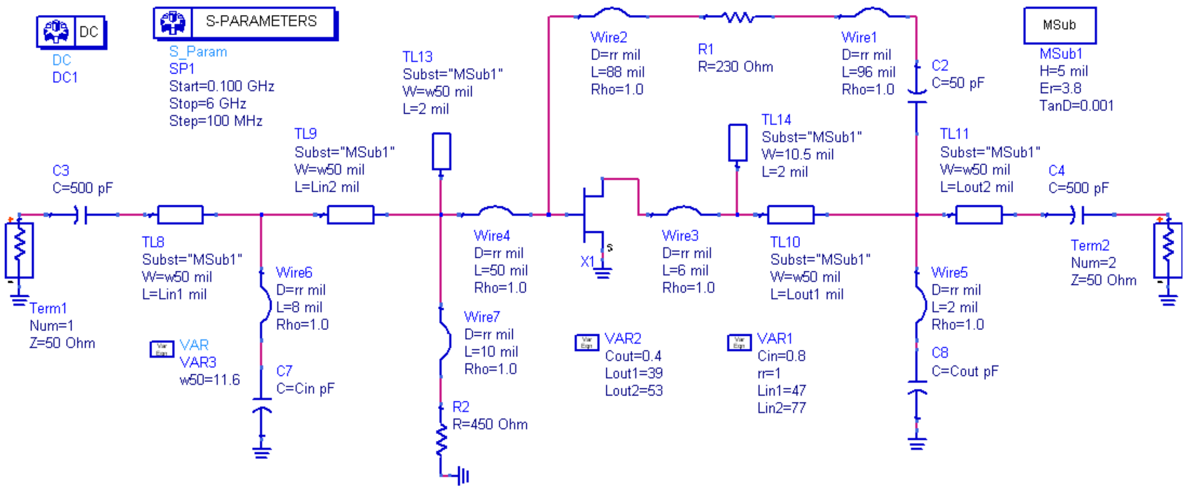

Figure 2.15 Small signal simulation schematic in ADS

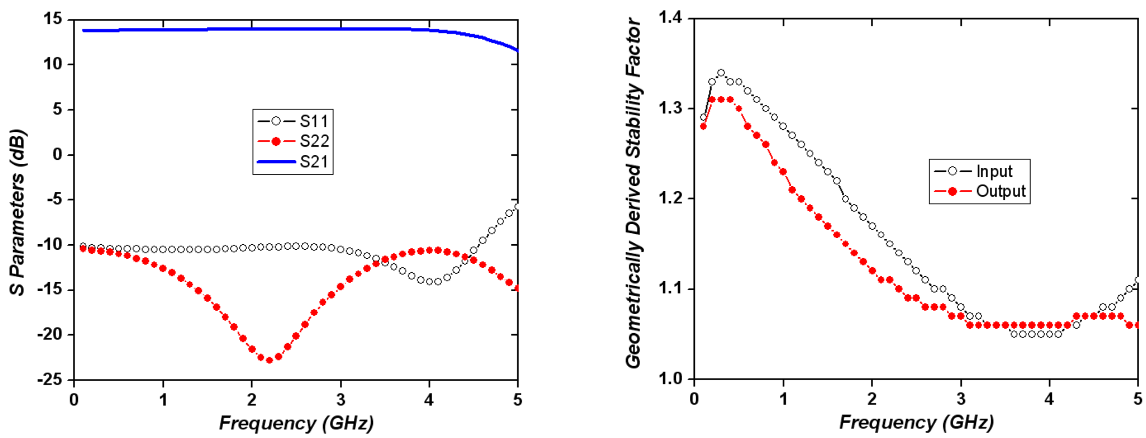

(a) (b)

Figure 2.16 (a) S parameters; (b) Stability

2.5.1 Feedback power amplifier circuit and measured results

The feedback power amplifier was fabricated at MITEQ Inc. using a hybrid microwave integrated circuit technology. Corn coils and MIM (Metal-Insulator-Metal) capacitors were used to achieve the wideband operation and the bonding wires act as small inductors both for the DC bias and RF matching. The circuit implemented is shown in Figure 2.19. Figure 2.20 compares the simulated and measured small signal S-parameters. A good agreement has been achieved between the simulation results and measurement results. The input/output return loss is better than 8.4 dB. The measured small signal gain is 14 (±0.9) dB over 0.1 to 4.5 GHz. Figure 2.21 shows both the simulated and measured output power and drain efficiency for a 3-dB compression point. The measured P_{3dB} output power is higher than 30 dBm and the drain efficiency is higher than 22% over 0.1 to 5 GHz. The measured output power and drain efficiency are noticeably lower than in the large signal simulation results, which could be related to the accuracy of the nonlinear device model utilized. A significant gain-drop of around 2 GHz also exists. This is believed to be an inherent device problem.

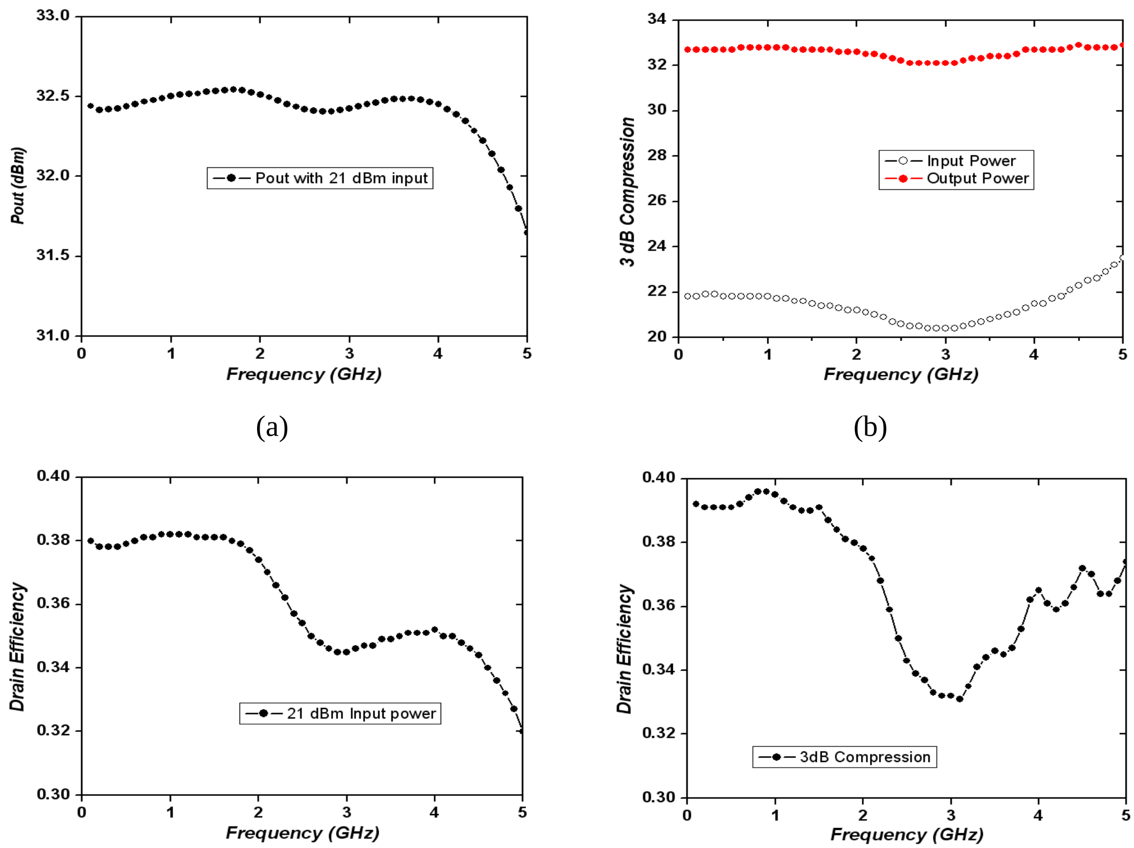

(a) (b)

(c) (d)

Figure 2.17 Large signal performances: (a) Output power with 21dBm input power; (b) Input/output power for 3-dB gain compression; (c) Drain efficiency with 21 dBm input power; (d) Drain efficiency for 3-dB gain compression

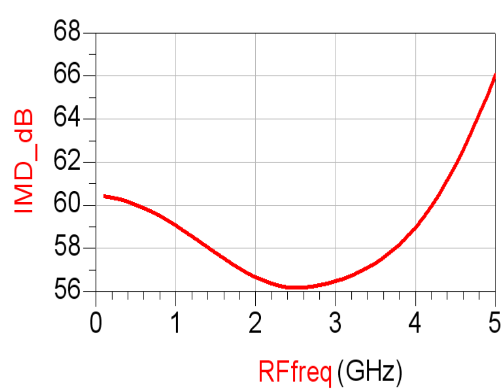

Figure 2.18 Simulated IMD with Pin=0 dBm

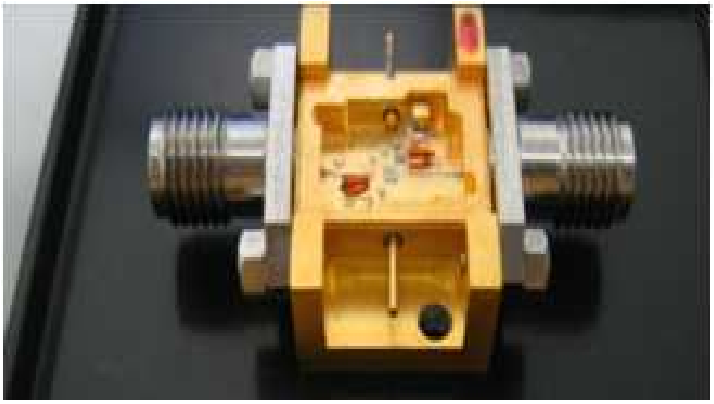

Figure 2.19 Fabricated feedback PA with housing

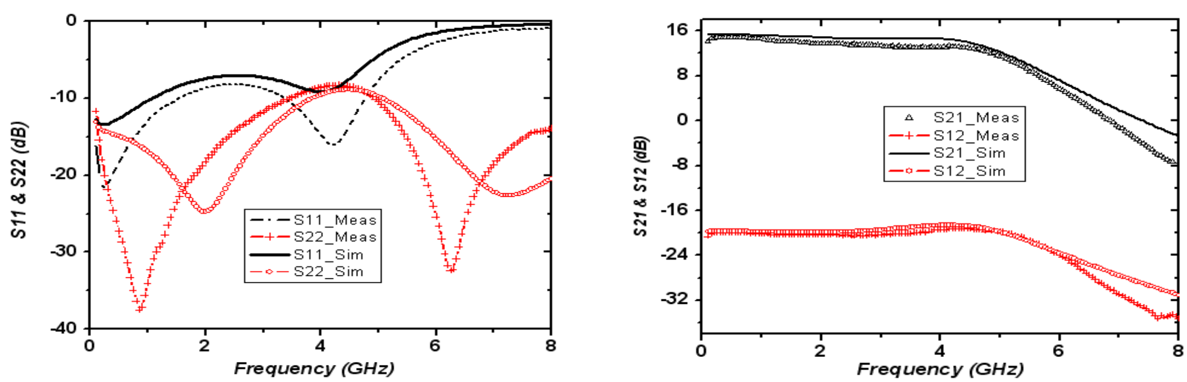

(a) (b)

Figure 2.20 Simulated and measured S parameters: (a) S_{11} and S_{22}; (b) S_{21} and S_{12}

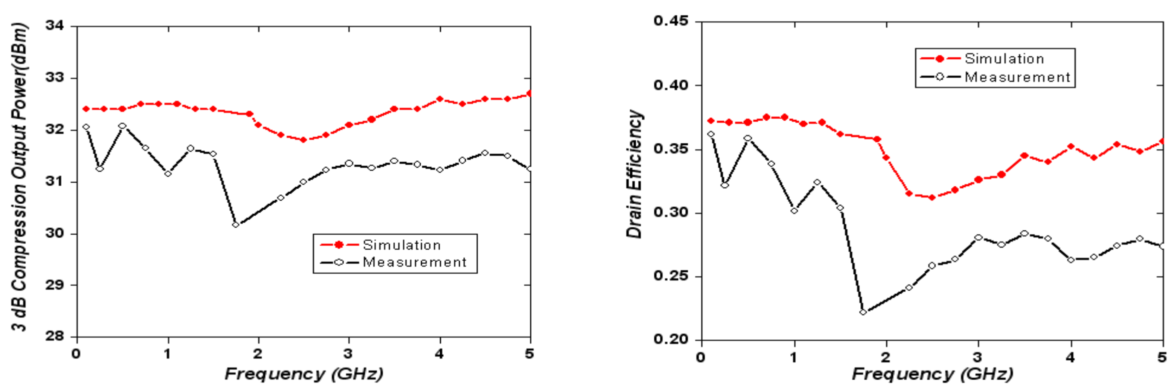

(a) (b)

Figure 2.21 Simulated and measured power performance of feedback PA: (a) Pout; (b) Drain efficiency

2.6 Distributed Power Amplifier Development

2.6.1 *Circuit design overview*

In a conventional distributed amplifier design, there are two input and output artificial transmission lines with a number of FETs connected in shunt (shown in Figure 2.22). These artificial lines are comprised of different L-type cells, the series arm of each cell is made of a lumped inductor and the gate/drain impedance of the FET is the shunt arm of the gate/drain line. These artificial transmission lines are terminated by their characteristic impedances. As the signal travels down the gate line, each transistor is excited by a traveling wave and transfers the signal to the drain line through its transconductance. Therefore, the signal delays on the drain line are adjusted to add in the forward direction as they arrive at the output, while the reverse wave goes through different cells and have unequal path delays. Their summation is then frequency dependent and will have peaks and valleys. For example, at low frequency where the delays are insignificant, the output power would split equally between the load and reverse terminations [1].However this strategy to design a distributed power amplifier will have a low efficiency operation and low power capability which eventually would result on low gain as well due to the relatively high loss of these artificial lines.

There are typically two techniques that have been used to enhance the distributed power amplifier's efficiency. The first technique is used to reduce the losses of the gate line. Ayasli et al. [21]proposed to couple the FETs to the gate line through series capacitors to simultaneously increase both their power capabilities and efficiency. However, the implementation of this technique has led to significant gain drop. Fortunately, the GaN HEMT can alleviate this gain drop due to its inherent higher transconductance. Meanwhile, a second technique based on drain line tapering without terminating the drain line that was originally introduced by Ginzton/Hewlett et al. [22], and implemented later on by Chick [23]has been used to increase the drain efficiency. The cost is a degraded output VSWR, but, due to the high impedance characteristics of GaN HEMTs this should be a less costly trade-off. Hence, in our design we have used both techniques.

The DPA was initially designed and optimized using the well established design criterion for a stable linear small signal wideband performance like that of [24]. Subsequently, this design was modified based on the large signal performance analysis of the GaN HEMTs for high power operation. Finally the modified DPA design was optimized to achieve both a high drain efficiency and high output power while sustaining an adequate input/output return loss over wideband. AWR Microwave Office 2007 [25] has been utilized through the entire design process with a non-linear device model for GaN HEMT from Cree Inc.

2.6.2 *State of the art of distributed power amplifier and design goal*

Similar to the feedback amplifier, the distributed power amplifier can be developed using either monolithic (MMIC) or discrete devices (Hybrid MIC). Table 2-8 presents the state of the art of the distributed power amplifiers. As shown here, our work here achieved a medium output power and bandwidth, but to maximize the PAE, and gain over a broadband for a low implementation cost. The design details, simulation results will be presented in the next section.

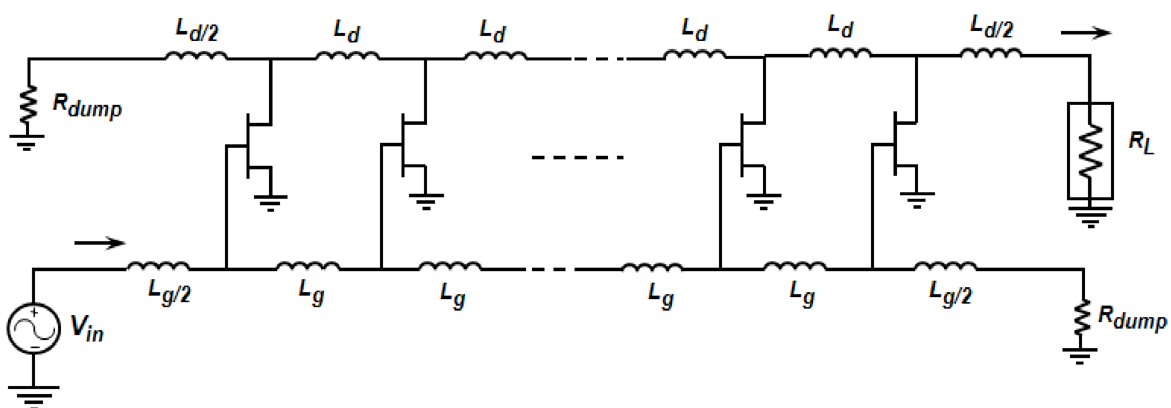

Figure 2.22 Schematic diagram of a conventional distributed amplifier

Table 2-8 State of the art of distributed power amplifier

	This work (Achieved)	A. Pavio [26]	L. Zhao [27]	L. Zhao [28]	Tan Teik Siew[29]	J.Ph.Fraysse[30]	J.Gassmann
Power	>37 dBm (5W) Saturated	>40 dBm (10W) Saturated	>30 dBm (1W) Saturated	>37.5 dBm (5.6W) Saturated	>30 dBm (1W) Saturated	>33 dBm (2W) N/A	>37 dBm (5W) Saturated
PAE	0.02 to 2.5 GHz >30% 2.5 to 3 GHz >27%	0.02 to 2 GHz >30%	0.8 to 2.1 GHz >38%	0.1 to 2 GHz >25%	0.1 to 0.65 GHz >26%	2 to 8 GHz >20%	20 to 15 GHz >20%
Gain (dB)	>13.5	>11	>10	>11	>13	>9	>10
Small signal bandwidth	0.02 to 3.5 GHz	0.02 to 2.5 GHz	0.8 to 2.3 GHz	0.1 to 2 GHz	0.1 to 0.6 GHz	2 to 8 GHz	2 to 15 GHz
Device type	Cree GaN HEMT Die	Nitronex GaN HEMT Die	GaAs pHEMT package	LDMOS	MOSFET package	Cascode HBT	GaN HEMT
# Device	3	4	5	4	3	4x2	5
Fabricated	PCB	PCB	LTCC	LTCC	PCB	MMIC	MMIC
Class	AB	AB	B	B	AB	A	AB

2.6.3 Small signal simulation and design process

The operation frequency range of the DPAs is generally limited by the size of the utilized active devices. At low frequencies close to DC, for example, the distributed power amplifier is equivalent to having the power devices connected in shunt. Subsequently, when we use larger devices to achieve relatively higher power, they would have smaller drain-source resistance (R_{ds}). As point out by Nicals et al., the small device can have good S_{22}, but as device size increase, S_{22} climbs rapidly. So it is difficult to achieve good output return loss at low frequency using large size device. This would require a special matching network to achieve good output return losses at low frequencies. At the same time, the large size device has larger gate-source (C_{gs}) and drain-to-source (C_{ds}) capacitances, which limits its high frequency performance. As a compromise and to circumvent this problem, our design is based on a medium size GaN HEMT device to potentially achieve a good output return loss down to 0.02 GHz. Specifically, the selected device is a GaN HEMT (Cree CGH60002DE), which is the same device as we used to design negative feedback power amplifier in the previous section.

The gain of the distributed amplifier is typically a function of both the number of amplifier stages and the attenuation associated with the gate and drain lines. Theoretically, the optimum number of stages required to maximize the gain of a distributed amplifier can be deduced from the explicit expressions/graphs described by the complex function of the gate and drain lines attenuation derived by Beyer et al. [31]. But in practice, the typical number of stages in a distributed power amplifier has been found to be in the range of 3 to 6. Subsequently, the number of stages in our design has been restricted to only three in order to avoid using extremely high-impedance transmission lines, as will be described in the next section.

A small signal design for a conventional three stage distributed power amplifier was first simulated. The design was based on utilizing uniform gate and drain lines with characteristic impedance of Z_0=50 Ω. The C_{gs} of a HEMT is typically bigger than C_{ds} that can cause phase imbalance between the gate and drain lines' phase velocities. There are two ways to decrease this phase imbalance. There are two ways to decrease this phase imbalance. One way is to add C_d to the drain line to increase the equivalent "C_{ds}". Another way is to add a series capacitance C_{ga} to the gate of each HEMT to decrease the equivalent "C_{gs}". Figure 2.23 compares the small signal simulation results of conventional and capacitively coupled DPAs with ideal lumped elements. The simulation results clearly show that after adding a series gate capacitor, C_{ga}, the gain bandwidth is significantly improved however there is a considerable gain drop because of the voltage division across the C_{gs} and C_{ga} capacitors.

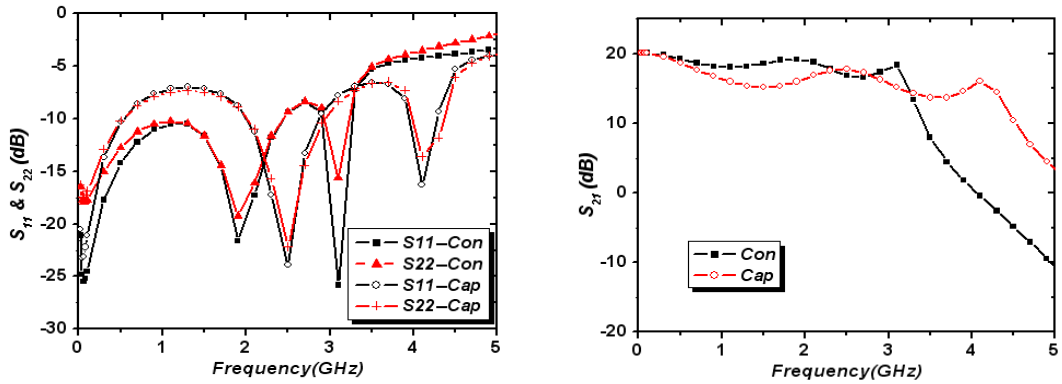

(a) (b)

Figure 2.23 Small signal simulation results of conventional (Con) and capacitively coupled (Cap) DPAs: (a) S_{11} and S_{22}; (b) S_{21}

The above analysis is the first step in the DPA design, however it requires large-signal behavior consideration in order to optimize output power and drain efficiency over the frequency band. Therefore, a Harmonic Balance (HB) simulator has been employed to simulate and optimize the power performance of the DPA.

2.6.4 Large signal design consideration and stability analysis

As a second step in designing a high performance distributed power amplifier, after using the basic design equations to give initial design values, we used simulated load pull results to find an equivalent optimal load, and then we selected an optimal load line impedance to apply the tapered drain line technique. Finally, we optimized the circuit with ideal components followed by more realistic lumped element components. It is imperative here to check the internal stability of the DPA in all design steps especially for the inter-stage matching networks.

A non-linear device model for GaN HEMT from Cree Inc. was used for our large signal simulation. This non-linear model is an electrothermal model, which includes the self-heating effects by utilizing a thermal resistance calculated from finite element analysis of die. Utilizing the simulated load-pull results, it was determined that when the GaN HEMT is biased as a class AB (V_{ds}=28 V) and has a quiescent drain current around 50 mA (which is about 12 % of I_{dss}), the desired device output load impedance for optimal output power with over 55% drain efficiency can be represented by an equivalent parallel RC load of 98 Ω and 0.4 pF (valid from 1 to 4 GHz with approximately 35.5 dBm output power). Also, as described by Duperrier et al. [32], when the equivalent input characteristic conductance of the device is determined at the maximum operating frequency, an almost constant gate voltage amplitude can be reached over a wide frequency band. Subsequently, using a large signal S parameter analysis, we have extracted a C_{gs} of 1.3 pF (at 4 GHz) for this design.

The tapered drain line technique has been used to minimize the total GaN HEMT's drain line output current in the reverse direction while ensuring that all the currents from the GaN HEMTs are fed in the forward output load. The practical implementation of this technique, however, is not straightforward. For example, the drain line impedance of the first device in the input side is R_{opt} (impedance for optimal output power), while the drain line impedance at the output side is $R_{opt}/3$ (for a three stage case) [23]. Now, if R_{opt} is much higher than 50 Ω, we will have a drain line with very narrow width at the input side, which could limit the DC current capability. Alternatively, if R_{opt} is much less than 50 Ω, then we will need a multi-stage LC broadband matching network to transform the $R_{opt}/3$ equivalent impedance into a 50 Ω line, which is very challenging, especially when the bandwidth spans several octaves. In our design, initially the drain line impedance R_{opt} was selected as a compromise, around 105 Ω (which deviates by less than 10% from the 98 Ω). At the same time, a series gate coupling capacitance was selected in order to have the same gate voltage swing for each GaN HEMT, which means each GaN HEMT on the gate line has a relatively smaller coupling capacitor than the next ($C_{ga1} < C_{ga2} < C_{ga3}$, here we used $C_{ga1}//C_{gs} \approx C_{ds}$). A large resistor ($R_{dump}$=1200 Ω) was also added to the high impedance end of the drain line. It slightly improved the output return loss and the gain flatness while minimizing the overall power dissipation. However, its impact was insignificant and can be easily removed in the final design. Meanwhile, a gate series resistor, R_g was selected to be 750 Ω. This large resistor is in parallel to C_{ga} to realize the gate bias path and maintain the stability of the amplifier at low frequencies.

Figure 2.24 shows a schematic of the simplified tapered drain line DPA circuit for initial optimization. Table 2-9 gives some equations which we modified from [29] to calculate the initial parameter values for Figure 2.24. The specified optimization goals were set to achieve a relatively flat output power and the highest average drain efficiency over the 0.2 to 4 GHz bandwidth with a 27 dBm input power, while being unconditionally stable and sustaining better than 10 dB input/output small signal return loss. Table 2-10 gives the optimized parameter values, where C_{d1}, C_{d2}, C_{out1}, C_{out2}, L_{gin} and L_{out} are used to improve the input/output matching.

The predicted optimized results for the design with ideal elements are 39.4 +/- 0.3 dBm output power and over 40% PAE for a 27 dBm input power. The input/output return losses are better than 10 dB in the 0.2 to 4 GHz frequency range. With a 27 dBm input power, the large signal gain is about 12 dB, which is approximately compressed by 3 dB.

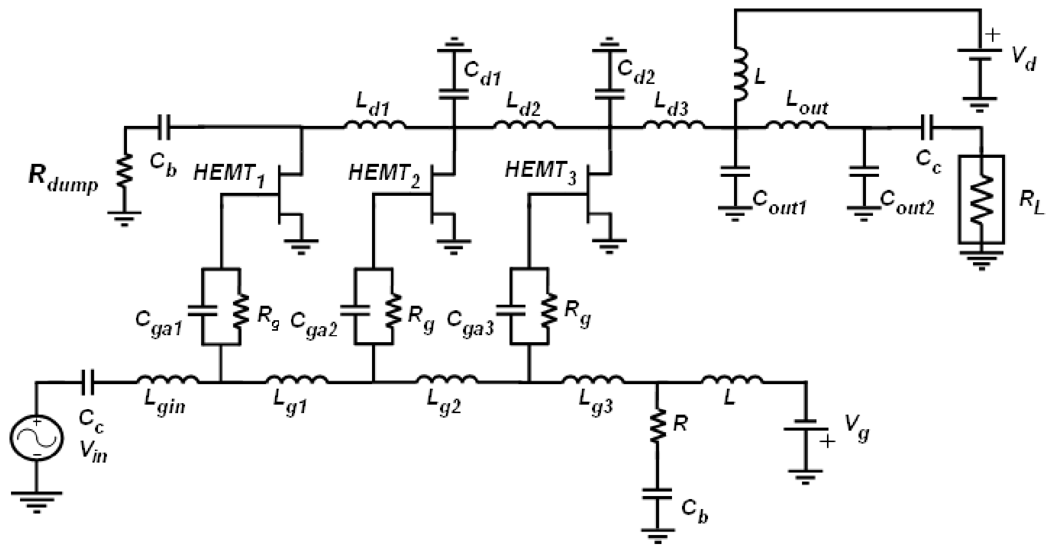

Figure 2.24 Schematic of the simplified tapered drain line DPA with idea lumped elements

Table 2-9 Initial parameters for the simplified tapered drain line DPA

Parameter	Value	Parameter	Value	Parameter	Value
C_{gs}	1.3 pF	$C'_{gs(1,2,3)}$	$C_{gs}//C_{ga(1,2,3)}$	C_{ds}	0.4 pF
L_{g1}	$(Z_0)^2\ C'_{gs1}$	C_{ga1}	1.3 pF	L_{d1}	$(R_{opt})^2\ C_{ds}$
L_{g2}	$(Z_0)^2\ C'_{gs2}$	C_{ga2}	1.4 pF	L_{d2}	$((2/3)R_{opt})^2\ C_{ds}$
L_{g3}	$(Z_0)^2\ C'_{gs3}$	C_{ga3}	1.5 pF	L_{d3}	$((1/3)R_{opt})^2\ C_{ds}$
R_{opt}	105 Ω	Z_0	50 Ω	R_{dump}	1200 Ω

Table 2-10 Optimized parameters of the simplified tapered drain line DPA

Parameter	Value	Parameter	Value	Parameter	Value
L_{g1}	2.0 nH	L_{d1}	5.2 nH	C_{ga1}	1.6 pF
L_{g2}	2.1 nH	L_{d2}	2.2 nH	C_{ga2}	1.8 pF
L_{g3}	2.2 nH	L_{d3}	0.6 nH	C_{ga3}	2.0 pF
L_{gin}	0.5 nH	C_{d1}	0.6 pF	C_{out1}	1.2 pF
L_{out}	2.1 nH	C_{d2}	0.2 pF	C_{out2}	0.7 pF

As the last step in the design we have replaced the ideal inductors and capacitors/resistors by either transmission lines or more realistic models for lumped element components. Additionally, we have accounted for many circuit discontinuities including T-junction discontinuities and actual wire wedge-bonding. As expected, a noticeable degradation in both the power bandwidth product and the small signal performance of the DPA were observed. Additionally the output power and efficiency have dropped significantly at high frequencies due to the non-optimum device loading. AWR Microwave Office 2007 was used here again to re-optimize the circuit and to improve the output power and drain efficiency while maintaining a good return loss for wideband operation. The final design was realized as shown in Figure 2.25, where the small valued capacitors (C_{d1}, C_{d2}, C_{out2} shown in Figure 2.24) that are shunted to the drain line were absorbed into the T junction discontinuities to simplify the circuit's implementation. To quantify the power performance of the DPA, however, we used the 3 dB (instead of the 1 dB) compression point. Since GaN HEMTs exhibit a soft power compression characteristic. Figure 2.26 show the simulated large signal S parameters (with a 27 dBm input power), output power, and PAE under a 3-dB compression.

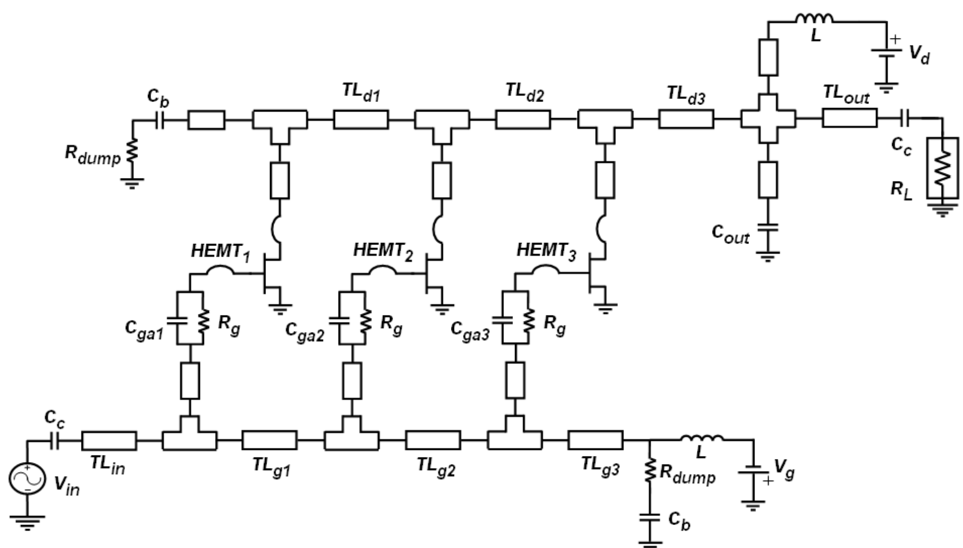

Figure 2.25 Schematic of the optimized tapered drain line DPA

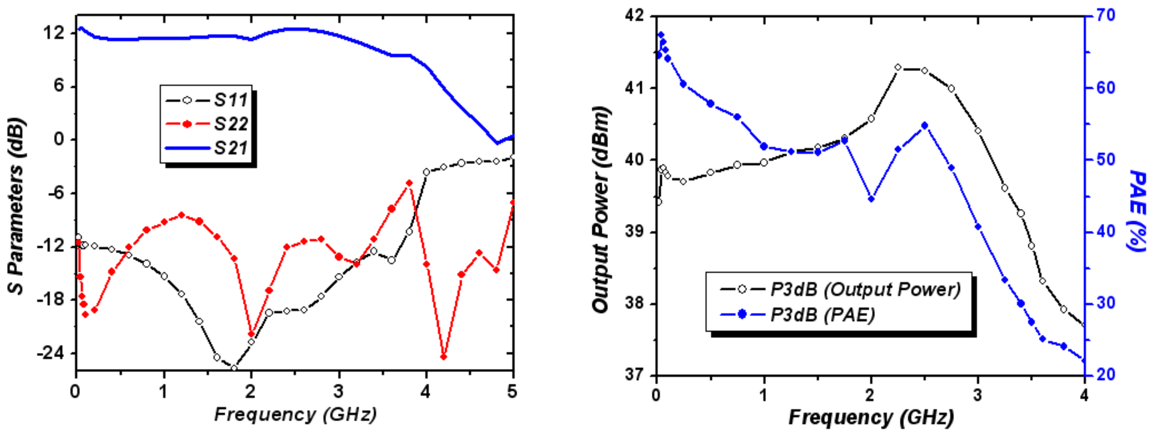

(a) (b)

Figure 2.26 Simulation results: (a) large signal S parameters with a 27 dBm input power; (b) P_{3dB} performance of the optimized DPA.

The amplifier design was also checked for stability especially at low frequencies. Generally, the standard method for checking the stability of a designed amplifier is to use the well known stability factors K and B1 but this may not be sufficient for the stability analysis of a distributed amplifier [33]. Although the standard analysis indicates that the DPA is stable, it is still possible for the DPA to be unstable due to any inter-stage oscillations that may exist between any two cascaded stages. Therefore, a modified S-probe (GPROBEM) analysis developed by Campbell et al. [34] has been applied to the input/output of each HEMT to analyze the "internal" stability where a value less than one would correspond to an unconditional stability. Figure 2.27 shows the stability index of each device. The indicated stability indices of all the S-probes are less than one from 0.02 to 8 GHz, which indicates that the DPA is unconditionally stable across the whole operating frequency range.

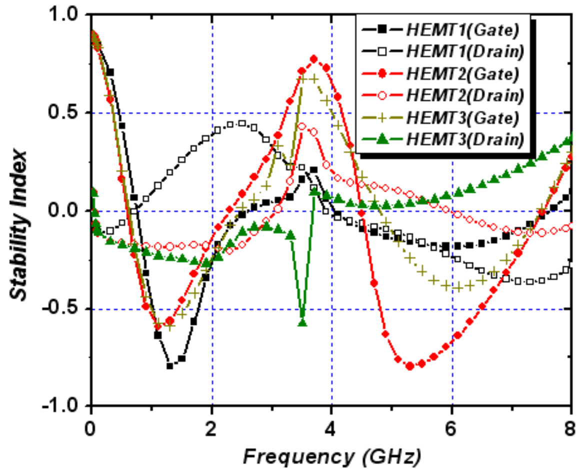

Figure 2.27 Stability indices of the optimized DPA

2.6.5 *Circuit implementation and experimental results*

The designed DPA has been fabricated and assembled directly on a brass plate to minimize thermal effects. The circuit was printed on Rogers' RT5880 soft substrate, with a ½ oz Cu. All lumped elements were surface mounted on the soft-board, and the three discrete active devices were directly attached to the base. The drain lines were meandered to reduce the circuit size. Figure 2.28 shows the implemented DPA which occupies only a 50 mm by 18 mm surface area.

The simulated and measured small-signal S parameters are compared and good agreement has been demonstrated as seen in Figure 2.29. The measured input/output return losses are better than 9 dB from 0.03 to 3.5 GHz, and the DPA gain is approximately 15.1 dB with ± 1.7 dB flatness from 0.1 to 3.5 GHz. Figure 2.30 shows the measured power performance of the DPA where the output power is greater than 36.3 dBm from 0.02 to 3 GHz and the PAE is higher than 22% based on a 3-dB compression point. At 37.3 dBm saturated output power level, the PAE exceeds 27% over the 0.02 to 3 GHz band. The DPA measured large-signal results are in good agreement with simulations at low frequencies indicating the accuracy of the Cree large-signal model. At high frequency, however, there is a noticeable difference between the simulated and measured results and could be related to some parasitic effects.

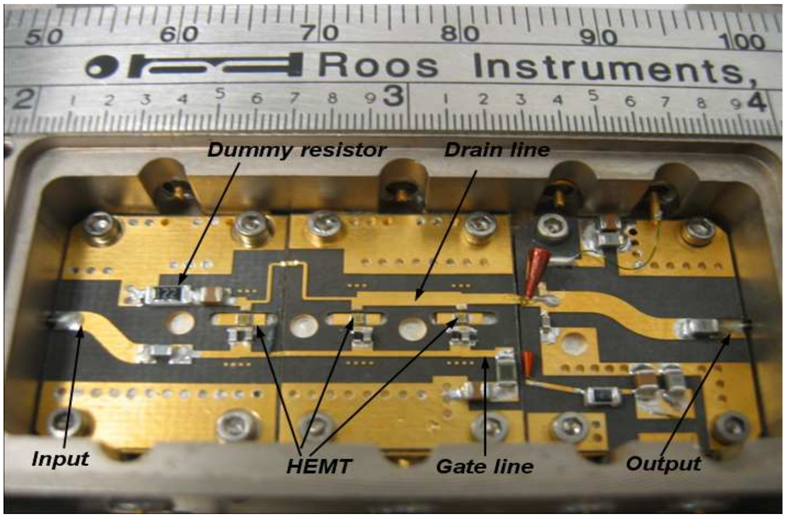

Figure 2.28 Implemented hybrid DPA

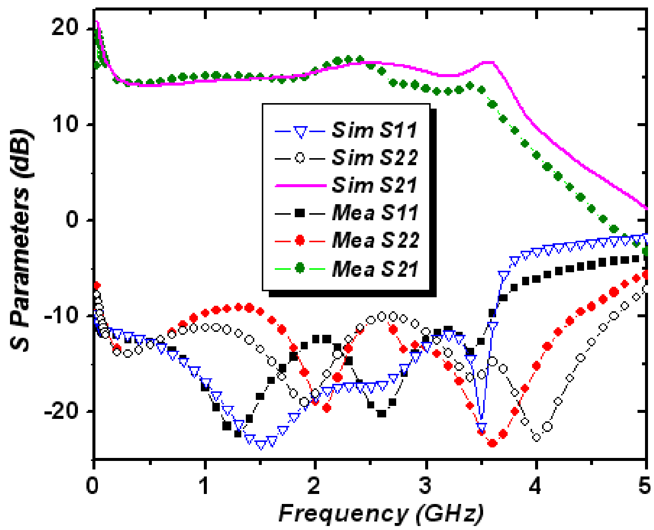

Figure 2.29 Simulated & measured small signal S parameters of optimized DPA

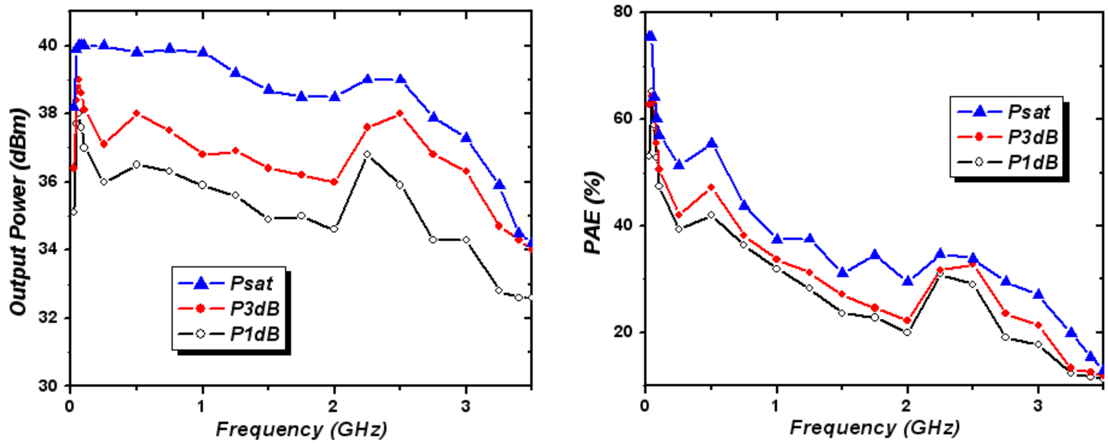

(a) (b)

Figure 2.30 Measured power performance of the optimized DPA: (a) Output power; (b) PAE

2.7 Conclusion

Distributed amplifiers and feedback amplifiers are conventionally used for low power amplification over wide frequency range. Fortunately, the recent development of GaN devices opens the possibilities of achieving higher power levels over a wide frequency range as well. However, the design of such a DPA and a feedback power amplifier over a wide frequency band is different from the conventional designs, and generally requires the utilization of large signal analysis to achieve a high drain efficiency and output power. It is also recommended to utilize both the capacitive division in the gate lines and the line-tapering of the drain circuitry to further improve the power performance of the DPA. A major challenge in designing such high gain DPAs is achieving wideband stability. A modified S-probe (GPROBEM) analysis is recommended here to insure internal and overall stability of the DPA. Our hybrid DPA implementation uses medium size GaN HEMTs and has been successfully designed and fabricated, and it provides greater than 5 W (37 dBm) output power and over 27% PAE in the 0.02 to 3 GHz frequency range. Our hybrid feedback power amplifier has been successfully developed using medium size GaN HEMs to achieve greater than 1W (30 dBm) output power and over 22% drain efficiency in the 0.1 to 5 GHz frequency range.

Chapter 3 Investigation of LINC transmitter

3.1 LINC Transmitter Overview

In modern digital communication systems, various modulation schemes have been applied to achieve high spectrum efficiency. These schemes include high order M-ary quadrature amplitude modulation (QAM) and orthogonal frequency division multiplexing (OFDM). However, these signals are characterized by high peak-to-average power ratios (PAPRs) which exploit deep envelope fluctuations. These unavoidable phenomena constitute a serious problem for the nonlinear behavior of power amplifiers, and also cause a major problem for the modern communication systems since it is essential to achieve a high linear-efficient RF amplification.

Therefore, linearity is crucial in minimizing signal distortion in order to maintain low levels of error vector magnitude (EVM) and adjacent channel leakage ratio (ACLR). At the same time, efficiency enhancement techniques are needed to achieve the highest performance and cost savings for the next generation base-station applications. For example, efficiency techniques significantly influence the thermal management, reliability, and operating costs of the base stations. However, highly linear performance is difficult to realize while simultaneously achieving high efficiency. A number of approaches have been used to solve this problem [4, 35]. Table 3-1 lists a variety of these approaches and summarizes the pros and cons of each.

One good candidate is the LInear amplification with Nonlinear Components (LINC) that can be used to simultaneously achieve relatively high efficiency and linearity. The concept of out-phasing amplification is a technique proposed by Chiréix [36] in 1935, and was introduced again as LINC, by Cox, in 1974 [37]. The LINC principle is based on decomposing an amplitude modulated signal into two constant-envelope components using a Signal Component Separator (SCS). The SCS is utilized to perform such decomposition by either a DSP algorithm [38] or an analog RF circuit [39]. The resulting two constant-envelope components can then be amplified individually by two high efficiency non-linear amplifiers. During this amplification, the constant-envelope signals are immunized against distortion. After amplification, they are then properly combined to create the linear-amplified original signal, as shown in Figure 3.1.

Table 3-1 Linearization and Efficiency Enhancement techniques

	Advantages	Disadvantages
Linearization techniques		
Power back-off	- Simple	- Low efficiency
Pre-distortion	- Feasible	- Requires extensive modeling
Feed-forward	- Stable	- Difficult to match and suffers from drifting
Feed back	- Simple, not sensitive to poor PA modeling	- Stability concerns
Efficiency enhancement techniques		
EER (Khan Envelope Elimination and Restoration)	- High efficiency - Medium band	- Poor linearity due to AM-PM conversion
LINC (linear amplification using non-linear components)	- Great potential - Potential wide band	- Need to compromise between efficiency and linearity
ET(envelope tracking)	- Wide band - Using linear amplifier	- Need baseband PD** - Difficult for time alignment
Doherty Technique	- Good for PAR** between 3 to 6 dB	- Narrow band - Need linearization

Notes: PAR--- peak to average ratio; PD--- pre-distortion;

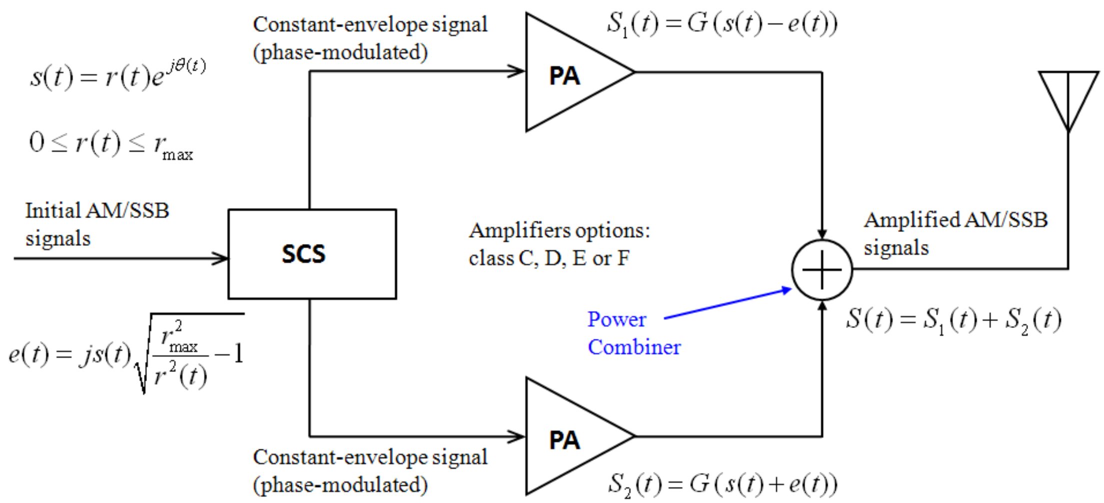

Figure 3.1 A simplified LINC transmitter schematic [40]

After Cox [37], the LINC approach has been applied to a variety of wireless applications. Multiple variations/modifications on the LINC approach have been proposed to improve the linearity and efficiency of the modern wireless communication systems. For example, ELINC (Enhanced Linear Amplification with Non-linear Components) and MILC (Modified Implementation of the LINC Concept) are modified versions of the basic LINC transmitter. The ELINC transmitter can achieve both better modulation accuracy and good out-of-band spectral performances over the conventional LINC transmitter without physically adjusting the branches' conditions. The MILC is based on allowing a limited and controlled amplitude variation of the separated signals so that nonlinear amplifiers can still be used. This approach is designed to offer an efficient way for amplifying signals with high crest factors (the crest factor is the ratio between the average and peak signal levels**)**. Moreover, The MILC approach is less sensitive to branch imbalances. Table 3-2 lists some of these approaches.

As shown in

Figure 3.1, a complex representation of the band-limited source signal can be written as

$$s(t) = r(t)\ e^{j\theta(t)}\ ; \qquad (\,0 \le r(t) \le r_{\max}\,)\ . \tag{Eq 3.1}$$

This signal is split by the SCS into two signals, $S_1(t)$ and $S_2(t)$, with modulated phases and constant-envelope

$$S_1(t) = s(t) - e(t)\,; \tag{Eq 3.2}$$

$$S_2(t) = s(t) + e(t)\,; \tag{Eq 3.3}$$

$$e(t) = js(t)\sqrt{\frac{r_{\max}^2}{r^2(t)} - 1}\ . \tag{Eq 3.4}$$

Then, each signal is amplified by a high efficiency non-linear PA

$$S_{1a}(t) = G\ S_1(t)\,; \tag{Eq 3.5}$$

$$S_{2a}(t) = G\ S_2(t)\,; \tag{Eq 3.6}$$

where G is the voltage-gain of the PA.

After amplification, the two signals are added together with a summing network. Next, the input signal will be retrieved, but efficiently amplified with minimal distortion

$$S_{out}(t) = S_{1a}(t) + S_{2a}(t) = G\ (S_1(t) + S_2(t)) = G\ S(t)\,. \tag{Eq 3.7}$$

In this case, the emphasis is on maximizing the efficiency of the utilized amplifiers, while the use of constant-envelope signals help in reducing and even eliminating the need for highly linear PAs. However, it introduces a new set of potential challenges, indicated below.

Table 3-2 Survey of various types of demonstrated LINC transmitters

Type	Advantage	Disadvantage
LINC with Chiréix combiner [41]	-High efficiency	-Poor linearity, required pre-distortion to improve linearity -Narrow band
Quadrature LINC [42]	-Higher tolerance to gain and phase mismatches between the two branches -Use I & Q signals to reduce the phase modulation spreading angle -Use isolated power combiner to achieve high linearity	-Low average efficiency for high PAR signal due to isolated power combiner -Requires two combining steps -Requires 4 amplifiers compared to 2 for conventional LINC -More complex structure
Mode-Multiplexing LINC [43]	-Switch between balance class B and LINC according to threshold power to achieve high average efficiency	-Lower PA instantaneous efficiency due to class B operation -Medium linearity
Multilevel LINC [44]	-Shrink the combining angle to multilevel to improve average efficiency of Wilkinson power combiner	-Need pre-distortion to improve linearity Complex system
MILC [45]	-Use threshold amplitude to achieve high average combining efficiency	-Need pre-distortion to compensate low linearity
Bias Control LINC [46]	-Higher linearity than conventional LINC with a high output power -High average efficiency	-Omit the combiner's effects -Lower linearity than conventional LINC with lower output power
Enhanced LINC [47]	-Higher tolerance to branch mismatch -No need to physically adjust the combining circuits	-Complexity -Same efficiency with conventional LINC transmitter
LINC with power reuse technology [48]	-High linearity; Improving overall efficiency	-The efficiency improvement depends on the DC rectifier -Low efficiency for high PAR signal

For a wideband LINC transmitter, there are two main challenges:

(a) the need for a high efficiency non-linear wideband PA;

(b) the requirement of a low loss wideband power combiner.

The specific requirements for the power combiners and power amplifiers utilized for the LINC transmitter will be briefly discussed in the next two sections. Further details will be shown in Chapters 4 and 5.

3.2 Investigation of the Power Amplifiers for the LINC Transmitter

The efficiency of the LINC transmitter is also dependent upon the specific efficiency characteristics of the individual PAs utilized. For the LINC transmitter chain, a variety of PAs can be considered, including class A, B, AB and C (Conventional PAs), and class D, E, and F (SMPAs). The SMPAs are well known in achieving a relatively high efficiency. A comparison between the various SMPAs operations (class D, E and F) that employ the transistors as switches and the conventional mode PAs that employ the transistors as current sources shows that the efficiency of the SMPAs are substantially higher. Thus, the SMPAs will be utilized in our investigation. At the same time, in the LINC transmitter, mentioned in the previous section, either isolated or non-isolated power combiners can be used for various applications. For example, if an isolated power combiner is utilized, then the PA selection is relatively unrestricted. However, if a non-isolated power combiner is chosen, each PA will see a time-varying load presented at its output port. This will then cause significant interaction between the output's signals. Subsequently, these interactions must be carefully accounted for.

Besides having a higher efficiency, SMPAs are also less susceptible to parameter variations, such as output matching network components, and could impose a lower thermal stress on the utilized transistors than the thermal stress generated in a conventional mode PA operation. Therefore, SMPAs can compete with conventional mode PAs in LINC applications.

In our collaboration with Rockwell Collin Inc., a voltage-mode class D PA has been selected for wideband LINC application, however, class E can be used as well. In this study, we will discuss the design details of the selected wideband class D PA in Chapter 4.

3.3 Investigation of the Power Combiners for the LINC Transmitter

The average efficiency of a LINC transmitter is generally the product of the non-linear power amplifiers' efficiency and the efficiency of the combiner, given that the SCS portion's efficiency can be assumed to be almost a 100%. SCS portion only consume a very small fraction of the DC power when compared with the usage for the PAs. Meanwhile, the individual power amplifier's efficiency can be maximized for a constant-envelope signal by operating in either a class C or an overdriven class B, or in a SMPA mode. Subsequently, the overall efficiency of the LINC transmitter remains dependent on the combining structure utilized. The combiner's efficiency, in turn, depends on the signal's dynamics, i.e. its crest factor and probability distribution function (PDF), as well as on the combiner's topology [49]. The selection of the optimum combiner would also greatly impact overall performance.

Generally, there are four kinds of combiners that can be used at the output combing stage, as shown in Figure 3.2 (the Wilkinson, the Chiréix, the hybrid, and the non-isolated combiners). These four types of combiners can be separated into two categories: Isolated and Non-isolated.

Table 3-3 Comparison of power combiners

Table 3-3 compares the pros and cons of the above mentioned combiners.

The Chiréix combiner will not be considered in this dissertation due to its narrow band performance as we are only considering wide band components. Typical methods of the design and simulation of wideband power combiners will be presented in Chapter 5. The details of how the other combiners affect the linearity or the efficiency of the LINC transmitter will be discussed later in Chapter 6.

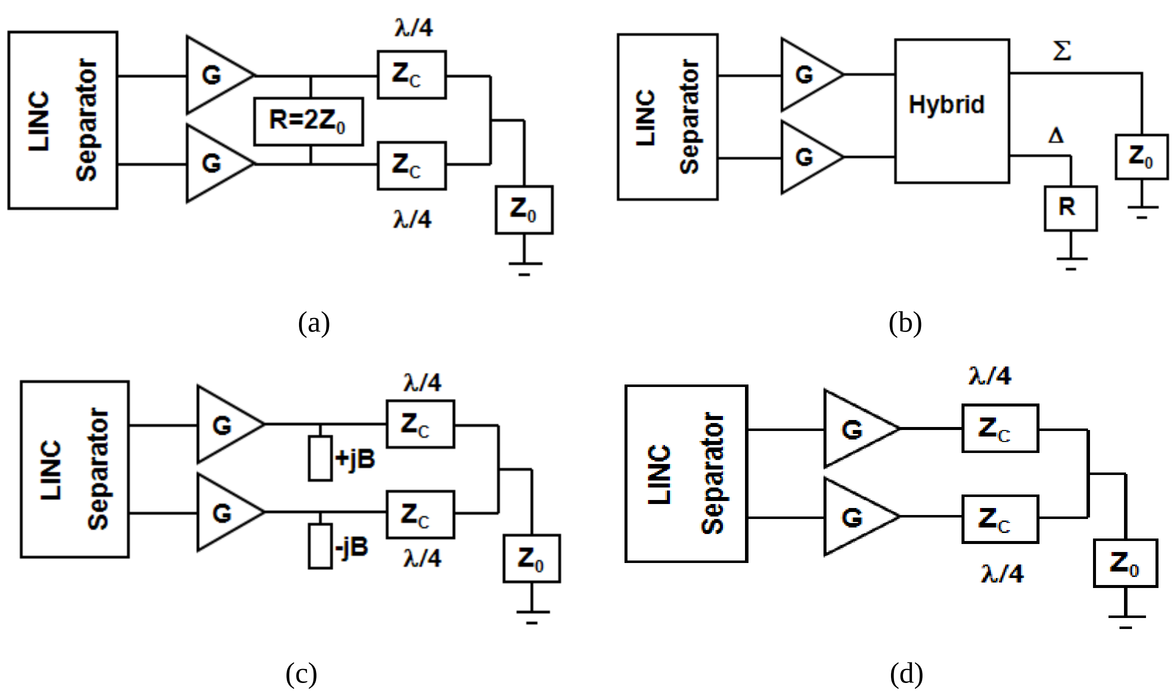

Figure 3.2 Power Combiners: (a) Wilkinson combiner; (b) Hybrid combiner; (c) Chiréix combiner; (d) Conventional non-isolated combiner (modified Chiréix).

Table 3-3 Comparison of power combiners

	Type	Advantages	Disadvantages
Isolated Combiners	Wilkinson combiner	Preserves a high linear performance and it has a simple structure	$\eta_{AVG} = \sum_{i=1}^{N} p(\theta_i)\cos^2(\theta_i)$
	Hybrid combiner	Preserves the high linear performance and can be used for power recycling.	$\eta_{AVG} = \sum_{i=1}^{N} p(\theta_i)\cos^2(\theta_i)$
Non-isolated Combiners	Chiréix combiner	Has very high efficiency[49] $\eta_{AVG} = \sum_{i=1}^{N} p(\theta_i)\eta(B,\theta_i)$	Narrow band and a very poor linearity, needs pre-distortion [49]
	Conventional non-isolated combiner	Structure is optimized for high efficiency and has a simplified structure	It has a medium linearity due to the load-pull of the matching network

Note: η is the combining efficiency, which is defined by: $\eta = P_{sum} / (P_{sum}+P_{diss})$; here P_{sum} is the summing power and P_{diss} is the dissipated differential power; B is the shunt reactance of the Chiréix Combiner; $p(\theta)$ is the probability distribution function (PDF) of the decomposition angle.

3.4 LINC System Simulation

Recently Electronic Design Automation (EDA) tools have become extremely powerful, which makes communication system simulations more practical and accurate. The LINC transmitter can be simulated using different methods, according to the input signals, via an Agilent Advanced Design System (ADS). Table 3-4 shows different methods to simulate the LINC transmitter.

Here, a LINC transmitter [50] with a sine wave (shown in Figure 3.3) and a 16QAM (shown in Figure 3.5) signals will be shown to demonstrate the basic premise of the LINC transmitter. In Figure 3.3, in the input section, a 5-port network is utilized to symbolically define the equations for the signal decomposition, denoted by the block SDD5P (a 5-Port Symbolically Defined Device). The two tone signals are set at 1 MHz intervals away from the center frequency (100 MHz, for example). The P_{avs_in} is used to define the input power of the two tone signals. The two-tone signal can be presented as $s(t) = r(t)\, e^{j\theta(t)}$, $(0 \le r(t) \le r_{\max})$, so r_{max} is set at 1.778V, which relates to a 15 dBm input power (P_{avs_in}=15 dBm). The node signal V_1 equals s(t), V_2 equals js(t) by passing a signal equals to V_1 through a 90 degree phase shifter, and V_3 equals –js(t) by similarly passing a signal equal to V_1 through a -90 degree phase shifter. So, in the SDD5P, output signals are given by

$$V_4 = V_1 + V_2\sqrt{\frac{r_{\max}^2}{V_2^2 + V_1^2} - 1}; \qquad \text{(Eq 3.8)}$$

$$V_5 = V_1 + V_3\sqrt{\frac{r_{\max}^2}{V_3^2 + V_1^2} - 1} \qquad \text{(Eq 3.9)}$$

where V_4 and V_5 are constant-envelope signals for the two branches. For more details, refer to Appendix B.

Amp1 and Amp2 are two ideal amplifiers which can be replaced by any customized power amplifiers. In the output section, a Wilkinson combiner (PWR1) is used, but it can be replaced by other combiner types. As shown in Figure 3.4, the two PAs' output signals have strong nonlinear performance (i.e. IMD=10 dB), but the output signal of the isolated combiner is highly linear (i.e. IMD=29 dB).

Table 3-4 Simulation methods for LINC transmitter

Signal Type	Analysis Method
Sine wave	Harmonic Balance Simulation (an example is shown in Figure 3.3)
16QAM / IS-95CDMA / Pi/4 DQPSK	Envelope Simulation (an example is shown in Figure 3.4)
Custom defined signal	Ptolemy & Matlab co-simulation (an example will be given in Chapter 6)

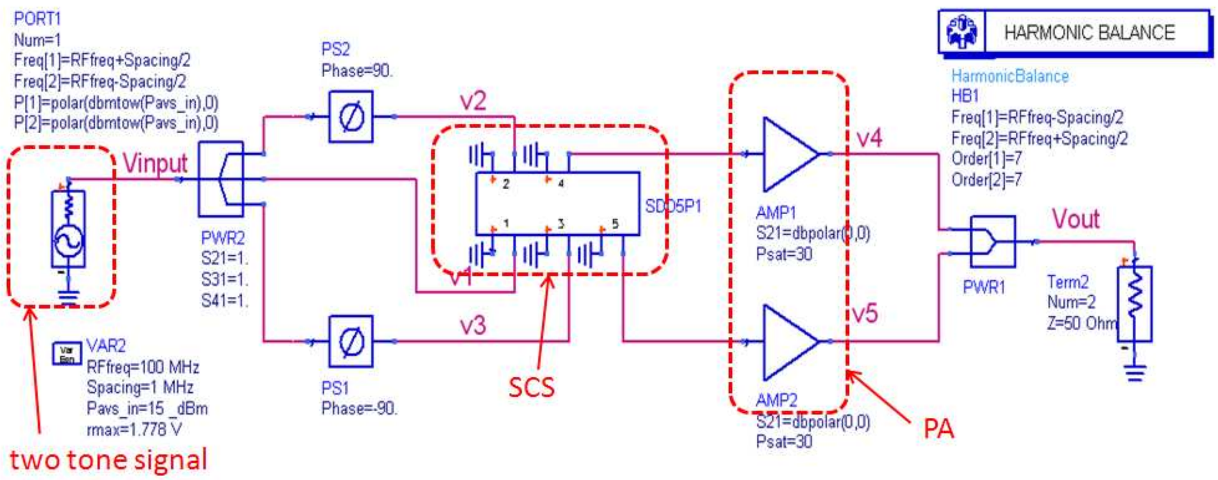

Figure 3.3 LINC transmitter using Wilkinson combiner

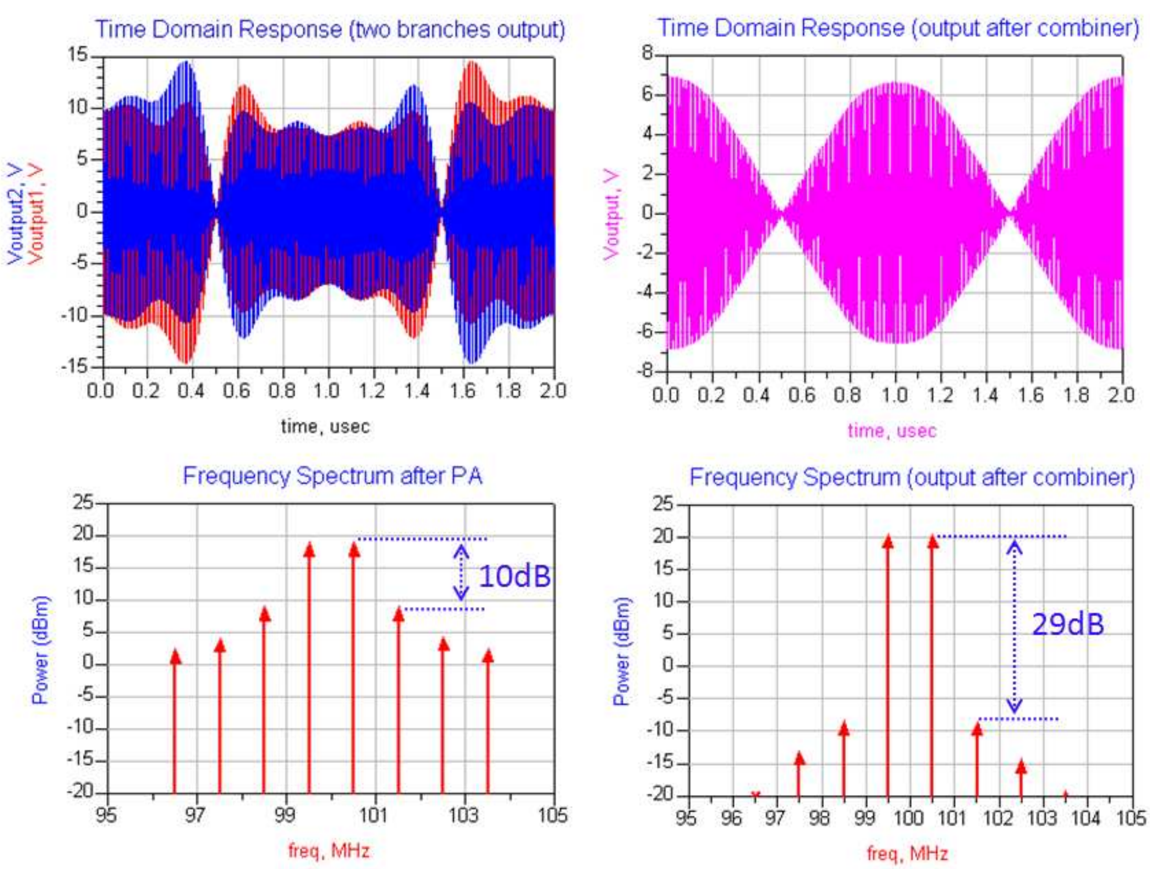

Figure 3.4 Simulation results of LINC transmitter using Wilkinson combiner

In the left part of Figure 3.5, there is an ADS pre-defined modulated source (Source_QAM_1), which can be used to generate a 16 QAM signal. In the middle of Figure 3.5, each constant-envelope baseband signal is up-converted to an RF signal via an IQ modulator (MOD1&MOD2). Two constant-envelope RF signals are amplified by two saturated amplifiers (AMP1 and AMP2), and then combined with a Wilkinson combiner (PWR1).

The time domain constant-envelope RF signals are shown in Figure 3.6 a&b. On the right side of Figure 3.6a, the time domain output power shows a high PAR which is 5.96 dB. Figure 3.6c compares the spectrums of a reference signal (red), an amplified branch signal (aqua) and a combined output signal (blue). As shown in Figure 3.6c, the normalized amplified constant-envelope signal (aqua) occupies a wider frequency band and the out band's signal is cancelled after combining. The ACPR of the combined output signal is better than -52 dBc, which verifies the high linearity of the LINC transmitter. However, the efficiency of the LINC transmitter is related to the PAs performance. Further simulation of LINC transmitter will be discussed in the Chapter 6.

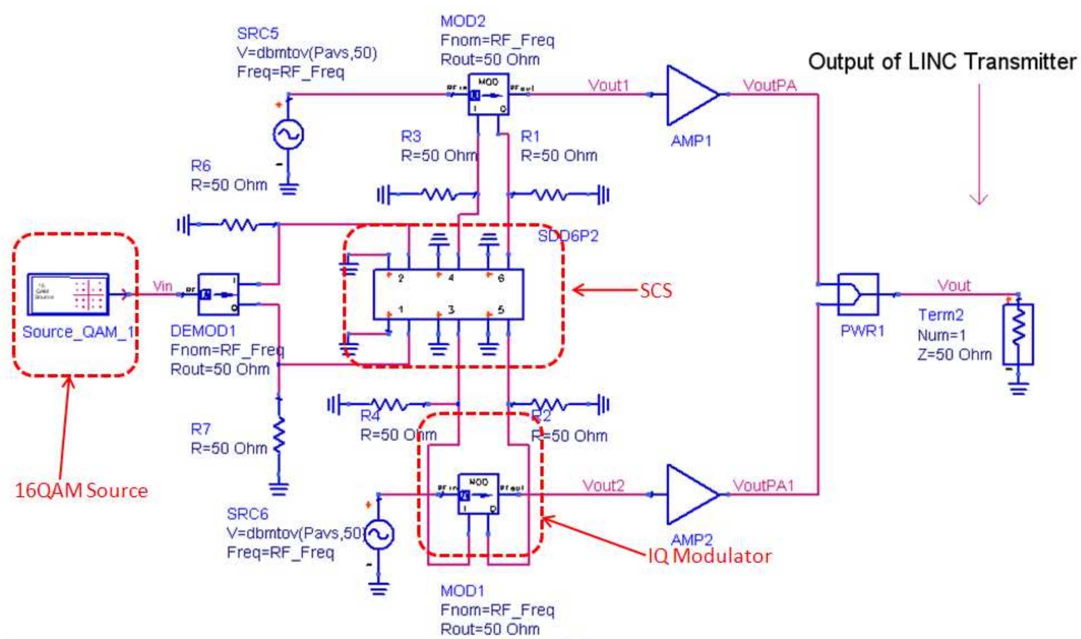

Figure 3.5 LINC transmitter with a 16 QAM signal [50]

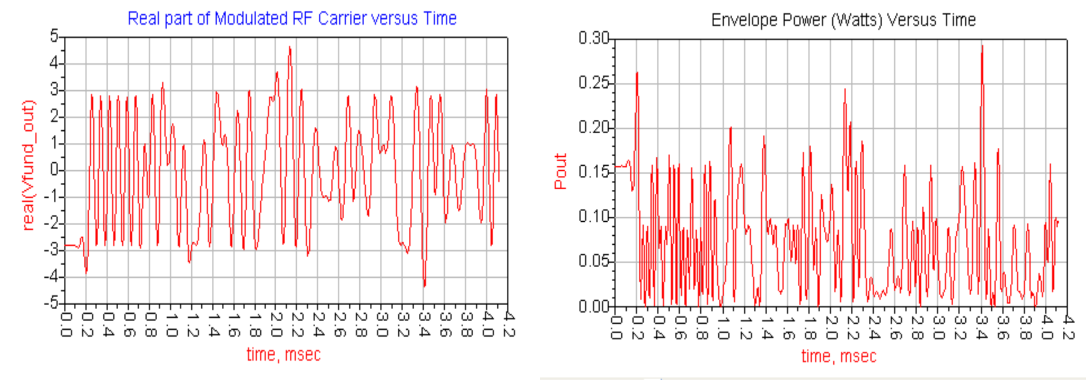

(a)

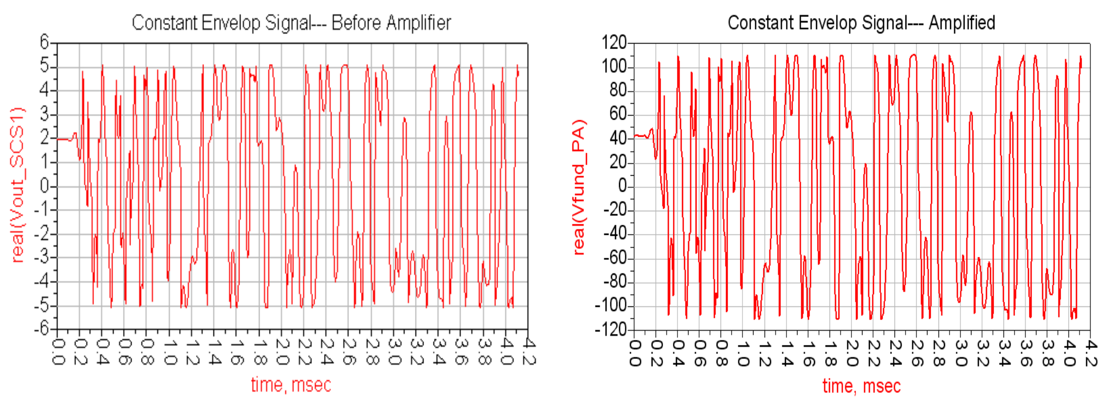

(b)

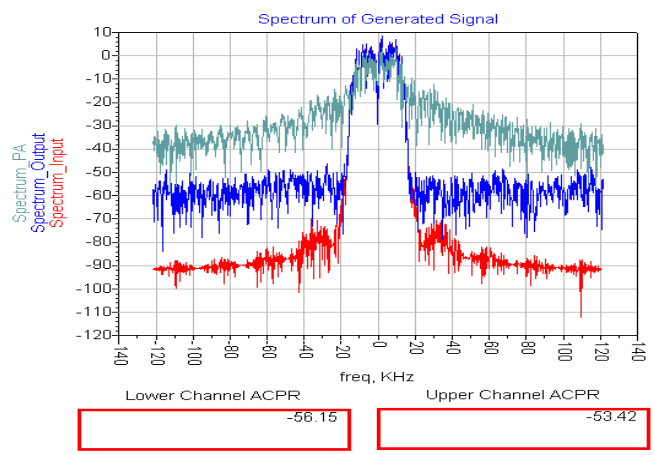

(c)

Figure 3.6 Simulation results of a LINC transmitter with 16 QAM signal: (a) Modulated RF carrier signal and envelope power; (b) Constant-envelope signals before and after power amplifier; (c) Spectrum of initial signal (red), amplified signal (aqua) and combined signal(blue)

Chapter 4 Wideband Class D Development

4.1 Introduction

Switching-mode power amplifiers (SMPA) have a relatively high efficiency. This is based on a comparison to the conventional mode PAs which employ the transistors as current sources. Therefore, the SMPA are preferable to the conventional mode PAs for LINC applications. Besides having a higher efficiency, SMPAs are also less susceptible to parameter variations. The SMPAs could impose a lower thermal stress on the transistors than the conventional mode PAs. From an application point of view, FM and PM communication systems are well-suited to take advantage of the SMPA's high efficiency, regardless of their nonlinearity. However, SMPAs are not suitable for AM communication systems without implementing advanced linearity and efficiency enhancement techniques. Therefore, the LINC and EER, using SMPAs, are commonly used to create highly linear signals. The overall efficiency of the LINC and EER transmitters is dependent upon the specific efficiency characteristics of the individual PAs. Therefore, it is crucial to select the correct device technology.

GaN HEMTs, for example, have been extensively utilized for a superior performance at high frequencies in a SMPA operation. The high thermal conductivity of GaN HEMTs on a SiC substrate provides superior characteristics relative to either the GaAs or the Si counterparts, makes this technology well-suited for high power and high temperature applications. Additionally, GaN HEMTs have high power density, high breakdown voltage and low parasitic capacitances, making them more suitable for high power and high efficiency SMPA implementations at high frequencies.

SMPAs have different class designations. They range from D through S. Many of these classes have been developed and published [51]. "Class D" amplifiers were first discussed by Baxandall [52], but have not been fully researched yet, especially for wideband applications. Therefore, we have picked class D amplifiers to investigate for their potential in our investigation. Our investigation was sponsored by Rockwell Collins Inc.

A class D amplifier employs a pair of active devices and a loaded output tank circuit. The devices are driven into saturation and act as a two-pole switch that generates either a rectangular voltage or current waveforms at the input of the loaded tank circuit. The tank output circuit is tuned to only allow the switching frequency and reject all other harmonics, resulting in a sine-wave output waveform. The design details of our developed wideband, high efficiency, class D PA based on GaN HEMT technology, will be described in the following sections.

4.2 Basic Concept of Class D Power Amplifier and the State of the Art

Ideally, a class D PA works as a switch, either having a high current with a zero voltage or having a high voltage with a zero current, as shown in Figure 4.1. Subsequently, the efficiency of an ideal class D PA is 100%.

Traditionally, there are two typical types of class D PAs. Namely, a transformer coupled voltage-mode class D (VMCD) and a transformer coupled current-mode class D (CMCD). The two configurations are shown in Figure 4.2. These circuits are comprised of two switching devices working under push-pull mode, a resonant RLC tank circuit, an input balun transformer, and an output balun transformer. The two modes, VMCD and CMCD, are dual circuits. The VMCD has a constant center-tap voltage V_{dd} with a capacitor and a series RLC tank. The CMCD has a constant center tap current I_{dd} with an RF chock and a shunt RLC tank. Subsequently, the VMCD can have a rectangular drain voltage with a half-sine drain current and the CMCD can have a rectangular drain current with a half-sine drain voltage, as shown in Figure 4.3.

For CMCD, the RF chock inductor supplies a constant current I_{dd}. Meanwhile, both the I_{ds1} and I_{ds2} are rectangular waves alternating between 0 and I_{dd}. These two out-phase currents are combined in the output transformer (m/n is the turns ratio), and the output current of the transformer is $I_{total}= m/n\ (I_{ds2}-I_{ds1})$, or a rectangular wave. Ideally, the parallel output tank circuit acts as an open circuit at even harmonics and short circuit at odd harmonics, therefore, the V_{out} is a sine-wave. At the same time, V_{out} is transformed back by an output transformer (TF_2) to make V_{ds1} and V_{ds2} appear as half-sine waves.

Figure 4.1 Operation region of class D PA

Similarly, for the VMCD, an RF capacitor supplies a constant voltage of V_{dd}. Each V_{ds} is a rectangular wave with alternating peak values of 0 and $2V_{dd}$. The two out-phase voltages add in the output transformer, and the output voltage of the transformer "V_{total}=m/n (V_{ds2}-V_{ds1})" is a rectangular wave. The series output tank circuit acts as a short circuit at even harmonics and open circuit at odd harmonics, therefore the I_{out} is a sine wave. At the same time, I_{out} is transformed back by the output transformer (TF_2) to make I_{ds1} and I_{ds2} appear as half-sine waves.

Generally, the C_{ds} will cause power dissipation given by ($P_{diss} = \frac{1}{2} C_{ds} V_{ds,off}^2$) for every period, where $V_{ds,off}$ is the drain-source voltage when the switch is closed, due to the charging-discharging process. Ideally, if $V_{ds,off}$ is zero, the power dissipation becomes zero. This is called zero voltage switching (ZVS). Usually, CMCD PAs can achieve the ZVS scenario, whereas VMCD PAs typically cannot. The relationship between V_{dd}, I_{dd}, R_L and the m/n ratio for a given output power will be depicted in the next section, as they relate to our specific design goals. Multiple variations of these two basic modes have already been developed. They have been published [42, 53-59] with noticeably improved performances.Table 4-1 represents the state of the art of class D PA. In a parallel effort with the Rockwell Collins' group, we investigated the use of a Cree device operating at 28 V, while they investigated a Eudyna device with an operating point of 50V. With the Cree device, we were able to achieve a 63% drain efficiency with at least a 20W output power over the 50 to 550 MHz bandwidth. However, further improvement can be achieved with a more precise tuning. Meanwhile, at Rockwell, they achieved a 60% efficiency with at least a 60W output power over the 30 to 450 MHz bandwidth[42].

Here, we summarize our design process for a class D PA as indicated in Figure 4.4. Additional design and simulation details will be given in the next sections.

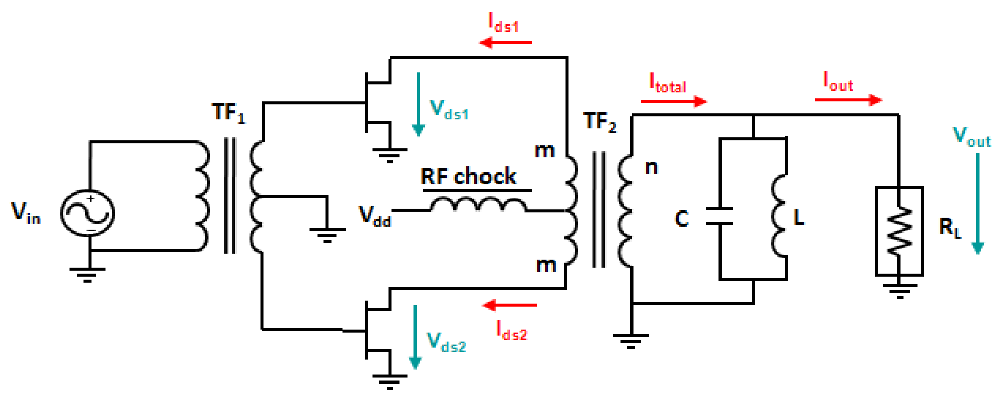

(a)

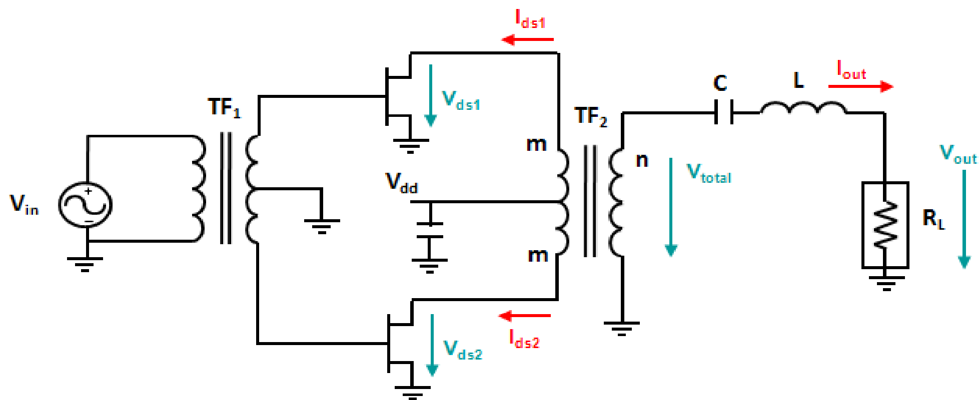

(b)

Figure 4.2 Class D PA configurations: (a) CMCD; (b) VMCD

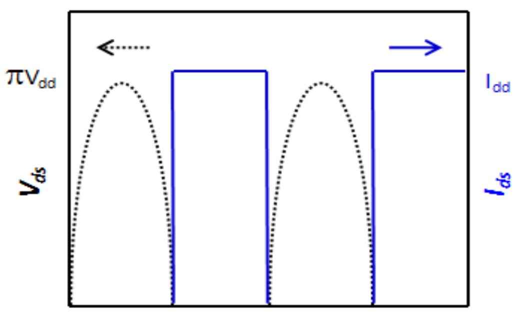

$$I_{dd} = \frac{\pi^2}{8}\frac{V_{dd}}{R}$$

(a)

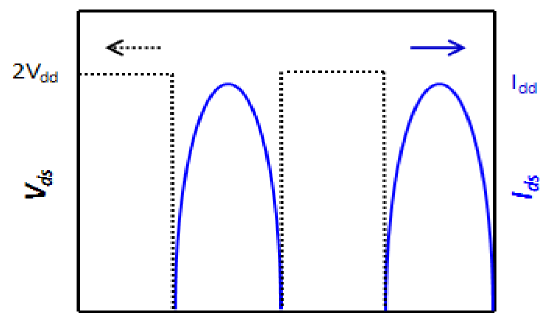

$$I_{dd} = \frac{8}{\pi^2}\frac{V_{dd}}{R}$$

(b)

Figure 4.3 Class D PA transient waveforms: (a) CMCD; (b) VMCD

Table 4-1 State of the art of class D power amplifier

	This work	A. Long [54]	K. Ji-Yeon [55]	H.Nemati [56]	H. Kobayashi[57]	Frederick H. Raab [58]	Gustavsson [59]	G.Hegazi [53]	G.Hegazi [42]
Power	20 W	13W	50 W	20.3 W	0.29 W	100W	20W	56W	60W
Gain (dB)	14.5	14	10	15.1	N/A	N/A	10.6	14	14
Drain Efficiency	63%	60.3%	63%	71%	76.3%	83%	65%	53%	60%
Class	VMCD	CMCD	CMCD	CMCD	CMCD	VMCD	CMCD	VMCD	VMCD
BW (MHz)	50 - 550	N/A	N/A	90	N/A	0.1 to 3	40	30 - 450	30 - 450
Freq (MHz)	50 - 550	1000	1800	1 000	900	0.1 to 3	1000	30 - 450	30 - 450
Device	Cree GaN HEMT CGH40010F	Ericsson Si LDMOS PTF 10135	Freescale LDMOS MRF19045	Freescale LDMOS MRF282	Infineon GaAs MESFET CLY5	MOSFET	Eudyna GaN HEMT EGN010MK	Eudyna GaN HEMT EGN045MK	Eudyna GaN HEMT EGN045MK

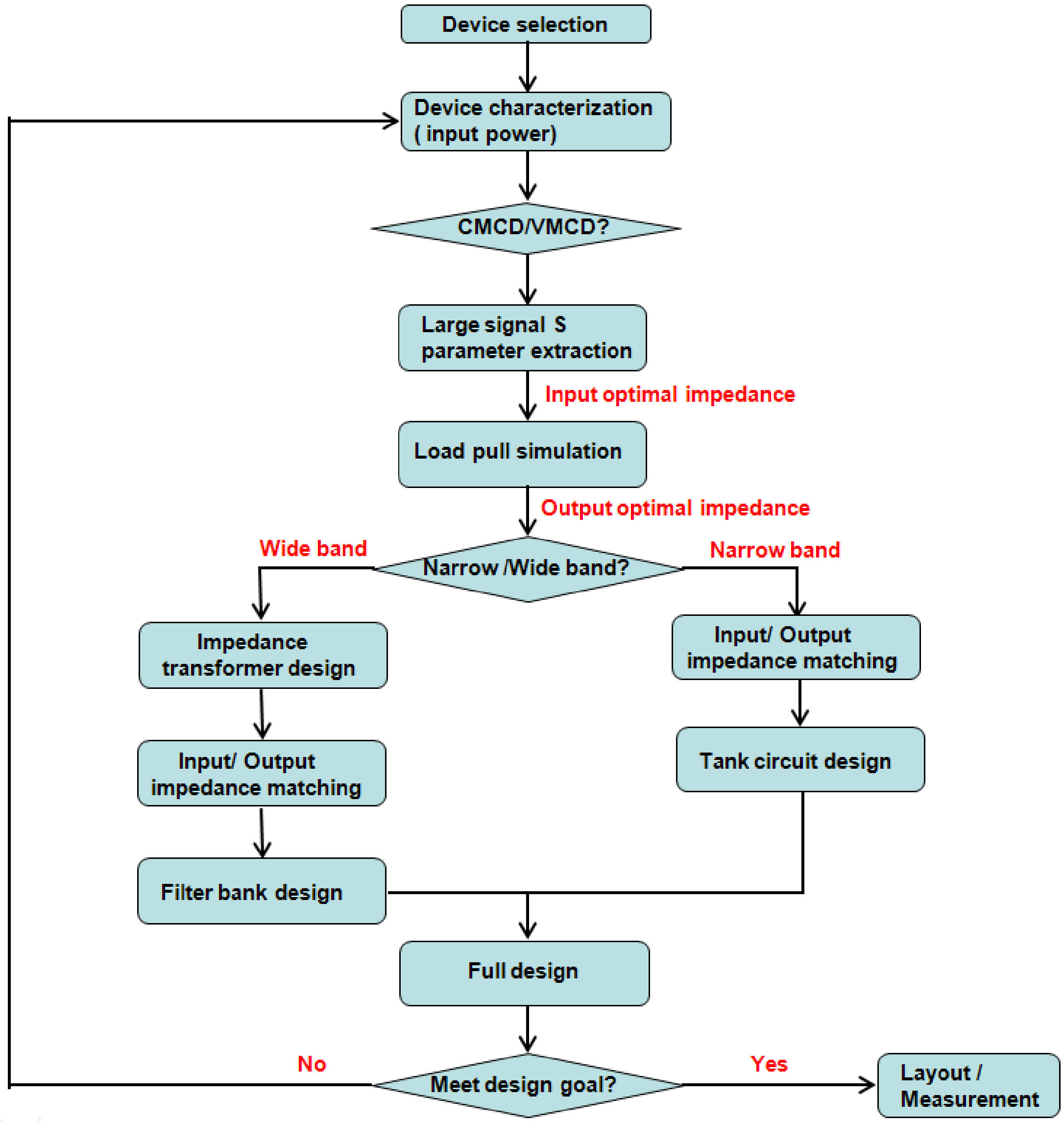

Figure 4.4 Class D PA design flow

4.3 Device Selection for Class D PAs

Ideally, a class D PA can achieve 100% drain efficiency. However, in any practical circuit, the parasitic of the device, for example, C_{ds} and the lead inductance, L, can cause losses on the order of $0.5C_{ds}V^2$ and $0.5LI^2$ respectively, due to their charging-discharging processes. These losses cause a significant drop in drain efficiecny. At the same time, additional factors related to the device parameters can cause further efficiency degradation[60]. For example, the saturation voltage of the transistor (V_{DCsat}), and the ON-resistor of the transistor (R_{ON}) should have low values. Additionally, in order to have a device working as a switch and generating a rectangular wave, its gain cut-off frequency (f_T) should be at least 10 times higher than its switching frequency so that its spectrum allows the generation of higher order harmonics. Here a CREE GaN device (CGH40010F) was selected to design a class D PA.

Table 4-2 shows the basic GaN device compliance matrix and its compliance matrix selected for use. As shown here, CREE CGH40010F is a good candidate to design a class D PA.

Table 4-2 GaN performance in terms of device requirements for class D PA

	Device requirements of a class D PA	GaN HEMT performance (CGH40010F) as example
High frequency switching	gain cut off frequency (f_T) --- the higher the better; usually about 10 times of the operating frequency	>20 GHz
High output power	breakdown voltage--- the higher the better	>84V
High efficiency	on-resistor --- the smaller the better gain --- the higher the better	~1.1 Ω > 20 dB @ 500MHz
Low DC current consumption	drain current --- the lower the better	I_{ds} = 2.7 A, usually less than 1A
Wide band	small input /output / feedback capacitance	C_{GS}= 5 pF C_{DS}= 1.32 pF C_{GD}= 0.43 pF

4.4 Device Characterization

A class D PA should be biased close to the device pinch-off and its optimal load impedance should be carefully selected. As a first step in the design, and to understand device performance, a DC sweep was applied using Agilent ADS and is shown in Figure 4.5. Therefore, we have selected a V_{gs}= -3V to be close to the pinch-off voltage of the device, shown in Figure 4.6. Also, as recommended by the vendor (CREE), we selected a drain voltage of V_d =28V.

4.5 Class D Power Amplifier Topology

Generally, the ZVS operation is preferred, as previously explained, since it can minimize energy dissipation and increase the power amplifier's drain efficiency. Additionally, the parasitic capacitances can be absorbed into the parallel output tank circuit for a high frequency operation. However, these advantages of CMCD are outweighed by various, serious disadvantages such as the required large inductor (RF choke) that would introduce an additional power loss and the use of a rectangular-wave drive that yields higher power losses in the gate circuit. Additionally the loss due to switching the large rectangular currents using active devices would cause switching losses and may have additional saturation losses[60]. Alternatively, the VMCD behaves like an ideal voltage source and whose output voltage is independent of the load. These factors indicate that it is a good candidate for LINC applications[61]. The VMCD is also preferable in terms of its peak voltage and impedance transformer implementation as well.

The design equations of a VMCD are given in Ref [60] and are summarized in Table 4-3, which gives the output power, drain current, and drain voltage of an idealized operation of the class D PA. The utilized GaN HEMT's breakdown voltage (84 V) is relatively high, allowing a trade-off of power for efficiency via the optimum choice of its resistive load (R_L). Therefore, a VMCD topology has been selected for this study. Here, an initial value of R_L (equivalent load resistance), has been determined as in the ideal VMCD topology. However, we still need to find the optimal impedance load of the real device to achieve both a high efficiency and output power. Additionally, for a more reliable and stable operation, the drain voltage (V_{dd}) has been set at 28 V so that the peak drain voltage (56 V for VMCD) is more than 20% below its breakdown voltage (84 V). Additionally, the 1:2 impedance transformer is much easier to implement than a (2/3) impedance transformer, as will be explained in Chapter 5. At the same time, since the device is biased close to the pinch-off, the stability analysis, using small signal S-parameters, is not valid. A large signal analysis is needed to check stability and perform the load pull analysis.

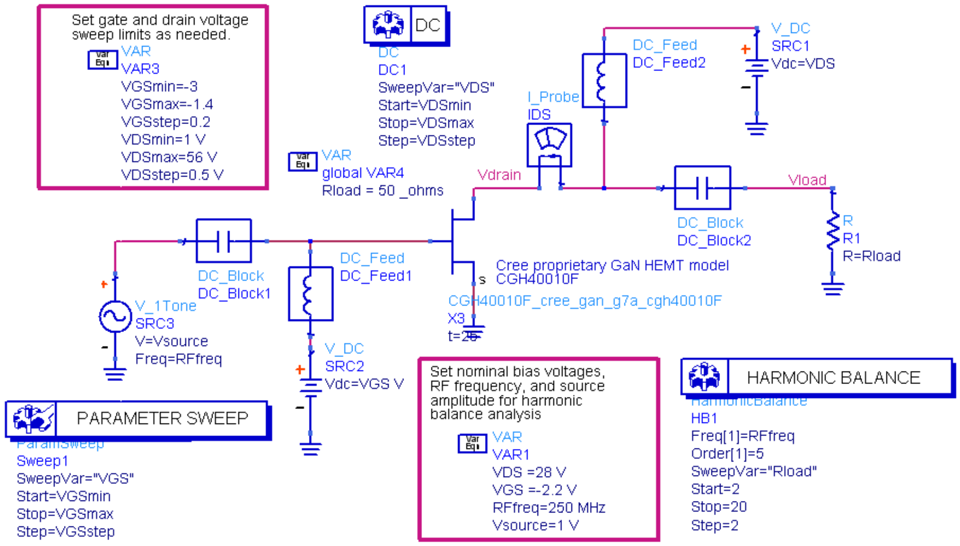

Figure 4.5 DC sweep schematic

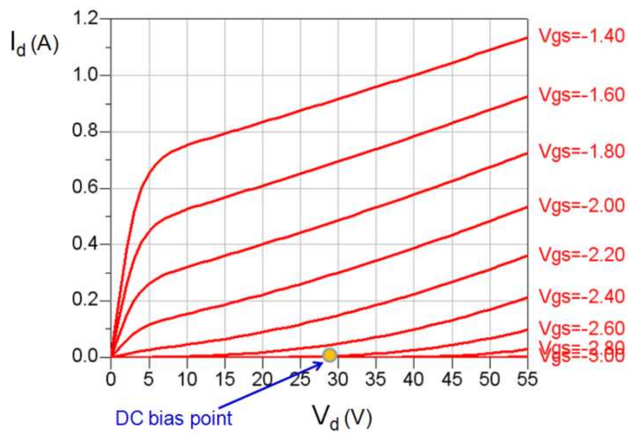

Figure 4.6 DC IV characteristics

Table 4-3 Current and voltage requirements for an ideal class D power amplifier operation

	VMCD	CMCD
Output Power (>20W for two device together)	$P_O = \frac{8}{\pi^2}\frac{V_{dd}^2}{R} = 25.4$	$P_O = \frac{\pi^2}{8}\frac{V_{dd}^2}{R} = 29.3$
m/n	$(1/2)^{0.5}$	$(2/3)^{0.5}$
(R_L=50Ohm); $R=(m/n)^2 R_L$	50/2=25	50x2/3=33
V_{dd}(V)=28 V	28	28
I_{dd}(A)	$I_{dd} = \frac{8}{\pi^2}\frac{V_{dd}}{R} = 0.91$	$I_{dd} = \frac{\pi^2}{8}\frac{V_{dd}}{R} = 1.05$
I_{om} (A) peak current	$I_{om} = \frac{4}{\pi}\frac{V_{dd}}{R} = 1.42$	$I_{om} = I_{dd} = 1.05$
V_{om} (V) peak voltage	$V_{om} = 2V_{dd} = 56$	$V_{om} = \pi V_{dd} = 88$

Based on our selection of the VMCD rather than the CMCD, the output power would be slightly less than that of the CMCD. The peak voltage $2V_{dd}$ utilized would be significantly lower than the breakdown voltage 84 V, as compared to the required peak voltage for a CMCD operation which would exceed the device ratings.

4.6 Large Signal Analysis

Although a CMCD amplifier must have a rectangular-wave drive, the VMCD version can be driven by either a rectangular-wave or a sine-wave signal [51]. Obviously, a sine-wave drive is usually preferred since it takes less power and is much easier to generate. Meanwhile, the driver for the VMCD with HEMTs must produce a relatively large enough gate sinusoidal voltage to ensure a DC saturation and cutoff. Figure 4.7 shows the simulation figure, which sweeps the input power. Figure 4.8 shows the drain voltage of a GaN HEMT (as half of the VMCD) as a function of the input power. As shown here, the GaN HEMT should be driven into saturation (P_{in}=25 dBm) to operate as a switch and generate the desired symmetrical rectangular-wave voltage at the drain. However, an over-drive power (P_{in}=30 dBm) also causes an overshoot and an asymmetrical output voltage waveform.

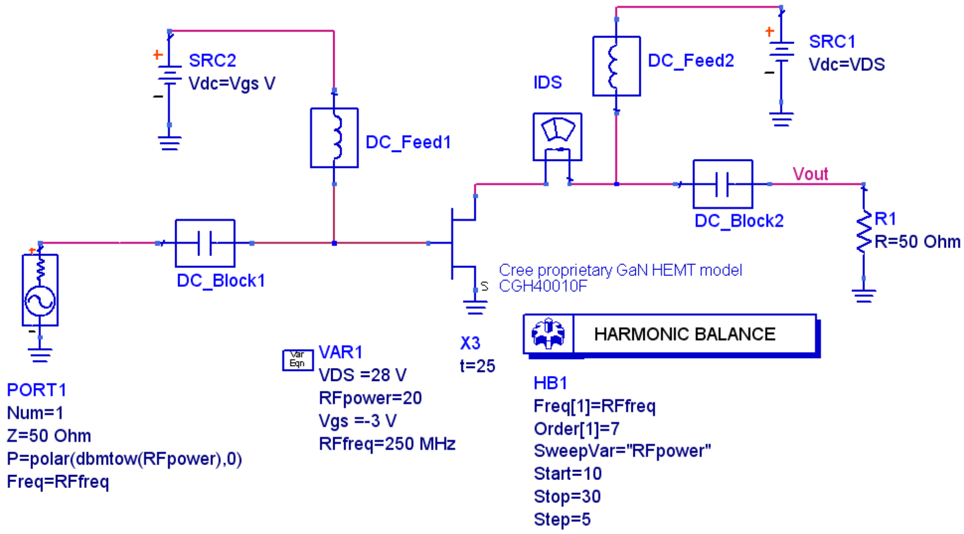

Figure 4.7 Input Power sweep schematic

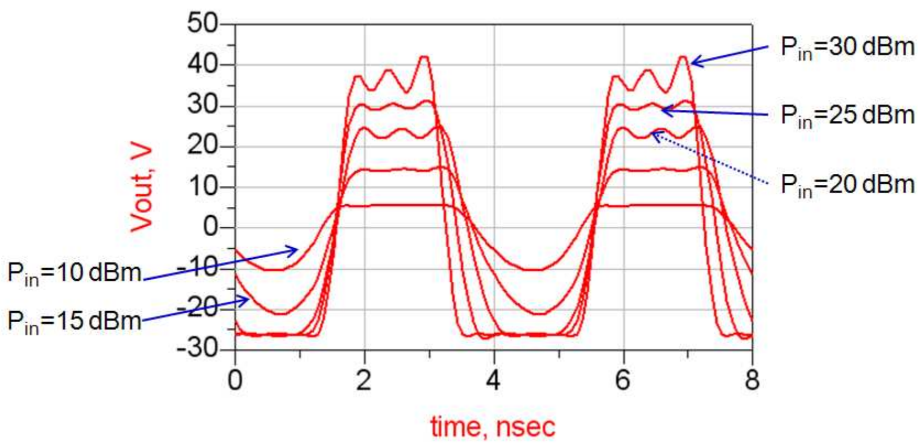

Figure 4.8 Transient drain voltage vs. input power

However, a serious problem in the design of a wideband power amplifier could cause instabilities. These instabilities can give rise to either frequency divisions, spurious oscillations, or both. The prediction of these instabilities requires a large-signal stability analysis instead of using the conventional small signal S parameter analysis given that the VMCD device is biased close to its pinch-off condition to achieve a high efficiency. Figure 4.9 shows a large signal S-parameter simulation schematic diagram. The large signal stability factor, K, and the stability measure, B1[62], are shown in Figure 4.10a. Having both K > 1 and B1>0 is sufficient for circuit stability. Based on this analysis, it was discovered that the VMCD PA is stable when adding a 10 Ω series resistor at the gate. However, with only a 2 Ω resistor parallel with a 20 pF capacitor series with the gate-pin, the VMCD achieves stability during the measurement.

Figure 4.10b shows the input impedance of the device. As a trade-off, we decided to use a wideband ferrite loaded coaxial 1:2.25 impedance transformer to match the input over a wideband. The details of the ferrite loaded coaxial 1:2.25 impedance transformer will be described in Chapter 5.

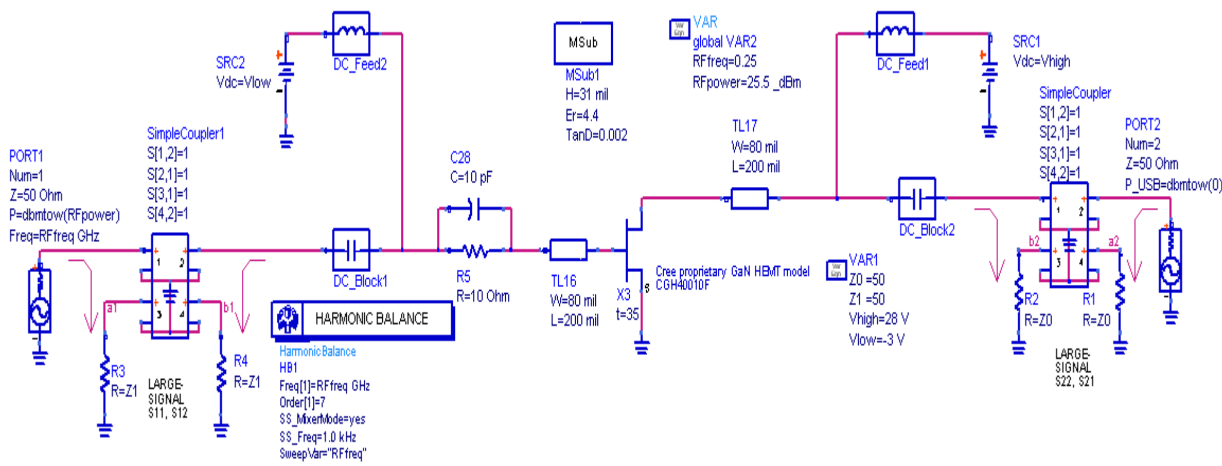

Figure 4.9 ADS simulation setup for large signal S parameters

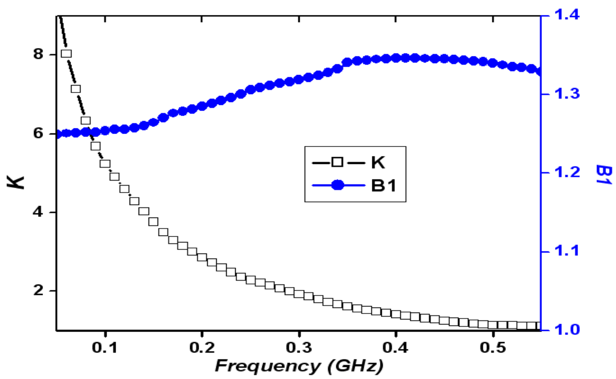

(a)

RFfreq (GHz)	Zin1
0.050	124.616 - j65.665
0.100	80.095 - j75.436
0.150	52.749 - j69.359
0.200	36.876 - j60.302
0.250	27.753 - j51.915
0.300	21.941 - j44.809
0.350	17.997 - j38.731
0.400	15.379 - j33.400
0.450	13.779 - j28.582
0.500	13.032 - j24.276
0.550	12.726 - j20.632

(b)

Figure 4.10 Large signal stability performance: (a) Stability factors and measure; (b) Input impedance

The input and output matching networks were optimized using ADS to sustain a high drain efficiency for a wideband operation. Generally, for a narrow band application, the desired output power can be obtained with different combinations of DC supply voltage and load resistance. However, for a wideband application, the output power and drain efficiency need to be compromised with the achievable operating bandwidth. Therefore, a load-pull simulation (shown in Figure 4.11) for a single device with a close to pinch-off bias has been carried out over a wide frequency range. Its simulation results at 200 MHz/400 MHz are shown in Figure 4.12. Based on the load pull simulation analysis shown in Figure 4.12, the load impedance required to achieve over a 42 dBm and 70% drain efficiency from a single device has a real part close to 25 Ω. So, in this wideband design, a 1:1 balun is used to combine the two drain signals into one output signal and, at the same time, transforming the 25 Ω to a 50 Ω at the output circuit. The efficiency will be higher than even 74% if the imaginary part is accounted for as well.

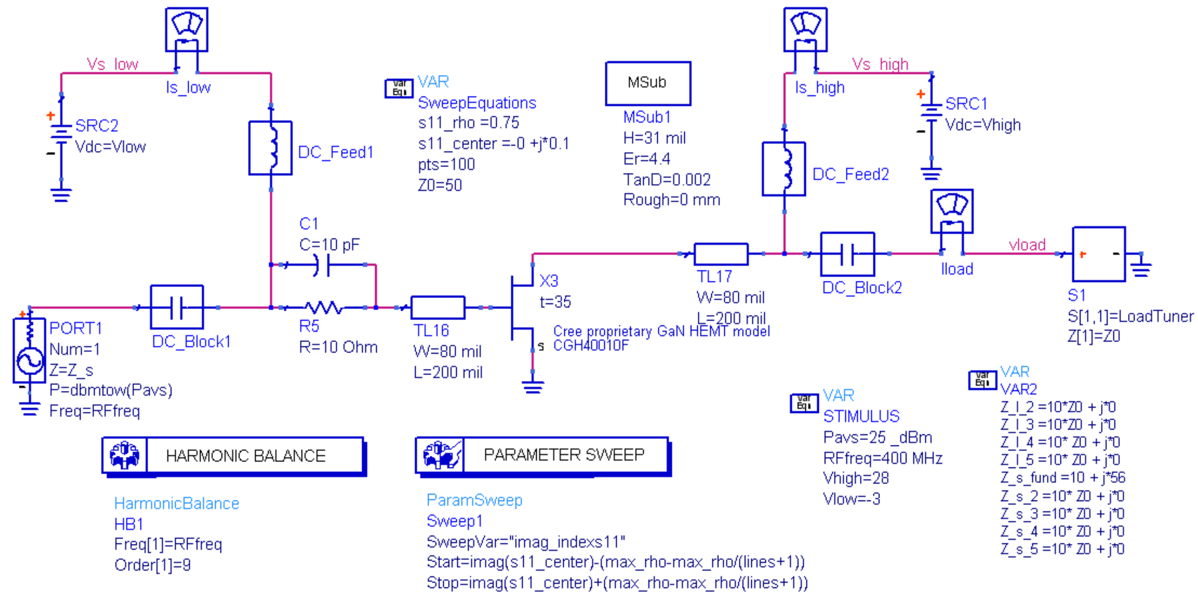

Figure 4.11 Load-pull simulation schematic

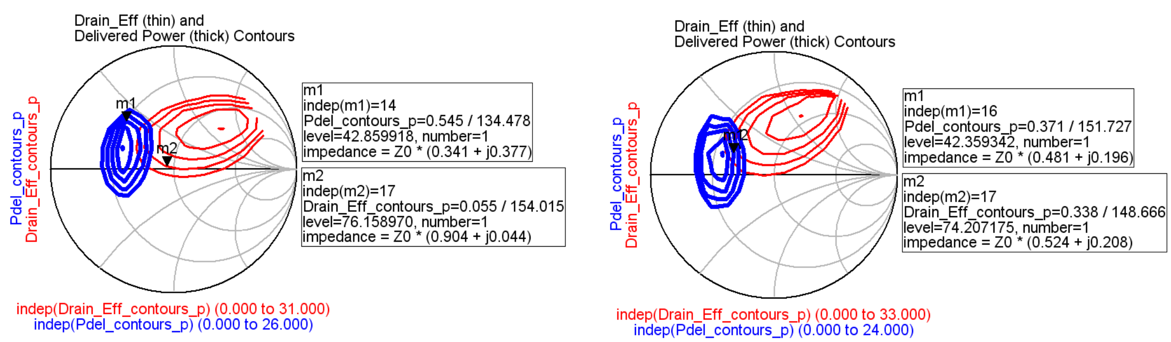

(a) (b)

Figure 4.12 Drain efficiency and delivered power contours: (a) 200MHz; (b) 400MHz

4.7 Filter Design

For a narrow band, class D PA, serial or shunt output tank circuits are used to filter a sine wave output signal and reject all higher harmonics. Using a push-pull topology, the second harmonic signals are cancelled in the output balun. However, for a wideband class D PA in practice, the preferable output circuit is a set of switchable low pass filters instead of a series or a shunt harmonic termination to cover the 50-550 MHz operation. These output filters can be made by active or passive components. Although using an active filter can increase the output power, it also consumes more DC power and decreases the overall efficiency. So in our application, we have selected a passive filter. Here, we have designed four low pass filters (60MHz/ 100MHz/ 200MHz/ 300MHz) to cover the 50-300 MHz range. However, for the frequency 300MHz to 550 MHz, we can use the output transformer's cutoff performance to reject the third harmonics at 900MHz to 1650MHz.

In this VHF/UHF band operation, lumped elements (L & C) can still be used to design low pass filters. The elements' Q is important in achieving a low insertion loss of the filter. We can use either the classic equations to get an initial filter design, or alternatively, the AWR Microwave Office[25] can be used to synthesize a five-order Chebyshev low pass filter to adequately reject out-of-band signals. Using more elements will increase the loss of the filter. Figure 4.13 shows the schematic of a low pass filter. Table 4-4 gives the values of L and C for those filters. The simulation and measured results are shown in Figure 4.14. Figure 4.15 shows four low pass filters. Each filter is a ladder network comprised of high Q ATC capacitors and air-core Coilcraft inductors mounted on a FR4 substrate, as indicated by C and L, respectively. The measured results of the low pass filters are shown in Figure 4.16. The filters have an insertion loss of approximately 0.25 dB over the required frequency range.

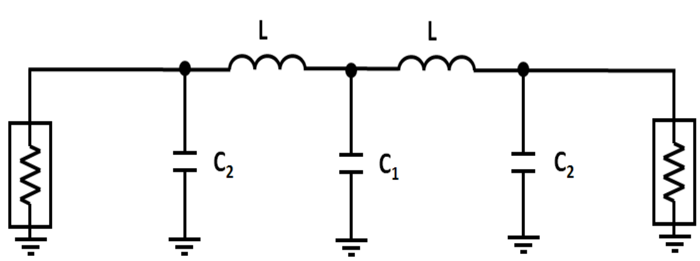

Figure 4.13 Low pass filter schematic

Table 4-4 Parameters of low pass filters

Band edge frequency	60 MHz	100 MHz	200 MHz	300 MHz
C1 (ATC 100A)	110 pF (Q=302)	56 pF (Q=469)	30 pF (Q=192)	20 pF (Q=249)
C2 (ATC 100A)	68 pF (Q=413)	33 pF (Q=181)	18 pF (Q=267)	13 pF (Q=329)
L (Coilcraft)	169 nH (Q=114)	82 nH (Q=120)	47 nH (Q=135)	33 nH (Q=130)

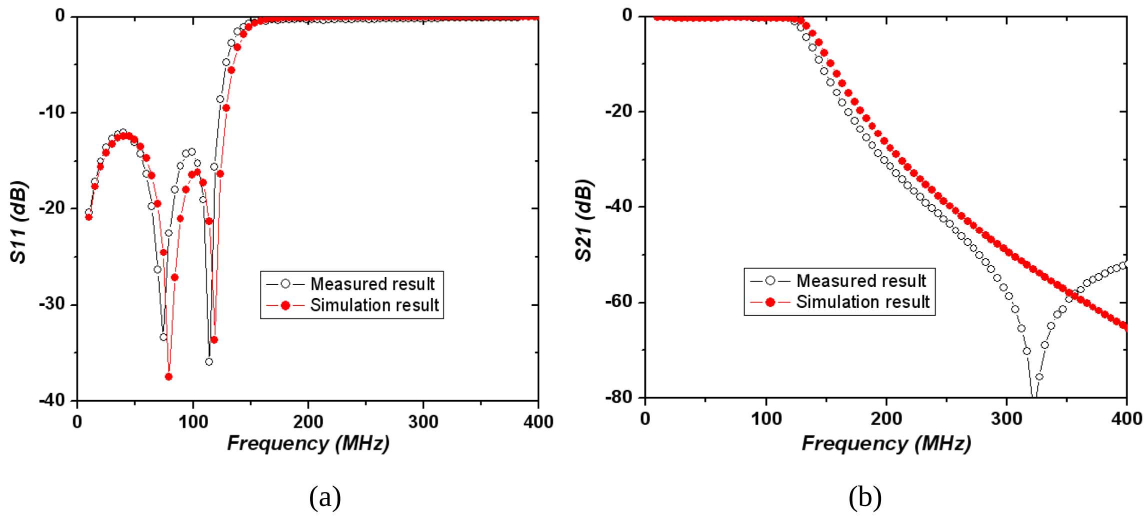

Figure 4.14 Simulated and measured results of 100MHz low pass filter: (a) S_{11}; (b) S_{21}

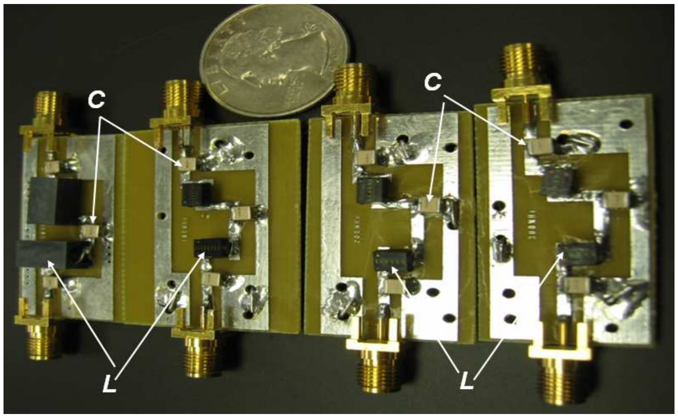

Figure 4.15 Fabricated filters (60MHz/100MHz/200MHz/300MHz)

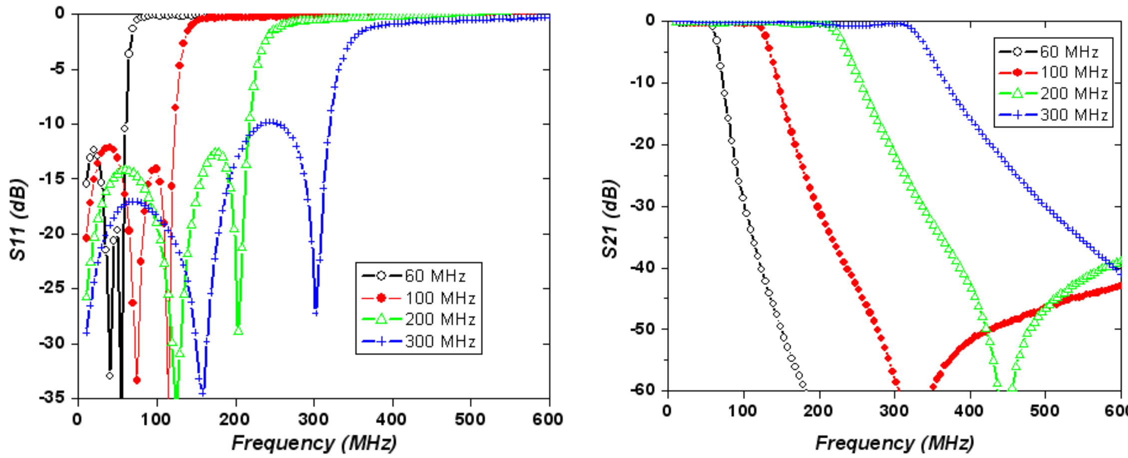

(a) (b)

Figure 4.16 Measured results of filters: (a) S_{11}; (b) S_{21}

4.8 Circuit Simulation and Implementation

A simulation schematic of the designed wideband VMCD PA is shown in Figure 4.17. On the input side, the input signal is divided into two out-of-phase signals by a 2-way 180 degrees wideband power divider using a Mini-Circuits 180 degree splitter (SYCSJ-2-42-2+). Subsequently, a wideband 1:2.25 impedance transformer is used in the input section of each amplifier to transform a 50 Ω to a 25 Ω in order to improve the amplifier's drain efficiency over a wide frequency range. Additionally, a shunt capacitor (C_b=1.5 pF) is connected between the two input branches and is used as a bridge to improve the balance between these two branches. As shown in Figure 4.2b, the output transformer not only combines the two out-phase signals, but also works as an RF choke to block the RF signal leakage to the DC source. However, it is difficult to build a conventional transformer to cover the 50 to 550 MHz frequency range. It is far easier to build a transmission line balun for this frequency range.

In this design, we decided to separate the signal combining and the DC feeding functions of the output transformer using two different blocks: two additional twisted-isolated wires for DC feeding and a ferrite loaded transmission line 1:1 balun as a signal combiner. A bead ferrite core has been added to the twisted-isolated wires to improve the overall low frequency drain efficiency. The ferrite core loaded 1:1 balun, is used to combine the two drain signals into one output signal and transforms the 25 Ω to a 50 Ω at the same time, as shown in Figure 4.17.

The VMCD was built on a FR4 substrate with a dielectric constant of 4.4 and a thickness of 1.57 mm. It is shown in Figure 4.18. In practice, a switchable low pass filter bank should be used instead of the series harmonic termination to cover the 50 to 550 MHz operation. However, for demonstration, we used several low pass filters to manually cover the wideband operation.

4.9 Simulation and Measured Results

It is imperative to include the higher order harmonics when simulating the saturated amplifier nonlinear performance using the Harmonic Balance simulator. In the nonlinear analysis, it is preferable to use the fine tuning tool rather than using an automatic optimization to avoid convergence problems. Figure 4.19a show the drain voltage and current at 200 MHz, where the drain voltage is a slightly distorted rectangular wave with a 56 V peak value and the current is a slightly distorted half sine wave. This distortion is due to the parasitic nature of the device. Although, for a narrow band VMCD, the distortion can be minimized by fine tuning the matching network, but for a wideband VMCD we have to trade off this distortion for wideband output power and efficiency operation. Our simulated output power and drain efficiency are higher than 44.2 dBm and 64%, respectively with input power equals 28 dBm. The over 50 to 550 MHz bandwidth is shown in Figure 4.19b.

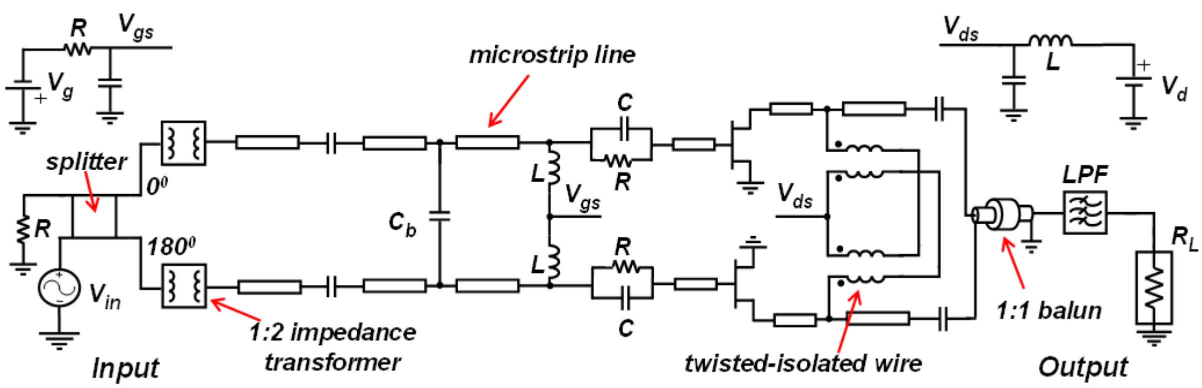

Figure 4.17 Full circuit simulation schematic

(Note: The ADS schematic is shown in Appendix C, Figure C8.)

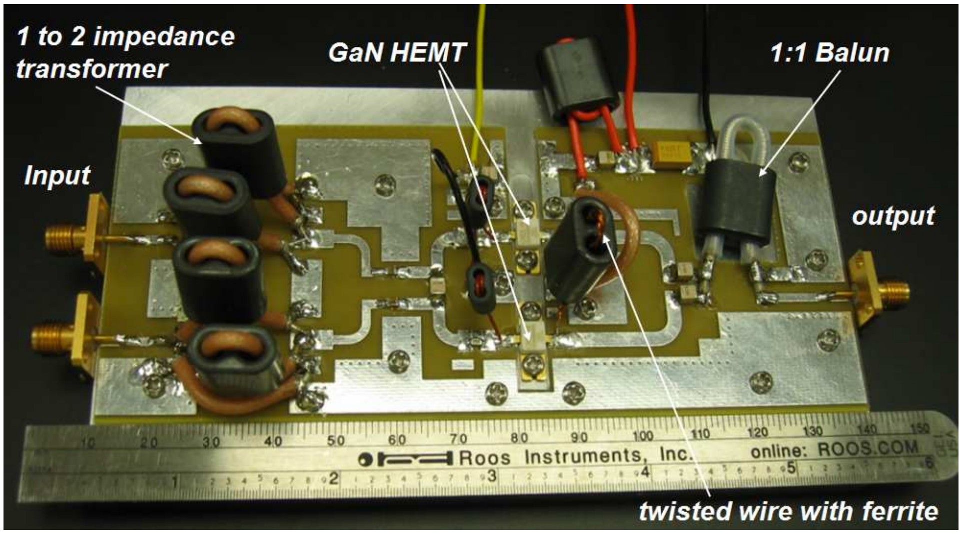

Figure 4.18 Fabricated VMCD PA

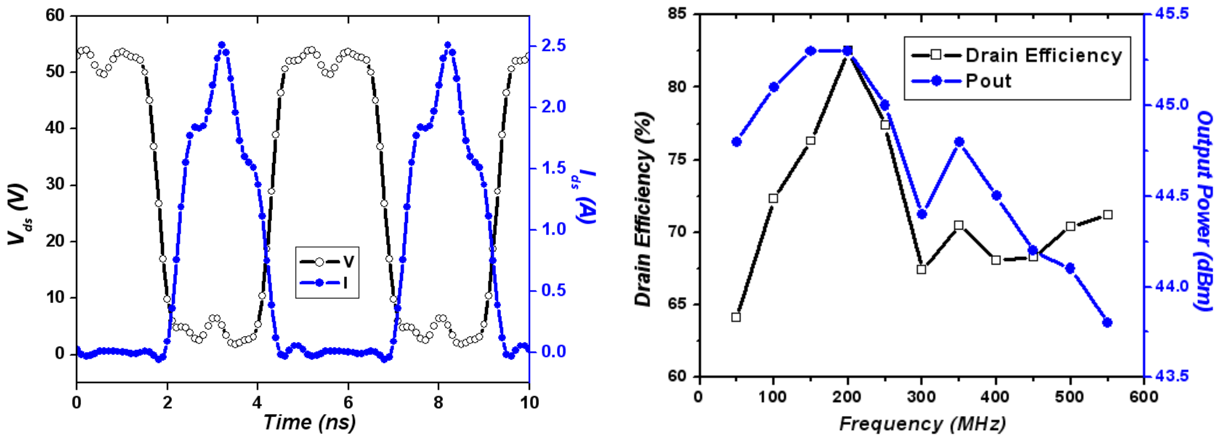

(a)

(b)

Figure 4.19 Simulation results: (a) Drain voltage and current @ 200 MHz; (b) Output power and drain efficiency

Experimentally, it is essential to sustain the high efficiency for the various input power levels, but the drain efficiency drops significantly for lower input power levels. However, by decreasing the drain voltage as well, the drain efficiency can be sustained with a relatively lower input power. This is a key feature for a LINC application which handles signals with significant levels of variations. Typically, our highest measured drain efficiency was achieved when the class D PA was biased close to its pinch-off – this is consistent with our simulation predictions. Our drive level has been adjusted to provide the best scenario between the input/output power, efficiency, and peak voltage. Figure 4.20a shows the measured drain efficiency and output power of the fabricated VMCD PA as a function of frequency with an input power of 28.5 dBm and a 28 V drain voltage. Reported results will be slightly degraded if we account for the filter loss of 0.25 dB as well.

The measured output voltage linearly increases as a function of drain voltage for a fixed input power of 28.5 dBm, as shown in Figure 4.20b. In addition, the measured gain of this PA is higher than 14.5 dB with an input power of 28.5 dBm over the operating frequency range. These measured results indicate that the class D PA has the highest drain efficiency and output power around 250 MHz. Further improvements of the measured results, shown in Figure 4.20a, and compared to Figure 4.19b, can be achieved by fine tuning the assembled circuits.

Even though, the amplifier has not been evaluated for linearity, it is expected that the GaN devices, as usual, have a soft power compression characteristic which could reduce linearity. At the same time, the SMPA operation requires significant gain compression to generate higher harmonics. Subsequently, its carrier-to-inter-modulation distortion ratio (C/IMD) will be rapidly degraded. Therefore, applications of class D amplifiers that require high linearity should utilize EER or LINC subsystems for external linearization.

4.10 Conclusion

A VHF/UHF high power wideband VMCD PA using GaN HEMTs was simulated, fabricated, and tested. The measured drain efficiency was in the range of 63% to 72% over a wide frequency (50 to 550 MHz) with an output power from 43 to 45 dBm. Generally, the GaN HEMT’s very small value R_{on} helps to lower the power loss. The GaN HEMT’s small parasitic drain to source capacitance (C_{ds}), results in higher drain efficiency and a larger bandwidth when compared to other device technologies, such as Si LDMOS. It is possible to obtain a greatly increased performance in both drain efficiency and output power for narrow band applications. However, to achieve a wideband operation, the drain efficiency and output power need to be compromised. Finally, from an insertion loss perspective, using a wideband reconfigurable filter rather than a filter bank may be a better solution for overall high efficiency.

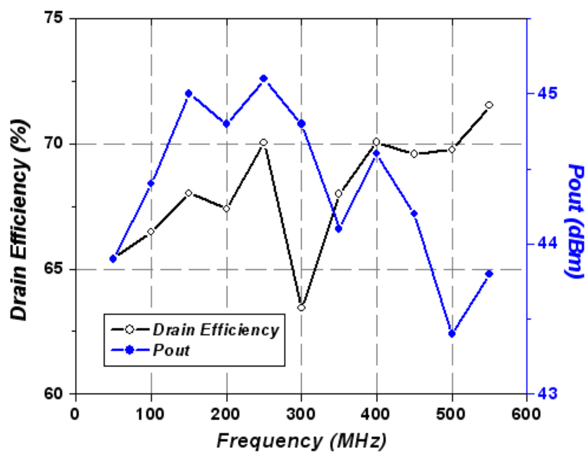

(a)

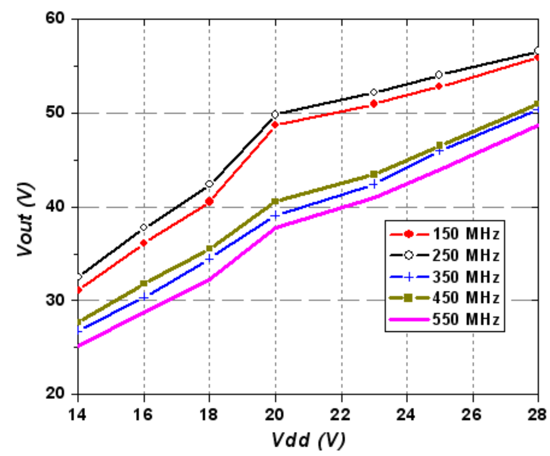

(b)

Figure 4.20 Measure results: (a) Output power and drain efficiency; (b) Variation of the measured output voltage as a function of drain voltage.

Chapter 5 Power Combiners Development

5.1 Introduction

In Chapter 3, LINC architecture was proposed to achieve high linearity and high efficiency amplification with two out-phase constant envelope signals used to drive two nonlinear switching-mode amplifiers. Their optimally designed nonlinear output signals are properly combined to sustain high linearity and efficiency performance simultaneously. Generally, these combiners are either non-isolated (i.e. without isolation between input ports --- Chiréix combiner or Modified Chiréix combiner) or isolated (i.e. with adequate isolation between its input ports--- Wilkinson or Hybrid). Their design equations, simulation methods, and measured results will be discussed in detail in this chapter.

For non-isolated combiners, even-mode excitation of the input ports are transmitted directly to the output ports without reflection. Meanwhile, the odd-mode excitation is reflected back to the input ports. For the isolated combiners, the reflection of the odd-mode excitation is suppressed and dumped into its isolation resistors. In practical circuits, the non-isolated power combiner designed for high efficiency operation will produce significant interaction between the two combined amplifiers, thus leading to an unacceptable distortion. Alternatively, to preserve the high linearity, it is better to employ power combiners with adequate isolation between the two input ports. However, this may degrade overall efficiency and a compromise is generally required [49].

At VHF/UHF frequency ranges, combiners can be fabricated using a combination of wire-wound transformers, lumped elements, microstrip lines, or quarter-wave transformers. Table 5-1 compares the various ways of implementing power combiners at VHF/UHF frequency ranges. As a good candidate to achieve high power and wideband applications, varieties of ferrite loaded coaxial line segments are used for fabricating transmission line transformers to circumvent size, bandwidth, and power handling constraints. Examples of such coaxial line based transmission line transformer designs will be demonstrated in the following sections.

Simulation of the combiners with transmission line transformers is generally carried out using equivalent circuit or EM modeling. Equivalent circuit simulation is used for classic structures, which helps RF engineers to design a multitude of circuits in a simple and fast way, as well as achieving acceptable results. On the other hand, 3-D EM simulations should be used to simulate more complicated non-planar structures, but are time consuming. The use of mixed EM and circuit analysis could be adequate, though.

Table 5-1 Comparison of power combiner implementations for VHF/UHF frequency range

Implementation	Features	Problems
Wire-wound transformer	- Classical design method available - Medium size	- Unacceptable insertion loss at its self-resonant frequency
Microstrip line	- Easy to implement; - Simple to extend to multi-section; - Tapered lines with printed thin film resistors are feasible for low power combiners.	- Narrow band - Multi-section has higher insertion loss and requires non-standard isolation resistors - Bulky at low frequency
Lumped element	- Low cost - Compact size - Easy to simulate	- Low power - Need multi-section to achieve wide band
Ferrite loaded coaxial line	- High power; - Wideband potential;	- Simulation is critical - Better to use EM simulation to account for its sensitivity to the mounting package and ferrite loading

In this chapter, isolated and non-isolated power combiners will be thoroughly discussed, and some design examples will be given. Both equivalent circuit and 3-D EM models will be applied to simulate the combiner structures. Baluns are very typical elements in the design of VHF/UHF combiners. Hence, in the following, we will introduce a balun design and demonstrate its use in designing impedance transformers. It will be followed by the demonstration of a non-isolated combiner design. Subsequently, an even/odd model will be extracted for an isolated combiner, and the introduction of a novel design based on a flux canceling scheme with a 3-D EM simulation will be presented. Also, a power recycling combiner will be presented with its measured results.

5.2 Balanced-Unbalanced Transformer Modeling

Broadband balun transformers are useful in developing various circuits, such as push-pull amplifiers. The baluns are basically used to convert balanced lines to unbalanced lines and to provide impedance transformation as well. The challenge in designing baluns is in achieving wide band coverage while maintaining a low insertion loss within a compact size. In the VHF/UHF frequency band, combiners can be either fully comprised of coaxial-lines or semi-rigid ferrite loaded coaxial lines. The latter are generally used to extend the combiner's operation to low frequencies. However, their performance is highly dependent on the utilized ferrite core material which should be optimally selected.

5.2.1 Balun design consideration

Conventionally, there are two types of ferrite core materials available in the market, manganese-zinc and nickel-zinc. Additionally, there are three commonly utilized shapes for the ferrite cores, the bead, the multi-hole, and the toroid shapes. The performance of the broadband balun transformer is generally a trade-off between the ferrite's permeability, its loss, and the wires' ohmic losses. In fact, the ferrite permeability affects the operating frequency range, as its operation at relatively high frequencies generally requires the utilization of low μ_r materials to avoid the high losses associated with high μ_r materials. Nevertheless, using relatively low μ_r cores can limit their shielding effectiveness at relatively low frequencies.

The shape of the ferrite core also affects the linearity performance. Ferrite cores, when saturated due to any excessive eddy currents, can lead to significant nonlinearities, extra core losses, heat dissipation, and nonlinearity distortion. To minimize these saturation effects, multi-hole cores are preferred so that only the web between the holes would be saturated in case of high currents. This leads to a reduced overall saturation and subsequently, a significant reduction in overall nonlinearity, which is different from using individual beads that would be completely saturated. Additionally, multi-hole cores generally have a lower insertion loss as they require fewer wire connections compared to the toroidal cores with the same inductance [63].

The use of equivalent circuit or EM modeling in the broadband balun transformers can significantly speed up their design cycle. Some circuit models have already been developed. For instance, Sevick [64] proposed an equivalent circuit model for the balance/unbalance transformer (with bead core)—shown in Figure 5.1. In this model the choking inductance, $L_{c,}$ can efficiently suppress the common mode currents (currents flowing in both conductors of the transmission line that are in phase and in the same direction). However, this model is only valid for the transformers with bead cores (for further detail refer to Ref. [64]). In order to extend this model to represent transformers with multi-hole cores, the 3-D EM simulation software (CST Microwave Studio [65]) can be used to simulate the two structures (shown in Figure 5.2) — i.e. one with a bead core and the other with a multi-hole core. The two modeled structures are comprised of 35 Ω coaxial lines with a 60mm-length, while all the cores' lengths are identical at 7.6 mm. Through the EM analysis, it was obviously clear that the multi-hole ferrite core structure is approximately equivalent to the structure with one bead, but its core material has double the others permeability value. For example, a bead ferrite core with a permeability of 250 is approximately equivalent to a multi-hole ferrite core with a permeability of 125 --as can be noticed from the full EM simulation results of the two core shapes shown in Figure 5.3. This observation can significantly simplify the modeling and extend the use of the equivalent circuit models. It will be utilized in our subsequent modeling efforts of the combiners.

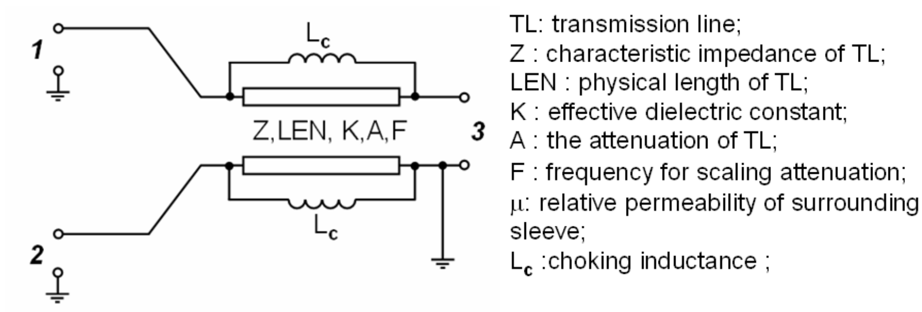

Figure 5.1 Balun Equivalent model [64]

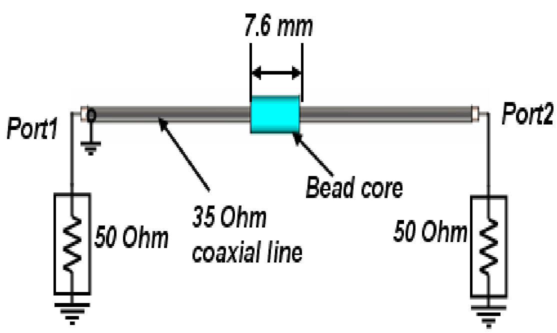

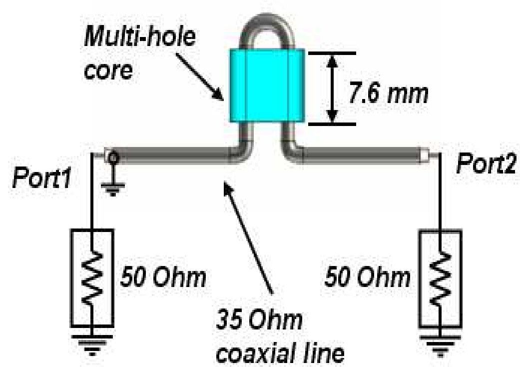

(a) (b)

Figure 5.2 CST model: (a) Bead core structure; (b) Multi-hole core structure

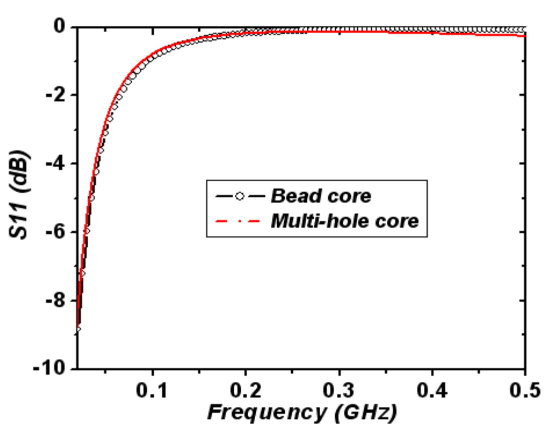

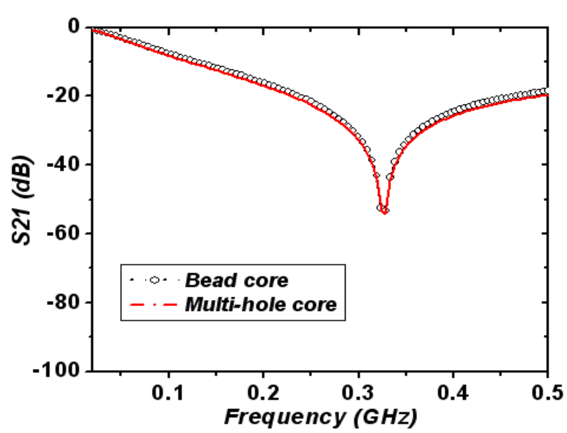

(a) (b)

Figure 5.3 CST simulation results of bead core structure with ε_r=250 and multi-hole core structure with ε_r =125: (a) S_{11}; (b) S_{21}

5.3 Fractional Ratio Equal Delay Impedance Transformer Design

Baluns, as previously mentioned, can be used for converting the unbalanced inputs to balanced outputs, but can also be used for impedance transformation. Therefore, they will be utilized here to provide a 1:2 impedance transformation. Meanwhile, Sevick [64] and Myer [66] have devised a simpler alternative synthesis procedure for a 1:2.25 impedance transformer instead of a 1:2 design. This synthesis method is much simpler and will be adapted here. The 1:2.25 impedance transformer is comprised of three transmission line sections that will sufficiently provide a satisfactory performance in terms of both impedance match and insertion loss. However, the synthesis procedure only reveals the circuit topology and does not provide a means to determine the required line lengths and the ferrite loading. Thus, a precise design recipe is still needed and will be developed in this effort.

Similar to Sevick's transformer design [66], the developed transformer section has three 33.33 Ω coaxial lines, as shown in Figure 5.4. On the low impedance side, coax1 is connected in parallel to a series combination comprised of coax2 and coax3. Meanwhile, on the high impedance side, coax1 is connected in series with a parallel combination of coax2 and coax3. Only coax1 and coax2 are encircled by multi-hole ferrite cores in order to suppress any eddy currents on their outer shields. In our implementation, rather than utilizing customized 33.33 Ω coaxial lines, commercially available 35 Ω lines are used, which did not noticeably affect overall performance. The structure was then simulated using ADS and a multi-hole ferrite core based balun model. Several commercially available ferrite materials were investigated in this simulation, as shown in Figure 5.5. It is clear we can use a multi-hole ferrite core with a μ_r as low as 125 to get an acceptable performance at 20 MHz, thus circumventing the use of high μ_r materials that are generally lossy, as previously discussed in the balun design. 50-mm coaxial lines have been used as a compromise between the physical dimension limitations and the coaxial line insertion loss performance.

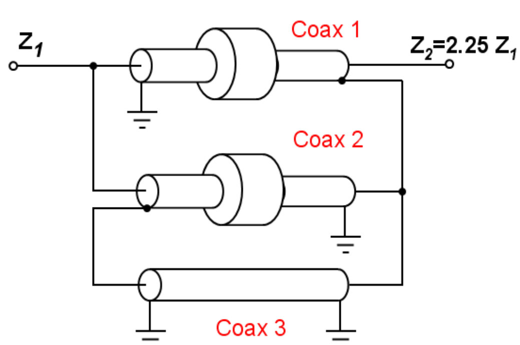

Figure 5.4 Simple model of a 1:2.25 impedance transformer

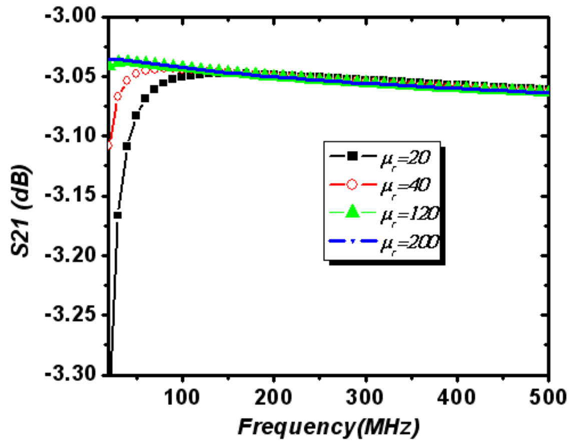

Figure 5.5 S_{21} vs. relative permeability

5.4 Non-isolated Power Combiner Analysis

The designed non-isolated combiner consists of two sections: a splitter (microstrip line T junction) and a fractional ratio equal delay coaxial transformer [64]. The T-junction splitter has an equal power split ratio at low frequencies, but it does not provide a significant isolation. The developed circuit has been fabricated using coaxial line segments and ferrite cores mounted on a standard printed circuit board. The non-isolated combiner was modeled using ADS and fabricated, as shown in Figure 5.6a and b, respectively. Its measured results indicate that it has better than a 25 dB output return loss for the summing port and less than a 0.28 dB insertion loss over a wide frequency range of 30 to 450 MHz. Meanwhile, as expected for any non-isolated combiner, the structure has a poor input match and isolation—as indicated by S_{22} and S_{23} shown in Figure 5.7. This figure compares the simulated and measured results. Clearly, they are in sufficient overall agreement. Meanwhile, the combiner's low insertion loss over the 30 MHz to 450 MHz frequency range indicates that the ferrite core type/shape has not added any significant insertion loss. Here, two multi-hole core with μ_r=125 (12-365-K, from Ferronics, Inc) are used.

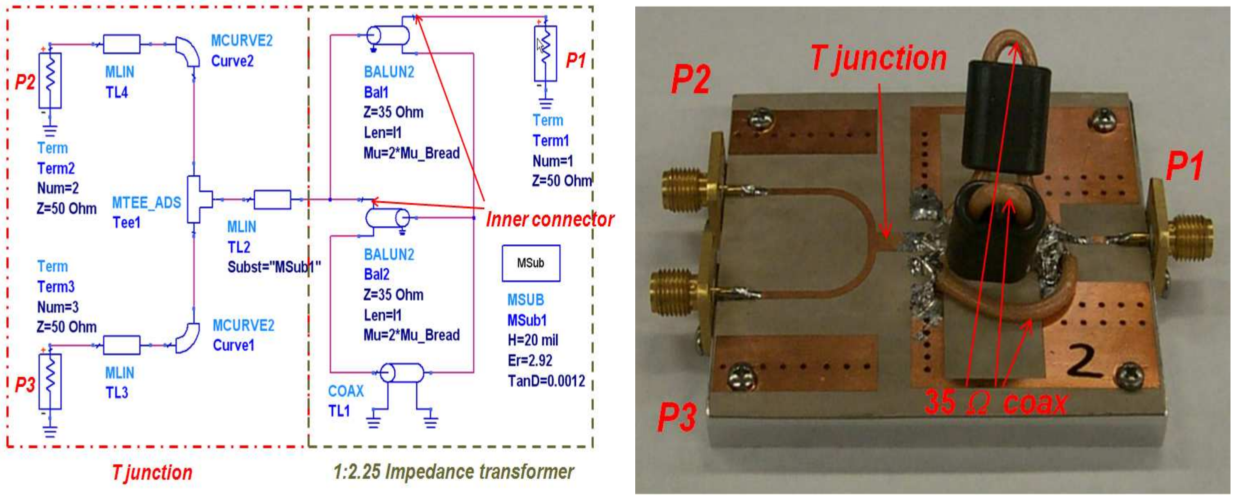

(a) (b)

Figure 5.6 (a) Simulation schematic of non-isolated combiner in ADS; (b) Fabricated non-isolated combiner

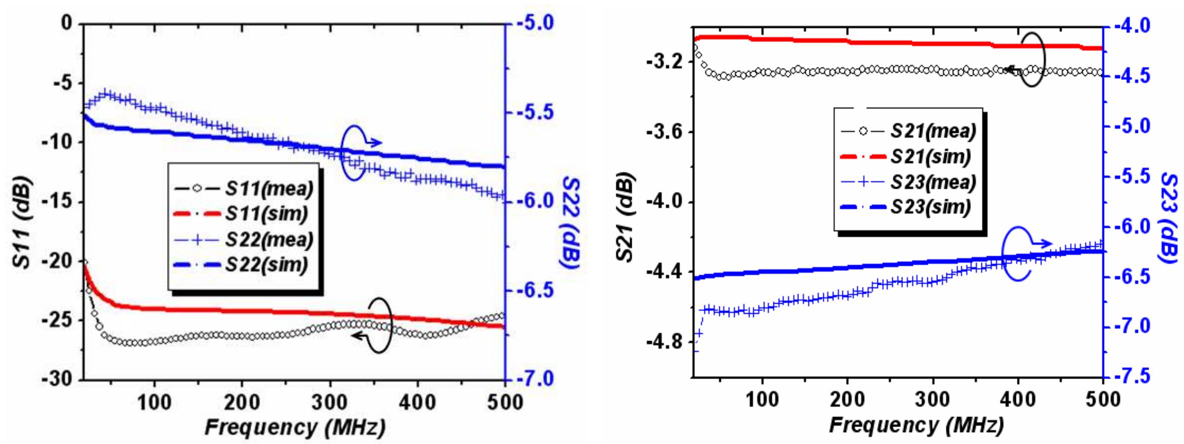

(a) (b)

Figure 5.7 Simulated and measured results: (a) S_{11} and S_{22}; (b) S_{21} and S_{23}

5.5 Isolated Power Combiner Analysis

Power combiner isolation can be sufficiently established by properly adding isolation resistors that bridge the two input ports of a splitter. The splitter can be designed either to provide the splitting only, or both the splitting and the impedance transformation. In either case, the in-phase excitation of the input ports, as stated before, are combined at the output port. However, the out-of-phase excitation of the input ports is dumped directly to the isolation resistors rather than being reflected back to the input ports. Therefore, a high isolation between the two input ports exists while sustaining a good match at both the input and output ports. As a good starting point for our design, we will first investigate Edward's wide band VHF/UHF combiner that can operate over a decade bandwidth [67]. Its analysis will be initially discussed in detail below, and subsequently, we will further present our modified structure with accurate EM modeling to achieve an even better performance.

5.5.1 Analysis of Edwards' 1:2 splitter (combiner) section

Based on the bandwidth requirements of the Wilkinson combiner, a synthesis function (like Chebychev or Butterworth) is used to determine the number of quarter-wave impedance transformer sections. However, it is difficult to achieve more than a decade bandwidth with a compact size. For even wider operating bandwidth, R. L. Edwards patented an isolated power combiner [67] with a very simple structure. It alternatively uses two sections: one for splitting the input port to two ports (splitter), and a fractional ratio equal delay impedance transformer (i.e. 1:1.25) to achieve more than a decade bandwidth.

The splitter is comprised of four ferrite loaded coaxial lines. Each ferrite loaded coaxial line works as a transmission line transformer. The splitter's low frequency operation is limited by the permeability of the ferrite cores, and its high frequency operation is limited by the length of the utilized coaxial line. The rule of thumb for the coaxial line length is to use lines with approximately one half wavelengths at the highest operating frequency. Meanwhile, the design of the fractional ratio equal delay impedance transformer is described in the previous section.

The splitter structure design of [67] was adapted here with the structure fabricated using coaxial lines surrounded by ferrite cores. The coaxial lines are cross-connected in a bridge configuration**,** where the inner conductors are crossed-over and the outer conductors (the shields) remained connected. Meanwhile, the isolation resistors are bridged across the shields at the input side and between the inner conductors at the output side, as shown in Figure 5.8a. Additionally, Ref [67] has recommended the use of four ferrite bead cores to suppress the common mode eddy currents of the coaxial line and has been adapted here, as these currents can cause performance degradation.

To get an idea about the eddy current levels and the adequate μ_r required, ADS was used to simulate the splitter. The ADS AC simulator was used to monitor the values of the currents and voltages at various points under the in/out-of-phase excitation to drive the even/odd mode equivalent circuits. Figure 5.8b shows the schematic of the AC test bench used in ADS. Meanwhile, the equivalent circuit is shown in Figure 5.9. The ferrite permeability is presented by the parameter (Mu-Bead). As expected, the monitored currents and voltages values at different points in the even mode equivalent circuit were completely independent of the permeability of the ferrite since there is no outer surface currents in the coaxial lines. Most of the RF signal is transmitted from the input ports to the output port in this case; hence a zero value was used in the model. On the other side, based on the calculated currents of the various monitored points, a relatively high permeability ferrite core is needed for the odd mode circuit, especially at the low frequency end. Therefore, it was determined that a ferrite core material with a Mu-Bead of approximately 250 should be sufficient to suppress the eddy currents and dump the unbalanced signals into the combiner's isolation resistors.

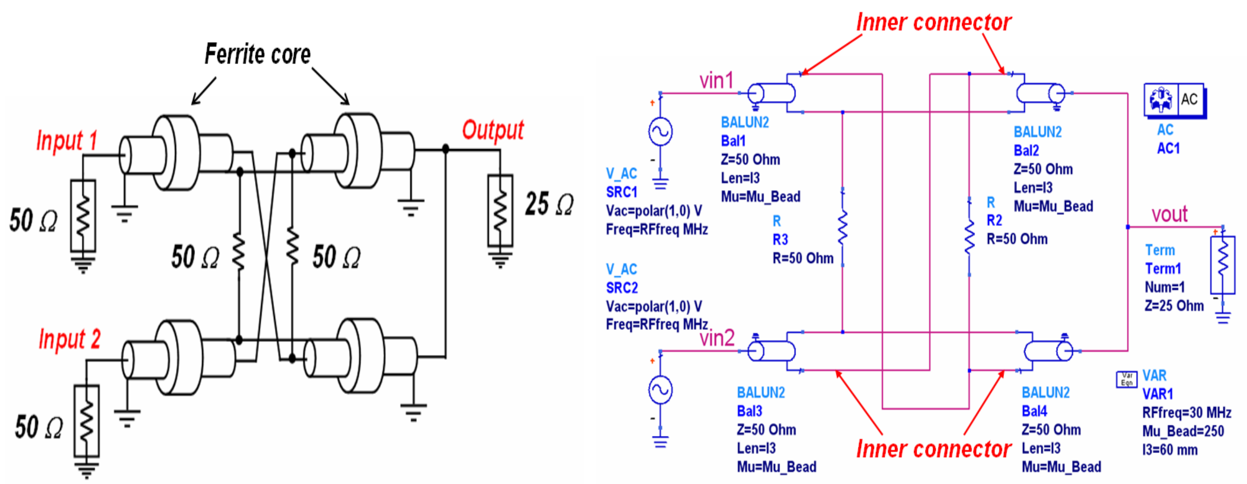

(a) (b)

Figure 5.8 (a) Patented splitter (after[67]); (b) Splitter AC simulation schematic in ADS

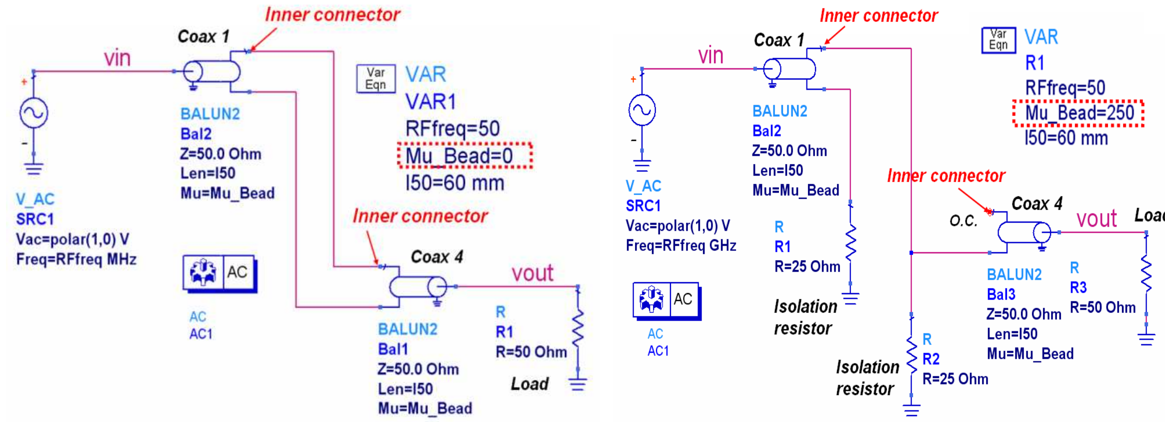

(a) (b)

Figure 5.9 (a) Even mode equivalent model; (b) Odd mode equivalent model

5.5.2 Analysis of the modified structure

The previously described structure was modified to provide a means for flux-reduction/cancellation, thus reducing the required material permeability, μ_r. The modification is shown in shown in Figure 5.10, where the two input and output coaxial lines, coax1 and coax2, and coax3 and coax4, respectively, go through the magnetic cores from their opposite sides. By this arrangement, the flux in the magnetic core is significantly reduced (i.e. canceled) for in-phase combining, allowing a higher power handling without driving the ferrite cores into saturation, i.e. helping to increase the power handling capability. Meanwhile, the out-of-phase signals would see the high inductance due to the odd mode flux doubling. In this case, the lower μ_r (125) would be sufficient to extend the combiner's operation to lower frequencies. Currents would be effectively blocked and forced to pass through the isolation resistors rather than being reflected back to the inputs. Obviously this will render a better isolation and an improved return loss performance.

Since the equivalent circuit can not accurately predict the performance of the coax lines when going through the toroid core, it is necessary to use a full-wave EM simulation; at least for the splitter section to accurately evaluate its performance. It is worth mentioning that our EM model, based on CST, accounts for the radiation losses due to the bridge structure discontinuities, the wires' ohmic losses and space alignment effects. In our analysis, we used the equivalent circuit model previously developed for the other section for faster analysis. The EM simulation results were represented by an S-parameter matrix and have been imported to the ADS simulator to be used in conjunction with the 1:2.25 impedance transformer circuit model, as shown in Figure 5.11a. The simulated results of the combined circuits are shown in Figure 5.12.

This novel design was then fabricated using coaxial lines with only two ferrite cores for the splitter section, as shown in Figure 5.11b. In addition, two 35 Ω coaxial lines with ferrite cores and one 35 Ω coaxial line have been used to assemble the 1:2.25 impedance transformer. Additionally, two 50 Ω ATC power resistors were placed in the back of the test fixture for heat dissipation, and a power capacitor was added between the two branches of the splitter to compensate for the bridge discontinuity and to minimize the amplitude and phase imbalances. However, this capacitor caused a slight increase in insertion loss at high frequencies. The compensated combiner was then tested. Its measured insertion and return losses agreed well with the simulation and were better than half a dB and 18 dB respectively over a wide frequency range (30 MHz to 450 MHz). The measured combiner isolation exceeded 28 dB, and the phase imbalance is less than 4 degrees, as shown in Figure 5.12. These results were compared to a combiner structure built based on the original idea and, as expected, the modified structure demonstrated a better input match and isolation, validating our assumptions.

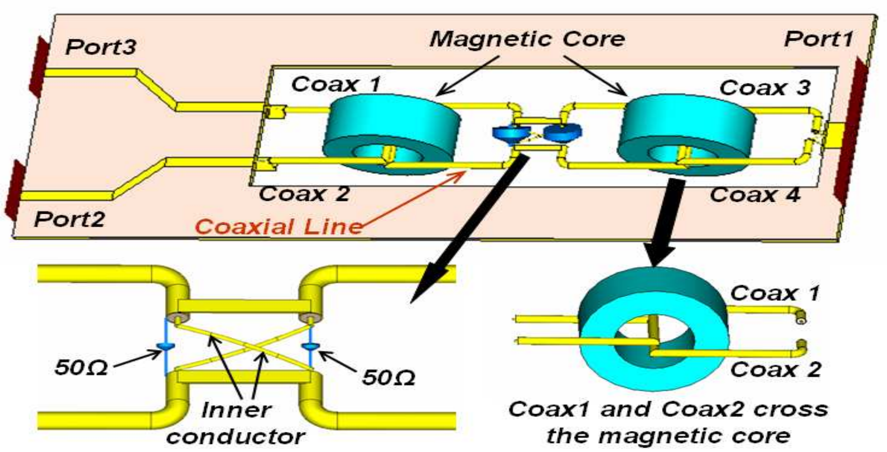

Figure 5.10 CST model of the modified splitter; ATC power resistors were utilized in our implementation and have modeled as ideal 50 Ω resistors given that their small parasitic capacitance (1.0 pF) can be neglected

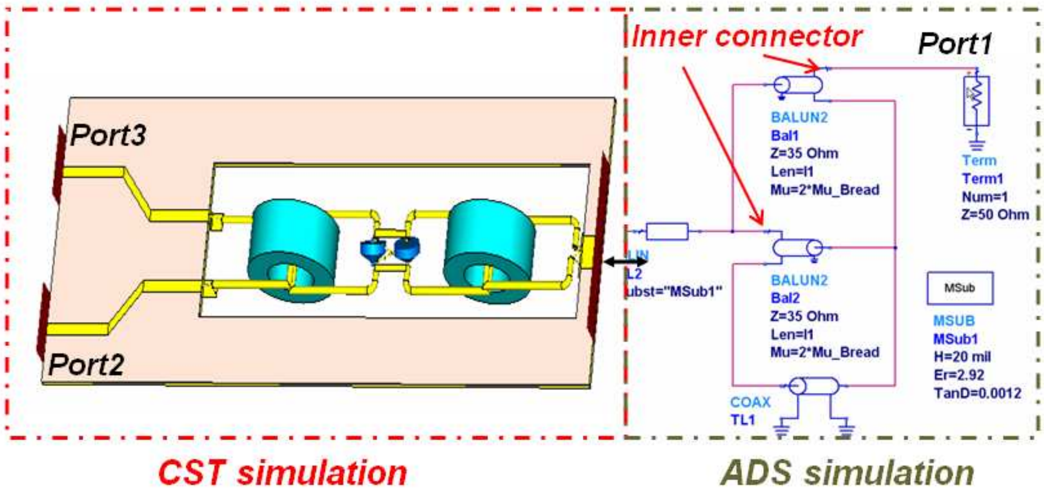

(a)

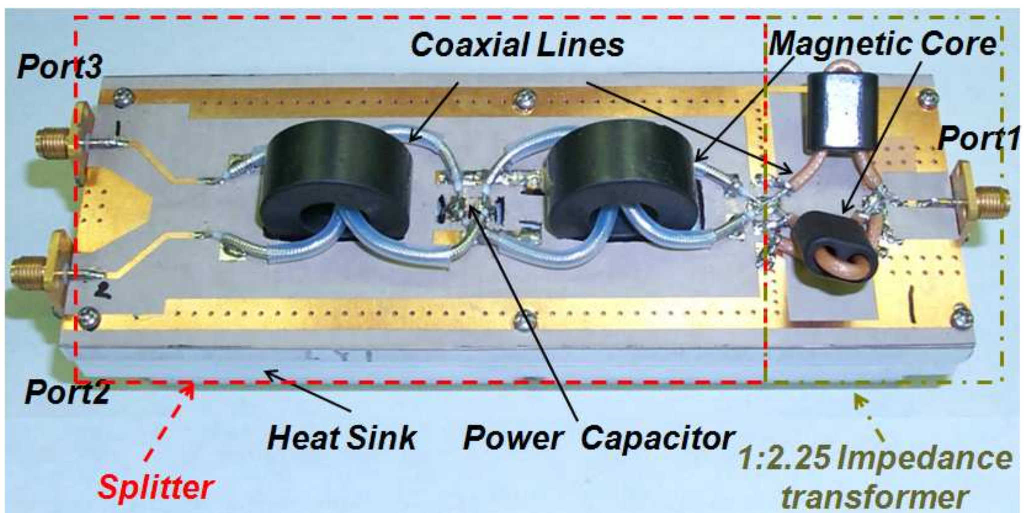

(b)

Figure 5.11 (a) Simulation structure (combined CST & ADS) (b) Fabricated combiner (the splitter with the 1:2.25 impedance transformer)

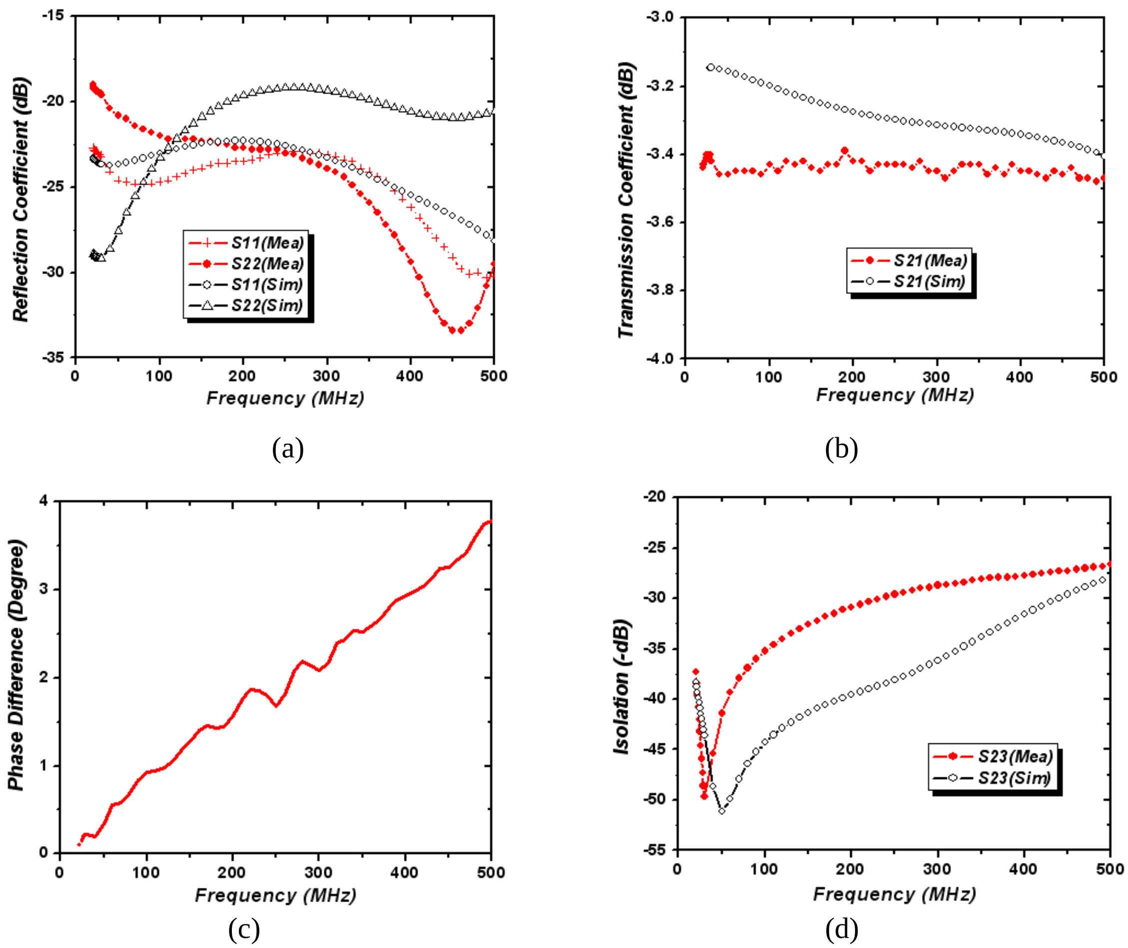

Figure 5.12 (a) Reflection coefficient at various ports; (b) Transmission coefficient of the two branches; (c) Measured phase imbalance between the two input ports (port 2 and port 3); (d) Isolation between the two input ports (port 2 and port 3)

5.5.3 *Power recycling combiner*

The isolated combiners can also be used as part of a high linear, high power amplifier application, where the combining efficiency is of great concern. Consequently, instead of using the two 50 Ω floating resisters to dissipate the unbalanced signals, they can be replaced by two 1:1 Guanella baluns to recycle this presumed dissipated (unused) power. Subsequently, the overall system efficiency would improve as the unbalanced power can be easily converted to DC power and fed back to the power supply [68]. Figure 5.13 shows the fabricated combiner which has five ports. Port 1 is the input, and ports 2 & 3 are the outputs, while ports 4 and 5 are used for power recycling. The developed combiner was tested. Its measured insertion and return losses were less than 0.6 dB and 16 dB, respectively, over a wide frequency range (30 MHz to 450 MHz). Meanwhile, the combiner's isolation has exceeded 23 dB, and its amplitude and phase imbalances are less than 0.15 dB and ±1 degrees respectively, as shown in Figure 5.14. Further improvements can be obtained when optimizing the 1:1 balun design to improve the performance at the high frequency end.

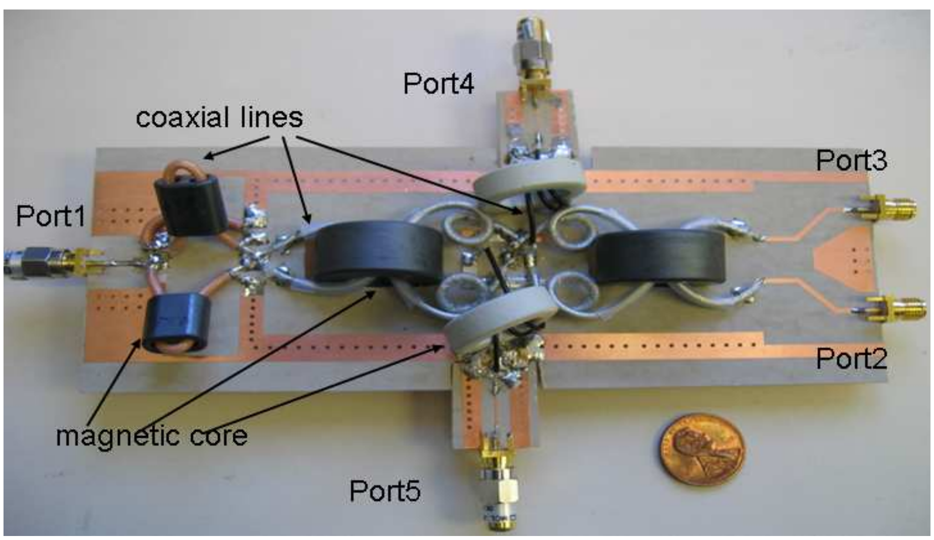

Figure 5.13 The five-port combiner, where ports 2 and 3 are the inputs, port 1 is the output, and ports 4 and 5 are the outputs used for power recycling

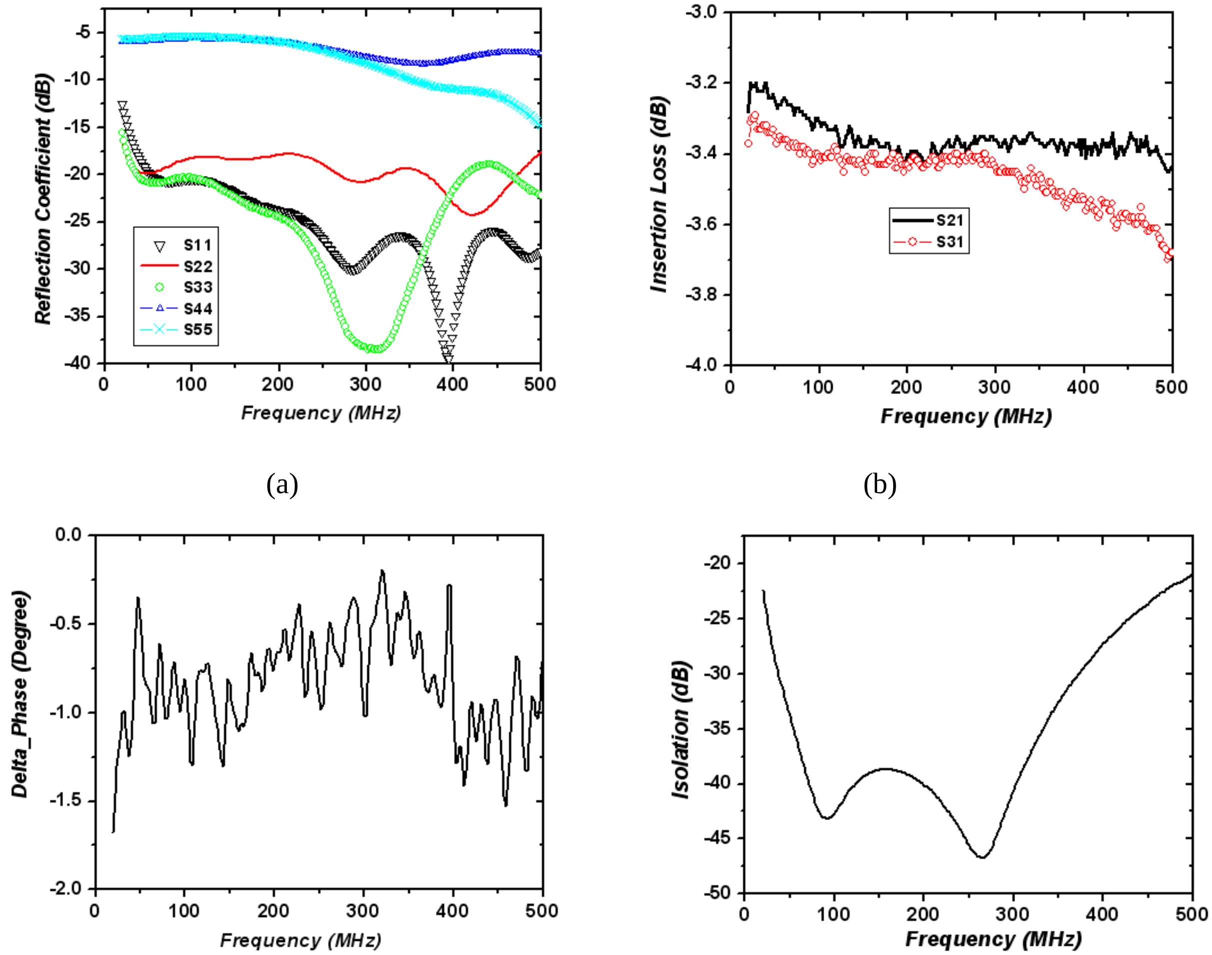

(a) (b)

(c) (d)

Figure 5.14 (a) Reflection coefficient of various ports; (b) Insertion loss of the two branches; (c) Phase imbalance between the two branches; (d) Isolation between the two input ports (port 2 and port 3)

5.6 Conclusion

Modeling various types of VHF/UHF isolated and non-isolated combiners using equivalent circuits and 3-D EM structures has been investigated to accurately predict their performance. Previous models were either too simplistic or only addressed very basic structures. Moreover, the presence of the ferrite cores and the use of non-planar coaxial line segments for fabrication make modeling and design challenging. Development of such models should assist in optimizing the performance of the commonly needed multi-octave power combiners used for various wireless applications.

Ferrite core saturation, however, has been a major hurdle in developing power combiners. Here, a novel structure was recommended in order to improve the overall performance, including the return loss and isolation. The idea is simple and is based on flux cancellation using ferrite cores cross-bridging, which causes flux cancellation for the even mode and flux doubling for the unwanted odd mode. It is believed that better IMD performance can be obtained this way. However, this was not experimentally validated. Both the isolated and non-isolated power combiners have been demonstrated via models developed based on equivalent circuits or full-wave EM analysis.

Chapter 6 Adaptive Bias LINC

While the LINC transmitter eliminates the need for highly linear amplifier components, it introduces a new set of potential challenges. For example, it is still difficult to simultaneously achieve both a high average efficiency and high linearity. Therefore, the properties of the power combiner utilized in the LINC transmitter would strongly influence the selection of its amplifiers [61]. To be specific, as discussed in Chapter 3, the isolated power combiner usually has a higher linearity and a lower average efficiency. On the other hand, the non-isolated combiner usually has a higher average efficiency with a lower linearity. Here, we will present a new scheme to simultaneously achieve both goals. The use of the non-isolated/isolated power combiner with narrow band/wide band SMPAs will be evaluated first, then the different LINC approaches will be compared. Finally, a new adaptive bias LINC transmitter concept will be discussed, analyzed, and simulated to simultaneously achieve a relatively high efficiency and high linearity.

6.1 Background of Non-isolated/Isolated Combiner for Power Combining

The non-isolated/isolated power combiners with PAs for the narrow band LINC transmitter have been theoretically evaluated by [69]. However, this evaluation did not take the realistic effects of the PA loading into account. Here, more realistic SMPA models will be applied to investigate the linearity and efficiency of a simplified LINC transmitter network.

6.1.1 Efficiency evaluation

For simulating the efficiency of the LINC transmitter, two sine wave signals with conjugate phasors will be used to represent the two decomposition-signals of the LINC transmitter [49]. Both the wideband and narrow band performances will be demonstrated for comparison purposes. Here, the product of the drain efficiency of the SMPA multiplied by the combiner's efficiency will be assumed to be the efficiency of the overall LINC transmitter.

- Narrow Band Load Pull Effects

Obviously, the efficiency of the LINC transmitter using a tee combiner (i.e. reactive Wilkinson combiner) is affected by the equivalent time varying load impedance depicted at the output of the amplifiers. This time varying load impedance is typically calculated based on the instantaneous current phasors entering the combining tee-junction. Definitely, the loading will affect the operating conditions of each amplifier. It is important to account for such reflections/loading and investigate its effects on the efficiency of overall performance. For example, with the higher load impedance, a larger proportion of the amplifier's output signal will be reflected back to the same port. To evaluate such an effect, we have carried out a simulation for a LINC transmitter utilizing a narrow band class D PA in association with either an ideal non-isolated or ideal isolated combiners (as shown in Figure 6.1). Two single-tone sources with an angle of $\pm$theta are used to present the two out-phasing constant- envelope signals in the two branches. We then swept the theta angle from 0 to 90^0, assuming a uniform distribution of these decomposition angles. In Figure 6.1a, a split-T junction is used as the non-isolated combiner. Meanwhile, a hybrid combiner is used as an isolated combiner and is shown in Figure 6.1b.

In our calculations, we have evaluated the overall efficiency using the following equation

$$Efficiency = P_{out}/P_{dc} \qquad \text{(Eq 6.1)}$$

where P_{out} is the output power of the combiner and P_{dc} is the total DC power consumption of the two PAs. Subsequently, based on the simulation results, it was obvious that even the load pull effects of the class D PA are accounted for and the entire efficiency of the non-isolated combiner system would be better than that of the isolated combiner for a narrow band class D PA (as shown in Figure 6.2). This is especially true for large decomposition angles, given that the combining efficiency of the isolated combiner drops as a function of $\cos^2$(theta).

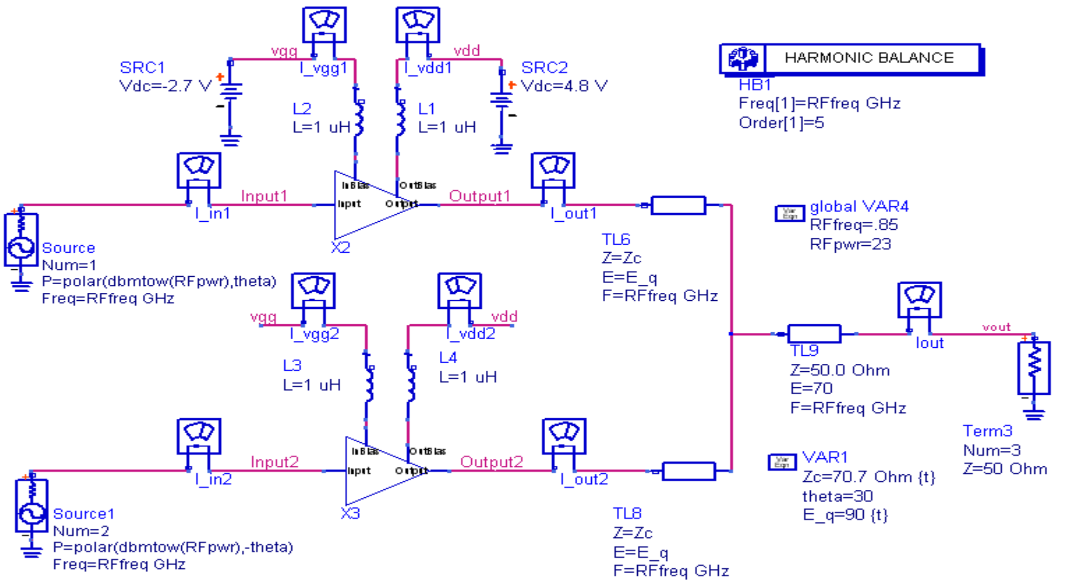

(a)

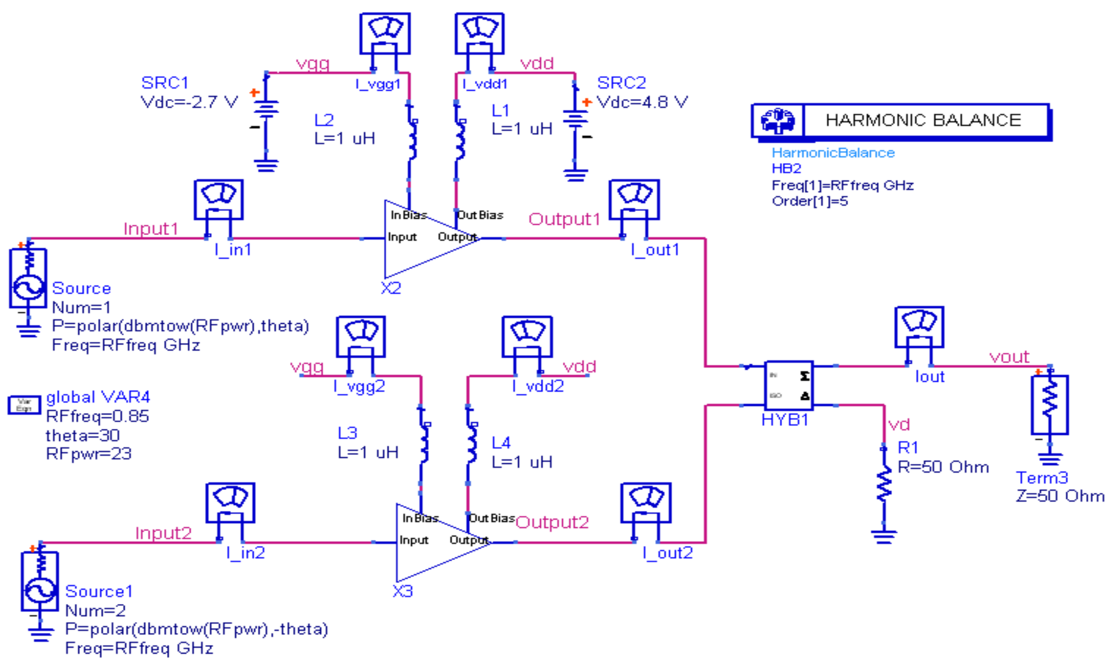

(b)

Figure 6.1 Narrow band class D PA with combiners: (a) Non-isolated; (b) Isolated

(Note: The narrow band of the class D PA model with its simulation results are shown in Appendix C and Figures C1 and C2.)

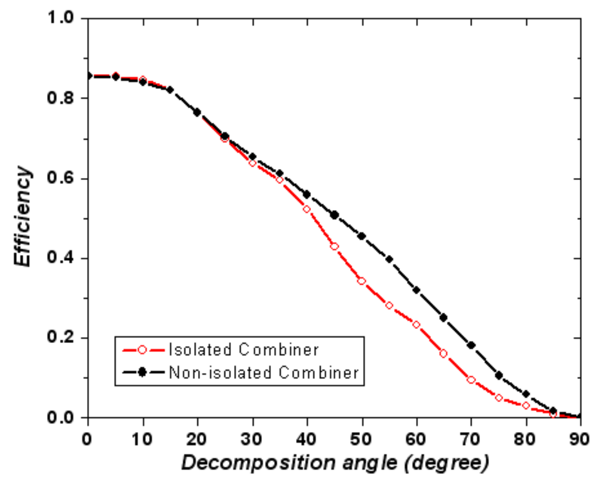

Figure 6.2 Efficiency vs. decomposition angle

- Wide Band Load Pull Effects

For wide band applications, however, our conclusion is different from that of the narrow band and will be indicated here, assuming that we need to add a matching network to the class D PAs to sustain its gain flatness and obtain a high output power level over the entire band. Here, we evaluate the wideband performance of the system by replacing the previously used narrow band class D PAs and combiners with wideband ones, as shown in Figure 6.1. Then, we perform numerous simulations at different input power levels and over a wide range of operating frequencies. The results in Figure 6.3a demonstrate that the non-isolated combiner achieves a higher efficiency than that of the isolated combiner at certain frequencies, but achieves a lower efficiency at other frequencies, as shown in Figure 6.3b. So, from an efficiency point of view, either approach can be utilized, but other preferences may need to be taken into account if factors such as linearity are considered at the same time. Details of our investigation when accounting for linearity will be discussed in the next section.

6.1.2 Linearity evaluation

Linearity is an important parameter when evaluating the performance of a LINC transmitter. Here, we use a two-tone signal to estimate the linearity of a LINC transmitter, shown in Figure 6.4. In each branch, a driver amplifier is used to drive the class D power amplifiers to saturation (shown in Appendix C, Figures C1 and C2), thus achieving a high overall efficiency. Details of similar test benchmarks (Figure 3.4) with ideal amplifiers have previously been provided in Chapter 3.

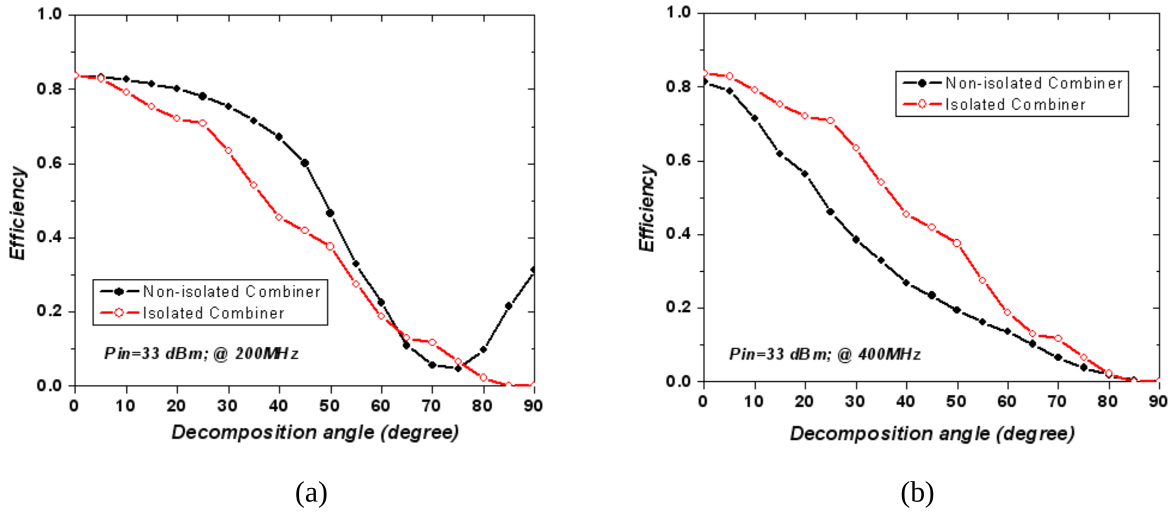

Figure 6.3 Efficiency vs. Decomposition angle: (a) 200 MHz; (b) 400 MHz

(Note: The wide band class D PA model with its simulation result is shown in Appendix C and Figures C3 and C4.)

Based on our linearity performance evaluation, shown in Figure 6.5, we discovered that when utilizing an isolated combiner, the IMD levels are much lower than that of a non-isolated combiner. This means that high linearity can be achieved when we have high isolation between the utilized non-linear class D PAs. In other words, the LINC transmitter can produce better linearity performance. Hence, when linearity is the prime consideration, isolated combiners are preferred.

In short, it is obvious that using isolated combiners is preferred, since it achieves efficiency similar to that of the non-isolated combiners, while producing a higher linearity than the non-isolated combiners for wideband applications. Moreover, additional efficiency enhancements can be achieved upon recycling the power in the difference port (details have been discussed in Chapter 5). However, if the efficiency is of major concern as well, searching for special and novel combining schemes is also recommended. For example, in the next section, we will introduce a novel adaptive bias LINC transmitter concept to achieve a relatively high efficiency and linearity for signals with high peak-to-average ratios.

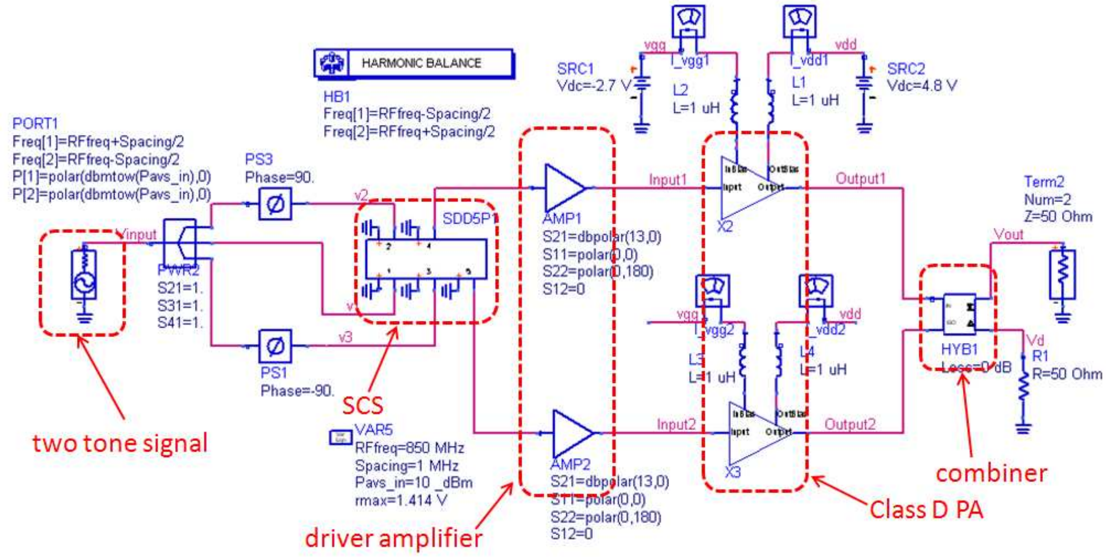

Figure 6.4 LINC transmitter with two-tone signal

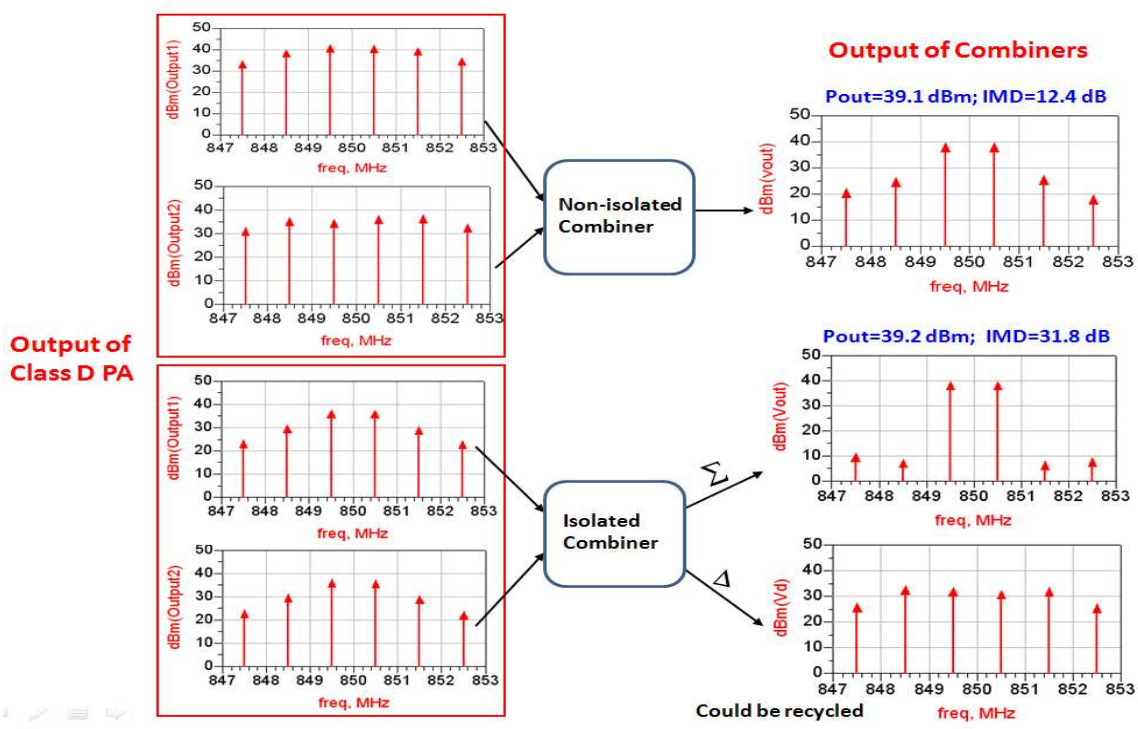

Figure 6.5 Simulation results of the LINC transmitter with two-tone signal using isolated/ non-isolated combiners

6.2 Basic Idea of the Adaptive Bias LINC Transmitter

Many researchers have recognized [49], as clearly demonstrated in the previous section, that neither the isolated nor the non-isolated power combiners can simultaneously achieve linearity and high average efficiency with a conventional LINC transmitter, so a tradeoff between linearity and efficiency is generally accepted. While the individual PAs are designed to operate with high efficiency, the primary problem with a conventional LINC resides in combining the two output signals $S_1(t)$ and $S_2(t)$ after they are amplified appropriately. As was clearly discussed in the previous section, the combining efficiency will depend on the decomposition angle between the two signals, which can render low operating efficiencies. In fact, when the amplitude of the signal, A(t), is much less lower than its maximum amplitude, r_{max}, the two signals, $S_1(t)$ and $S_2(t)$, are almost out of phase and the instantaneous efficiency is close to zero. On the other hand, when $A(t) = r_{max}$, the two signals are in phase and efficiency is at its maximum. The decomposition angle, the signal amplitude and the peak-to-average ratio, i.e. the signal's properties are functions of the modulation scheme. Therefore, when designing a LINC transmitter, the PA performance and the signal properties, such as PAR, need to be accounted for in order to minimize the corresponding decomposition angle while optimizing the design for the amplifiers and combiners.

The concept of changing the DC bias of the power amplifiers to improve the overall efficiency of the LINC transmitter is not new. For example, W. Young Yun et al. [46] have suggested adjusting the DC bias of the SMPA to achieve high efficiency of the SMPA with small signals levels; however, their analysis did not consider the combiner's loading and decomposition angle effects. C. Yuan-Chuan [44] proposed adjusting the decomposition angle of the two branch signals and changed the DC bias of the PA, plus adding pre-distortion circuits. He suggested a DC bias with discrete multi-levels determined by the signal statistic performance. However, only a conventional PA performance was treated and the combiner's combining effect was not accounted for.

In parallel with the aforementioned ideas of adjusting the DC bias, we have introduced an Adaptive Bias LINC concept that completely accounts for the combiner's loading. The concept will be discussed here. In our approach, high linearity is first achieved using an isolated combiner while the LINC transmitter's efficiency is improved by changing the DC bias of the SMPAs, based on the total effects of the combiner, the SMPA, and input signal properties. We use voltage-mode class D power amplifiers (VMCD) which can act as ideal voltage sources. Their output voltages are linearly proportional to the drain bias, while their drain efficiency, even when the drain bias is changing, can still be high. These properties are necessary for developing an adaptive bias LINC transmitter and will be discussed in detail later. First we will discuss various, useful properties of the class D PA before analyzing the overall concept.

6.2.1 Voltage-mode class D power amplifier (VMCD) characteristics

The VMCD PA ideally has 100% drain efficiency, as is well known. If so, then the RF output power is assumed to be equal to the input dc power, we can relate the dc voltage to the RF signal through the following

$$P_{dc} = P_o \qquad \text{(Eq 6.2)}$$

where

$$P_{dc} = V_{dc} \cdot I_{dc}\ , \qquad \text{(Eq 6.3)}$$

but

$$I_{dc} = \frac{8}{\pi^2}\frac{V_{dc}}{R} \qquad \text{(Eq 6.4)}$$

$$R = \left(\frac{m}{n}\right)^2 R_L \qquad \text{(Eq 6.5)}$$

$$P_o = \frac{V_o^2}{2R_L} = P_{dc} = \frac{8}{\pi^2}\frac{V_{dc}^2}{R} \Rightarrow \frac{V_o}{V_{dc}} = \frac{4}{\pi}\frac{n}{m} \qquad \text{(Eq 6.6)}$$

where P_{dc} : DC power, P_o : output RF power, *m/n* : transformer turns ratio, I_{dc} : DC current, V_{dc} : DC voltage, and V_o : output voltage. Further details about the VMCD operation can be found in Chapter 4.

In other words, the output RF voltage is ideally linearly proportional to the dc applied voltage as indicated by Eq 6.6. However, due to the parasitic of the realistic devices, there is a slight deviation from these ideal characteristics and is not easily accounted for when using only the above simplified equations.

Therefore, in our analysis, we used a VMCD (the schematic of the VMCD amplifier is shown in Appendix C, Figure C5). Our evaluation and its simulation results are shown in Figure 6.6. It is clear that with a constant input power, both the output voltage (V_{out}) and voltage gain are still almost linearly proportional to V_{dc}, but the efficiency has a noticeably, slight deviation from linear behavior, as shown in Figure 6.6b. A similar performance has also been noted for the CMCD devices [55]. It is important to mention that there is a measurable phase shift in the output voltage, which is linearly proportional to the applied V_{dd}, as shown in Figure 6.6d. This linear phase shift should be accounted, and compensated, for to minimize the "VDD-PM" distortion, explained in further detail in the following section.

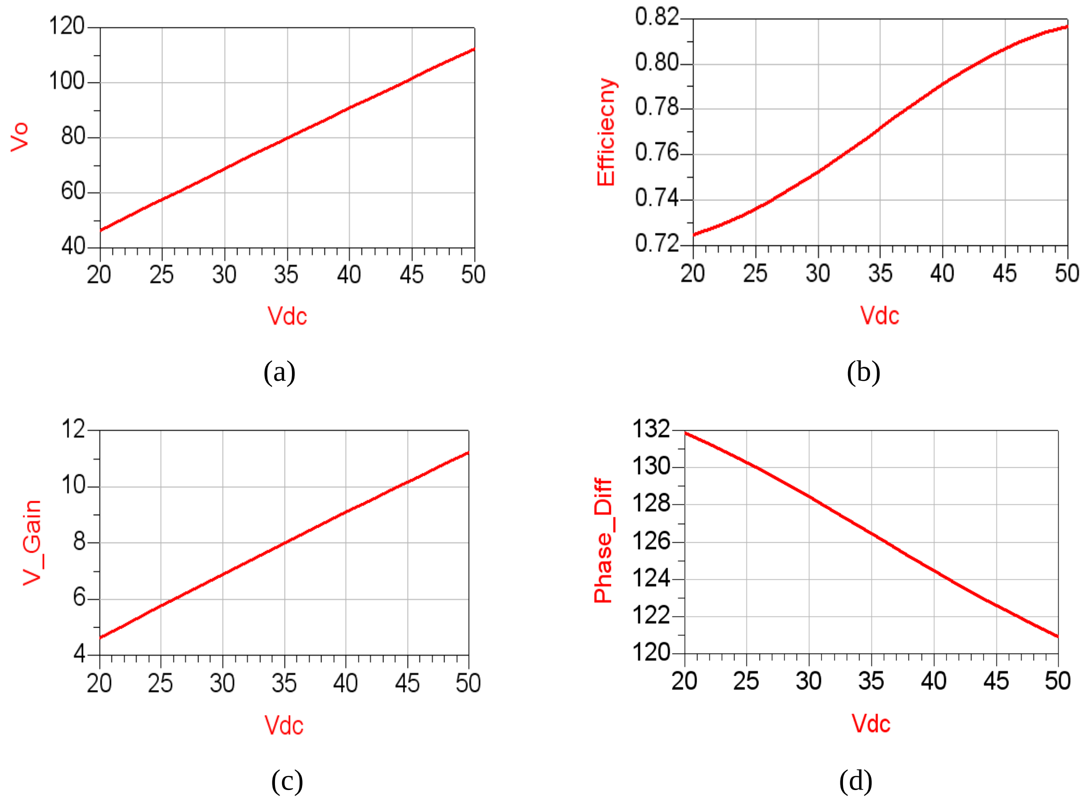

Figure 6.6 Drain voltage vs. (a) Output voltage; (b) Efficiency; (c) Voltage gain (defined by output voltage over input voltage); (d) Phase shift between input and output

Based on the performance shown in Figure 6.6, and while keeping a high efficiency performance, we can decrease the drain bias of the VMCD to achieve a smaller output voltage. This could lead to effectively reducing the decomposition angles, thus improving the combining efficiency. Additional details and comparisons between the conventional and adaptive bias LINC transmitters will be given in the next section.

6.2.2 Adaptive bias LINC vs. conventional LINC

Figure 6.7 shows both the conventional LINC and the adaptive bias LINC transmitters with detailed signal flow charts. Here, G represents the gain of the PA, S(t) is the input amplitude modulated signal, A(t) is the signal amplitude, ω is the carrier frequency, r_{max} is maximum amplitude of A(t), and α is an adaptive bias index that will be developed in our analysis here. In this approach, based on the angle $\phi(t)$ of the signals, the phasor angle *g(t)* is defined as

$$\cos(g(t)) = \begin{cases} \cos(\phi(t)) & for\ \ \phi(t) < \phi_{threshold} \\ \alpha\cos(\phi(t)) & for\phi(t) > \phi_{threshold} \end{cases} \qquad \text{(Eq 6.7)}$$

Based on the value of the phase $\phi(t)$, the gain of the amplifier needs to be adjusted to G/α for $\phi(t) > \phi(t)_{threshold}$. The factor, α, selection will be shown in detail in the following section.

In Figure 6.7b a lookup table is used to store the gain information of PAs with different drain bias conditions. The details of the SCS were given in Chapter 3.

Figure 6.8 is a comparison of the decomposition angle of a conventional and adaptive bias LINC transmitter, which shows that with an adaptive bias LINC, the decomposition angle is smaller so the combining efficiency increases.

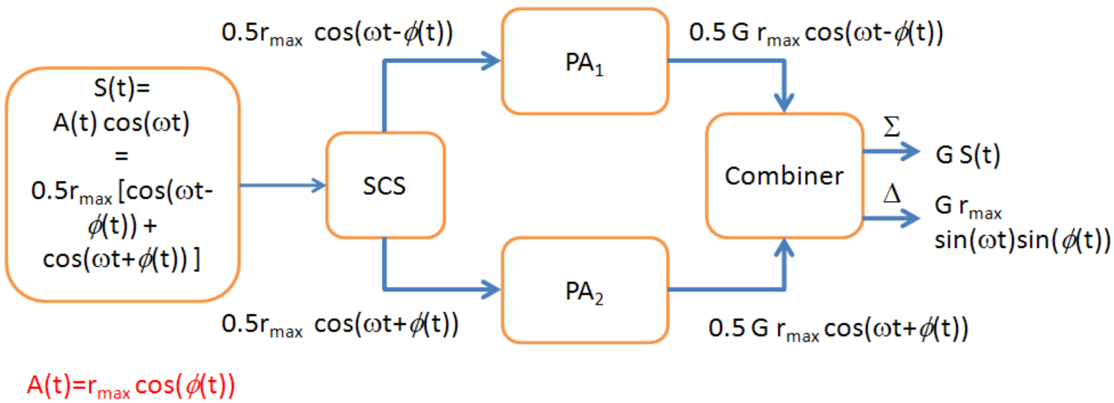

(a)

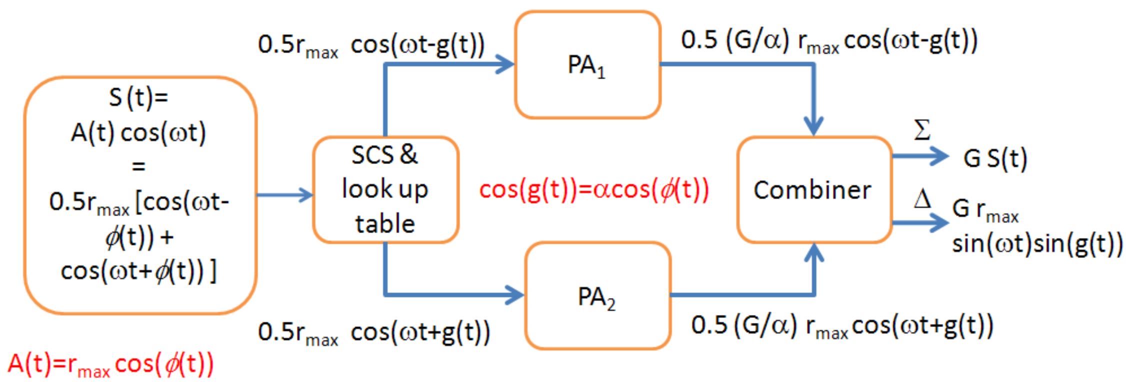

(b)

Figure 6.7 Transmitter Schematics: (a) Conventional LINC; (b) Adaptive bias LINC

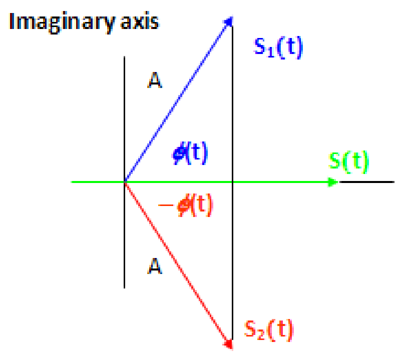

(a)

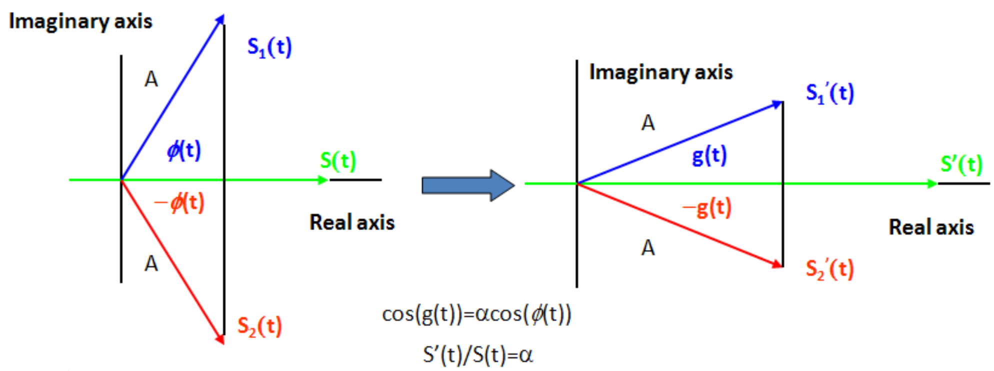

(b)

Figure 6.8 Signal decomposition: (a) Conventional LINC; (b) Adaptive bias LINC

In our proposed adaptive bias LINC transmitter model, the concept is based on decreasing the decomposition angle for small signal levels to sustain a high average combining efficiency. However, the voltage-gain of the PAs needs to be decreased accordingly. Thus, the output signal of the adaptive bias LINC is the same as the conventional LINC. Since the efficiency of the LINC transmitter is the product of the combiner and PAs' efficiency, to achieve an overall high efficiency, the efficiency of the PAs should not be significantly reduced when lowering the voltage-gain of the PAs. A high overall efficiency can be attained using our recommended concept. For example, and shown in Figure 6.6, when the drain bias voltage is reduced, the voltage-gain of the VMCD is decreased while sustaining over a 70% overall efficiency. Table 6-1 summarizes the different signals of the conventional LINC and adaptive bias LINC transmitter at different stages of their processes.

Ideally, "α" is restricted to $(1/\cos(\phi(t)) > \alpha > 1)$, however, in practical designs, the range of "α" is limited by the PA performance, as shown in the follow:

Table 6-1 Comparison of the signals of the conventional LINC and adaptive bias LINC

	Conventional LINC	Adaptive Bias LINC
Input AM signal (to SCS); S_{in} is output of SCS unit	$A(t) = r_{\max}\cos(\phi(t))$ $\phi(t) = \cos^{-1}(A(t)/r_{\max})$ $S_{initial}(t) = S_{in}(t) =$ $A(t)\cos(\omega t)$	$1/\cos(\phi(t)) > \alpha > 1$ $\cos(g(t)) = \alpha\cos(\phi(t)) \Rightarrow$ $g(t) = \cos^{-1}(\alpha\cos(\phi(t)))$ $A(t) = r_{\max}\cos(\phi(t))$ $B(t) = r_{\max}\cos(g(t)) = \alpha A(t)$ $S_{initial}(t) = A(t)\cos(\omega t)$ $S_{in}(t) = B(t)\cos(\omega t)$
Input PM signal (to PAs)	$S_1(t) = 0.5r_{\max}\cos(\omega t + \phi(t))$ $S_2(t) = 0.5r_{\max}\cos(\omega t - \phi(t))$	$S_1(t) = 0.5r_{\max}\cos(\omega t + g(t)))$ $S_2(t) = 0.5r_{\max}\cos(\omega t - g(t))$
Input amplified PM signal (to isolated combiner)	$0.5G\, r_{\max}\cos(\omega t + \phi(t))$ $0.5Gr_{\max}\cos(\omega t - \phi(t))$ G is the gain of PA under V_{dc1}	$0.5(G/\alpha)r_{\max}\cos(\omega t + g(t))$ $0.5(G/\alpha)r_{\max}\cos(\omega t - g(t))$ G/α is the gain of PA under V_{dc2}
Output amplified AM signal (from the sum port of isolated combiner)	$\sqrt{2}G(S_1(t) + S_2(t)) =$ $\sqrt{2}G\cos(\omega t)\cos(\phi(t)) =$ $\sqrt{2}G\, A(t)\cos(\omega t)$	$\sqrt{2}(G/\alpha)(S_1(t) + S_2(t)) =$ $\sqrt{2}(G/\alpha)\cos(\omega t)\cos(g(t)) =$ $\sqrt{2}(G/\alpha)B(t)\cos(\omega t) =$ $\sqrt{2}G\, A(t)\cos(\omega t)$
Decomposition angle	ϕ(t) ϕ(t)>g(t)	g(t) ϕ(t)>g(t)
Efficiency	$\eta_{combiner} = \dfrac{\overline{\lvert S_\Sigma(t)\rvert^2}}{\overline{\lvert S_\Sigma(t)\rvert^2} + \overline{\lvert S_\Delta(t)\rvert^2}}$	depends on the decomposition angle;

For a VMCD:

When V_{dc1} changes to V_{dc2} (V_{dc2}<V_{dc1}):

According to Figure 6.6,

$$G_1 / G_2 = \alpha \qquad \text{(Eq 6.8)}$$

Subsequently, the output signal of the PA decreases and is now given by

$$V_{o21} = (G_2 / G_1) V_{o11} \qquad \text{(Eq 6.9)}$$

where G_2,G_1 are the voltage-gains under V_{dc2}, V_{dc1} respectively.

For a isolated combiner:

When the combining angle changes from ϕ(t) to g(t), the output signal increases

$$V_{o22} = \cos(g(t)) / \cos(\phi(t))\ V_{o12} \qquad \text{(Eq 6.10)}$$

Then, the combing efficiency increases from $\cos^2(\phi(t))$ to $\cos^2(g(t))$.

Ideally, if we want the signal to be amplified linearly with the adaptive bias scheme, we need to have $G_2 / G_1 = \cos(\phi(t)) / \cos(g(t)) = \alpha$. We can either select *g(t)* according to G_2/G_1 or select G_2/G_1 according to *g(t).* In order to achieve a high combining efficiency of the combiner, to keep *g(t)* small, it is better to have (*cos(g(t))*=1 for the highest combining efficiency. However, we may not have a solution for V_{dc2} (which relate to V_{o2}), given that $V_{o2} = V_{o1} \dfrac{\cos(\phi(t))}{\cos(g(t))}$, special when $\cos(g(t))$ is close to 1.

So, we prefer to select different levels of V_{dc} and pick g(t) according to a discrete set of V_{dc1} / V_{dc2} ratios. Therefore, the threshold angle can be selected using θ_{th}=arcos (G_2 / G_1), given that we are going to use only two different levels of drain bias. Meanwhile, if we use different discrete levels of V_{dc}, it is possible to produce even a higher average combining efficiency, but the adaptive bias LINC transmitter will become progressively more complicated. In this chapter, only two discrete levels of V_{dc} are considered. The above analysis, however, does not take into account both the nonlinearity of the PAs and the properties of the different input signals. Therefore, in the next section, an advanced EDA tool will be applied to simulate a more realistic adaptive bias LINC transmitter based on real devices to account for nonlinearity and signal properties.

As is a simple example, for illustration purposes, let us re-plot Figure 6.6 b&c as follows:

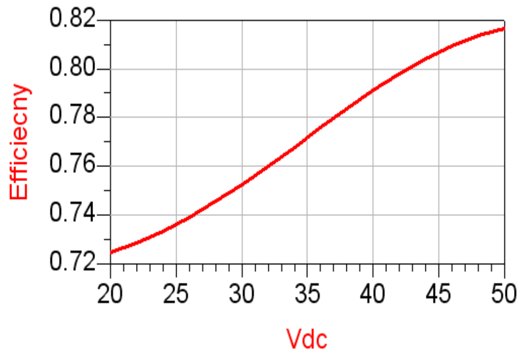

(b)

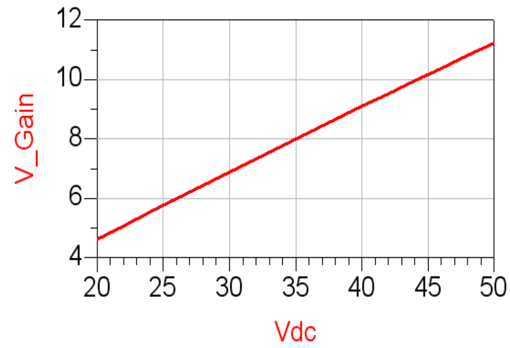

(c)

In this case, we select two DC bias conditions. One is 50V where the drain efficiency (eff1) of VMCD is 82% and the voltage-gain (G1) is 11.2. The other condition is 25V and the associated drain efficiency (eff2) of the VMCD is 73.8%, with a voltage-gain (G2) of 5.8.

Then, the threshold angle can be selected using θ_{th}=arcos $(G_2 / G_1) = 59^0$.

Now if we assume the decomposition angle to be $\phi(t) = 75^0$, then we pass the threshold and the outcome will be different based on the LINC scheme utilized.

Case1. Using a conventional LINC, the overall efficiency is $eff\_all1 = eff1 \times \cos^2(75^0) = 0.055$

Case2. Applying the adaptive bias scheme, if we want to utilize the smallest new decomposition angle g(t)=0 in order to have linear amplification, we need to have $G2 = G1\cos(\phi(t)) = 11.2 \times 0.259 = 2.9$. However, from Figure 6.6c, we can see that within the acceptable V_{dc} range, the voltage-gain is higher than 4.8. Hence, we have to reduce the decomposition angle according to the possible voltage-gain, as shown in Figure 6.6c. In this case, we will pick V_{dc} to be 25V with a G2=5.8 and the drain efficiency (eff2) of the VMCD is 73.8% with a 25V drain bias.

Accordingly:

$$\alpha = G2 / G1 = 11.2 / 5.8 = 1.93,$$

$$g(t) = \cos^{-1}(G1\cos(\phi(t)) / G2) = \cos^{-1}(0.5) = 60^0,$$

$$eff\_all2 = eff2 \times \cos^2(60^0) = 0.186.$$

So, the overall efficiency increases from 5.5% (conventional LINC) to 18.6% (adaptive bias LINC).

6.3 Adaptive Bias LINC Transmitter Simulation

6.3.1 Simulation tools overview

To simulate an adaptive bias LINC transmitter, we first summarize the available simulation tools. We can use Matlab to generate either a sine wave or a modulated signal for the adaptive bias scheme. Additionally, Matlab can also be used to display and compare the original signal and amplified output signal. Envelope simulator (an ADS simulator) will be used to simulate the RF sub-circuit (power amplifier and power combiner). Meanwhile, Ptolemy (an ADS simulator) is used to combine the Matlab and the Envelope simulator, as shown in Figure 6.9.

To simulate the adaptive bias LINC transmitter, we use Matlab to generate a modulated baseband signal and decompose it into two constant envelope baseband signals emulating the SCS and look-up tables. Subsequently, the Matlab module exports the two constant envelope baseband signals into a Ptolemy simulation environment. Within the Ptolemy environment, these two RF signals are up-converted into RF signals and then imported into a sub-level simulation environment (Envelope simulator). In the sub-level environment, the two RF signals are fed to power amplifiers and summed by an isolated combiner. Afterwards, the output of the isolated combiner is exported back to the Ptolemy environment. The amplified RF signal is then down-converted into baseband, and finally, Matlab can be used to plot and compare the amplified baseband signal with an initial reference baseband signal. Our Matlab code is shown in Appendix E.

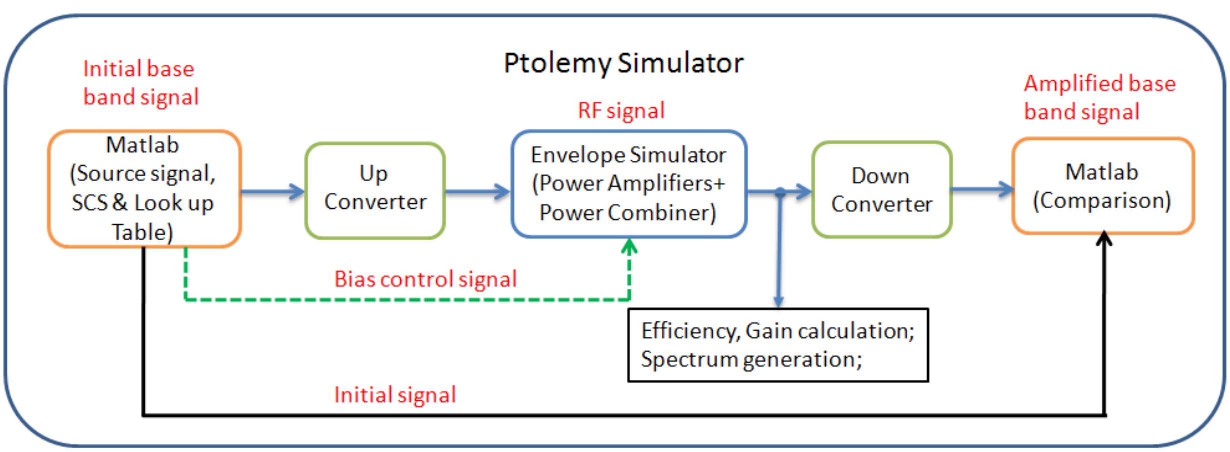

Figure 6.9 Simulation contents

6.3.2 *Modulation*

- 16 QAM

Spectral efficiency is an important issue for wireless communication systems, since there is a bandwidth limitation for each application defined by the FCC. Linear modulation schemes have been applied to effectively increase the spectral efficiency, such as a filtered M-ary PSK and a M-ary QAM (quadrature amplitude modulation). In this study, a 16 QAM will be used as an example for a non-constant envelope signal.

QAM is a modulation technique where the symbols have both amplitude and phase variations. It can be viewed as a complex amplitude-modulated carrier. The QAM signal constellation is a rectangular grid with points uniformly spaced along each axis, as shown in Figure 6.10. With M as the number of possible transmitted waveforms, an M-QAM modulation combines every $\log_2 M$ bits into an individual symbol and the symbol rate is $\log_2 M$ times less than the bit data rate. In the *n*th symbol interval, a QAM signal can be expressed as [70]

$$s(t) = A_c(a_{In} + ja_{Qn})e^{j(2\pi f_c t+\theta_c)} \qquad \text{(Eq 6.11)}$$

where the information amplitudes a_{In}, and a_{Qn} independently range over the sets of equi-probable values:

$$a_i = (2i - 1 - \sqrt{M}), \quad i = 1, 2, ..., \sqrt{M}\ , \ a_l = (2l - 1 - \sqrt{M}), \quad l = 1, 2, ..., \sqrt{M} \qquad \text{(Eq 6.12)}$$

respectively, and the I and Q subscripts denote the inphase and quadrature channels.

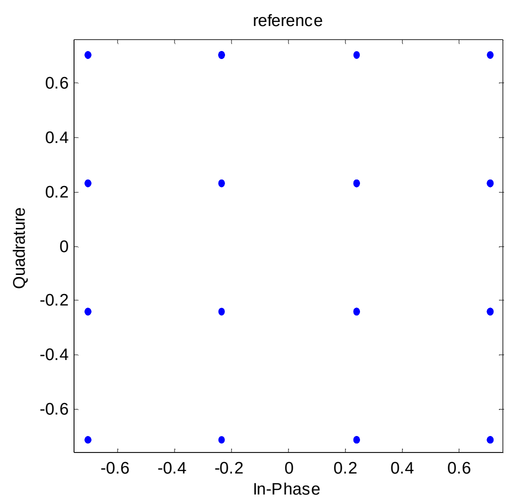

Figure 6.10 Constellation of an ideal 16 QAM signal used as a reference signal

6.3.3 Illustrative Matlab simulation

Here some Matlab code is first used to simply demonstrate how the adaptive bias scheme affects the average efficiency of the isolated combiner. Here, the decomposition angle is has a uniform distribution of 0 -90^0, which can be illustrated by the following example:

For a threshold decomposition angle: $\theta_{th}= arcos\ (G_1/G_2)$

where $V_{dc1}>V_{dc2}$, $G_1>G_2$, and θ_n is the new decomposition angle.

There are two states:

State 1 when $\theta \leq \theta_{th}$; biased by V_{dc1} and the voltage-gain of the VMCD is G_1;

$\theta_n = \theta$; i.e. keeps the angle the same

State 2 when $\theta > \theta_{th}$; biased by V_{dc2} and the voltage-gain of the VMCD is G_2;

$\theta_n = arcos\ ((G_1/G_2)\ cos(\theta))$, here $\theta_n < \theta$; and we need to reduce the angle to θ_n.

For example, if we assume that $G_1/G_2= 2$, then the threshold angle is $\theta_{th}= 60^0$. Figure 6.11 depicts a conventional LINC scheme, the vectors of the two amplified branch signals(S_1 and S_2), change smoothly upon increasing the decomposition angle, the output power (P_{out}), and its combining efficiency decreases upon increasing θ in accordance with $\cos^2(\theta)$ dependence. However, with an adaptive bias scheme, the operation is divided into two cases as shown in Figure 6.12:

a) When the decomposition angle (θ) is smaller than the threshold angle ($\theta_{th}= 60^0$), the output power (P_{out}), dissipated power (P_{diss}), combining efficiency, and the two amplified branch signals are still similar to the conventional LINC scheme.
b) However, when the decomposition angle is larger than the specified threshold angle, the combining angle changes and the dissipated power (P_{diss}) decreases, increasing the combining efficiency. The magnitude of the two amplified branch signal (S1 and S2) decreases while the angle between the two decreases, according to the adapted design scheme. Thus, the average combining efficiency increases from 50% to over 60%. This is not a significant improvement, but, and it should be pointed out, that with a high PAR signal, the improvement will be significantly pronounced.

We have applied a sine signal to the adaptive bias LINC transmitter. In the next section, we will apply the 16 QAM signal to the adaptive bias LINC transmitter and show that the 16 QAM signals have a high peak-to-average ratio, validating our previous claim of achieving an efficiency improvements for high PAR signals.

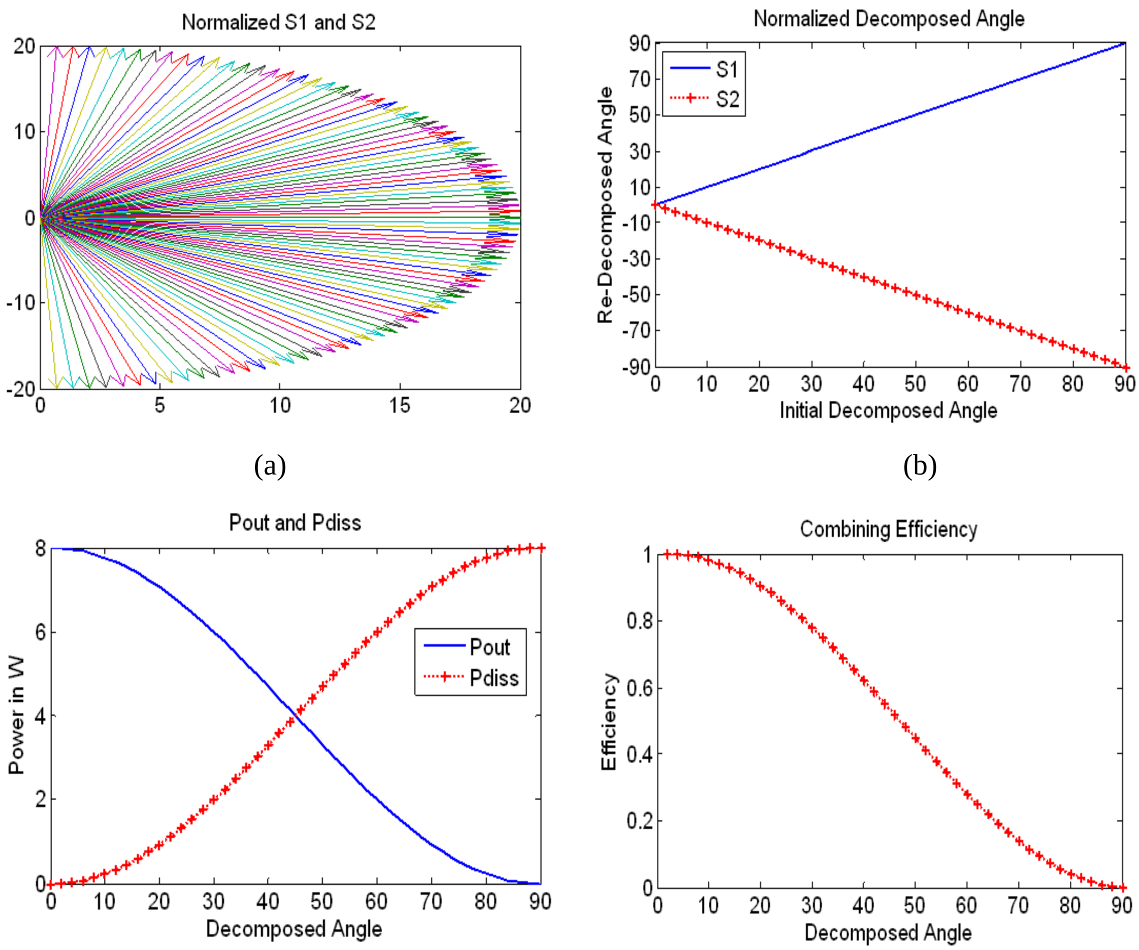

(a) (b)

(c) (d)

Figure 6.11 Conventional LINC: (a) Decomposed vectors; (b) Decomposed angles; (c) Output sum power and dissipated power; (d) Combining efficiency

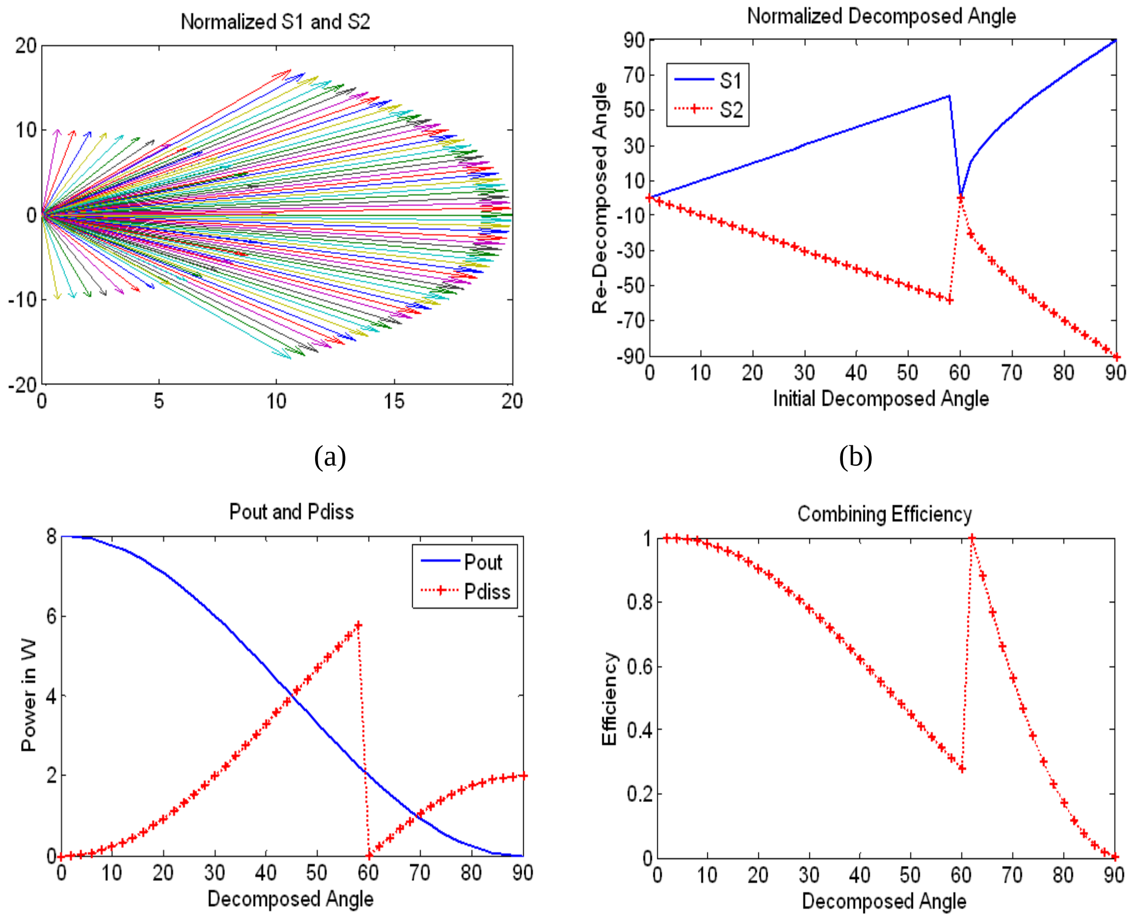

(a) (b)

(c) (d)

Figure 6.12 Adaptive bias LINC: (a) Decomposed vectors; (b) Decomposed angles; (c) Output sum power and dissipated power; (d) Combining efficiency

6.3.4 *Matlab, Envelope and Ptolemy co-simulation*

Utilizing Matlab, we ran a single frequency simulation as an example, but the results can be generalized for a wideband performance. In our simulation, we used an ideal voltage controlled amplifier to predict the combining efficiency employing an adaptive bias scheme, followed by a customized GaN VMCD to include the PAs nonlinearities.

- Ideal Voltage Controlled Amplifier Case

The modulated signal contents are defined and shown in Table 6-2. Here, the modulated signals are decomposed into signal's I and Q parts. Here, G1, G2 is the magnitudes of the voltage-gain and "d" is the phase different of the power amplifier with different bias (d=0 for ideal voltage control amplifier case). The schematic of the Matlab, Envelope, and Ptolemy co-simulation, with a 16 QAM signal, is shown in Figure 6.13. The block "QAM" is the Matlab module used to generate the baseband 16 QAM signal (S(t)), the decomposed constant envelope signals (S1(t) and S2(t)), and the voltage signal (V_{dd_in}). The blocks "C1" and "C2" transform the complex baseband signals into timed RF signals. The block "C3" transforms the control signal (which is used to control the drain bias of power amplifier) from the phasor presentation into the rectangular presentation. Subsequently, the block "F1" transforms the real part of the control signal into a timed signal. The block "X2" includes the Envelope simulator, the power combiner, and the power amplifiers. In this simulation, ideal voltage controlled amplifiers (the detail of these amplifiers are shown in Appendix C, Figures C6 & C7) are used, and the PA efficiency is assumed to be 100%, so the overall efficiency exactly equals the combining efficiency (defined by $P_{out}/(P_{out}+P_{diss})$). The block "O1" is used to export the simulation data from the Envelope simulator to the Ptolemy environment. The block "T2" transforms the timed RF signal into a complex baseband signal. The block "P1" packs the complex data into a matrix and then exports it to a Matlab module. The block "B1" merges the two input matrix into one output matrix. The adaptive bias scheme is applied to the LINC transmitter by changing the baseband signal in the block "QAM" and by changing the bias voltage of the voltage controlled amplifiers in the block "X2".

Table 6-2 Modulated signals with adaptive bias scheme

$\theta_{th} = \cos^{-1}(G_2 / G_1)$	$\lvert\theta_1(t) = -\theta_2(t)\rvert <= \theta_{th}$	$\lvert\theta_1(t) = -\theta_2(t)\rvert > \theta_{th}$
Initial base band signal	$s(t) = r(t)e^{j\theta(t)} = s_i(t) + j\,s_q(t)$ $0 \le r(t) \le r_{\max}$	$s(t) = r(t)e^{j\theta(t)} = s_i(t) + j\,s_q(t)$ $0 \le r(t) \le r_{\max}$
Branch 1	$s_{1i}(t) = s_i(t) - s_q(t)\sqrt{\frac{r_{\max}^2}{r^2(t)} - 1}$ $s_{1q}(t) = s_q(t) + s_i(t)\sqrt{\frac{r_{\max}^2}{r^2(t)} - 1}$ $s_1(t) = s_{1i}(t) + j\,s_{1q}(t)$ $\theta_1(t) = angle(s_1(t))$	$angle\_s_{1n}(t) = \cos^{-1}(G_1 / G_2 \cos(\theta_1(t)) - d$ $s_{1n1}(t) = (\lvert s_1(t)\rvert e^{j(angle\_s_{1n}(t))} / G_1)\,G_2$ $rs(t) = real(s_{1n1}(t) + s_{2n1}(t))$ $qs(t) = imag(s_{1n1}(t) + s_{2n1}(t))$ $s_{1in}(t) = rs(t) - qs(t)\sqrt{\frac{r_{\max}^2}{rs^2(t) + qs^2(t)} - 1}$ $s_{1qn}(t) = qs(t) + rs(t)\sqrt{\frac{r_{\max}^2}{rs^2(t) + is^2(t)} - 1}$ $s_1(t) = s_{1in}(t) + j\ s_{1qn}(t)$
Branch 2	$s_{2i}(t) = s_i(t) + s_q(t)\sqrt{\frac{r_{\max}^2}{r^2(t)} - 1}$ $s_{2q}(t) = s_q(t) - s_i(t)\ \sqrt{\frac{r_{\max}^2}{r^2(t)} - 1}$ $s_2(t) = s_{2i}(t) + j\ s_{2q}(t)$ $\theta_2(t) = angle(s_2(t))$	$angle\_s_{2n}(t) = -\cos^{-1}(G_1 / G_2 \cos(\theta_2(t)) - d$ $s_{2n1}(t) = (\lvert s_2(t)\rvert e^{j(angle\_s_{2n}(t))} / G_1)\,G_2$ $s_{2in}(t) = rs(t) + qs(t)\ \sqrt{\frac{r_{\max}^2}{rs^2(t) + qs^2(t)} - 1}$ $s_{2qn}(t) = qs(t) - rs(t)\ \sqrt{\frac{r_{\max}^2}{rs^2(t) + qs^2(t)} - 1}$ $s_2(t) = s_{2in}(t) + j\ s_{2qn}(t)$

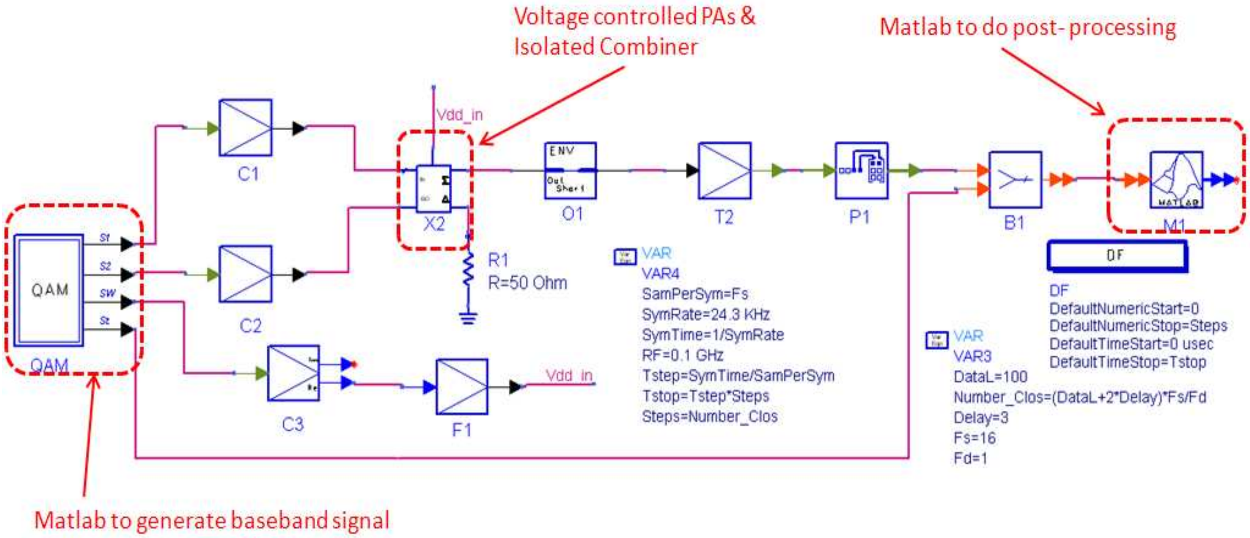

Figure 6.13 Simulation schematic for 16QAM signal with ideal voltage controlled amplifier
(Note: The details of sub-circuits are shown in Appendix D.)

Figure 6.14 shows the simulation results for the conventional LINC case, while Figure 6.15 is for the adaptive bias LINC case. As shown in Figure 6.14a, the bias controlled signal (V_{dd_in}) is constant all the time, however it switches between two values in Figure 6.15a. The constant envelope signal's spectrum, in each branch, occupies a wide frequency range in both cases, as shown in Figure 6.14c and Figure 6.15c. In each case, the 16 QAM signal has a high PAR=5 dB, the average efficiency increases from 55% to 70% with the adaptive bias scheme. Also, by comparing the spectrum of the initial and output signal, it is obvious that both the conventional LINC and the adaptive bias LINC scheme will not decrease linearity. This is shown in Figure 6.14d and Figure 6.15d. To achieve a more realistic result, a customized VMCD is used to replace the ideal voltage control amplifier in the next section.

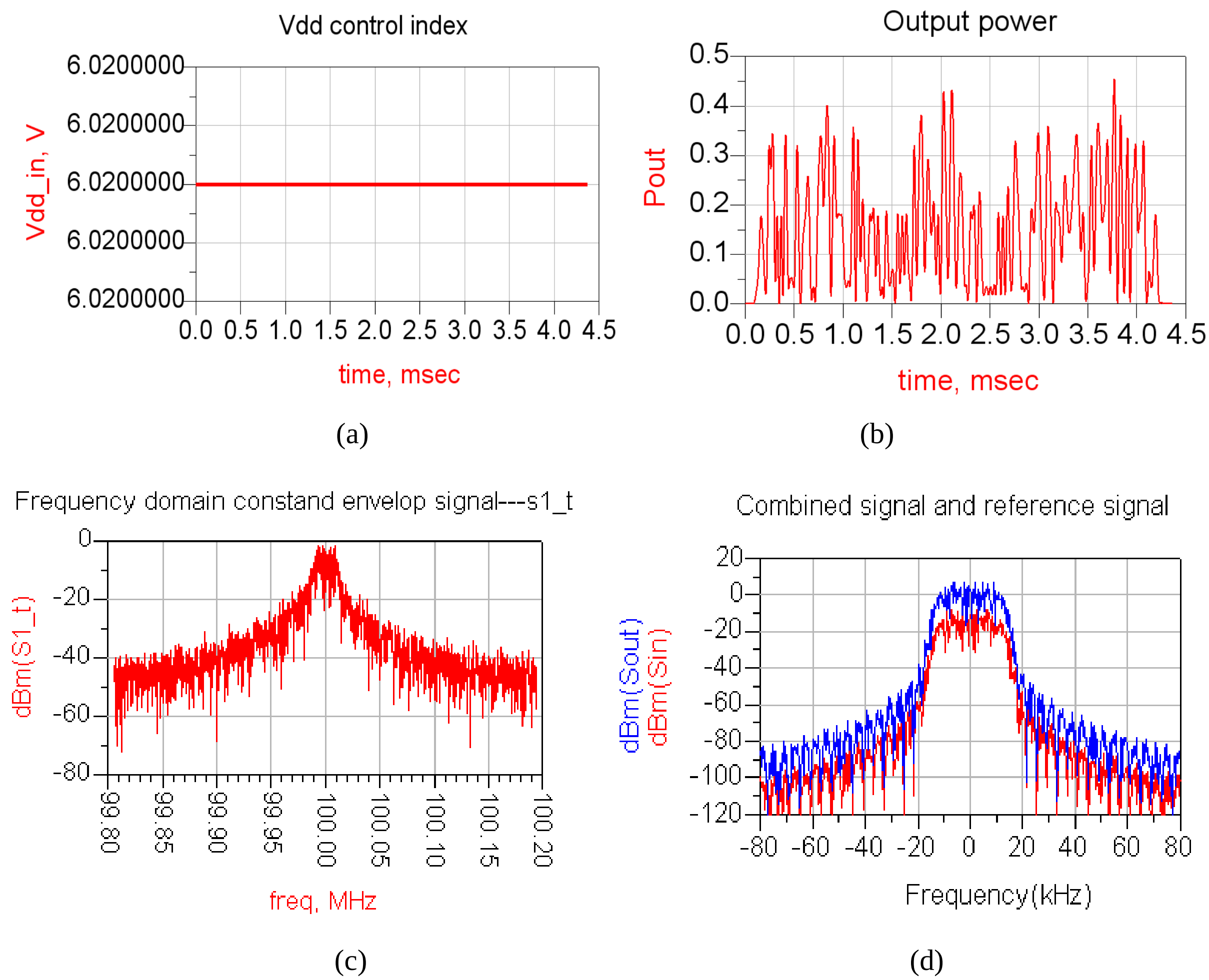

Figure 6.14 Simulation results of conventional LINC transmitter: (a) Voltage control signal in time domain; (b) Power spectrum of the output signal; (c) Spectrum of constant envelope signal; (d) Spectrum of combined and reference signal (blue--- combined signal, red--- reference signal)

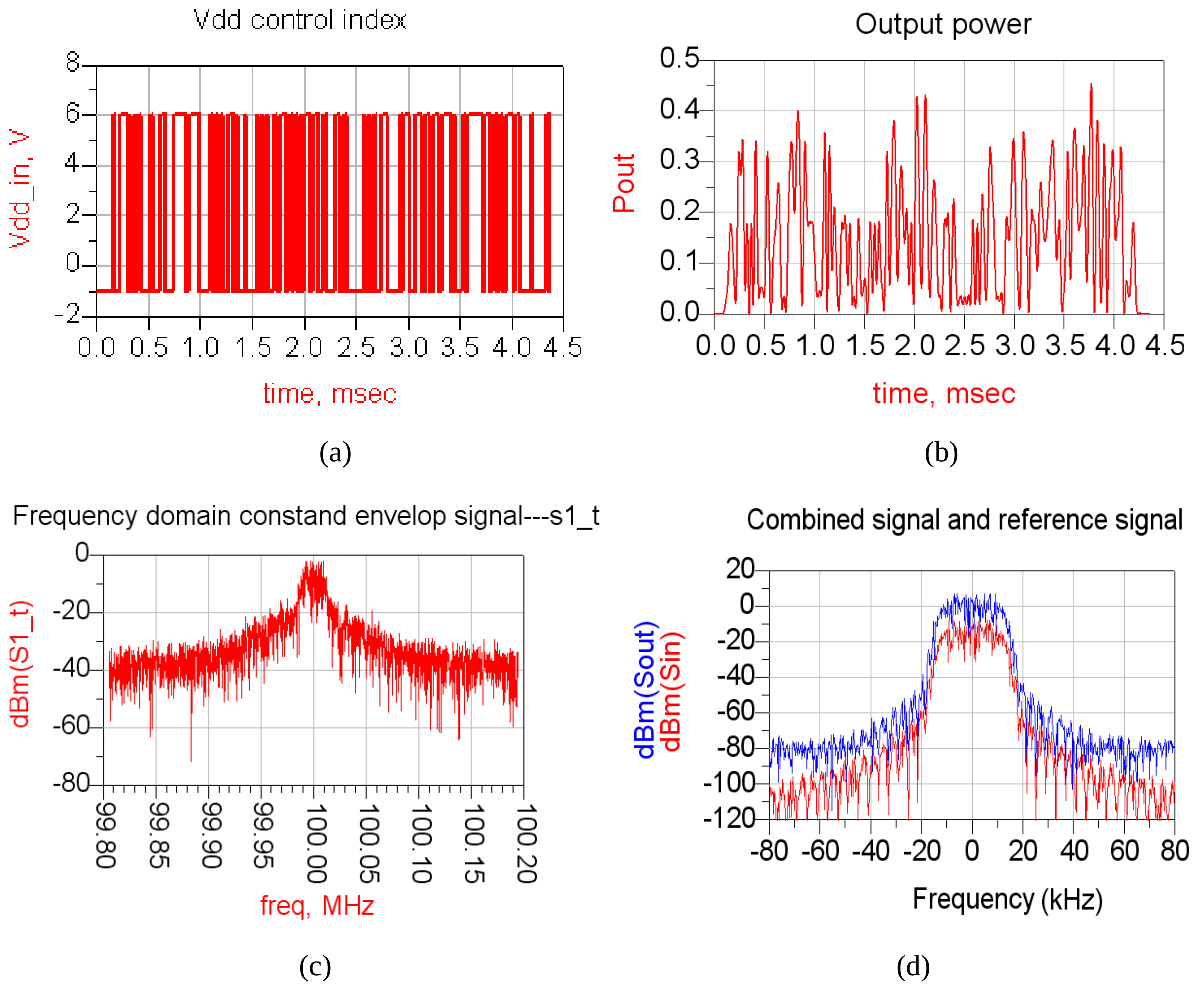

Figure 6.15 Simulation of adaptive bias LINC transmitter: (a) Voltage control signal in time domain; (b) Power spectrum of the output signal; (c) Spectrum of constant envelope signal; (d) Spectrum of combined and reference signal (blue--- combined signal, red--- reference signal)

➢ GaN VMCD Case

Here a more realistic VMCD is applied, and a driver amplifier is used to push the VMCD to saturation. Figure 6.16 shows the Matlab, Envelope, and Ptolemy co-simulation schematics. There is a phase shift, when the VMCD switches between the two different biases. If this phase shift isn't compensated, it will cause a "VDD-PM" distortion. Thus, phase compensation (adding the different phase shift to the baseband signals calculated from Figure 6.6d; for example, shows the phase difference between 50V and 25V bias is 9^0) is needed to sustain the linearity. The average efficiency increase from 25.6% to 36.3% when an adaptive bias scheme is applied with a 16QAM signal (PAR=5 dB). Figure 6.17a shows that although the adaptive bias transmitter cannot achieve the same ACPR as a conventional LINC transmitter, it does achieve a ACPR=-50 dBc, which is sufficient for a 16QAM communication system [71]. Figure 6.17b shows the normalized constellation. The EVM of the conventional LINC is 1.23%, and the EVM of the adaptive bias LINC is 1.41%.

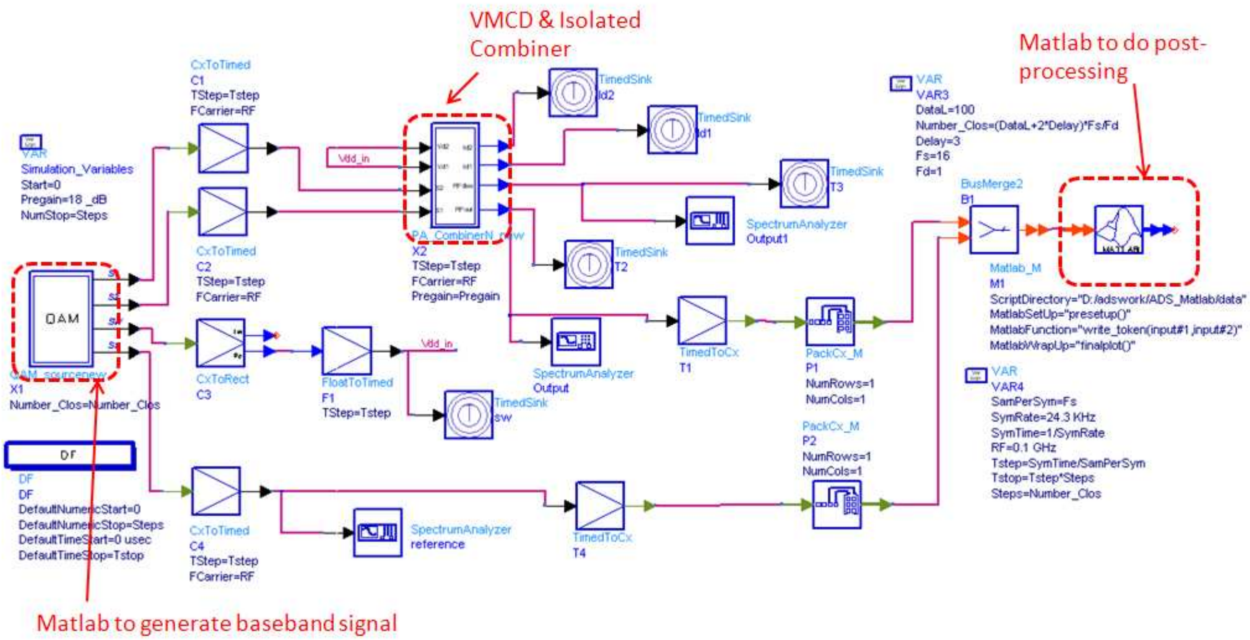

Figure 6.16 Schematic of adaptive bias LINC transmitter with GaN VMCD

(Note: The details of sub-circuits are shown in Appendix D.)

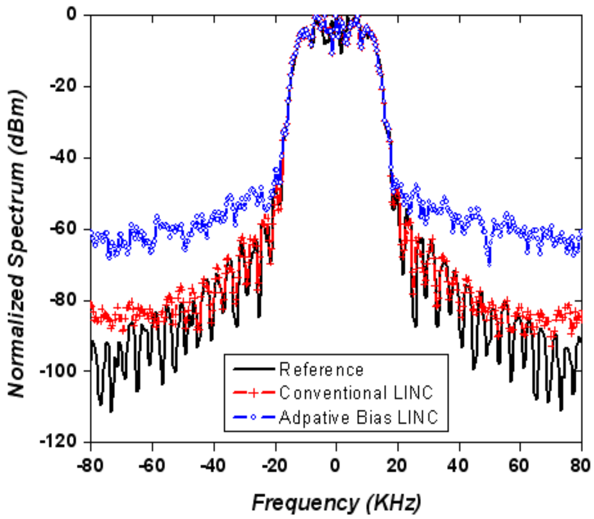

(a)

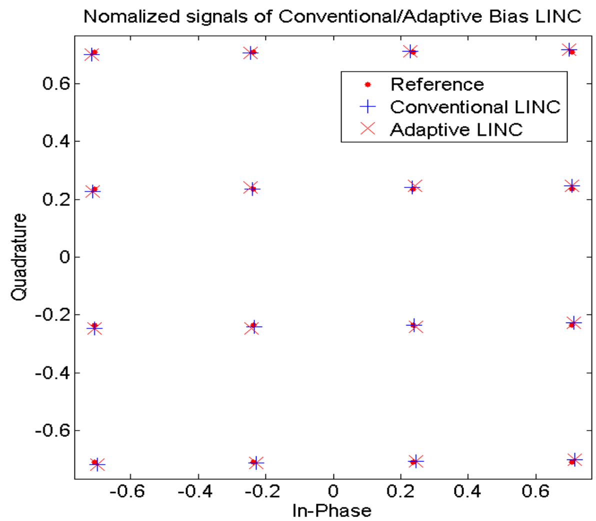

(b)

Figure 6.17 Simulation results: (a) Normalized spectrum; (b) Normalized constellation

6.4 Implementation Concept of the Adaptive Bias LINC Transmitter Consideration

In the following section, we will discuss the practical implementation of our adaptive bias concept. For illustration, a simple sketch of the implementation of the Adaptable Bias LINC transmitter is shown in Figure 6.18. In this illustration, the FPGA stores the voltage-gain and the phase shift of the PAs under different V_{dc} bias conditions at each frequency in a look-up table. The FPGA receives the base band signal and changes the decomposition angle according to the look-up table to produce a smaller combining angle, thus the combining efficiency of the combiner increases. Simultaneously, the FPGA guides the PA bias network in changing the bias with the small delay ($\tau 2$) and sets a delay ($\tau 1$) to the new output decomposition signal for the baseband signal. $\tau 1$ and $\tau 2$ are adjusted during the experiment so that the signal arrives at the PA immediately after the PA's bias has been changed. Subsequently, the new output decomposition signal goes through the same PA chain and produces a lower gain and sustains a higher PA and combiner efficiencies at the same time. For linearity, the adaptive bias scheme is sensitive to any gain and the phase imbalance between the two branches is similar to that of the conventional LINC. This means that the methods proposed by G. M. Hegazi et al. [72], L. Sundstrom et al. [73], and P. Garcia [74] can be applied to further improve the adaptive bias LINC transmitter. Although multilevel biases can improve the whole average efficiency further, it will complicate the power supply and the look-up table, forcing a compromise between the two. Furthermore, power reuse schemes can still be applied to recycle the differential power to improve overall efficiency.

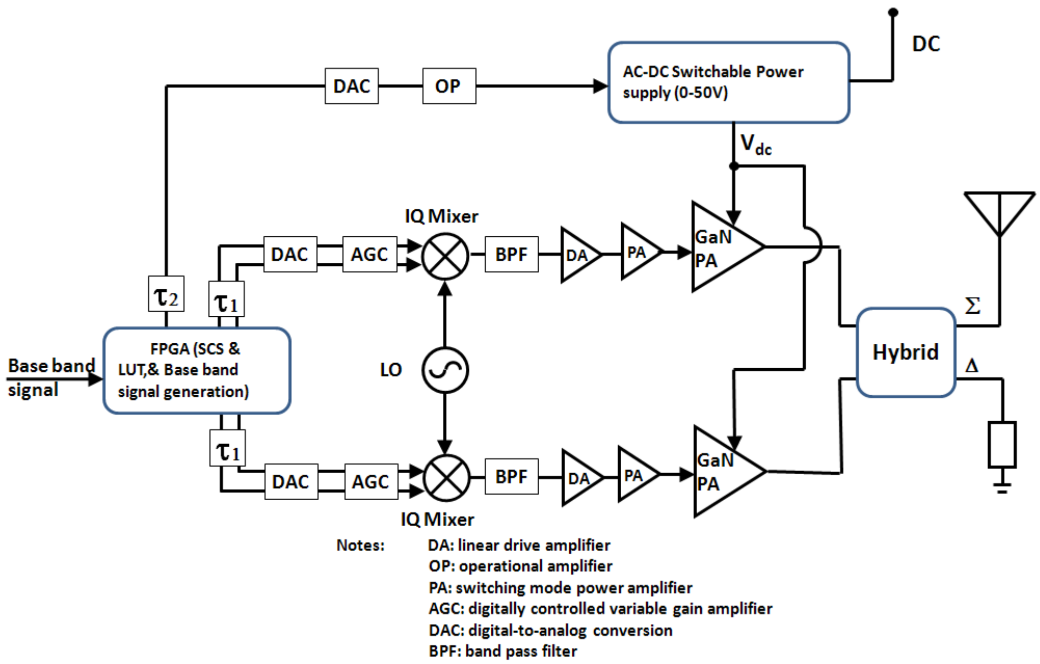

Figure 6.18 Adaptive bias LINC transmitter

6.5 Conclusion

While the LINC transmitter eliminates the need for highly linear power amplifiers, it is still difficult to simultaneously achieve both a high average efficiency and high linearity, especially for high PAR signals. A novel adaptive bias scheme was proposed in this chapter. The scheme employs a SMPA (which can have high efficiency) which can obtain a different voltage gain for diverse DC bias setting while sustaining a relatively high efficiency. High linearity is first achieved with an isolated combiner and the necessary signal processing. Then, efficiency is improved by changing the DC bias of the SMPA based on the combiner, the SMPA, and the input signal properties. While the input power of the SMPA is constant, the multi-level DC bias is determined by the PA's performance. This novel scheme can help improve the average efficiency of a LINC transmitter while sustaining a relatively high linearity.

Chapter 7 Investigation of Low Cost Technologies for Broadband Applications

Broadband technology is exponentially expanding to cover multiple applications. One hurdle is technology fabrication costs. Here, two low-cost alternatives are presented to produce wideband components and antennas. The first alternative, Substrate Integrated Waveguides (SIWs), is a rectangular guide created within a substrate by adding a top metal over the ground plane and caging the structure with rows of plated via-holes on either side. Using SIW technology, the waveguide can be easily integrated with the planar circuit without the high cost of mechanical assemblage. The second alternative, Dielectric image guides (DIG), is also an excellent candidate for developing an alternative low-cost technology for wide band mm-wave applications without expensive precision fabrication. The SIW technology will be discussed in the first section, and then the DIG-based technology will be presented in the second section.

7.1 Substrate Integrated Waveguide (SIW) Technology

7.1.1 Background of SIW technology

Conventionally, metallic waveguides still play an important role in microwave and millimeter wave circuits and systems. The waveguides have advantages of low loss, high Q factor and high power capability, etc. However, they are bulky, heavy, and expensive to fabricate, and it is difficult to integrate microwave and millimeter wave planar circuits with the metallic waveguides. The concept of SIW technology was first proposed in 1992[75]. SIW technology makes it possible to realize the waveguide in the substrate and it provides an elegant way to integrate the waveguide with microwave and millimeter wave planar circuits. Since its inception, a vast range of SIW components, such as filters, antennas, transitions, couplers, power dividers, and oscillators, have been proposed and studied.

SIW structures are fabricated on printed circuit boards with the SIW sidewalls constructed from lined via-holes rather than the solid fences used in conventional metallic waveguides, shown in Figure 7.1. This technology is simple, less expensive than its predecessors, and even renders light structures. S. Yang et al. [76] presented an extensive full parametric study of SIW structures based on a full-wave, 3D analysis using Ansoft HFSS[77]. In this chapter, one Vivaldi antenna array, applying SIW technology, will be used as an example to demonstrate how a low-cost wideband application can be achieved.

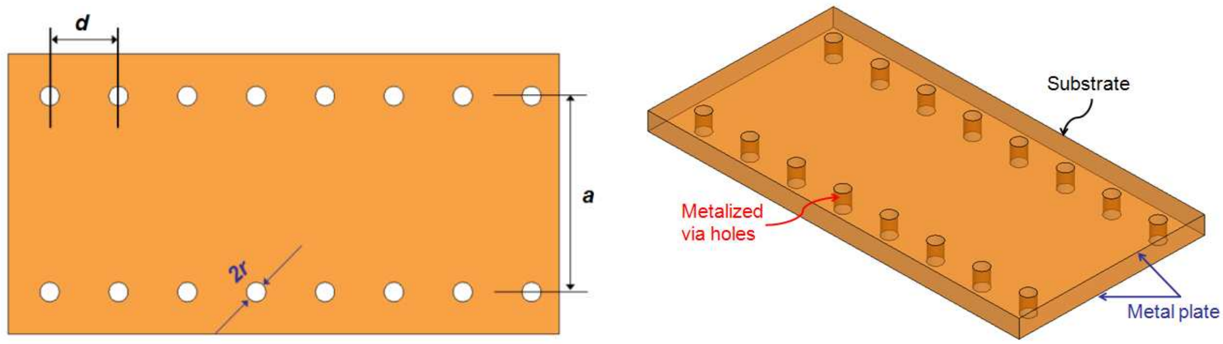

(a) Top view (b) 3D view

Figure 7.1 Substrate integrated waveguide on dielectric substrates

7.1.2 Background of Vivaldi antenna and the state of the art

Ultra-wideband (UWB) antennas are a class of broadband antennas with considerably wide bandwidths. Following is a definition for UWB antennas, according to their impedance bandwidths, communicated by the Federal Communications Commission (FCC). An antenna whose minimum operating frequency is f_L and whose highest operating frequency is f_H can be classified as a UWB antenna if

$$FBW = 2\frac{f_H - f_L}{f_H + f_L} > 0.2 \quad or \quad BW = f_H - f_L > 500MHz \qquad \text{(Eq 7.1)}$$

where FBW is the fractional bandwidth of the antenna.

When compared with conventional narrow-band systems, it is challenging to design an antenna for a UWB system. Therefore, trade-offs are made between wide bandwidth, good input match, compact size, low-cost, high radiation efficiency and minimal dispersion.

Table 7-1 summarizes the characteristics of different UWB antennas. According to Table 7-1, Vivaldi antenna is a good candidate for UWB application. The Vivaldi antenna belongs to the tapered slot antennas (TSA) class. Vivaldi antennas are extremely suitable for UWB antenna applications due to their varied features. These features include a high gain, simple design, narrow beam width in the E-plane, and a relatively wide operating bandwidth. The Vivaldi antennas are excellent candidates for array manufacturing as they do not necessitate wide lateral dimensions [78]. The Vivaldi antenna was used in several UWB applications such as See-Through-Wall Imaging[79], Indoor Localization Systems[80], and Breast Tumor Detection[81]. However, overall performance is generally hindered by the need for a wideband feeding network. The network can cause significant insertion loss.

Here we propose to develop a wideband Vivaldi antenna array utilizing low cost SIW technology. Below are the design challenges:

1) Compact, low loss, wideband feeding network

2) Wideband SIW to the connector transition

3) Wideband Vivaldi antenna

Yang et al. [82] have employed a multitude of the wideband Wilkinson combiners to cover the 8-12 GHz bandwidth based on microstrip technology, but the overall insertion loss was substantially high (over 3.5 dB). Meanwhile, Hao et al. [83]-[84] utilized a SIW binary feed network that showed improved performance, but its 2.5 dB insertion loss is still inadequate for high performance receivers. Yang et al. [85] has developed an efficient SIW feed network, which has led to significant performance improvements. A thicker substrate was used to reduce the conductor loss, and to develop an optimized GCPW feed to the binary SIW structure to improve both the bandwidth and return loss performance. This prevents the excitation of higher order modes normally associated with the use of microstrip lines on thick substrates. The proposed antenna array consists of three parts: (1) an array of eight printed radiating elements (Vivaldi antenna) placed along the axis (2) a feeding network printed on the same dielectric substrate with the radiating elements and (3) a wideband SIW to the connector transition. Design details of the proposed wideband transitions and feeding networks, together with the simulations and experimental results of the fabricated structure, will be presented in the following sections.

Table 7-1 UWB Antenna Characteristics

Type	Bandwidth	Gain	Size	Cost
Crossed Monopole	Wide	Low	Small	Low
Conical	Wide	Medium	Medium	High
Bowtie	Wide	Medium	Small	Low
TEM	Wide	Medium	Bulky	High
Taper Slot (Vivaldi)	Wide	High	Medium	Medium

7.1.3 Design of wideband GCPW to SIW transition

Due to the extreme thickness of the substrate, a GCPW has to be used to prevent excitation of the higher order modes, present if a conventional microstrip line is used. The junction consists of a GCPW whose center conductor and ground are linearly tapered to feed the SIW. In the previous implementation of this transition [86], an SMA connector was utilized and considered for the implementation. However, in this case, due to the use of a thicker substrate to reduce the feed network losses, the employment of conventional SMA connectors at the input feed port would not be practical. Therefore, the GCPW to SIW transition has been re-optimized to include an N-Type connector instead of the SMA, as shown in Figure 7.2a. Due to the larger size of the N-Type, as compared to the substrate height, the whole structure, including the N-Type connector, has to be simulated and optimized. A back-to-back transition was fabricated as shown in Figure 7.2b. The measured results show that the designed transition operates over a bandwidth of 2 GHz with an insertion loss of less than 0.7 dB. This is slightly higher than the simulation results using Ansoft HFSS, shown in Figure 7.2c.

7.1.4 Feeding network

The developed binary feed network construction is based on the extensive use of optimized compact T-junction designs. The T-junction designs were previously developed by Songnan Yang[87] in our team through direct translation from its metallic waveguide version [88, 89] to SIW. In this implementation, an equivalent “a” dimension of SIW has been selected to give a relatively wide bandwidth for a single stage T-junction, as well as an acceptable insertion loss. Next, the spacing between combining stages was judiciously selected to achieve a wideband, compact, 1 to 8 power divider in three stages connected in the cascade. A back-to-back 1 to 8 power divider was fabricated, as shown in Figure 7.3a. The divider is very compact, and its measured back-to-back insertion loss from 7.5 to 8.5 GHz is less than 2.5 dB. This insertion loss is much lower than similar measurements reported by [83, 84]. As mentioned in [86], this kind of SIW feeding network can provide a balanced power division over the wide band. Both the balanced power split and low insertion loss should assist with increasing the gain and overall efficiency of the antenna array. Meanwhile, the use of thick substrates and optimized T-junctions has created an improvement in performance. At the same time, the input port has a commendable return loss over the 7 to 9 GHz frequency range. Figure 7.3b shows the reflection coefficient and the transmission coefficient of the structure shown in Figure 7.3a.

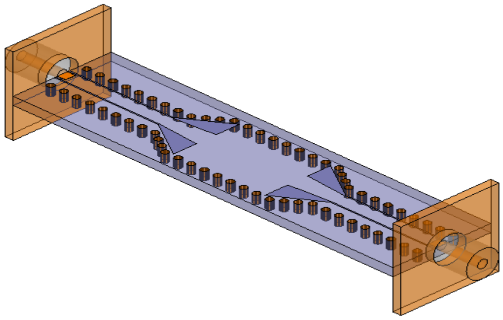

(a)

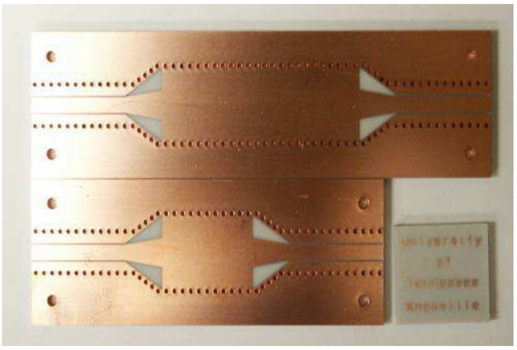

(b)

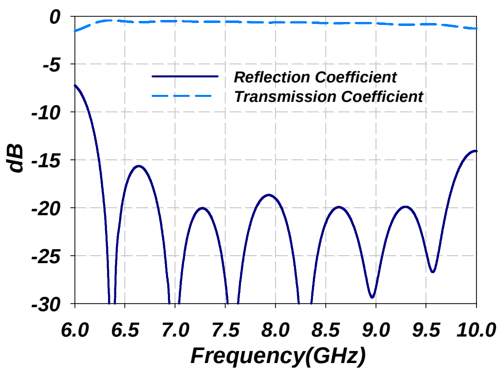

(c)

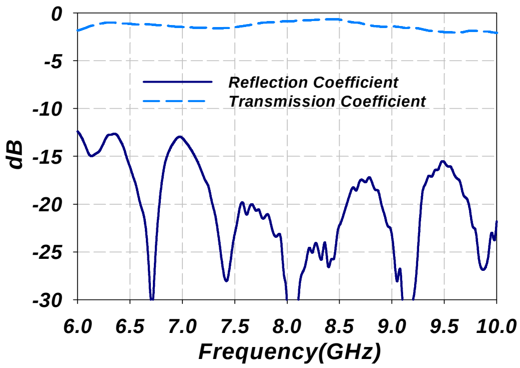

(d)

Figure 7.2 (a) N-Type connector to SIW back to back transitions model in Ansoft HFSS; (b) Manufactured GCPW to SIW back to back transitions; (c) Simulated results; (d) Measured results

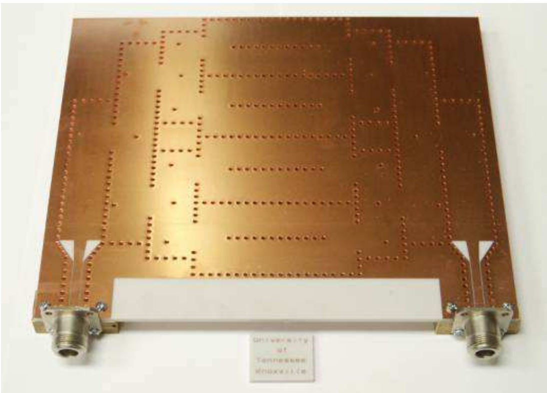

(a)

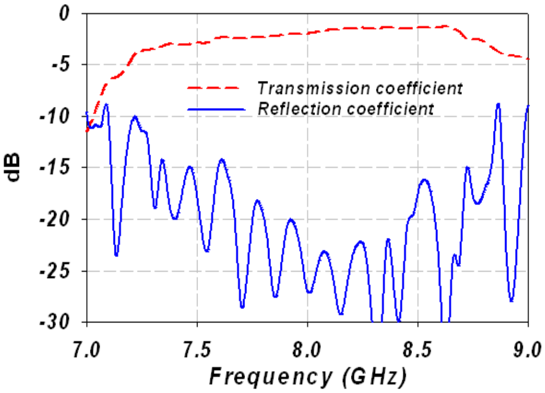

(b)

Figure 7.3 (a) Back-to-back 1 to 8 feeding network; (b) Measured reflection coefficient and the transmission coefficient of the back-to-back 1 to 8 feeding network

7.1.5 *Single antenna element design*

For SIW technology, a number of antennas can be used. Included are H-plane horns, slot antennas, tapered-slot traveling wave antennas, etc. H-plane horns would require very thick substrates in order to achieve a low return loss over a wideband. This would increase the system's overall cost. Slot antennas have the advantage of being small and can be used in a traveling wave array configuration to form a 2D-array. However, the differential phase shift between the elements will change with frequency, causing a beam squint. To have the beam direction constant with frequency, SIW feeding tapered slot antennas have been chosen. The taper can be linear (LTSA), exponential (Vivaldi), elliptical, or constant width (CWTSA)[90]. Linear elements are generally easier to design due to the relatively small number of parameters that need to be optimized. However, the elements need to be long enough to be a good match over a wideband, as described in [84], where an 80 mm taper length was utilized. Instead of using the wideband balun, a SIW has been used to feed a Vivaldi antenna. Two configurations have been investigated (shown in Figure 7.4). For a compact and wide band operation, the taper lengths selected were 27 mm. The first element is a LTSA. The LTSA demonstrated an acceptable return loss, but only covered a narrow band. The second element is an exponentially tapered element, whose taper rate was optimized to obtain a low return loss. Figure 7.5a shows that over a 10 dB return loss can be achieved in simulation. As shown in Figure 7.5b higher gain over wideband can b achieved when using exponentially tapered element. The design detail of the single element is shown in Figure 7.6, with its dimensions shown in Table 7-1. Figure 7.7a shows the fabricated single element Vivaldi antenna. Figure 7.7b indicates the measured return loss of the single element Vivaldi antenna is less than 10 dB over 5.5 to 9 GHz.

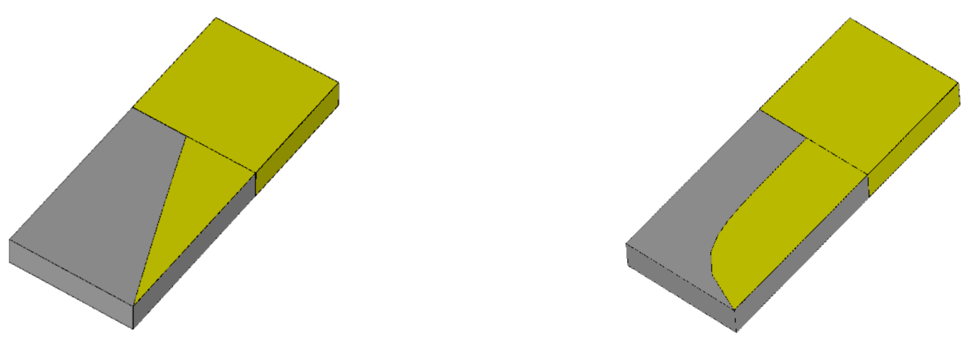

(a) (b)

Figure 7.4 The two investigated elements: (a) Linearly tapered slot antenna; (b) Exponentially tapered slot antenna

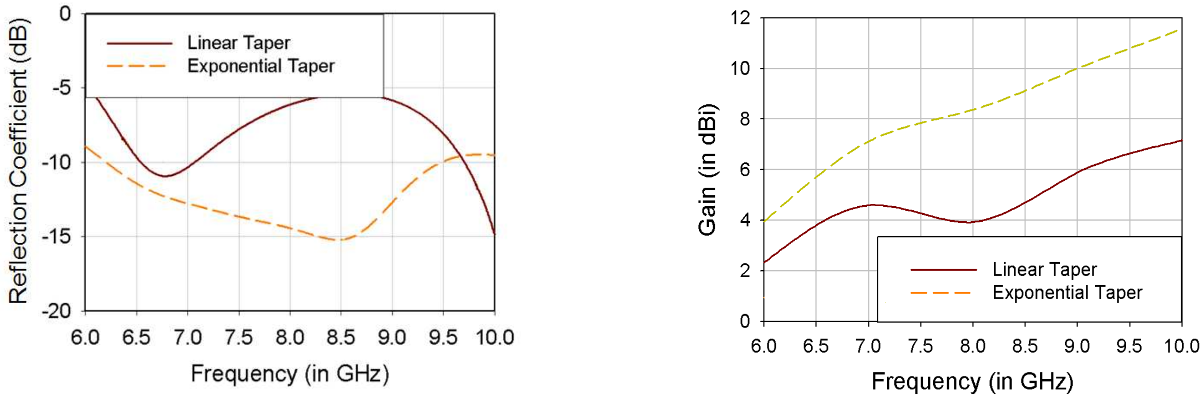

(a) (b)

Figure 7.5 (a) Reflection coefficients of two elements; (b) Gains of the two elements.

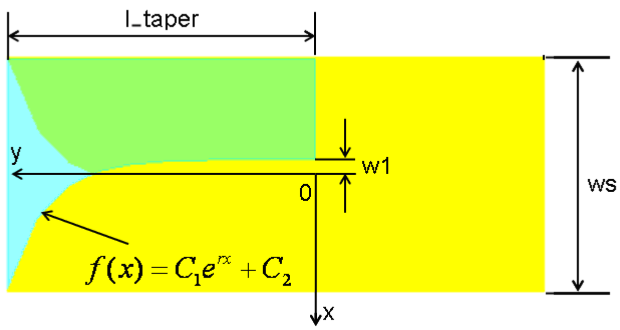

$$C_1 = \frac{(w1 + ws)}{2}(e^{r*l\_taper} - 1)$$

$$C_2 = -\frac{(ws + w1 * e^{r*l\_taper})}{2}(e^{r*l\_taper} - 1)$$

Figure 7.6 Configuration of the proposed antipodal Vivaldi antenna

Table 7-2 Parameters of single element antenna

l_taper (mm)	r	w1(mm)	ws (mm)
27	0.3	1.25	20.5

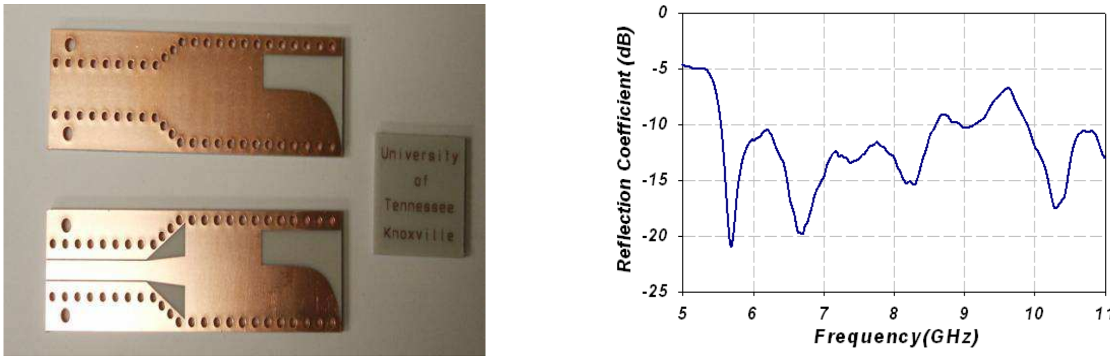

(a) (b)

Figure 7.7 (a) Fabricated single element; (b) Measured reflection coefficient

7.1.6 Eight elements array design

For the design, it is required that the array have a small return loss, high gain, and minimum structure losses (i.e. achieve high radiation efficiency) to reduce the antenna noise temperature and obtain a high G/T ratio. An E-plane uniform distribution has been chosen with a binary feed network to allow a uniform excitation over the required wide- band. The optimum design would be to set the spacing between the elements so that it is ~0.8λ at the highest operating frequency (λ_{min}). No grating lobes would appear over the operating band while achieving the maximum possible gain. Also, the increase in the gain vs. frequency is partially compensated by an increase of the conductor and dielectric losses, which also increases with frequency. This allows a better fidelity over the operating band. Another point to consider in this array design is the mutual coupling between elements which affects the return loss of the single element when placed in an array configuration. Three, five and seven-element arrays have been evaluated to check the mutual coupling between the elements. The three element array structure is shown in Figure 7.8a, as an example. Shown in Figure 7.8b, the mutual coupling shifts the return loss center frequency of the center array element and would require re-tuning. Meanwhile, the mutual coupling from the non-adjacent element is extremely small.

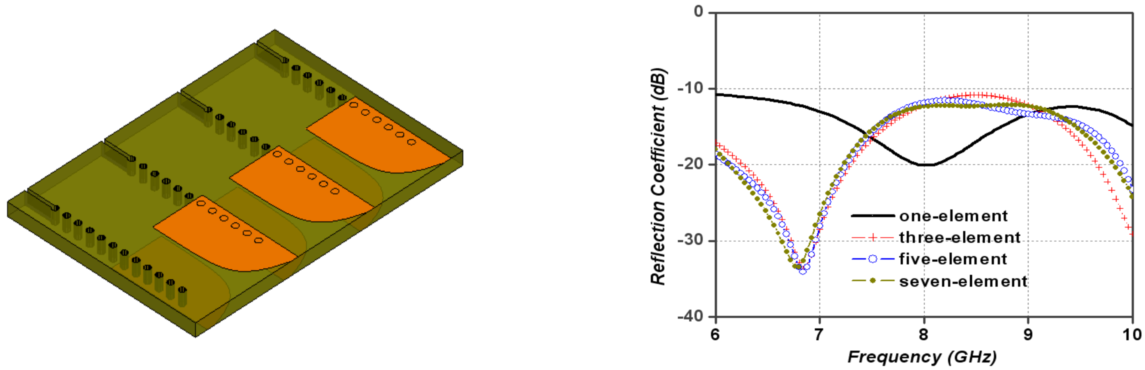

(a) (b)

Figure 7.8 (a) Test structure for the mutual coupling effect; (b) Reflection coefficient of the center element vs. element numbers

The Vivaldi antenna array is designed to operate over a 7 to 9 GHz frequency range. It was printed on a 125mil thick Neltec NY9208 substrate with a dielectric constant of 2.08 and a loss tangent of 0.0006. Figure 7.9 shows the manufactured eight-element Vivaldi array, where eight Vivaldi antenna elements are fed using a SIW structure feeding network.

7.1.7 Array measured results

The measured input return loss and radiation patterns are shown in Figure 7.10a, b & c. The return losses of the array are, for the most part, better than 10 dB over a 2 GHz bandwidth. A gain of 12 dB is sustained over the 2 GHz bandwidth for the eight-element array. The efficiency of the Vivaldi array has exceeded 75% and only utilizes a 7x7 in^2 real-estate area as compared to [82] with a 12x18 in^2 area for a similar gain at its center frequency (10 GHz). Note that the conductor loss has been significantly reduced in this case. The reduction in the radiation efficiency is actually due to the reflection loss rather than conductor loss. Thus, the array G/T ratio has demonstrated significantly improved values as compared to the one previously developed using Wilkinson power dividers [82].

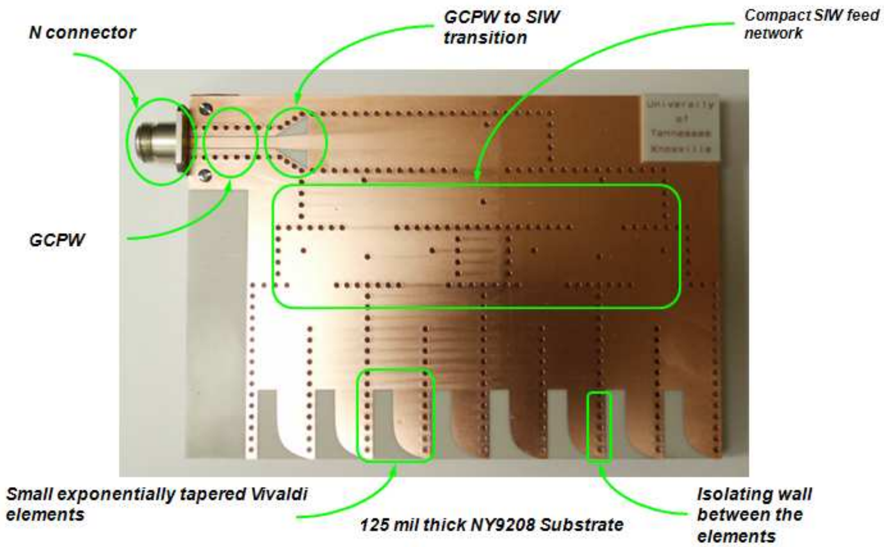

Figure 7.9 Eight elements Vivaldi array

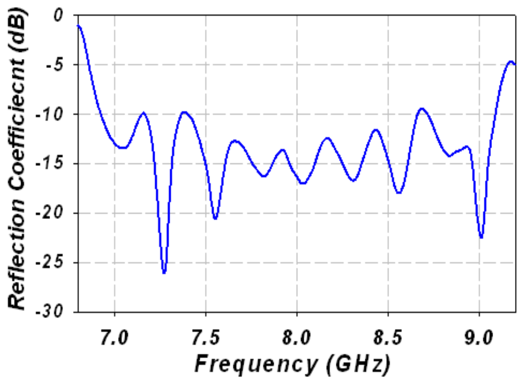

(a)

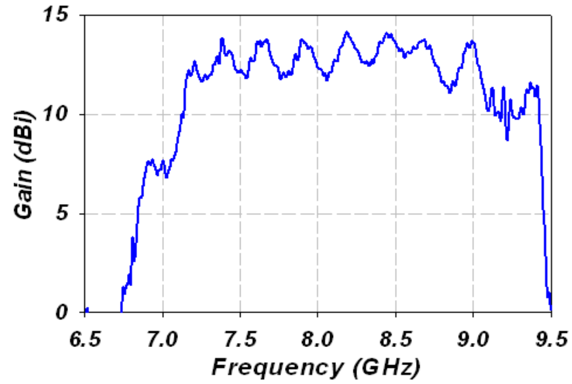

(b)

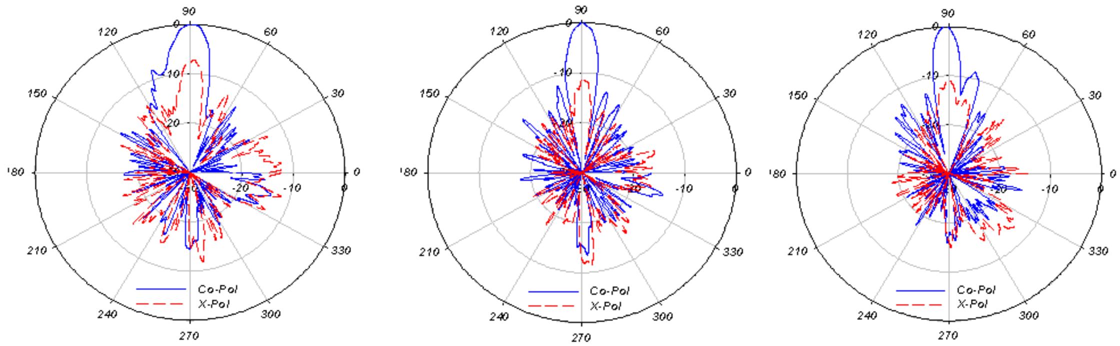

E-Plane

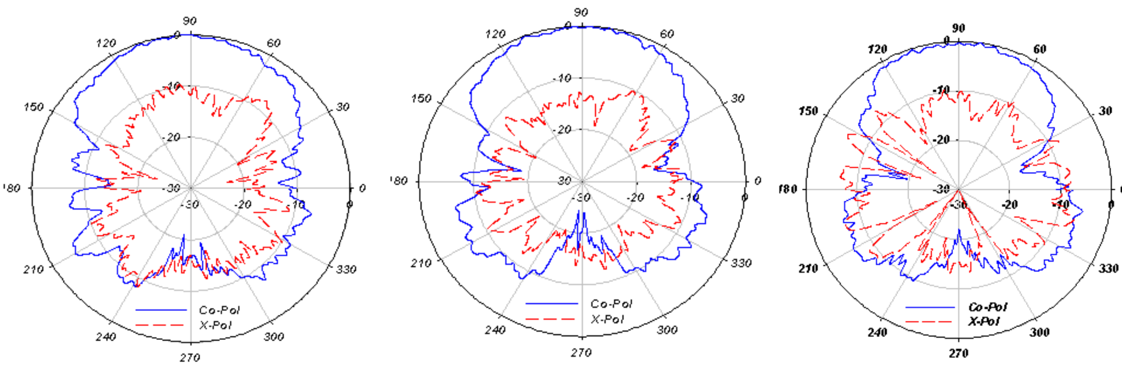

H-Plane

7.2 GHz　　8 GHz　　8.8 GHz

(c)

Figure 7.10 (a) Reflection coefficient of the array; (b) Gain vs. Frequency; (c) Radiation pattern vs. Frequency

7.2 Background of DIG

The Dielectric Image Guide (DIG) lines are excellent candidates for developing low cost alternative technology for millimeter wave applications as shown in Table 7-3. Generally, the lines are utilized to construct a variety of high performance millimeter wave passive circuit and antenna components, and can be enhanced if integrated with dielectric resonators (DRs). DRs can be easily coupled to the DIG lines and both can be produced from a variety of materials including tunable materials such as silicon and ferrite. Silicon, for example, has proven useful in developing optically tunable components (like power dividers, filters, modulators and couplers). Likewise, ferrite materials can be current-controlled and are used to develop circulators and antennas.

The DIG technology has been extensively developed for multiple applications including antennas and their related feed networks. Researchers have already generated a multitude of wide-band transitions and components, but the researcher’s designs are generally based on using a line with a width, ‘a’, larger than its height, ‘b’. Here, we revisit many of these configurations, but present the alternative of using lines with much narrower widths compared to their heights. Instead of using a low dielectric material, our proposed DIG lines are constructed of a high dielectric constant material, which has a similar dielectric constant of that for the DR material. Such alternative geometry/material can lead to a wider transition bandwidth, a larger coupling dynamic range, and a simpler radiating structure. Here, we will describe an alternate wideband metal waveguide-to-dielectric image guide transition first. Then, we will present various types of the recently developed low cost passive structures including low-loss tunable power dividers, wideband circulators, and optically controlled devices (such as variable attenuators). And then we will discuss diverse types of antennas and arrays, including beam forming and end-fire antennas based on the low cost DIG technology.

7.2.1 Wideband metal-waveguide to DIG transition

Efficient, low-loss transitions from conventional metal waveguides to planar dielectric guides of rectangular cross sections has been thoroughly investigated by multiple researchers. The designs developed include a tapered dielectric guide image line inside a conventional waveguide with a flared horn [91]. In this case, the DIG lines were comprised of a low dielectric constant material --- such as Teflon or polyethylene and the transitions were bulky. Subsequently, compact transitions were developed without flared horns or contacts between the metal waveguide and the dielectric guide line like that of Ref.[92]. These compact short transitions required a dielectric guide line tapering too, but have

Table 7-3 Millimeter wave component applications

Application	Sub- millimeter wave Advantages
Secure Communication- For example @ 60 GHz	- Wide band links; - Very compact transceivers; - Attenuation could significantly varies across the band;
Imaging	- Super resolution imaging; - Higher penetration compared to optical frequencies; - Non-harmful to human bodies.
Detection	-Chemical and biological detection using simple spectrometer; - using high Q resonant structures.
Collision avoidance radars	- Compact, light weight, directive antennas; - Simple steering schemes using material parameters control.
Indoor Communication	- Line of sight communication; - Positioning and localization.

undesirable radiation and needed extra support. These requirements make the structures difficult to integrate with other components.

An alternative transition, therefore, has been developed to overcome both the aforementioned bandwidth problem and to simplify the coupling to other lines [93]. The proposed DIG aspect ratio a/b (in this proposed design, a = 0.8 mm; b = 2.2 mm) is less than one, as shown in Figure 7.11, and is compared to conventional transitions with a/b >1. The transition was fabricated using a dielectric rod made of alumina with a dielectric constant of 9.8. Its performance was theoretically and experimentally evaluated, as shown in Figure 7.12. A typical back-to-back Ka-band transition was fabricated using a 60-mm long dielectric image guide with a 10 mm linear taper at both the input and output sides of the transition. Its measured results indicate an insertion loss of less than one dB over the 26-35GHz frequency range. This is equivalent to a bandwidth of over 25%. The Ansoft HFSS simulation results deviate slightly from the measurement results, but can be used as a good reference point for the design.

7.2.2 DIG circuit components

A variety of circuit components using the newly developed DIG transition have been developed to estimate the various features of the image guide line. Features include ease of construction and low leakage and reflections due to any bends or inhomogeneities in the line. The guided wavelength of the DIG line is determined by its dielectric constant and dimensions, namely, the a/b ratio. The guided wavelength along the DIG line for the fundamental mode for a<b (ε_r =9.8, a=0.8 mm and b=2.2 mm) was calculated based on Ref [94]. The wavelength is less than that of the a>b case (ε_r =9.8, a=2.2 mm and b=0.8 mm), as shown in Figure 7.13a. The newly proposed DIG (with dimensions a<b) provides convenient coupling to other components in close proximity, such as other DIG lines and dielectric or ferrite pucks. DRs are used as the basic building blocks for a variety of circuit components. Examples are shown in Table 7-4, and a brief summary of the components will be presented in the following subsections.

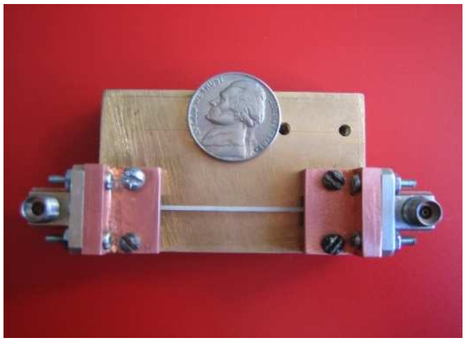

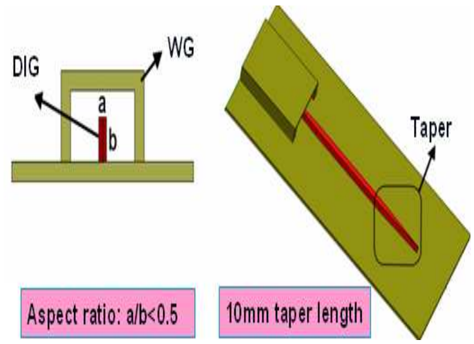

(a) (b)

Figure 7.11 Metal waveguide to DIG transition: (a) Fabricated test fixture; (b) Schematic

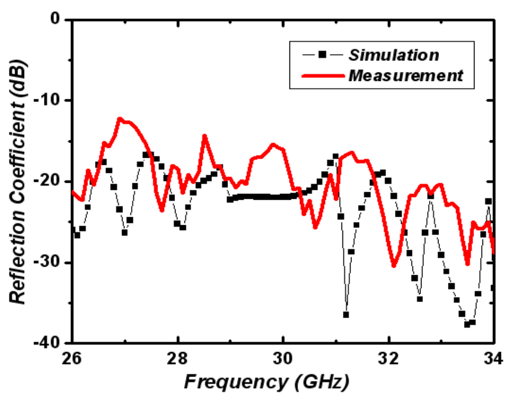

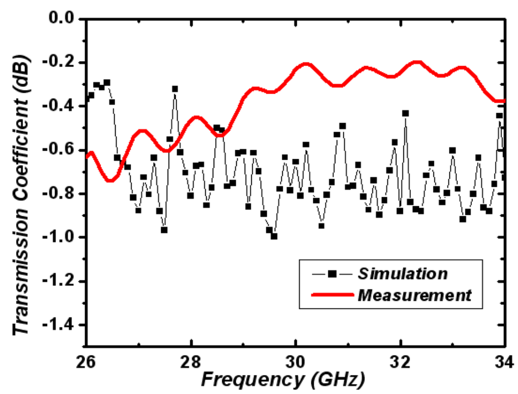

(a) (b)

Figure 7.12 Simulated and measured: (a) Reflection Coefficient; (b) Transmission Coefficient

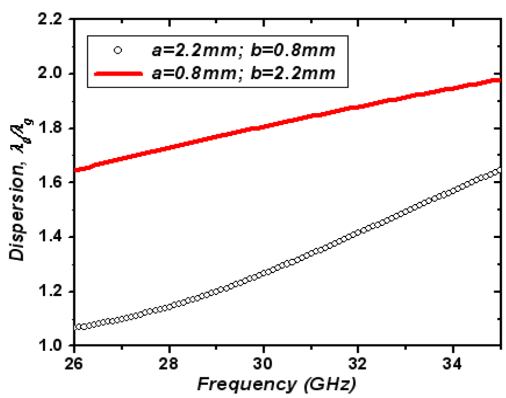

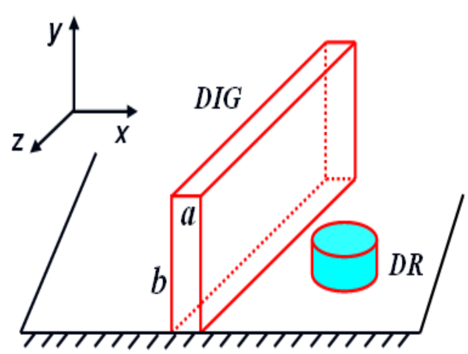

(a) (b)

Figure 7.13 (a) Dispersion of conventional and flipped DIGs; (b) DIG lines and dielectric puck placement

Table 7-4 Dielectric resonator modes and applications

Dielectric Resonator Mode	Applications	Comments
TE, TM, or hybrid mode	Wideband circulator and dielectric resonator antenna array	Small radius to height ratio, operates over a wide band, radiation degrades their Q's. Partially metalized pucks can be used to minimize their radiation.
Whispering Gallery mode	High performance filters and multiplexers	Large radius to height ratio, low radiation loss, extremely high Q's [95]

7.2.3 Tunable attenuators

Typically, a resistive card or sheet can be placed on the surface of a DIG line to build an attenuator. The attenuation level is a function of the card size and resistivity [96]. To build a tunable attenuator, as an extension of this concept, a semi-metallic plasma layer can be excited on the surface of a semiconductor material when optically illuminated using an LED [97]. By applying an IR irradiation, more free carriers are generated which can lead to a conductivity increase and subsequently, its insertion loss.

A tunable attenuator was fabricated. The attenuator is comprised of two parts: a low-loss alumina dielectric rod section that is bolted to a small silicon section, shown in Figure 7.14a. Without optical illumination, there is a minimal mismatch loss due to the close values of the dielectric constants. Meanwhile, under IR illumination, a 10 dB additional attenuation can be seen in Figure 7.14b, but the use of the longer wavelength irradiation, or more intensive illumination, will further increase the materials' bulk conductivity, causing larger attenuation levels. Three-level attenuation has been experimentally demonstrated by applying varying strengths of IR illumination. This performance, for example, is suitable for phased-array antenna applications that need to have amplitude control for beam forming.

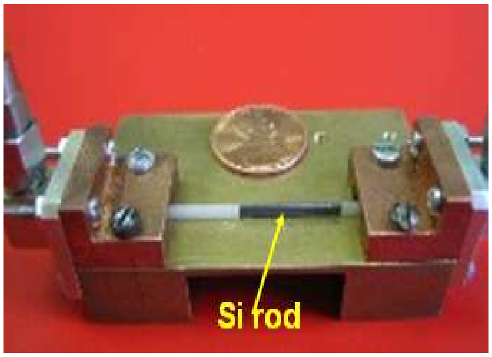

(a)

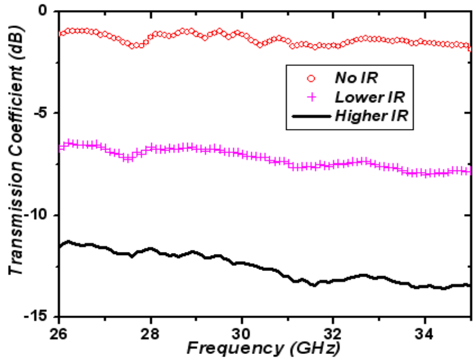

(b)

Figure 7.14 Optical controlled attenuators: (a) Fabricated attenuator; (b) Measured results

7.2.4 DIG antennas

DIG lines too are employed to build both antennas and their feeds. Various types of antennas can be designed including dielectric resonator arrays (DRAs), leaky waves and end-fire antennas. Additionally, beam forming can be accomplished upon tuning the DRs if constructed of a semiconductor material. In the following section, we demonstrate several of these applications.

- Antenna Feeds

Dielectric resonator antennas have been used in millimeter wave frequencies for many years. DR antennas have several advantages over microstrip patch antennas. The advantages include a smaller size, higher radiation efficiency, wider bandwidth, and no excitation of surface waves [98]. Various feed structures for the DRAs that have been previously investigated include microstrips, DIG lines, probes and slot apertures [93, 99-101]. The probe and slot aperture feeds are usually for narrow band applications. However, microstrip lines are typically used below X-band frequencies, as at millimeter wave frequencies losses become excessive and surface modes can be excited. Subsequently, DIG lines should be more suitable as their losses are significantly lower [102].

Conventionally, DIG lines (with dimensions a>b) have been used to feed DRs. For example, Wyville et al used DIG line to feed truncated DIG elements[103]. Here we utilize DIG lines with an a<b cross section to provide a wider coupling dynamic range. The lowest order mode of the DIG line is the E_{y11} mode, and it has dominant E_y, E_z, and H_x components, as shown in Figure 7.13b. Meanwhile, the DRA has a main radiating magnetic dipole mode that can be excited by the DIG, namely $TE_{0\gamma\delta}$. This mode has a large H_γ component and overlaps well with the E_{y11} mode of the DIG line. Subsequently, in designing a

dielectric resonator antenna array, both the DR diameter and spacing can be adjusted to optimize the antenna performance.

We have performed extensive parametric studies using Ansoft HFSS for a full EM analysis. The coupling analysis study between the DIG and the DRA is similar to that presented in [104] but for a/b <0.5. The analysis was conducted with an alumina rod of a=0.8 mm, b=2.2 mm, ε_r= 9.8, and a Si DR with a diameter =2.6 mm and height =1.5 mm and ε_r=11.2. Figure 7.15a illustrates the effect of the spacing between the DIG line and the DR on both its resonant frequency and coupling coefficient. Meanwhile, Figure 7.15b displays how the resonant frequency is very sensitive to the DR puck's height.

In addition, we investigated the use of different types of materials for fabricating the DRs to provide additional functionality. For example, for silicon or GaAs pucks, optical control can be used to control coupling to the DIG line, and for ferrites, a magnetic control can be used to control resonant frequencies. To have a more significant effect, it would be necessary to strongly irradiate those DRs to completely decouple them, i.e. substantially lower the Q's as they will act as parasitic elements even with relatively low Q's. The simulation results of a ten-element array with / without an IR and a 5-element array are shown in Figure 7.17. In the simulation, we simply set a higher loss tangent of the DR to model the IR illumination effects. While applying the IR to the first five elements (from the feed), the gain drops from 16.4 to 15.1, and the 3-dB beam width increase from 9^0 to 15^0 (the 5-element array has a gain of 14.7 dB and the 3-dB beam width is 15^0). The IR effect is much more significant than is demonstrated in Figure 7.16. For beam forming applications, the concept can be easily extended to include adjusting the coupling of the various DR elements of the array to conform to a given current distribution, such as Taylor or Chebyshev distribution by an IR illumination instead of physically varying the distance between the DR and the main line.

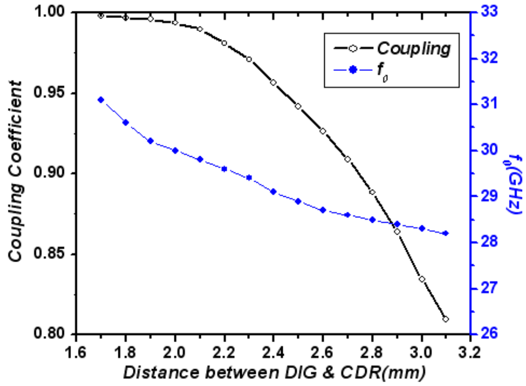

(a)

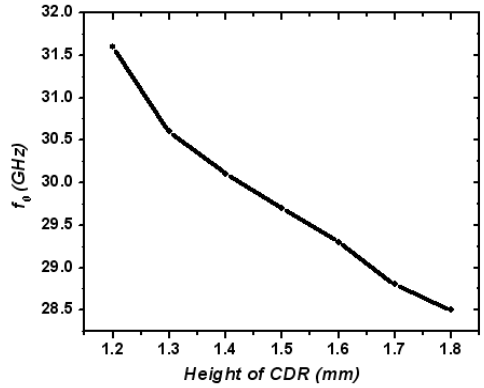

(b)

Figure 7.15 Parameters study: (a) Coupling and resonant frequency vs. distance between the DIG and CDR; (b) Resonant frequency vs. height of the CDR

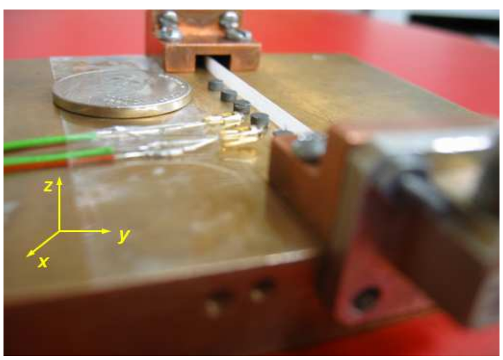

(a)

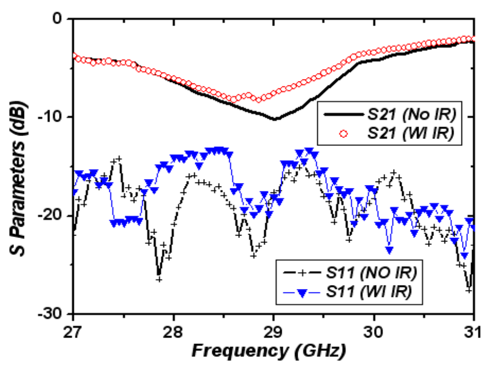

(b)

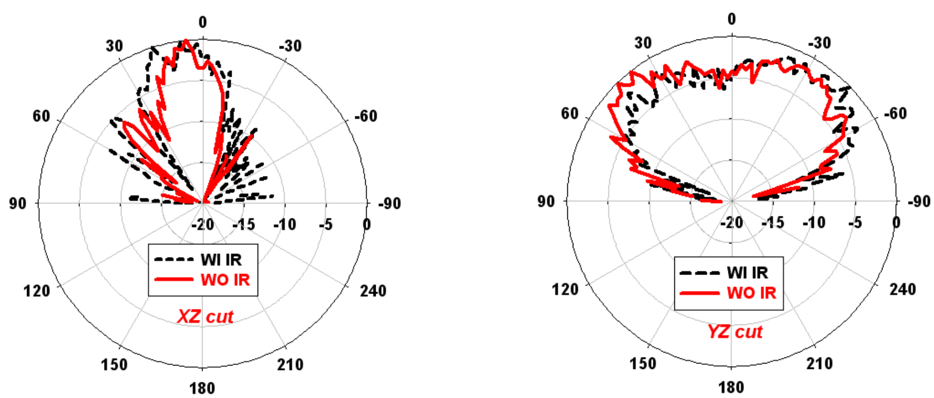

(c)

Figure 7.16 Optically controlled array: (a) Si resonator antenna array; (b) S parameters of the array; (c) Radiation patterns with/without IR illumination

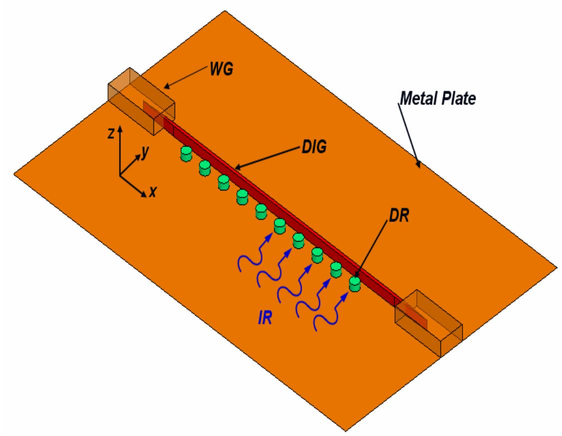

(a)

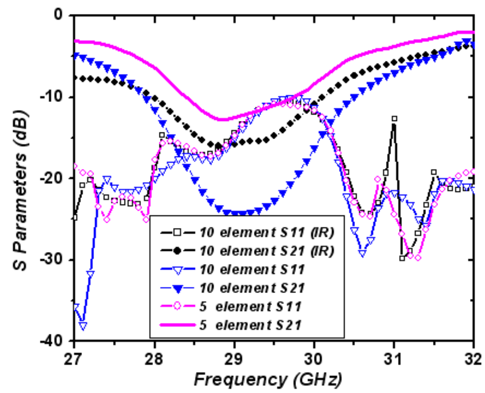

(b)

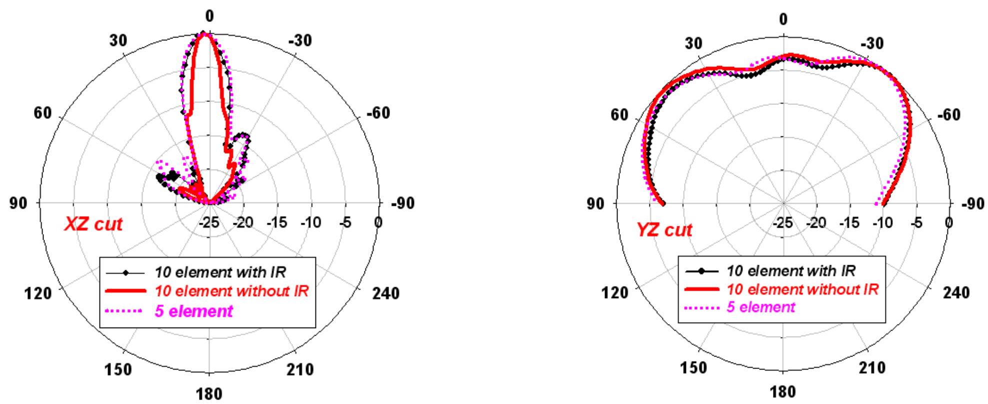

(c)

Figure 7.17 Optically controlled array: (a) 10-element Si resonator linear array; (b) Simulated S parameters; (c) Simulated radiation pattern with/without IR illumination

- End-fire Antenna

Tapered dielectric rod is a surface-wave low-cost simple antenna structure. The antennas are good directional radiators in the end-fire direction and can be utilized for various applications, including short-range point-to-point wireless communications. The radiation of the tapered dielectric rod antenna generally occurs along the tapered portion of the dielectric rod, increasing its effective aperture and subsequently, its gain over a wider frequency range. The presence of the ground plane increases its gain and acts as a support for the dielectric rod. To demonstrate, we fabricated an antenna made of alumina with ε_r=9.8 and tanδ=0.0003. The fabricated antenna is shown in Figure 7.18a. Meanwhile, Figure 7.18b shows the simulated and measured reflection coefficient, while Figure 7.18c compares the simulated and measured H-plane radiation patterns at three different frequencies. The measured gain is higher than 13 dBi over a 26 to 33 GHz frequency range. The discrepancy shown between the simulated and measured results is primarily due to the rods' fabrication low-tech tolerances.

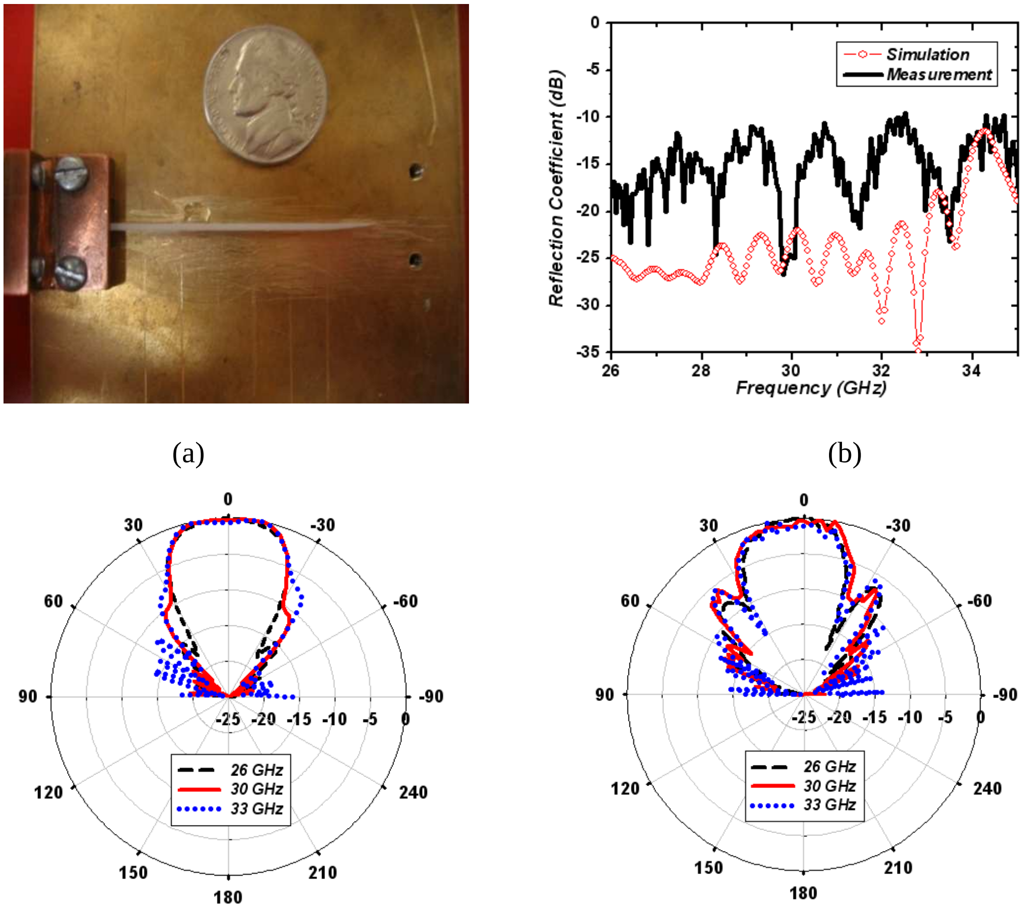

(a) (b)

(c)

Figure 7.18 End-fire antenna: (a) Fabricated end-fire antenna; (b) Simulated and measured reflection coefficients; (c) Simulated and measured radiation pattern

7.2.5 *Conclusion*

In the search for a low-cost technology to enhance the wide spread use of wideband technology, SIW proved to be a viable alternative. SIW technology is simple, less expensive, and renders light structures. Here, we have demonstrated its use via the development of a Vivaldi antenna array. The array feeds operate over a wideband with a lower insertion loss compared to previously developed feeds using microstrip lines. In our implementation, the SIW structure was optimally designed, and fabricated on a thick substrate to minimize conductor losses. The array employs a SIW binary divider to minimize the insertion loss of the feeding network. It has a common Grounded Coplanar Waveguide (GCPW) feed to sustain a satisfactory input match while preventing higher order modes excitation over a wide frequency range. The use of optimized T-junctions, and the integration of a GCPW feed, has also led to an even more improved performance with a significant loss reduction. The developed Vivaldi antenna array, which has high gain, narrow beam width in the E-plane & H-plane, and relatively wide bandwidth, is extremely useful for ultra wideband antenna applications such as See-Through-Wall Imaging, Indoor Localization Systems, and Breast Tumor Detection. Here, the Vivaldi antenna array design can easily be scaled to an mm-wave. SIW technology would be inordinately useful at mm-wave frequencies by achieving relatively high performance while remaining a low-cost alternative to micro-machining.

Another alternative for low cost mm-wave wide band components is the dielectric image guide; DIG is an excellent candidate for the development of a variety of millimeter and sub-millimeter wave components. Dielectric image guide line technology is a low fabrication cost technology when compared to micromachining. The use of a high dielectric constant image guide (with the dimension $a<b$) makes it easier to couple the guides to alumina, silicon, GaAs, and ferrite dielectric resonators, thus initiating a new set of applications. For example, high resistivity silicon is sensitive to IR illumination, while ferrite resonators can be controlled by DC magnetic fields. Low-loss power divider operations can be achieved using higher order WG modes. The development of image guide lines and corresponding power splitting structures allows the eventuation of 1D and 2D antenna arrays. Additionally, electronic tuning of the dielectric resonators can be employed to develop multi-functional DRA arrays for various beam forming antenna applications.

Chapter 8 Conclusion

In the following chapter, we briefly summarize our overall vision of this exciting field of research. Varying highlights will be given in areas we believe should be revisited in the near future to complement our findings.

8.1 Concluding Remarks

- There is an immediate need for RF/Microwave/Millimeter wave front-ends operating over wide bandwidths and at higher frequencies.
- Many applications, such as software defined radio and fourth generation “4G” converged wireless service RF front-ends, could benefit from these high power and efficient broadband amplifiers.
- High power applications can significantly benefit from the recent advancements of GaN HEMT devices. GaN HEMTs have a higher power density and a superior thermal and high breakdown voltage when compared to silicon LDMOS FETs and GaAs MESFETs of similar output power.
- GaN HEMT devices have small parasitic capacitances and large input/load impedances. They exhibit a broader bandwidth than the bandwidths demonstrated by other technologies.
- GaN HEMTs, under a class AB biasing, can be used for broadband feedback and use distributed power amplifier topologies to achieve a high power, wide band, while sustaining a high degree of linearity. Such designs can significantly benefit from the utilization of more accurate, large signal nonlinear device modeling.
- For high efficiency, switching power amplifiers, like the D/E/F modes, are more suitable for achieving high efficiency. Multiple narrow band switching mode PAs have been developed that are switched to toggle between wide bands. However, it is believed they can be replaced by one wide band, highly efficient PA with only switchable output filter banks or a reconfigurable filter.
- In many applications, since both linearity and efficiency are important to the PA design, various linearization and efficiency enhancements techniques can be utilized. The LINC approach has been useful in producing high power and high efficiency over a wide band while sustaining a high degree of linearity.
- In modern digital communication systems, various modulation schemes have been utilized to achieve a high spectrum efficiency. However, these signals are characterized by high peak-to-average power ratios (PAPRs), which exploit deep envelope fluctuations. Although the high efficiency and relatively

high linearity can be achieved at the peak power level, it is still difficult to achieve a high average efficiency for a high PAPRs signal.

- Novel schemes are required to address signals with high PAPRs. Schemes, such as the adaptive bias LINC, have been proposed and should be investigated further. The adaptive bias LINC scheme is independent of frequency, which increases its potential to work in wideband applications.
- Implementing the adaptive bias LINC scheme is still challenging. The challenges include how to design a high speed, switchable DC power supply, how to control the time delay to avoid the drain bias switching effect, and how to trade the number of DC levels to increase overall efficiency.
- More efficient, wide band combining techniques are needed, especially at the VHF/UHF frequencies. Multiple basic components, like low loss wide band transmission line ferrite transformers, need to be developed. Special techniques, such as flux cancelling, can help reduce ferrite cores' nonlinearities.

8.2 Areas Which Need to Be Revisited:

1) Synthetic design of wide band combiners based on advanced functional techniques.
2) Implementation of the proposed adaptive bias LINC scheme.
3) Pursuit of more accurate large signal nonlinear device modeling.
4) Investigation of other PA topologies for the LINC transmitter, including classes E and F in order to enhance efficiency.
5) Apply the developed hybrid designs to MMIC circuitries to reduce parasitic and push frequency performance even wider.

Bibliography

[1] B. S. Virdee, A. S. Virdee, and B. Y. Banyamin, *Broadband Microwave Amplifiers*. Norwood, MA: Artech House, 2004.
[2] D. Cox and R. Leck, "Component Signal Separation and Recombination for Linear Amplification with Nonlinear Components," *Communications, IEEE Transactions on*, vol. 23, pp. 1281-1287, 1975.
[3] R. Negra and F. M. Ghannouchi, "Switching-mode power amplifiers and their aplications in advanced wireless communication transmitters," in *IEEE Radio and Wireless Symposium*, 2008.
[4] S. C. Cripps, *RF Power Amplifiers for Wireless Communication*. Norwood, MA: Artech House, 2006.
[5] F. H. Raab, P. Asbeck, S. Cripps, P. B. Kenington, Z. B. Popovic, N. Pothecary, J. F. Sevic, and N. O. Sokal, "RF and Microwave Power Amplifier and Transmitter Technologyies--- Part1," *High Frequecny Electronics*, May 2003.
[6] "http://www.gainmicrowave.com/gallium_nitride_overview.php."
[7] S. Marsh, *Practical MMIC Design*: Artech House October 2006.
[8] Aethercomm, "Gallium Nitride HEMTs for High Efficiecny Power Amplifiers," May 2007.
[9] K. B. Niclas, "Reflective Match, Lossy Match, Feedback and Distributed Amplifiers: A Comparison of Multi-Octave Performance Characteristics," in *Microwave Symposium Digest, MTT-S International*, 1984, pp. 215-217.
[10] K. B. Niclas, W. T. Wilser, R. B. Gold, and W. R. Hitchens, "The Matched Feedback Amplifier: Ultrawide-Band Microwave Amplification with GaAs MESFET's," *Microwave Theory and Techniques, IEEE Transactions on*, vol. 28, pp. 285-294, 1980.
[11] "http://news.soft32.com/fujitsu%E2%80%99s-technology-for-gallium-nitride-hemt_4558.html."
[12] R. Borges, "Gallium nitride electronic devices for high-power wireless applications," www.rfdesign.com, Sep. 2001.
[13] I.D.Robertson and S.Lucyszyn, "RFIC and MMIC design and technology," London, United Kingdom: The Institution of Electrical Engineers, 2001.
[14] Y. Chung, S. Cai, W. Lee, Y. Lin, C. P. Wen, K. L. Wang, and T. Itoh, "High power wideband AlGaN/GaN HEMT feedback amplifier module with drain and feedback loop inductances," *Electronics Letters*, vol. 37, pp. 1199-1200, 2001.
[15] A. Sayed, S. von der Mark, and G. Boeck, "An ultra wideband 5 W power amplifier using SiC MESFETs," in *Microwave Conference, 2004. 34th European*, 2004, pp. 57-60.
[16] K. W. Kobayashi, C. Yao Chung, I. Smorchkova, R. Tsai, M. Wojtowicz, and A. Oki, "A 2 Watt, Sub-dB Noise Figure GaN MMIC LNA-PA Amplifier with Multi-octave Bandwidth from 0.2-8 GHz," in *Microwave Symposium, 2007. IEEE/MTT-S International*, 2007, pp. 619-622.
[17] H. J. Siweris, T. Grave, and W. Kellner, "Ultrawide Bandwidth Monolithic HEMT Feedback Amplifier," in *European Microwave Conference, 1998. 28th*, 1998, pp. 654-659.
[18] K. Karthikeyan, V. Ramakrishna, S. Keller, U. Mishra, M. J. W. Rodwell, and S. I. Long, "Broadband GaAs MESFET and GaN HEMT resistive feedback power amplifiers," *Solid-State Circuits, IEEE Journal of*, vol. 35, pp. 1285-1292, 2000.
[19] R. S. Pengelly, *Microwave Field-effect Transistors---Theory,Design and Applications*: Research Studies Press, 2005.
[20] W. R. Curtice and R. L. Camisa, "Self-Consistent GaAs FET Models for Amplifier Design and Device Diagnostics," *Microwave Theory and Techniques, IEEE Transactions on*, vol. 32, pp. 1573-1578, 1984.
[21] Y. Ayasli, S. W. Miller, R. Mozzi, and L. K. Hanes, "Capacitively Coupled Traveling-Wave Power Amplifier," *Microwave Theory and Techniques, IEEE Transactions on*, vol. 32, pp. 1704-1709, 1984.
[22] E. L. Ginzton, W. R. Hewlett, J. H. Jasberg, and J. D. Noe, "Distributed amplification," 1948, pp. 956-969.

[23] R. W. Chick, "Non-uniformly distributed power amplifier," US No. 5, 485,118, 1996.
[24] T. Y. Wong, *Fundamentals of Distributed Amplification*: Artech House, 1993.
[25] Microwave Office 2007, AWR Inc.
[26] A. Pavio and C. Xie, "GaN Devices Arm Distributed Amplifier," *Microwave&RF Magazine*, Feb 2008.
[27] Z. Lei, A. Pavio, and W. Thompson, "A 1 watt, 3.2 VDC, high efficiency distributed power PHEMT amplifier fabricated using LTCC technology," in *Microwave Symposium Digest, 2003 IEEE MTT-S International*, 2003, pp. 2201-2204 vol.3.
[28] Z. Lei, A. Pavio, B. Stengel, and B. Thompson, "A 6 watt LDMOS broadband high efficiency distributed power amplifier fabricated using LTCC technology," in *Microwave Symposium Digest, 2002 IEEE MTT-S International*, 2002, pp. 897-900.
[29] T. TeikSiew, M. F. Ain, and S. I. S. Hassan, "Large Signal Design of Distributed Power Amplifier with Discrete RF MOSFET Devices," in *RF and Microwave Conference, 2006. RFM 2006. International*, 2006, pp. 58-61.
[30] J. P. Fraysse, J. P. Viaud, M. Campovecchio, P. Auxemery, and R. Quere, "A 2 W, high efficiency, 2-8 GHz, cascode HBT MMIC power distributed amplifier," in *Microwave Symposium Digest., 2000 IEEE MTT-S International*, 2000, pp. 529-532 vol.1.
[31] J. B. Beyer, S. N. Prasad, R. C. Becker, J. E. Nordman, and G. K. Hohenwarter, "MESFET Distributed Amplifier Design Guidelines," *Microwave Theory and Techniques, IEEE Transactions on*, vol. 32, pp. 268-275, 1984.
[32] C. Duperrier, M. Campovecchio, L. Roussel, M. Lajugie, and R. Quere, "New design method of uniform and nonuniform distributed power amplifiers," *Microwave Theory and Techniques, IEEE Transactions on*, vol. 49, pp. 2494-2500, 2001.
[33] P. Gamand, "Analysis of the oscillation conditions in distributed amplifiers," *Microwave Theory and Techniques, IEEE Transactions on*, vol. 37, pp. 637-640, 1989.
[34] C. Campbell and S. Brown, "Modified S-Probe Circuit Element for Stability Analysis."
[35] F. H. Raab, P. Asbeck, S. Cripps, P. B. Kenington, Z. B. Popovic, N. Pothecary, J. F. Sevic, and N. O. Sokal, "Power amplifiers and transmitters for RF and microwave," *Microwave Theory and Techniques, IEEE Transactions on*, vol. 50, pp. 814-826, 2002.
[36] H. Chireix, "High power outphasing modulation," in *Proc.IRE*, Nov.1935, pp. 1370-1392.
[37] D. Cox, "Linear Amplification with Nonlinear Components," *Communications, IEEE Transactions on*, vol. 22, pp. 1942-1945, 1974.
[38] W. Gerhard and R. Knoechel, "LINC Digital Component Separator for multicarrier W-CDMA-signals," in *Microwave Symposium Digest, 2004 IEEE MTT-S International*, 2004, pp. 907-910 Vol.2.
[39] B. Shi and L. Sundstrom, "A LINC transmitter using a new signal component separator architecture," in *Vehicular Technology Conference Proceedings, 2000. VTC 2000-Spring Tokyo. 2000 IEEE 51st*, 2000, pp. 1909-1913 vol.3.
[40] X. Zhang, L. E. Larson, and P. M. Asbeck, *Design of Linear RF Outphasing Power Amplifiers*: Artech House 2003.
[41] J. Grundlingh, K. Parker, and G. Rabjohn, "A high efficiency Chireix out-phasing power amplifier for 5GHz WLAN applications," in *Microwave Symposium Digest, 2004 IEEE MTT-S International*, 2004, pp. 1535-1538 Vol.3.
[42] G. Hegazi, T. Chu, S. Heibel, J. Jordan, and H. Sasmazer, "Linear Wideband VHF/UHF Quad LINC Transmitter System," in *Military Communications Conference, 2007. MILCOM 2007. IEEE*, 2007, pp. 1-6.
[43] M. Helaoui, S. Boumaiza, F. M. Ghannouchi, A. B. Kouki, and A. Ghazel, "A New Mode-Multiplexing LINC Architecture to Boost the Efficiency of WiMAX Up-Link Transmitters," *Microwave Theory and Techniques, IEEE Transactions on*, vol. 55, pp. 248-253, 2007.

[44] C. Yuan-Chuan, J. Kai-Yuan, W. An-Yeu, T. Hen-Wai, and T. Bosen, "Multilevel LINC System Design for Wireless Transmitters," in *VLSI Design, Automation and Test, 2007. VLSI-DAT 2007. International Symposium on*, 2007, pp. 1-4.
[45] G. Poitau and A. Kouki, "MILC: Modified Implementation of the LINC Concept," in *Microwave Symposium Digest, 2006. IEEE MTT-S International*, 2006, pp. 1883-1886.
[46] W. Young Yun, Y. Jaehyok, Y. Youngoo, and K. Bumman, "SDR transmitter based on LINC amplifier with bias control," in *Microwave Symposium Digest, 2003 IEEE MTT-S International*, 2003, pp. 1703-1706 vol.3.
[47] G. Jian, "An enhanced linear amplification with non-linear component (ELINC) system," in *Radio and Wireless Conference, 2002. RAWCON 2002. IEEE*, 2002, pp. 173-176.
[48] R. Langridge, T. Thornton, P. M. Asbeck, and L. E. Larson, "A power re-use technique for improved efficiency of outphasing microwave power amplifiers," *Microwave Theory and Techniques, IEEE Transactions on,* vol. 47, pp. 1467-1470, 1999.
[49] A. Birafane and A. B. Kouki, "On the linearity and efficiency of outphasing microwave amplifiers," *Microwave Theory and Techniques, IEEE Transactions on,* vol. 52, pp. 1702-1708, 2004.
[50] Agilent (ADS) Design Guide, version: ADS2006A.
[51] A. G. N. O. Sokal, *Switch mode RF Power Amplifiers*: Newnes, 2007.
[52] P. J. Baxandall, "Transistor Sinewave Oscillators," in *Proc.IEE*, London, May, 1959, pp. 748-758.
[53] G. Hegazi, T. Chu, D. Abbey, J. Jordan, D. Callister, J. Ghylin, S. Heibel, G. Krug, S. Lin, and A. Fathy, "Wideband VHF/UHF Quadrature LINC Power Amplifier System," in *Gomac Tech*, March 2007.
[54] A. Long, Y. Jingshi, and S. I. Long, "A 13 W current mode class D high efficiency 1 GHz power amplifier," in *Circuits and Systems, 2002. MWSCAS-2002. The 2002 45th Midwest Symposium on*, 2002, pp. I-33-6 vol.1.
[55] K. Ji-Yeon, H. Dong-Hoon, K. Jong-Heon, and S. P. Stapleton, "A 50 W LDMOS current mode 1800 MHz class-D power amplifier," in *Microwave Symposium Digest, 2005 IEEE MTT-S International*, 2005, p. 4 pp.
[56] H.Nemati, "Design, Implementation and Evaluation of a Current-Mode Class-D Power Amplifier," Chalmers University of Technology, 2006.
[57] H. Kobayashi, J. M. Hinrichs, and P. M. Asbeck, "Current-mode class-D power amplifiers for high-efficiency RF applications," *Microwave Theory and Techniques, IEEE Transactions on,* vol. 49, pp. 2480-2485, 2001.
[58] F. H. Raab, M. Gladu, and D. Rupp, "A 100-W Class-D Power Amplifier for LF and MF," 2006.
[59] U. Gustavsson, "Design of An Inverse Class D Amplifier Using GaN-HEMT Technology." vol. MSc: Örebro University, 2006.
[60] M. Albulet, *RF Power Amplifiers*: Noble Publishing Assoicates, Jan, 2001.
[61] Y. Jingshi and S. I. Long, "Power Amplifier Selection for LINC Applications," *Circuits and Systems II: Express Briefs, IEEE Transactions on,* vol. 53, pp. 763-767, 2006.
[62] G. Gonzales, *Microwave Transistor Amplifiers*, Second ed.: Prentice-Hall, 1997.
[63] "Multi-Hole Wide Band Cores," Ferronics Inc. Application Notes.
[64] J. Sevick, *Transmission Line Transformer*. Atlanta, GA: Noble Publishing, 2001.
[65] CST Microwave Studio, version 2006.
[66] D. Myer, "Synthesis of Equal Delay Transmission Line Transformer Networks," *Microwave Journal*, March,1992.
[67] R. L. Edwards and B. L. Martin, "Wideband Transmission Line Signal Combiner/Divider," US Patent 4774481, Sep. 1988.

[68] Z. Xuejun, L. E. Larson, P. M. Asbeck, and R. A. Langridge, "Analysis of power recycling techniques for RF and microwave outphasing power amplifiers," *Circuits and Systems II: Analog and Digital Signal Processing, IEEE Transactions on*, vol. 49, pp. 312-320, 2002.

[69] C. P. Conradi, R. H. Johnston, and J. G. McRory, "Evaluation of a lossless combiner in a LINC transmitter," in *Electrical and Computer Engineering, 1999 IEEE Canadian Conference on*, 1999, pp. 105-110 vol.1.

[70] M. K. Simon and M.-S. Alouini, *Digital Communication over Fading Channels (2nd Edition)*: John Wiley & Sons, 2005.

[71] "Investigation of Transmit Spectra for Motorola's iDEN Radio System," www.braddye.com/iDENSpectraV1.2.pdf.

[72] G. M. Hegazi, T. T. Chu, and R. A. Groshong, "Improved LINC power transmission using a quadrature outphasing technique," in *Microwave Symposium Digest, 2005 IEEE MTT-S International*, 2005, p. 4 pp.

[73] L. Sundstrom, "Automatic adjustment of gain and phase imbalances in LINC transmitters," *Electronics Letters*, vol. 31, pp. 155-156, 1995.

[74] P. Garcia, J. de Mingo, A. Valdovinos, and A. Ortega, "An adaptive digital method of imbalances cancellation in LINC transmitters," *Vehicular Technology, IEEE Transactions on*, vol. 54, pp. 879-888, 2005.

[75] H.Furuyama, Japanese Patent (H4-220881), July,1992.

[76] S. Yang and A. E. Fathy, "Development of a Slotted Substrate Integrated Waveguide (SIW) Array Antennas for Mobile DBS Application " in *Antenna Applications Symposium*, IL, 2006, pp. 101-131.

[77] Ansoft HFSS(ANSYS Inc), version 10.

[78] K. Sang-Gyu and C. Kai, "A low cross-polarized antipodal Vivaldi antenna array for wideband operation," in *Antennas and Propagation Society International Symposium, 2004. IEEE*, 2004, pp. 2269-2272 Vol.3.

[79] Y. Yang and A. Fathy, "Design and Implementation of a Low-Cost Real-Time Ultra-Wide Band See-Through-Wall Imaging Radar System," in *Microwave Symposium, 2007. IEEE/MTT-S International*, 2007, pp. 1467-1470.

[80] M. R. Mahfouz, Z. Cemin, B. C. Merkl, M. J. Kuhn, and A. E. Fathy, "Investigation of High-Accuracy Indoor 3-D Positioning Using UWB Technology," *Microwave Theory and Techniques, IEEE Transactions on*, vol. 56, pp. 1316-1330, 2008.

[81] S. Salvador and G. Vecchi, "On some experiments with UWB microwave imaging for breast cancer detection," in *Antennas and Propagation Society International Symposium, 2007 IEEE*, 2007, pp. 253-256.

[82] Y. Yang, C. Zhang, S. Lin, and A. E. Fathy, "Development of an ultra wideband Vivaldi antenna array," in *Antennas and Propagation Society International Symposium, 2005 IEEE*, 2005, pp. 606-609 Vol. 1A.

[83] H. ZhangCheng, H. Wei, L. Hao, Z. Hua, and W. Ke, "Multiway broadband substrate integrated waveguide (SIW) power divider," in *Antennas and Propagation Society International Symposium, 2005 IEEE*, 2005, pp. 639-642 Vol. 1A.

[84] H. ZhangCheng, H. Wei, C. Ji Xin, C. Xiao Ping, and W. Ke, "A novel feeding technique for antipodal linearly tapered slot antenna array," in *Microwave Symposium Digest, 2005 IEEE MTT-S International*, 2005, p. 3 pp.

[85] S. Yang and A. E. Fathy, "Synthesis of an Arbitrary Power Split Ratio Divider Using Substrate Integrated Waveguides," in *Microwave Symposium, 2007. IEEE/MTT-S International*, 2007, pp. 427-430.

[86] S. Yang, E. Adel., S. Lin, A. E. Fathy, A. Kamel, and H. Elhennawy, "A highly efficient Vivaldi antenna array design on thick substrate and fed by SIW structure with integrated GCPW feed," in *Antennas and Propagation Society International Symposium, 2007 IEEE*, 2007, pp. 1985-1988.

[87] S. H. S. S. Yang, and A. E. Fathy, "Development of a Slotted Substrate Integrated Waveguide (SIW) Array Antennas for Mobile DBS Applications," in *Proc. Antennas Applications. Symp.* Montecello, IL, Sep. 2006.

[88] J. H. T. Takahashi, M, Ando and N, Goto, "A single-layer power divider for a slotted waveguide array using π-junction with an inductive wall," *IEICE Trans. Commun.*, vol. E79-B, no. 1, pp. 57-62, Jan. 1996.

[89] J. H. K. Fukazawa, M, Ando and N, Goto, "Two-way power divider for partially parallel feed in single layer slotted waveguide arrays," *IEICE Trans. Commun.*, vol. E81-B, no. 6, pp. 1248-1253, June. 1998.

[90] D. Schaubert, E. Kollberg, T. Korzeniowski, T. Thungren, J. Johansson, and K. Yngvesson, "Endfire tapered slot antennas on dielectric substrates," *Antennas and Propagation, IEEE Transactions on*, vol. 33, pp. 1392-1400, 1985.

[91] T. N. Trinh, J. A. G. Malherbe, and R. Mittra, "A Metal-to-Dielectric Waveguide Transition with Application to Millimeter-Wave Integrated Circuits," in *Microwave Symposium Digest, 1980 MTT-S International*, 1980, pp. 205-207.

[92] D. Lioubtchenko, Tretyakov, S., Dudorov, S., *Millimeter-wave Waveguides*: Springer, 2003.

[93] S. Lin, G. Suren, J. Wilson, and A. E. Fathy, "Novel Ka-band IR Controlled Dielectric Image Guide Components," in *Microwave Symposium Digest, 2006. IEEE MTT-S International*, 2006, pp. 1389-1392.

[94] V. K. e. a. Varadan, "Electronically steerable leaky wave antenna using a tunable ferroelectric material," *Smart Materials & Structures*,1994 - iop.org.

[95] D. Cros and P. Guillon, "Whispering gallery dielectric resonator modes for <e1>W</e1>-band devices," *Microwave Theory and Techniques, IEEE Transactions on*, vol. 38, pp. 1667-1674, 1990.

[96] D. D. King, "Circuit Components in Dielectric Image Lines," *Microwave Theory and Techniques, IRE Transactions on*, vol. 3, pp. 35-39, 1955.

[97] P. Blondy, D. Cros, P. Guillon, F. Balleras, and C. Massit, "W band silicon dielectric resonator for semiconductor substrate characterization," in *Microwave Symposium Digest, 1998 IEEE MTT-S International*, 1998, pp. 1349-1352 vol.3.

[98] K. M. Luk and K. W. Leung, "Dielectric Resonator Antennas," in *Research Studies Press Ltd, 2003*.

[99] M. Saed, Yadla, R., "Microstrip-fed low profile and compact dielectric resonator antennas," *Progress In Electromagnetics Research*, vol. *PIER* 56, pp. 151-162, 2006.

[100] A. A. Kishk, A. Ittipiboon, Y. M. M. Antar, and M. Cuhaci, "Slot excitation of the dielectric disk radiator," *Antennas and Propagation, IEEE Transactions on*, vol. 43, pp. 198-201, 1995.

[101] A. Al-Zoubi, A. Kishk, and A. W. Glisson, "Analysis of Aperture Coupled Dielectric Resonator Antenna Fed by Dielectric Image Line," in *Antennas and Propagation Society International Symposium 2006, IEEE*, 2006, pp. 2519-2522.

[102] T. Hori and T. Itanami, "Circularly Polarized Linear Array Antenna Using a Dielectric Image Line," *Microwave Theory and Techniques, IEEE Transactions on*, vol. 29, pp. 967-970, 1981.

[103] M. W. Wyville, A. Petosa, and J. S. Wight, "DIG feed for DRA arrays," in *Antennas and Propagation Society International Symposium, 2005 IEEE*, 2005, pp. 176-179 vol. 2A.

[104] F. Farzaneh, P. Guillon, and Y. Garault, "Coupling Between a Dielectric Image Guide and a Dielectric Resonator," in *Microwave Symposium Digest, MTT-S International*, 1984, pp. 115-117.

Appendices

Appendix A

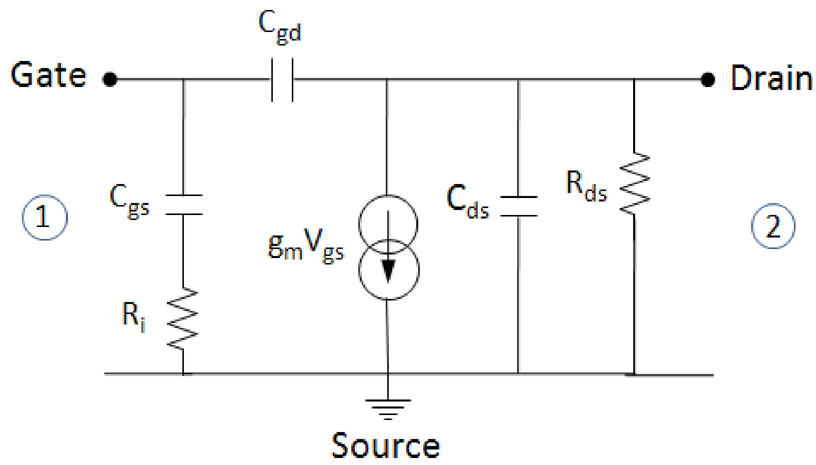

Figure A1. 7-element small signal FET model [1]

By the definition of Y-parameter, the admittance matrix for the two port network can be presented as:

$$\begin{bmatrix} I_1 \\ I_2 \end{bmatrix} = \begin{bmatrix} Y_{11} & Y_{12} \\ Y_{21} & Y_{22} \end{bmatrix} \begin{bmatrix} V_1 \\ V_2 \end{bmatrix};$$

And the parameters shown in Figure A1 can be calculated from the measured Y matrices [1]

$$C_{gd} = -\mathrm{Im}(Y_{12}) / \omega;$$

$$C_{gs} = \frac{\mathrm{Im}(Y_{11}) - \omega C_{gd}}{\omega} \left\{ 1 + \frac{[\mathrm{Re}(Y_{11})]^2}{[\mathrm{Im}(Y_{11}) - \omega C_{gd}]^2} \right\}$$

$$R_i = \left[\mathrm{Re}(Y_{11})\right] / \left\{ [\mathrm{Im}(Y_{11}) - \omega C_{gd}]^2 + \mathrm{Re}(Y_{11})^2 \right\}$$

$$g_m = \sqrt{[\mathrm{Re}(Y_{12})]^2 + [\mathrm{Im}(Y_{11}) - \omega C_{gd}]^2 [1 + \omega^2 C_{gs}^2 R_i^2]}$$

$$\tau = (1/\omega) \sin^{-1} \left\{ [-\omega C_{gd} - \mathrm{Im}(Y_{21}) - \mathrm{Re}(Y_{21}) \omega C_{gs} R_i] / g_m \right\}$$

$$C_{ds} = \left[\mathrm{Im}(Y_{22}) - \omega C_{gd} \right] / \omega$$

$$R_{ds} = 1 / \mathrm{Re}(Y_{22})$$

To illustrate the effect of the feedback resistor effects, the model presented in Figure A1 is simplified. The FET with resistive negative feedback circuit model is shown in Figure A2.

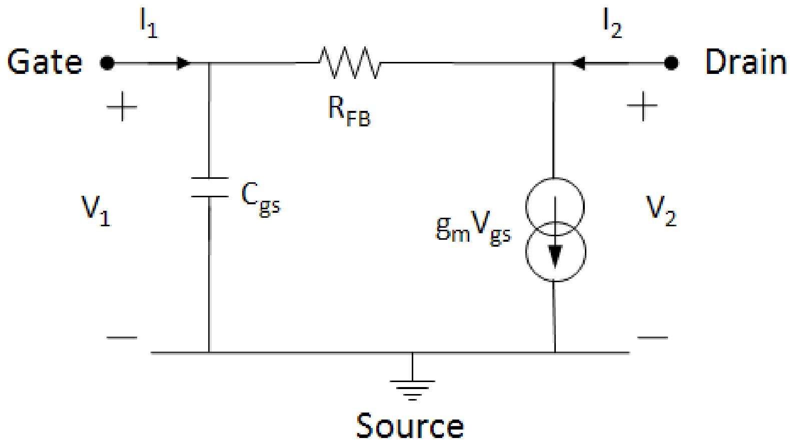

Figure A2. FET feedback equivalent circuit

$$\begin{bmatrix} I_1 \\ I_2 \end{bmatrix} = \begin{bmatrix} \frac{1}{R_{FB}} & -\frac{1}{R_{FB}} \\ g_m - \frac{1}{R_{FB}} & \frac{1}{R_{FB}} \end{bmatrix} \begin{bmatrix} V_1 \\ V_2 \end{bmatrix}$$

$$S_{11} = S_{22} = \frac{R_{FB} - g_m Z_0^2}{g_m Z_0^2 + 2Z_0 + R_{FB}}$$

$$S_{12} = \frac{2Z_0}{g_m Z_0^2 + 2Z_0 + R_{FB}}$$

$$S_{21} = \frac{2Z_0 - 2g_m Z_0 R_{FB}}{g_m Z_0^2 + 2Z_0 + R_{FB}}$$

Z_0 is the characteristic impedance, which equals 50 Ω here.

For a perfect matched input/output, the S_{11}=S_{22}=0, then:

$$R_{FB} = g_m Z_0^2;$$

$$G = S_{21} = 1 - \frac{R_{FB}}{Z_0};$$

From above equations, we can see that the gain of the resistive negative feedback amplifier depends on R_{FB}, not on the other S-Parameters. Therefore, the gain flatness can be achieved over a wideband with this resistive negative feedback.

Appendix B

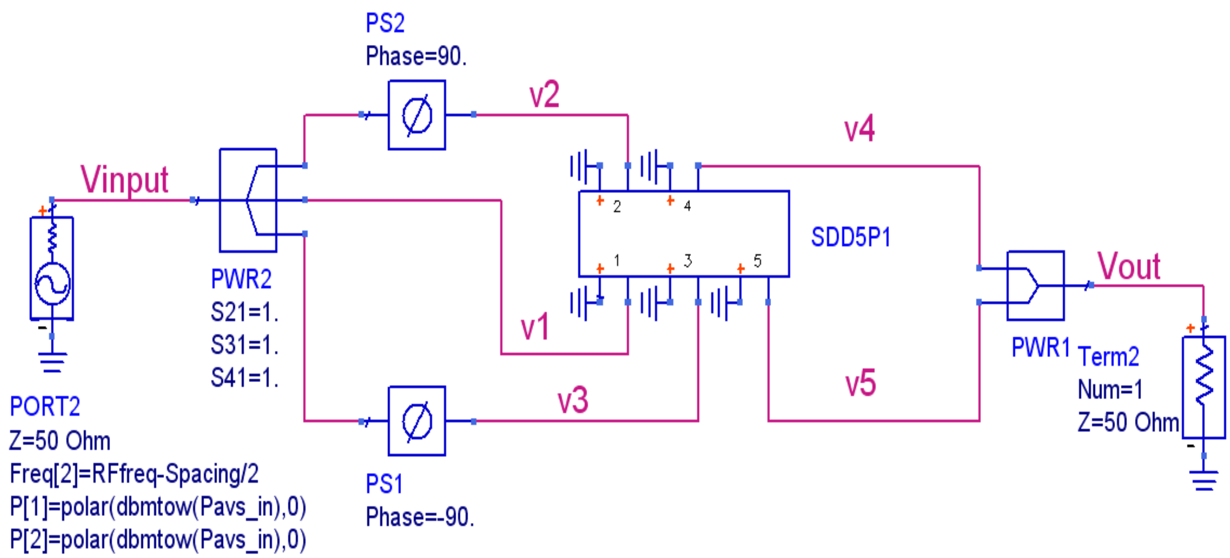

Figure B1. Simplified LINC transmitter

A complex representation of the band-limited source signal can be written as:

$$s(t) = r(t)e^{j\theta(t)} \; ; \; 0 \le r(t) \le r_{\max} \; ;$$

$$S_1(t) = s(t) - e(t)\,; \; S_2(t) = s(t) + e(t)\,; \;\; e(t) = js(t)\sqrt{\frac{r_{\max}^2}{r^2(t)} - 1}$$

Here we use sine wave (with a variable envelop) @ f_0, as examples to verify the concept shown in Figure B1.

$$v1(t) = \cos(2\pi f_1 t) + \cos(2\pi f_2 t)$$

$$v2(t) = \cos(2\pi f_1 t + 90^0) + \cos(2\pi f_2 t + 90^0) = 2\cos(2\pi \frac{f_1 + f_2}{2} t + 90^0)\cos(2\pi \frac{f_1 - f_2}{2} t)$$

$$= -2\cos(2\pi f_{env} t)\sin(2\pi f_0 t)$$

$$v3(t) = \cos(2\pi f_1 t - 90^0) + \cos(2\pi f_2 t - 90^0) = 2\cos(2\pi \frac{f_1 + f_2}{2} t - 90^0)\cos(2\pi \frac{f_1 - f_2}{2} t)$$

$$= 2\cos(2\pi f_{env} t)\sin(2\pi f_0 t)$$

$$v4(t) = v1(t) + v2(t)\sqrt{\frac{1}{\cos(2\pi f_{env}t)^2} - 1} = 2\cos(2\pi f_{env}t)\cos(2\pi f_0 t) -$$

$$2\cos(2\pi f_{env}t)\sin(2\pi f_0 t)\frac{\sin(2\pi f_{env}t)}{\cos(2\pi f_{env}t)} = 2\cos(2\pi f_{env}t)\cos(2\pi f_0 t) - 2\sin(2\pi f_{env}t)\sin(2\pi f_0 t)$$

$$= 2\cos(2\pi f_0 t + 2\pi f_{env}t)$$

$$v5(t) = v1(t) + v3(t)\sqrt{\frac{1}{\cos(2\pi f_{env}t)^2} - 1} = 2\cos(2\pi f_{env}t)\cos(2\pi f_0 t) +$$

$$2\cos(2\pi f_{env}t)\sin(2\pi f_0 t)\frac{\sin(2\pi f_{env}t)}{\cos(2\pi f_{env}t)} = 2\cos(2\pi f_{env}t)\cos(2\pi f_0 t) +$$

$$2\sin(2\pi f_{env}t)\sin(2\pi f_0 t) = 2\cos(2\pi f_0 t - 2\pi f_{env}t)$$

$$vout(t) = v4(t) + v5(t) = 4\cos(2\pi f_{env}t)\cos(2\pi f_0 t)$$

$f_1 = f_0 + f_{env}$; $f_2 = f_0 - f_{env}$, f_0 is the carrier frequency; f_{env} is the envelop frequency;

So here the v4 and v5 are constant envelop signals.

Appendix C

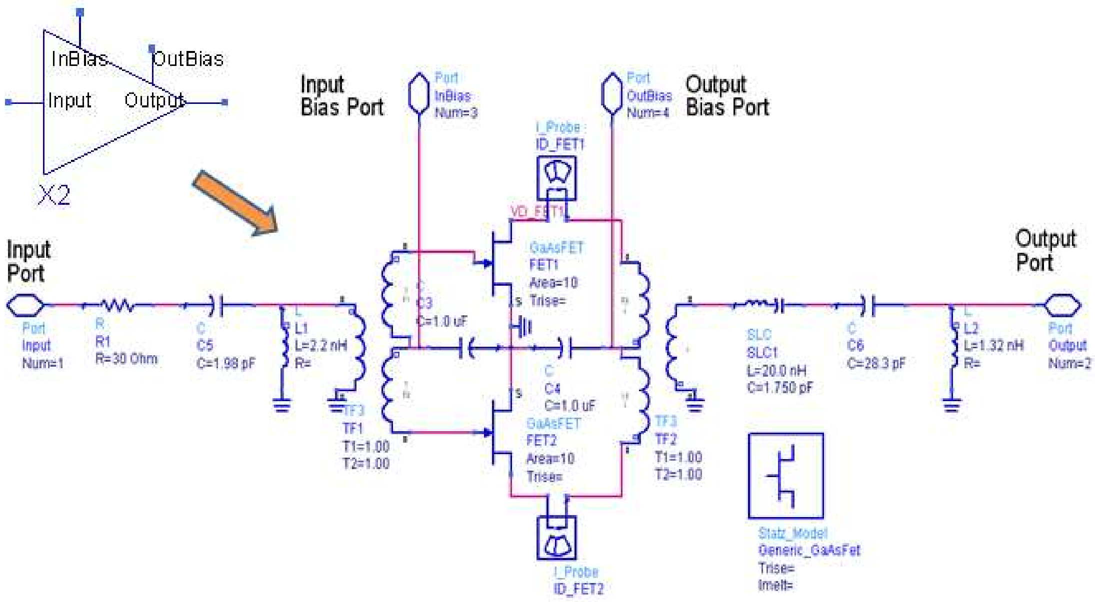

Figure C1. Narrow band class D power amplifier @ 850 MHz using GaAs FET

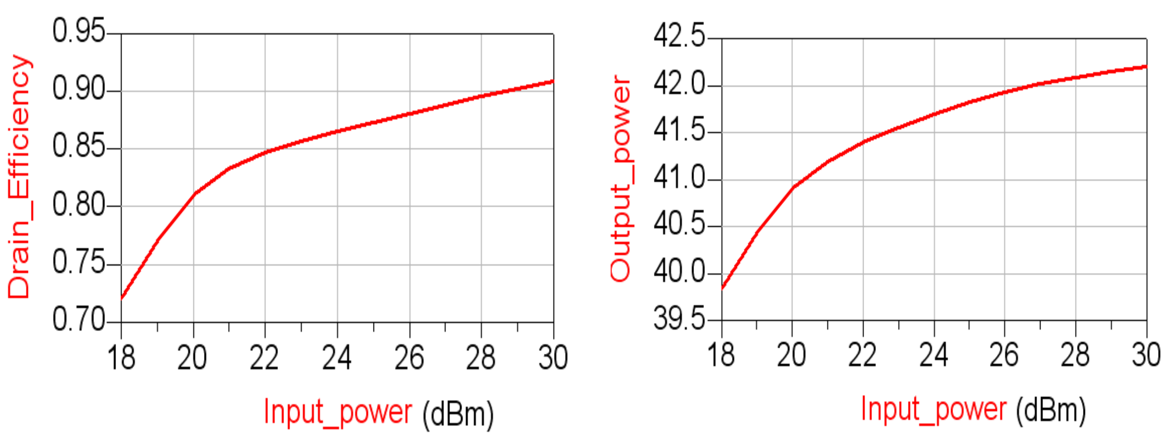

(a) (b)

Figure C2. (a) Drain efficiency vs. input power; (b) Output power vs. input power

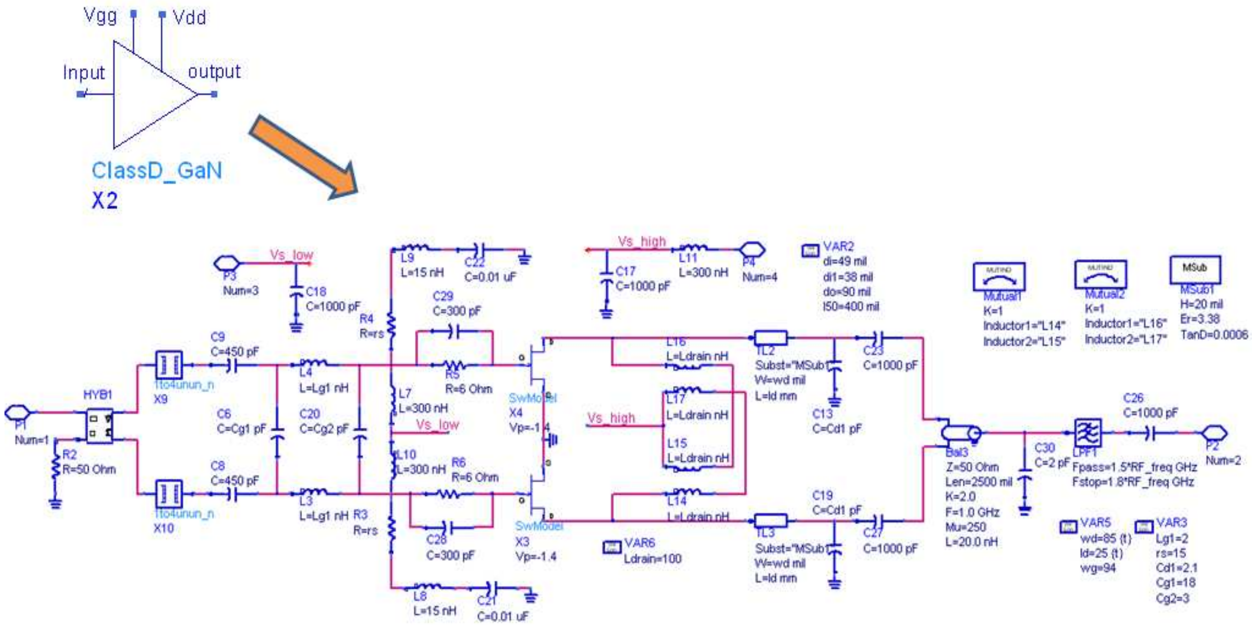

Figure C3. Wide band class D power amplifier (50 to 550 MHz) Eudyna GaN HEMT (EGN045MK)

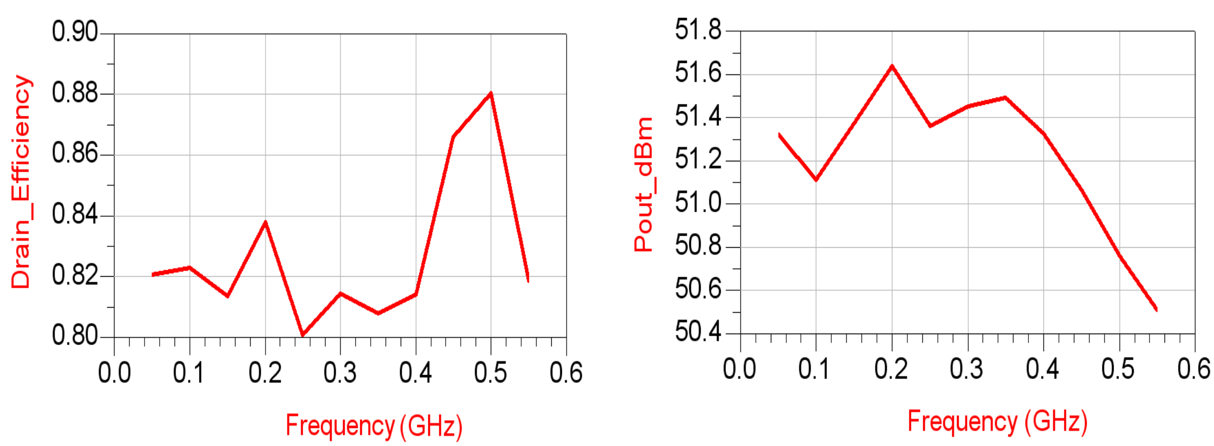

(a) (b)

Figure C4. (a) Drain efficiency vs. frequency; (b) Output power vs. frequency

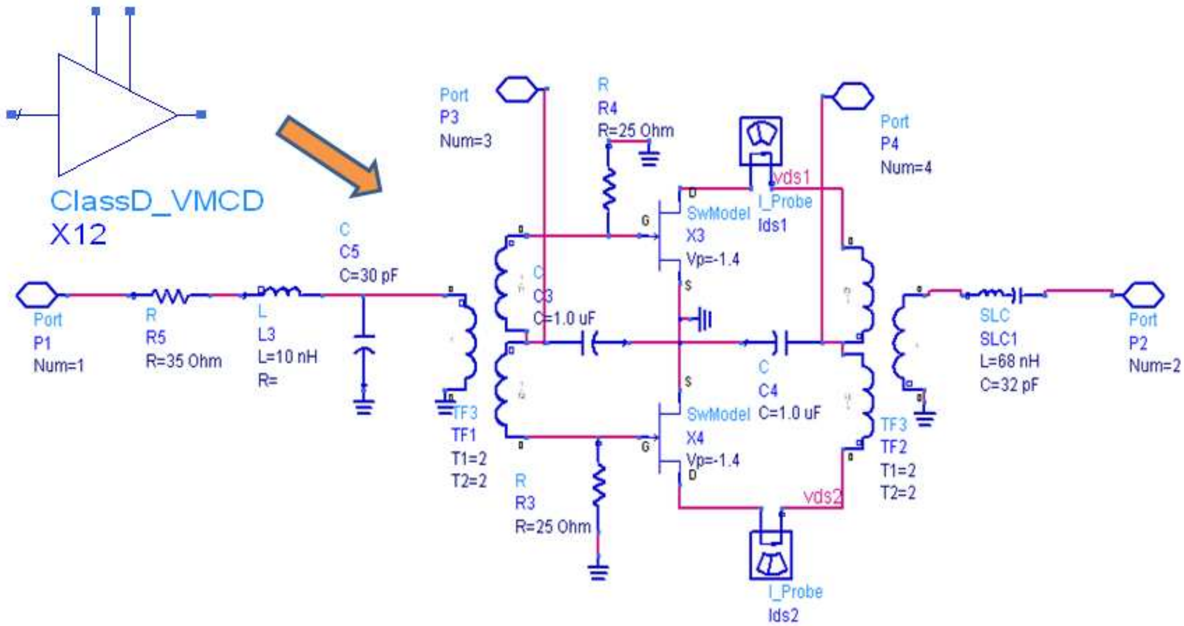

Figure C5. Narrow band Class D power amplifier @ 100 MHz using Eudyna GaN HEMT (EGN045MK)

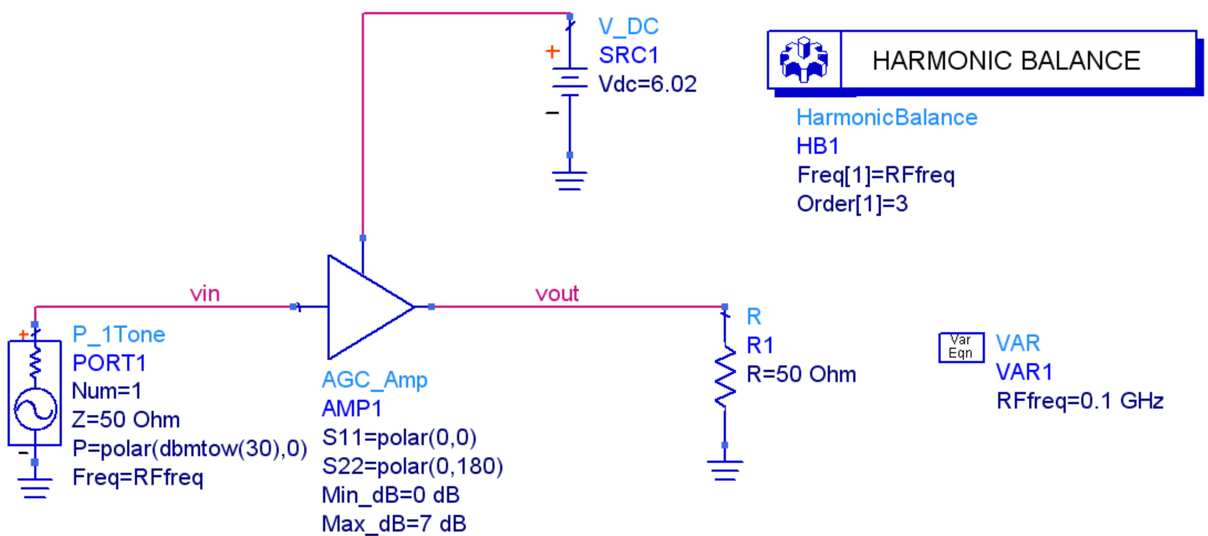

Figure C6. Test figure for voltage controlled amplifier

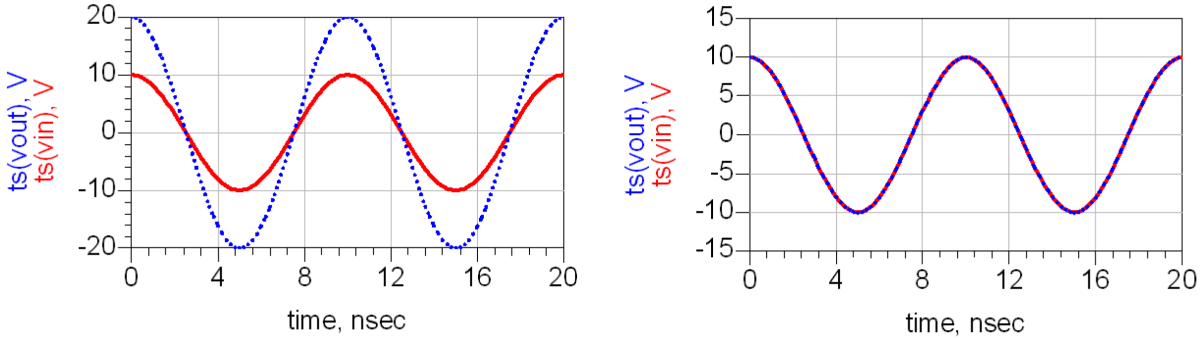

(a) (b)

Figure C7. Transient input and output waveforms: (a)V_{dc}=6.02V; (b) V_{dc}=-1V

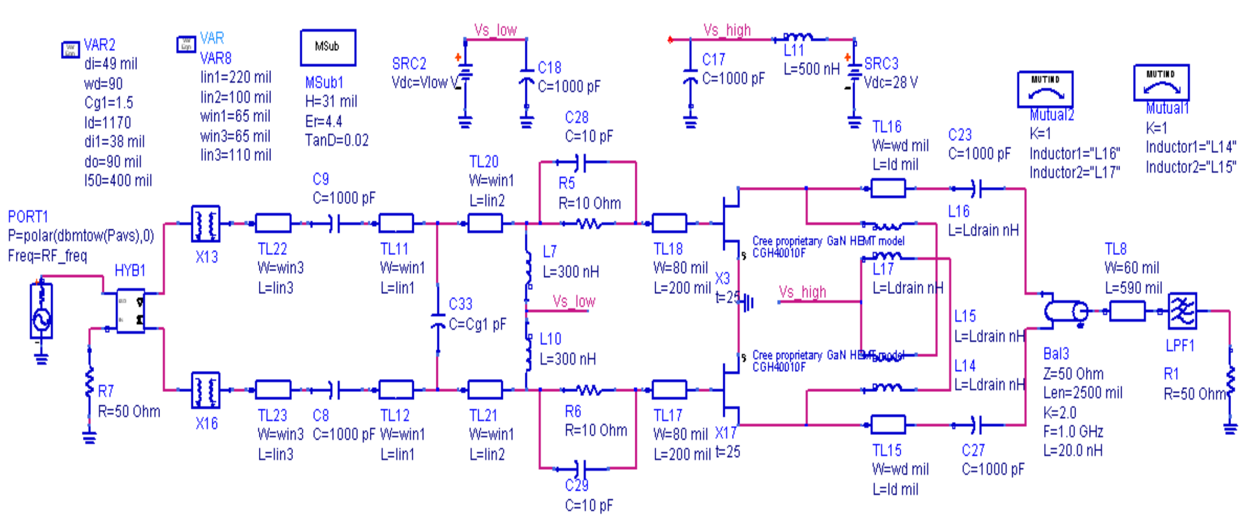

Figure C8. Wide band class D power amplifier (50 to 550 MHz) Cree GaN HEMT (CGH40010F)

Appendix D

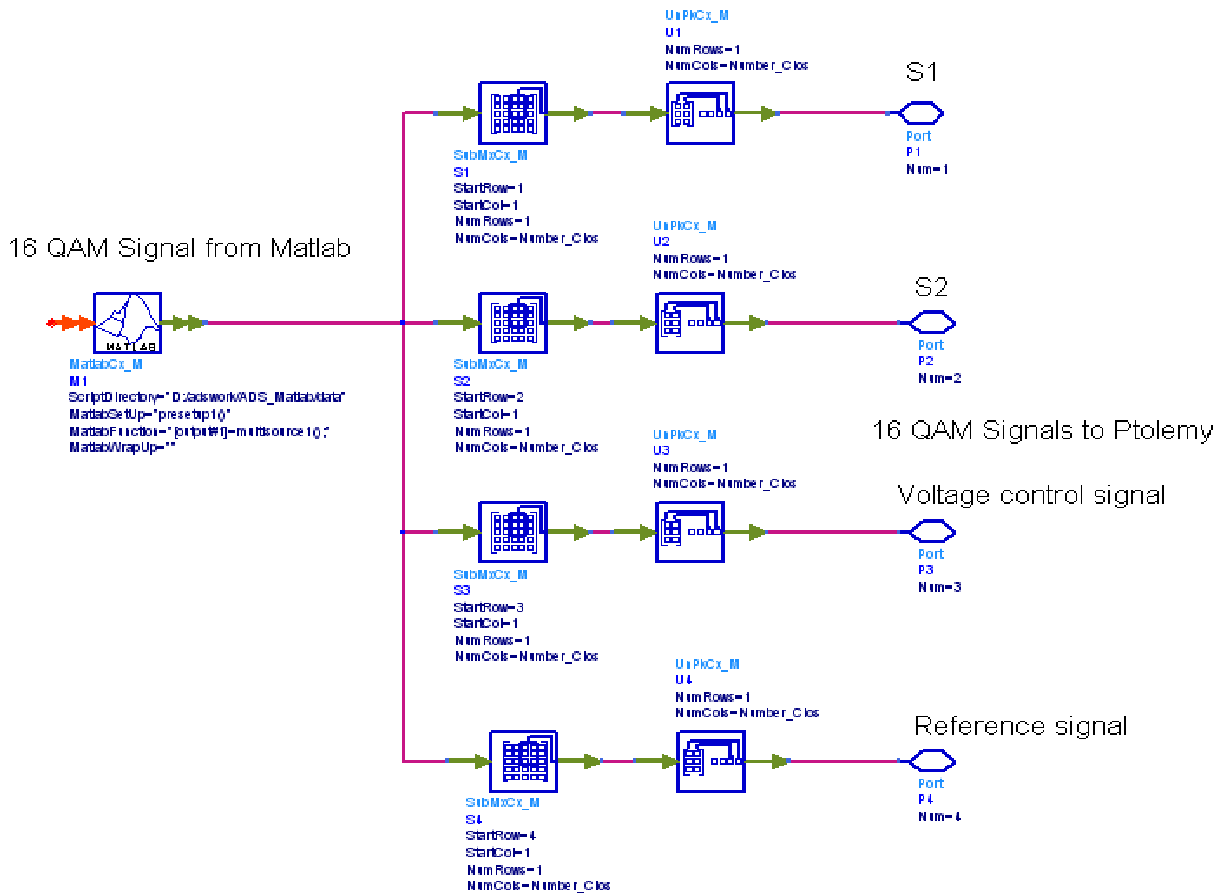

Figure D1. Sub-circuit of QAM signal generator

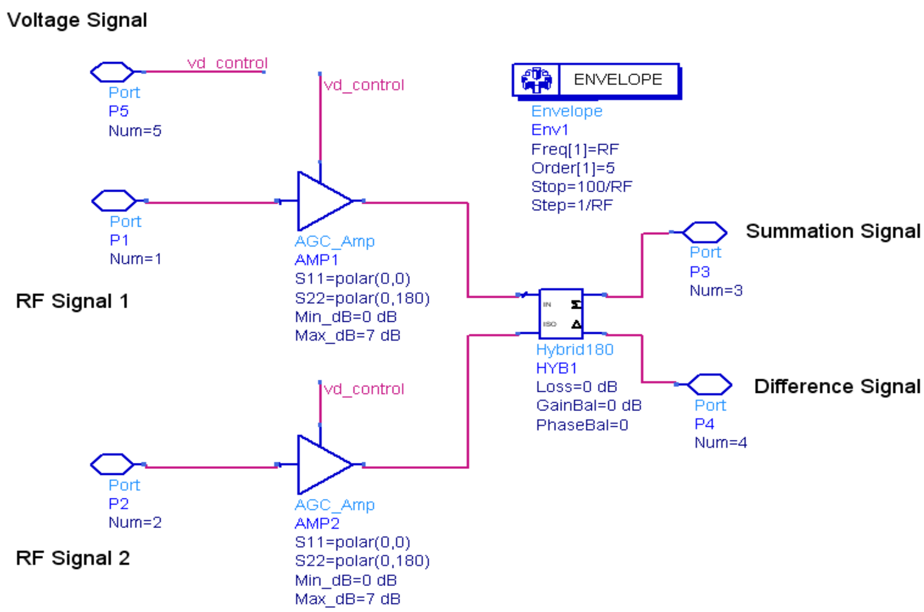

Figure D2. Sub-circuit of PA_Combiner unit

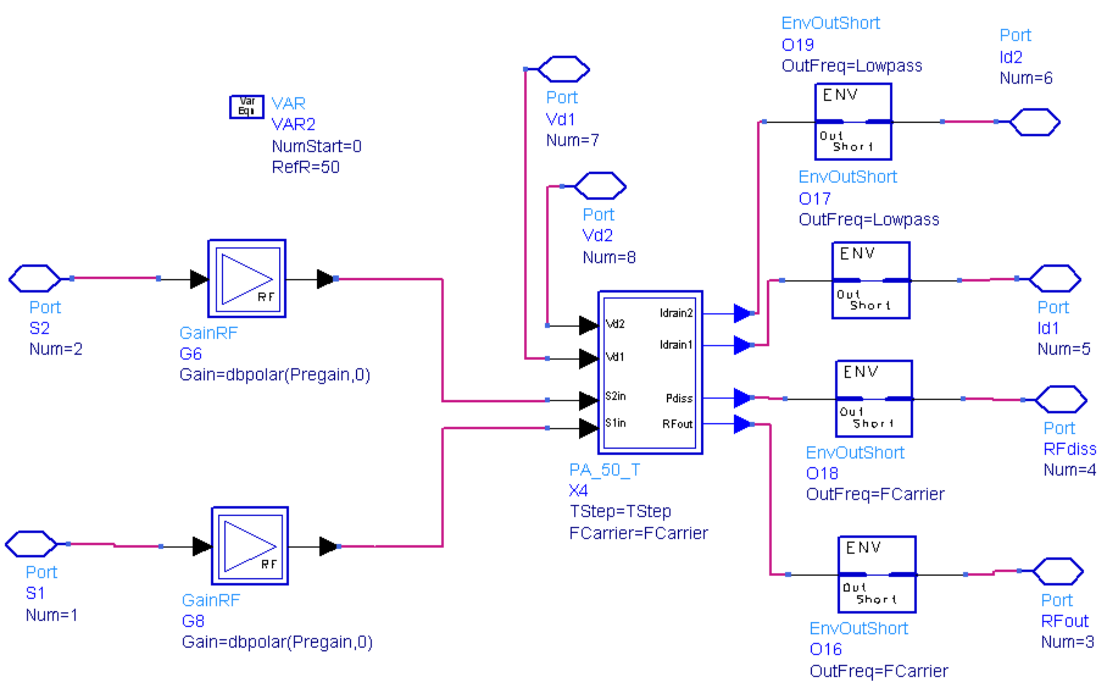

Figure D3. Sub-circuit of PA_CombinerN_new unit

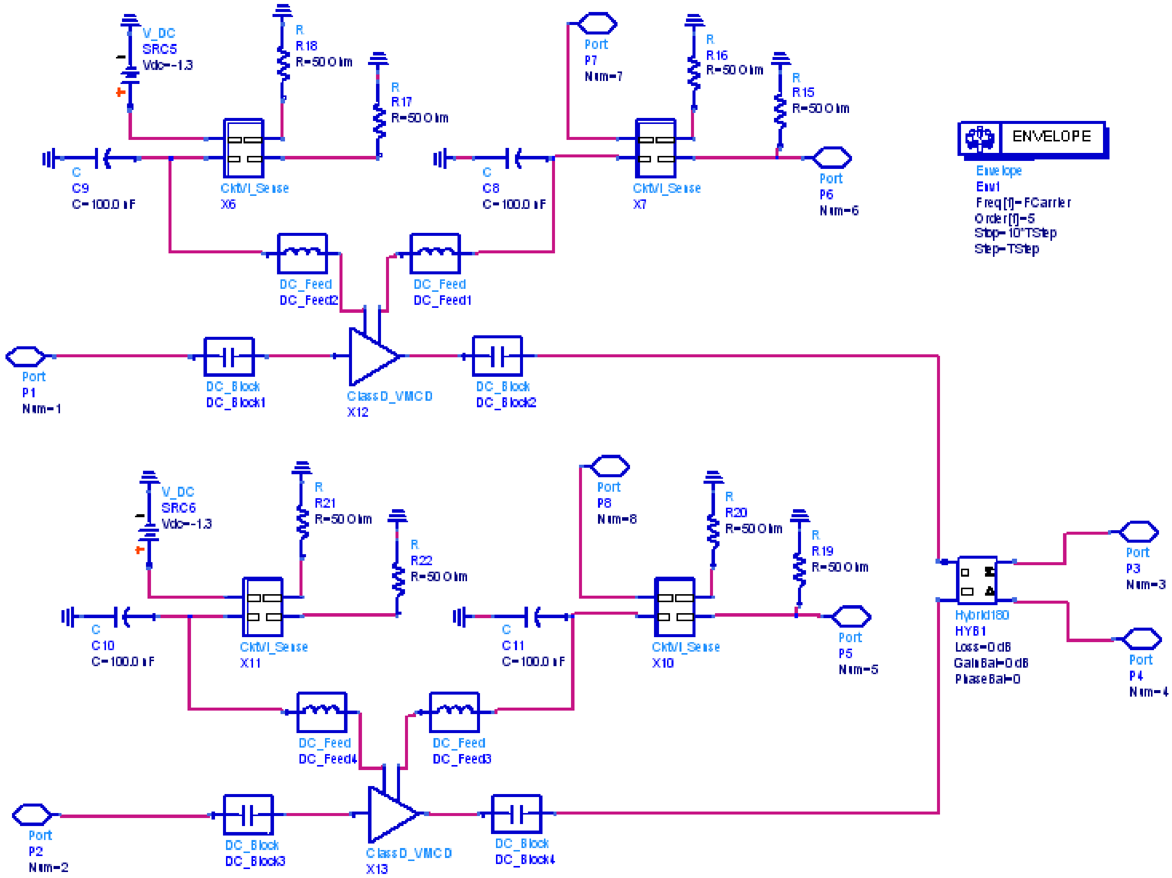

Figure D4. Sub-circuit of PA_50_T unit

Appendix E

```
%%%%%%%%%%%%%%%%%%%%%%%%%%%%%%%%%%%%%%%%%%%%%%%%%%%%%%%%%%%%%%%%%%%%%%%%%%%%%%%%%%%%%%%%%%%%%%%%%%%%%%%%%%%%%%%%%%%%%%%%%%%%%%%%%%%%%%%%%%%%%%%%%%%%%%%%%%%%%%%%
% function to generate the 16QAM with/without Adaptive bias scheme

function [s12_t]=multisource1()
clear all;
close all;
DataL=100;                            % bit number

Et=1e-12;                             % Calculation truncation error

M = 16;                               % Alphabet size
% x = randint(DataL,1,M);
x=dlmread('D:\adswork\ADS_Matlab\data\constant.txt');

% Use 16-QAM modulation to produce y.
const=modulate(modem.qammod(M),x);

scale = modnorm(const,'peakpow',1);    % Compute scale factor.
y = scale * const;                    % Modulate and scale to peak power =
1W.

Fd=1; Fs=16; Delay=3; R=.5; PropD = 0;

tx = [PropD: PropD + DataL - 1] ./ Fd;

v1=real(y);                                   % s_t=v1+j.*v2;
v2=imag(y);

% GA_M=[1,0.5,0.2];                 % Gain magnitude of voltage control PA
GA_M=[1,5.8/11.2,0.2];              % Gain magnitude of  SW Model PA
TA=acos(GA_M(2)/GA_M(1));           % Threshold angle

close all;

[ss_t1, to] = rcosflt(v1, Fd, Fs, 'normal/fir', R, Delay);
[ss_t2, to] = rcosflt(v2, Fd, Fs, 'normal/fir', R, Delay);

ss_t=ss_t1+j.*ss_t2;
stheta_t=angle(ss_t);

rmax=max(abs(ss_t));

Pin=(abs(ss_t)).^2;
Pin_max=max(Pin);
PAR_Input=10*log10(Pin_max/mean(Pin))

n=(DataL+2*Delay)*Fs/Fd;
```

```
for i=1:n
 if abs(ss_t(i))<Et
     ss_t(i)=0;
 end

 s1i_t(i)=GA_M(1)*(ss_t2(i)+ss_t1(i)*sqrt(rmax^2/(ss_t1(i)^2+ss_t2(i)^2+Et)-
1));
% Constant envelop signal of branch 1 I
 s1q_t(i)=GA_M(1)*(ss_t1(i)-ss_t2(i)*sqrt(rmax^2/(ss_t1(i)^2+ss_t2(i)^2+Et)-
1));
% Constant envelop signal of branch 1 Q
 s2i_t(i)=GA_M(1)*(ss_t2(i)-ss_t1(i)*sqrt(rmax^2/(ss_t1(i)^2+ss_t2(i)^2+Et)-
1));
% Constant envelop signal of branch 2I
 s2q_t(i)=GA_M(1)*(ss_t1(i)+ss_t2(i)*sqrt(rmax^2/(ss_t1(i)^2+ss_t2(i)^2+Et)-
1));
% Constant envelop signal of branch 2Q

 s1_t(i)=j.*s1i_t(i)+s1q_t(i);
 s2_t(i)=j.*s2i_t(i)+s2q_t(i);

 angle_s1(i)=angle(s1_t(i))-stheta_t(i);       % Normlized decomposed angle
 angle_s2(i)=angle(s2_t(i))-stheta_t(i);

 angle_s1(i)=mod(angle_s1(i),2*pi);            % Normlized decomposed angle
 angle_s2(i)=mod(angle_s2(i),2*pi);

 sw_t(i)=50;
% for voltage control amplifier use 6.02, for sw amplifier use 50
%  sw_t(i)=6.02;
% for voltage control amplifier use 6.02, for sw amplifier use 50

%%%%%%%%%%%%%%%%%%%%%%%%%%%%%%%%%%%%%%%%%%%%%%%%%%%%%%%%%%%%%%%%%%%%%%%%%%%%%
%%%
% Apply Adaptive Bias Method
%%%%%%%%%%%%%%%%%%%%%%%%%%%%%%%%%%%%%%%%%%%%%%%%%%%%%%%%%%%%%%%%%%%%%%%%%%%%%
%%%

%  if (abs(angle_s1(i))>=TA && abs(angle_s1(i))<=pi/2) ||
(abs(angle_s1(i))>pi/2 && abs(angle_s1(i))<=pi-TA)|| ...
%     (abs(angle_s1(i))>=pi+TA && abs(angle_s1(i))<=3*pi/2) ||
(abs(angle_s1(i))>3*pi/2 && abs(angle_s1(i))<=2*pi-TA)
%                 % Apply Adaptive Bias Scheme
% %   angle_s111(i)=angle_s1(i);
% %   angle_s222(i)=angle_s2(i);
%
%   aa=9/180*pi;         % phase compensate for sw amplifier
% %   aa=0;
%
%   angle_s1(i)=acos(GA_M(1)/GA_M(2)*cos(angle_s1(i)))-aa;
%   angle_s2(i)=-acos(GA_M(1)/GA_M(2)*cos(angle_s2(i)))-aa;
%
```

```
%   s1_t(i)=abs(s1_t(i))*exp(j*(angle_s1(i)+stheta_t(i)))/GA_M(1)*GA_M(2);
%   s2_t(i)=abs(s2_t(i))*exp(j*(angle_s2(i)+stheta_t(i)))/GA_M(1)*GA_M(2);
%   sw_t(i)=25;                              % for voltage control
amplifier use -1, for sw amplifier use 25
% %   sw_t(i)=-1;                              % for voltage control
amplifier use -1, for sw amplifier use 25
%
%   ss_t1(i)=real(s1_t(i)+s2_t(i));
%   ss_t2(i)=imag(s1_t(i)+s2_t(i));
%
%
s1i_t(i)=GA_M(2)*(ss_t2(i)+ss_t1(i)*sqrt(rmax^2/(ss_t1(i)^2+ss_t2(i)^2+Et)-
1));          % Constant envelop signal of branch 1 I
%   s1q_t(i)=GA_M(2)*(ss_t1(i)-
ss_t2(i)*sqrt(rmax^2/(ss_t1(i)^2+ss_t2(i)^2+Et)-1));
% Constant envelop signal of branch 1 Q
%
%   s2i_t(i)=GA_M(2)*(ss_t2(i)-
ss_t1(i)*sqrt(rmax^2/(ss_t1(i)^2+ss_t2(i)^2+Et)-1));
% Constant envelop signal of branch 2 I
%
s2q_t(i)=GA_M(2)*(ss_t1(i)+ss_t2(i)*sqrt(rmax^2/(ss_t1(i)^2+ss_t2(i)^2+Et)-
1));
% Constant envelop signal of branch 2 Q
%
%   s1_t(i)=GA_M(1)/GA_M(2)*(j.*s1i_t(i)+s1q_t(i));
%   s2_t(i)=GA_M(1)/GA_M(2)*(j.*s2i_t(i)+s2q_t(i));
%
%  end
%
%%%%%%%%%%%%%%%%%%%%%%%%%%%%%%%%%%%%%%%%%%%%%%%%%%%%%%%%%%%%%%%%%%%%%%%%%%%%%%%
%%%

end

s12_t=[s1_t;s2_t;sw_t;ss_t'];

%%%%%%%%%%%%%%%%%%%%%%%%%%%%%%%%%%%%%%%%%%%%%%%%%%%%%%%%%%%%%%%%%%%%%%%%%%%%%%%
%%%%%%%%%%%%%%%%%%%%%%%%%%%%%%%%%%%%%%%%%%%%%%%%%%%%%%%%%%%%%%%%%%%%%%%%%%%%%%%
% to clean the old file which is used to store the data from Ptolemy output

function presetup()
fopen('D:\adswork\ADS_Matlab\data\ref.txt','w');
fopen('D:\adswork\ADS_Matlab\data\test.txt','w');
close all;



%%%%%%%%%%%%%%%%%%%%%%%%%%%%%%%%%%%%%%%%%%%%%%%%%%%%%%%%%%%%%%%%%%%%%%%%%%%%%%%
%%%%%%%%%%%%%%%%%%%%%%%%%%%%%%%%%%%%%%%%%%%%%%%%%%%%%%%%%%%%%%%%%%%%%%%%%%%%%%%
% Written data from data from Ptolemy output

function write_token(ref,test)   % plot s_t and sout_t in constellation

preref=dlmread('D:\adswork\ADS_Matlab\data\ref.txt');
```

```
afref=[preref ref];
dlmwrite('D:\adswork\ADS_Matlab\data\ref.txt', afref);

pretest=dlmread('D:\adswork\ADS_Matlab\data\test.txt');
aftest=[pretest test];
dlmwrite('D:\adswork\ADS_Matlab\data\test.txt', aftest);


%%%%%%%%%%%%%%%%%%%%%%%%%%%%%%%%%%%%%%%%%%%%%%%%%%%%%%%%%%%%%%%%%%%%%%%%%%%%%%
%%%%%%%%%%%%%%%%%%%%%%%%%%%%%%%%%%%%%%%%%%%%%%%%%%%%%%%%%%%%%%%%%%%%%%%%%%%%%%
% flot the constellation of reference and amplified signals
function finalplot()   % plot s_t and sout_t in constellation

close all;
clear all;

ref=dlmread('D:\adswork\ADS_Matlab\data\ref.txt');
test=dlmread('D:\adswork\ADS_Matlab\data\test.txt');

Fd=1; Fs=16; Delay=3; R=.5; PropD = 0;

nn=size(ref,2)-Delay*Fs;

Pout=(abs(ref)).^2;
Pout_max=max(Pout);
PAR_Output=10*log10(Pout_max/mean(Pout))

for i=(Delay*Fs+1):nn
    ref1(i-Delay*Fs)=ref(i);
    test1(i-Delay*Fs)=test(i);
end

ref=downsample(ref1,Fs/Fd);
test=downsample(test1,Fs/Fd);

DataL=100;   % bit number


scatterplot(conj(ref(1:DataL)));
title('reference')
hold on;

scatterplot(test(1:DataL));
title('demodulation result')
```

Vita

Song Lin was born in Fujian, China on April 10, 1978. He earned his B.S and M.S degrees from the Radio Engineering Department, Southeast University, Nanjing, China in 2000 and 2004, respectively. He was with State Key Laboratory of Millimeter Wave, Nanjing, China from 2000 -2004. In August 2004, he joined the Microwave Circuit and Antenna Group at the University of Tennessee, Knoxville as a PhD candidate. At the University of Tennessee, Knoxville, he has worked with teams of fellow PhD students, professors, and the research team at Rockwell Collins Corp. In the summers of 2007 and 2008, he worked on wideband GaN power amplifier design (distributed and feedback amplifiers), the implementation of the hybrid microwave integrated circuit, and millimeter wave passive component design at MITEQ Inc as an RF Engineer Intern. He has been a teaching assistant for multiple undergraduate courses at the University of Tennessee, Knoxville. His research areas include: high efficiency and high linearity power amplifiers and transmitters; power combining technology; UWB components; RF/Microwave circuits, systems and antennas; and millimeter wave circuits and antennas. He is a member of IEEE. He is the recipient of the Chancellor's Award for Extraordinary Professional Promise. He has published numerous journal and conference papers, and has also presented his papers at several international conferences such as the IEEE International Microwave Symposium and at the IEEE International Symposium on Antennas and Propagation.